Imperial College London

Neutrino oscillation analysis using T2K data with additional single ring NCπ^0 samples

---

Daniel George Raymond Martin

Department of Physics

Imperial College London

February 19, 2024

Submitted in part fulfilment of the requirements for the degree of

Doctor of Philosophy

Declaration of Originality

I declare that this thesis was composed by myself, that the work contained herein is my own except where explicitly stated otherwise in the text, and that this work has not been submitted for any other degree or professional qualification. As part of the T2K and SK collaborations, data and inputs made by the collaborations as a whole are used for the work described and referenced where used. Pre-made software is used for execution of some parts of the work presented, notably:

- The photos used in Chapter 2 were collected by Patrick de Perio and Nick Prouse, the photogrammetry software used for the final Super-K reconstruction was developed by Nick Prouse. I developed the PMT feature recognition, labelling, and analysis process to generate PMT data points used for the reconstruction.

- The MaCh3 software used in the atmospheric neutrino data fit and oscillation analysis in Chapters 6 and 7 is developed and maintained by the T2K collaboration. I was responsible for developing, implementing, and analysing the impacts of the NCπ^0 samples and systematics within the MaCh3 framework.

Copyright Statement

The copyright of this thesis rests with the author. Unless otherwise indicated, its contents are licensed under a Creative Commons Attribution-Non Commercial 4.0 International Licence (CC BY-NC).

Under this licence, you may copy and redistribute the material in any medium or format. You may also create and distribute modified versions of the work. This is on the condition that: you credit the author and do not use it, or any derivative works, for a commercial purpose.

When reusing or sharing this work, ensure you make the licence terms clear to others by naming the licence and linking to the licence text. Where a work has been adapted, you should indicate that the work has been changed and describe those changes.

Please seek permission from the copyright holder for uses of this work that are not included in this licence or permitted under UK Copyright Law.

Acknowledgements

This thesis would not have been possible without the help and support of many, many people. First and foremost, I would like to thank my supervisor, Mark, for his guidance, help, and patience throughout the PhD. It is not easy doing the bulk of a PhD through a global pandemic and I owe it to Mark for keeping me going. Thanks to the entire Imperial long baseline neutrino group, who at various point have all chipped in suggestions and aid in weekly meetings. Notably, I would like to thank Ed and Charlie for putting up with some merciless questioning from myself. Thanks also to the TRIUMF photogrammetry group who helped with the SK reconstruction process from beginning to end.

Being part of the T2K collaboration has been a great experience. Working on SK shifts, the data reduction team, and through to performing an oscillation analysis has been enlightening to the sheer time, effort, and dedication that goes into these results. So thank you to everyone that has worked on T2K and SK. In particular, many thanks to the MaCh3 group, without whom this thesis would not have been possible.

Finally, I want to thank Alice and Brian, to whom I owe the world, but for now will have to accept a neutrino oscillation analysis. Thank you for putting up with me coming home to tap away at my computer and not help on the farm. Thanks to Sheila, Sally, and Martyn for letting me stay in their houses. Thank you to Brandon, and to Reuben, and to Deema, and all my friends and family that have supported me throughout this PhD. I am deeply grateful, and I hope you all know it.

Abstract

This thesis presents work done as part of the T2K and SK collaborations to perform an in-situ reconstruction of PMT locations in Super-K and the addition of single ring and two ring NCπ^0 event samples to the T2K oscillation analysis. Photos taken by drone in Super-K were segmented using machine learning algorithms to identify and reconstruct PMT positions. Feature recognition of PMTs is shown to be viable, though it proved difficult to uniquely identify PMTs for reconstruction.

Markov Chain Monte-Carlo techniques were used as part of the MaCh3 software framework to perform an oscillation analysis with new NCπ^0 samples using run 1-10 T2K data representing 19.664×10^{20} POT in FHC and 16.346×10^{20} POT in RHC. The dominant background to single ring electron-like ν_e appearance samples at Super-K is NCπ^0 events. The new NCπ^0 samples aim to constrain the background such that additional oscillated ν_e events can be exploited for increased sensitivity in oscillation fits. Super-K detector systematic uncertainties were updated to include the NCπ^0 samples with a new atmospheric neutrino fit, resulting in larger systematic uncertainties than previous analyses.

An oscillation fit with new NCπ^0 samples and Super-K detector systematics gives credible intervals of: $\sin^2(\theta_{13})$ =[0.0185, 0.0417], $\sin^2(\theta_{23})$ =[0.44, 0.58], Δm^2_{23} =NO:[2.4, 2.6] IO:[-2.6, -2.4], and δ_{CP} =[-π, -0.251] [2.551, π] to 2σ confidence. With the application of an additional $\sin^2(\theta_{13})$ constraint from reactor neutrino experiments, the intervals are: $\sin^2(\theta_{23})$ =[0.45, 0.58], Δm^2_{23} =NO: [2.4, 2.6] IO: [-2.6, -2.5], and δ_{CP} =[$-\pi$, -0.209] to 2σ confidence. Asimov fits show an additional 3.5% sensitivity to δ_{CP} with the NCπ^0 samples added. The credible intervals are in agreement with previous T2K analyses and no further constraint to δ_{CP} is found. A slightly stronger preference for normal mass ordering, upper $\sin^2(\theta_{23})$ octant is observed compared to T2K with 62.1% posterior probability.

Contents

Declaration of Originality 2

Copyright Statement 3

Acknowledgements 4

Abstract 5

Contents 6

1 Neutrino Physics **17**

1.1 History 17

1.2 Standard Model Neutrinos 19

1.3 Oscillations 20

1.4 The Tokai to Kamioka (T2K) Experiment 27

1.4.1 ND280 and INGRID 28

1.4.2 The Super Kamiokande (Super-K) Experiment 30

1.5 Neutrino interactions at Super-K 31

1.5.1 NC1π^0 Events 33

1.6 Future experiments and precision measurements 34

2 Photogrammetry **35**

2.1 Introduction 35

2.2 Machine Learning 37

2.3 Drone photos of Super-K 42

2.4 Constraints from Super-K construction 43

2.5 Tank Geometry . . . 45
2.6 Feature detection in drone images . . . 45
2.6.1 Training and augmentation . . . 46
2.6.2 CNN performance evaluation . . . 48
2.7 Analysis of segmented images . . . 50
2.7.1 Coarse PMT location . . . 50
2.7.2 Super module boundary location . . . 50
2.7.3 PMT labelling . . . 52
2.7.4 Ellipse fit to bolts . . . 53
2.7.5 Pruning bad PMTs . . . 53
2.7.6 Final sample of PMTs . . . 56
2.8 Photogrammetry reconstruction . . . 57
2.8.1 Feature analysis of reconstructed Super-K geometry . . . 58
2.9 Conclusions . . . 59

3 SK event simulation, reconstruction, and sample selection **61**
3.1 Simulation . . . 61
3.2 fiTQun reconstruction . . . 62
3.3 Super-K event selections . . . 63
3.3.1 Events Fully Contained in the Fiducial Volume (FCFV events) . . . 64
3.3.2 Single ring e-like selection . . . 65
3.3.3 Single ring e-like CC1π sample . . . 68
3.3.4 Single ring μ like sample . . . 69
3.4 Summary of Super-K Samples . . . 70

4 NCπ^0 Samples **71**
4.1 Single ring π^0 Selection . . . 72
4.2 Two Ring NCπ^0 Events . . . 77

4.2.1 Backgrounds . . . 83
4.2.2 NCπ^0 sample mass peak fit . . . 86

5 Bayesian statistics and MaCh3 **87**

5.1 Bayesian statistics . . . 88
5.2 Markov Chain Monte Carlo (MCMC) . . . 89
5.2.1 Metropolis-Hastings . . . 89
5.3 MaCh3 . . . 90

6 Super-K Detector Systematics **93**

6.1 Atmospheric Fit . . . 94
6.1.1 Hybrid π^0 sample . . . 96
6.2 Atmospheric fit results . . . 98
6.3 Detector Covariance Matrix . . . 102

7 Oscillation analysis **107**

7.1 The MaCh3 oscillation fit . . . 107
7.1.1 ND280 Samples . . . 110
7.1.2 Systematic parameters . . . 110
7.1.3 Fits performed . . . 114
7.2 Asimov fit with new Super-K detector matrix . . . 115
7.3 Asimov fit with additional NCπ^0 samples . . . 117
7.4 Data fit with the additional samples and covariance matrix . . . 119
7.4.1 Posterior predictions . . . 119
7.4.2 P-values . . . 121
7.4.3 Post-fit Parameters . . . 121
7.4.4 Oscillation parameter contours and credible intervals . . . 122
7.5 Result summary . . . 128

8 Conclusions **129**

A Appendix 1 **145**

B Appendix 2 - Additional OA fit plots **150**

B.1 Super-K and ND280 samples 150

B.2 Additional Posterior Predictions 154

B.3 Additional Data Fit Contours 164

List of Tables

1.1 Current measurements made for each PMNS parameter. 23

2.1 PMT selection efficiencies. 57

3.1 Software versions used in analysis for MC generation and event reconstruction. 61

3.2 FHC 1Re event rates 68

4.1 Efficiencies and purities of FHC and RHC one ring NCπ^0 sample. 74

4.2 NCπ^0 single ring sample interaction mode breakdown 74

4.3 FHC efficiencies and purities for 2RNCπ^0 samples. 78

4.4 NCπ^0 Two ring sample interaction mode breakdown 80

4.5 Final state breakdown for plots 83

4.6 FHC final state breakdown for 1R and 2R NCπ^0 samples 85

6.1 Parameters used in Super-K OA samples 94

6.2 Super-K detector systematic visible energy bins 94

6.3 Super-K detector systematic final state topologies 95

6.4 Binning for NCπ^0 samples in the detector covariance matrix 102

7.1 Oscillation parameters used in Asimov fits. 109

7.2 OA fits performed 114

7.3 Data event rates for NCπ^0 samples 119

7.4 Highest posterior point and 2σ CI 124

A.1 Binning for official T2K samples in the detector covariance matrix 149

List of Figures

1.1 The Standard Model of Particle Physics 20

1.2 Mass ordering for neutrinos. 25

1.3 The T2K experiment 27

1.4 T2K ν_μ survival probability 28

1.5 ND280 and INGRID experimental setups. 29

1.6 P0D π^0 events. 29

1.7 The Super-K experiment 30

1.8 Cherenkov rings 31

1.9 ν and $\bar{\nu}$ energies at Super-K 32

1.10 CC Feynman diagrams 33

2.1 Flowchart of development process 36

2.2 Neural network construction example 37

2.3 Example of encoder and decoder structure for a CNN. 38

2.4 Simple example of a feature convolution 39

2.5 Activation functions. 40

2.6 UNet construction. 42

2.7 Effect to dark noise after Tank Open Work. 43

2.8 Effect of altered tank geometry on event reconstruction. 44

2.9 Classes and validation of training. 45

2.10 Comparison of two class and three class training. 46

2.11 Effect of ISO noise on PMT identification. 47

2.12 Comparison of good and bad image reconstruction . . . 48
2.13 Horizontal and vertical scans of PMT masks for PMT location. . . . 49
2.14 Number of PMTs per image and bolts per PMT. . . . 51
2.15 Super module boundaries located by PMT mask scans . . . 51
2.16 Super module tracking between images. . . . 52
2.17 Definition of metrics to determine goodness of PMT segmentation. . . . 54
2.18 Pixel scores for PMTs by region. . . . 55
2.19 Evolution of number of reconstructed PMTs. . . . 56
2.20 Reprojection error definition. . . . 58
2.21 Reconstructed SK PMTs. . . . 59

3.1 Definition of ToWall and DWall parameters. . . . 64
3.2 e-like and μ-like event examples . . . 66
3.3 Summary plots of the 1Re Super-K samples . . . 67
3.4 True neutrino energy for 1Re1dcye Super-K sample . . . 69
3.5 True neutrino energy for 1Rμ Super-K samples . . . 70

4.1 NCπ^0 Feynman diagram and photon arrangement. . . . 72
4.2 Single ring NCπ^0 cuts after FCFV selection for FHC events. . . . 75
4.3 Final NCπ^0 sample plots for FHC events. . . . 76
4.4 2RNCπ^0 selection for FHC events. . . . 79
4.5 Final 2RNCπ^0 sample plots for FHC events. . . . 80
4.6 Figure of Merit plots for PID cuts in the 2R NCπ^0 sample . . . 82
4.7 2RNCπ^0 final state topologies and backgrounds . . . 84
4.8 π^0 mass fit . . . 86

5.1 MCMC parameter trace examples. . . . 91
5.2 Single parameter autocorrelation . . . 92

6.1 Atmospheric fit MC distributions . . . 96
6.2 hybrid-π^0 sample likelihood scans. . . . 97

6.3 Log Likelihood values for atmospheric fit . . . 98
6.4 Examples of event distributions in detector covariance matrix bins. . . . 100
6.5 Atmospheric fit parameter autocorrelations . . . 100
6.6 Atmospheric samples post-fit . . . 101
6.7 SK detector covariance matrices. . . . 103
6.8 Correlations from SK detector covariance matrix. . . . 104
6.9 Super-K detector covariance matrix errors with new NCπ^0 samples . . . 106

7.1 NCπ^0 MC used for fit . . . 109
7.2 ND280 fit CC1π samples . . . 110
7.3 Asimov fit with new covariance matrix . . . 115
7.4 Asimov contours with NCπ^0 samples . . . 116
7.5 1D Asimov δ_{CP} contours before and after adding NCπ^0 samples. . . . 118
7.6 Asimov fit $\sin^2(\theta_{23})$ octants and Δm^2_{23} mass ordering preferences. . . . 118
7.7 Posterior predictives for NCπ^0 samples. . . . 120
7.8 P-value calculation for all samples in data fit . . . 121
7.9 Cross-section parameter post-fit values with and without NCπ^0 samples . . . 122
7.10 Flux parameter post-fit values with and without NCπ^0 samples . . . 123
7.11 Data fit contours with steps for both mass orderings. . . . 124
7.12 1D oscillation analysis fit contours . . . 125
7.13 Data fit $\sin^2(\theta_{23})$ octants and Δm^2_{23} mass ordering preferences. . . . 126
7.14 NCπ^0 +SKDetSyst and T2K data contour comparison . . . 127

A.1 FCFV selections FHC . . . 145
A.2 FCFV selections RHC . . . 146
A.3 RHC 2RNCπ^0 cut by cut and summary plots. . . . 146
A.4 Atmospheric fit Data MC comparisons . . . 147
A.5 More atmospheric fit Data MC comparisons . . . 148

B.1 1Re, 1Rμ, and 1RCC1π MC . . . 150

B.2 Posterior predictions for the official T2K samples from the final data fit with NCπ^0 samples without RC. 160
B.3 Posterior predictions for the official T2K samples from the final data fit with NCπ^0 samples with RC. 161
B.4 Posterior predictions for the official T2K samples with updated SK detector systematics and no NCπ^0 samples without RC. 162
B.5 Posterior predictions for all T2K samples with updated SK detector systematics and no NCπ^0 samples with RC. 163
B.6 Data fit contours with normal ordering 164
B.7 Data fit contours with inverted ordering 165

List of Acronyms

T2K Tokai to Kamioka

Super-K Super Kamiokande

Hyper-K Hyper Kamiokande

IWCD Intermediate Water Cherenkov Detector

PMT Photomultiplier Tube

ID Inner Detector

OD Outer Detector

TOW Tank Open Work

FCFV Fully Contained in the Fiducial Volume

NC Neutral Current

CC Charged Current

1Re Single Ring Electron-like

1Re1de Single Ring Electron-like plus 1 decay electron

1Rμ Singe Ring Muon-like

1RNCπ^0 Single Ring NCπ^0

1RNCπ^0 Two Ring NCπ^0

CNN Convolutional Neural Network

MCMC Markov Chain Monte-Carlo

MaCh3 Markov Chain for 3 flavour oscillations

FHC Forward Horn Current

RHC Reverse Horn Current

CP Charge Parity

SM Standard Model of Particle Physics

SSM Standard Solar Model

PID Particle IDentification

Chapter 1

Neutrino Physics

This chapter introduces the neutrino, beginning with its history and discovery before delving into oscillation behaviour within and beyond the Standard Model of Particle Physics (SM) . The Tokai-to-Kamioka (T2K) and Super-Kamiokande (Super-K) experiments are described as well as the context and importance of Neutral current π^0 neutrino interactions.

1.1 History

Neutrinos were first theorised by W. Pauli when the observed distribution of electron energies from nuclear beta decay seemed to violate energy conservation. In such experiments, an electron ejected from the nucleus during a two-body β-decay should have a single known energy equal to the decrease in binding energy in the nucleus. However, a continuous energy spectrum was observed. Pauli proposed the neutron (as he called it) as a neutral spin-$\frac{1}{2}$ particle that obeyed the exclusion principle, did not travel at the speed of light, and had a mass similar to the electron [1].

In 1934, E. Fermi proposed a model for beta decay [2] where electrons and neutrinos can be created and annihilated and as such the classic β-decay can take place:

$$\begin{aligned} p &\rightarrow n + \nu_e + e^+ \\ n &\rightarrow p + \bar{\nu}_e + e^- \end{aligned} \tag{1.1}$$

The first direct detection of neutrinos by C. Cowan and F. Reines was through inverse beta decay from reactor antineutrinos in 1956 [3]. The muon neutrino, ν_μ, and therefore the concept of neutrino flavour, was discovered in pion decays at the Brookhaven AGS experiment in 1962 [4]. The tau neutrino was discovered in 2001 by the DONUT collaboration [5].

Solar neutrinos

Neutrino oscillations were first theorised in 1957 by B. Pontecorvo [6] and flavour oscillations in 1962 by Z. Maki, M. Nakagawa, and S. Sakata [7] following the discovery of the muon neutrino. The first indication for neutrino oscillations came from the Homestake experiment in 1964 [8]. A deficit of solar neutrinos was observed compared to the Standard Solar Model (SSM), which describes the structure, dynamics, and neutrino production of the Sun based on experimental observations [9]. This was further reinforced by the IMB and Kamiokande experiments which measured the same neutrino deficit and became known as the solar neutrino problem. The experiments measured electron neutrino interactions in their medium and not the total neutrino flux. The SNO experiment resolved the solar neutrino problem by measuring the total solar neutrino flux via neutral current and elastic scattering interactions on heavy water which agreed with the SSM. SNO also measured a deficit of electron neutrinos via charged current interactions when compared to the total neutrino flux, providing evidence for neutrino oscillations [10].

Atmospheric Neutrinos

Atmospheric neutrinos come from high energy cosmic ray interactions in the upper atmosphere which dominantly produces pions, and less abundantly kaons. Pions decay to, on average, two muon neutrinos and one electron neutrino per pion decay. The Super-Kamiokande (Super-K) experiment can measure the atmospheric neutrino flux as a function of zenith angle by reconstructing the incoming neutrino direction. Neutrinos produced in the atmosphere above Super-K travel a short distance, whereas those produced on the other side of the Earth have further to travel. Without neutrino oscillations, it would be expected that the muon neutrino flux would be equal across all zenith angles.

Super-K measured a drop in events dependent on zenith angle which indicated the neutrino flavours were oscillating, the first direct evidence of neutrino oscillations [11].

Reactor Neutrinos

Nuclear reactors provide an intense, terrestrial source of electron anti-neutrinos in the MeV energy range from nuclear fission. Reactor oscillation experiments measure inverse β decay events, $\bar{\nu_e} + p \rightarrow e^+ + n$. Generally, liquid scintillator is used as a target medium due to the low energy of neutrinos and the ease of building large scale experiments. Reactor experiments measure $\bar{\nu_e}$ disappearance and provide powerful constraints on oscillation parameters with careful choice of baselines [12, 13].

1.2 Standard Model Neutrinos

The Standard Model of particle physics (SM) was devised through theoretical and experimental effort throughout the 1970s and 1980s [15]. The SM describes the fundamental forces and elementary particles governing the universe. Figure 1.1 shows the current best understanding of fermions and bosons that exist. The SM has 12 fermions, the building blocks of matter, e.g. the up and down quark make up protons and neutrons. There are 6 quarks and 6 leptons separated by mass and flavour into three generations, (u,d), (c,s), and (t,b) in the quark sector and e, μ, τ in the lepton sector.

In the SM, neutrinos are neutral spin-$\frac{1}{2}$ fermions. Neutrinos have three flavour states named for their charged lepton counterparts; electron, muon, and tau neutrinos (ν_e, ν_μ, ν_τ) and interact via the weak force only, coupling to $W^\pm$ and Z bosons with these flavours. SM interactions are connected via a gauge symmetry of $SU(3)_C \times SU(2)_L \times U(1)_Y$ where $SU(3)_C$ determines the behaviour of strong interactions. $SU(2)_L \times U_Y$ is the gauge symmetry responsible for electro-weak interactions and is a unification of two underlying symmetries responsible for weak and electromagnetic interactions. Electro-weak unification was first theorised by Weinberg [16] and proven experimentally with the discovery of $W^\pm$ and Z bosons [17, 18].

In 1957, Wu et al. demonstrated maximal parity violation in the weak interaction by observing electron helicity in β decays of ^{60}Co, [19] meaning only left-handed chiral fermion fields interact via the

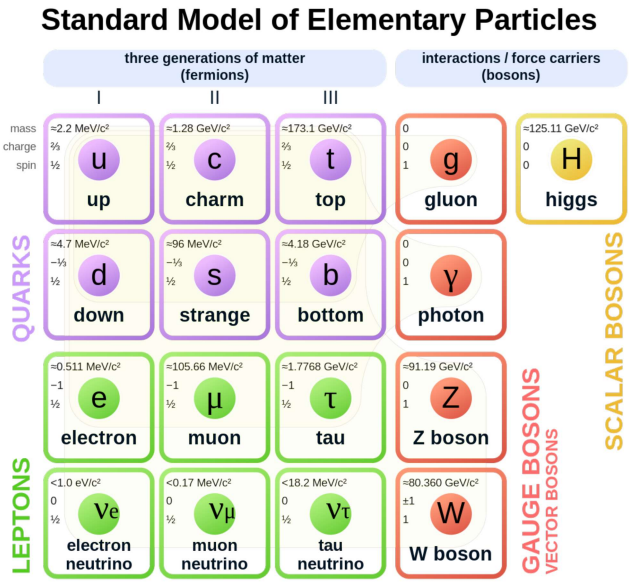


Figure 1.1: The Standard Model of Particle Physics [14]. On the right are four force carrying bosons. On the left are the building blocks of matter, Fermions. Neutrinos are spin-$\frac{1}{2}$ fermions with three flavours matching their lepton counterparts, e, μ, τ.

weak force. The left-handed fields transform under both $SU(2)$ and $U(1)$, whereas the right-handed fields transform only under $U(1)$ for all fermions. The electro-weak unification has interesting features that have profound effects on neutrino interactions. Neutrinos only interact via the weak force and so they only have a left-handed component.

1.3 Oscillations

To date, three flavours of neutrino have been discovered [3, 4, 5]. The total number of neutrinos can be measured experimentally from the decay width of the Z^0 boson as $N_\nu = 2.996 \pm 0.007$ [20] indicating that no further neutrinos exist that interact via the weak interaction.

The general form of neutrino oscillations has n neutrino flavour eigenstates, $|\nu_a\rangle$, that are related to n mass eigenstates, $|\nu_i\rangle$, via a unitary mixing matrix U. Neutrinos are not directly observed, only their products from weak interactions are visible and when a neutrino is produced it has a singular flavour from the weak interaction that produced it. Mass eigenstates then propagate at different velocities and interfere causing a time varying superposition of flavour eigenstates. When an interaction occurs, only one flavour interacts and is observed.

The following is a short derivation of the neutrino oscillation probability equations, more in depth analysis of oscillation probabilities is available in [12, 21, 22]. Starting with three neutrino mass eigenstates (ν_1, ν_2, ν_3) that are an admixture of flavour eigenstates (ν_e, ν_μ, ν_τ) related by a unitary matrix, U_{ij}:

$$\begin{bmatrix} |\nu_e\rangle \\ |\nu_\mu\rangle \\ |\nu_\tau\rangle \end{bmatrix} = \begin{bmatrix} U_{e1} & U_{e2} & U_{e3} \\ U_{\mu 1} & U_{\mu 2} & U_{\mu 3} \\ U_{\tau 1} & U_{\tau 2} & U_{\tau 3} \end{bmatrix} \begin{bmatrix} |\nu_1\rangle \\ |\nu_2\rangle \\ |\nu_3\rangle \end{bmatrix}. \tag{1.2}$$

A neutrino with initial flavour ν_e at $t = 0$, can be propagated to see how it evolves via the free particle wave equation,

$$\begin{aligned} |\Psi(0)\rangle &= |\nu_e\rangle = U_{e1}\,|\nu_1\rangle + U_{e2}\,|\nu_2\rangle + U_{e3}\,|\nu_3\rangle \\ |\Psi(\phi)\rangle &= U_{e1}\,|\nu_1\rangle\, e^{-i\phi_1} + U_{e2}\,|\nu_2\rangle\, e^{-i\phi_2} + U_{e3}\,|\nu_3\rangle\, e^{-i\phi_3}. \end{aligned} \tag{1.3}$$

Where,

$$\phi_i = E_i T - \boldsymbol{p}_i \cdot \boldsymbol{L} = (E_i - \boldsymbol{p}_i \cdot \boldsymbol{L})L = \frac{m_i^2 L}{2E}, \tag{1.4}$$

for a neutrino of energy, E, momentum, (p), after time T, travelling distance $\boldsymbol{L}$. Assuming the neutrino is travelling distance L in the x direction, $\boldsymbol{p}_i \cdot \boldsymbol{L} = p_i L$. Due to the low mass of neutrinos, the relativistic limit can be taken, $L \approx cT = T$, using natural units $c = \hbar = 1$. Equation 1.3 can be expressed in terms of the weak eigenstates from the unitarity of U,

$$\begin{aligned} |\nu_1\rangle &= U_{e1}^*\,|\nu_e\rangle + U_{\mu 1}^*\,|\nu_\mu\rangle + U_{\tau 1}^*\,|\nu_\tau\rangle \\ |\nu_2\rangle &= U_{e2}^*\,|\nu_e\rangle + U_{\mu 2}^*\,|\nu_\mu\rangle + U_{\tau 2}^*\,|\nu_\tau\rangle \\ |\nu_3\rangle &= U_{e1}^*\,|\nu_e\rangle + U_{\mu 3}^*\,|\nu_\mu\rangle + U_{\tau 3}^*\,|\nu_\tau\rangle\,. \end{aligned} \tag{1.5}$$

Substituting these into Equation 1.3 gives,

$$\begin{aligned}|\Psi(\phi)\rangle = &(U_{e1}U^*_{e1}e^{-i\phi_1} + U_{e2}U^*_{e2}e^{-i\phi_2} + U_{e3}U^*_{e3}e^{-i\phi_3})\,|\nu_e\rangle \\ &+ (U_{e1}U^*_{\mu1}e^{-i\phi_1} + U_{e2}U^*_{\mu2}e^{-i\phi_2} + U_{e3}U^*_{\mu3}e^{-i\phi_3})\,|\nu_\mu\rangle \\ &+ (U_{e1}U^*_{\tau1}e^{-i\phi_1} + U_{e2}U^*_{\tau2}e^{-i\phi_2} + U_{e3}U^*_{\tau3}e^{-i\phi_3})\,|\nu_\tau\rangle\,.\end{aligned} \tag{1.6}$$

So the initial state that was purely $|\nu_e\rangle$ in Equation 1.2 has components of all three flavours after travelling distance L. The oscillation probability can be calculated for each flavour transition and has a general form,

$$\begin{aligned}P(\nu_\alpha \to \nu_\beta) &= |\,\langle\nu_\beta|\Psi(L)\rangle\,|^2 \\ &= |U_{\alpha1}U^*_{\beta1}e^{-i\phi_1} + U_{\alpha2}U^*_{\beta2}e^{-i\phi_2} + U_{\alpha3}U^*_{\beta3}e^{-i\phi_3}|^2.\end{aligned} \tag{1.7}$$

Expanding this expression, a long process, and using Equation 1.4 gives,

$$\begin{aligned}P(\nu_\alpha \to \nu_\beta) = \delta_{\alpha\beta} &- 4\sum_{i>j} Re(U^*_{\alpha i}U_{\beta i}U_{\alpha j}U^*_{\beta j}\sin^2\left(\Delta m^2_{ij}\frac{L}{4E}\right) \\ &+ 2\sum_{i>j} Im(U^*_{\alpha i}U_{\beta i}U_{\alpha j}U^*_{\beta j}\sin\left(\Delta m^2_{ij}\frac{L}{2E}\right).\end{aligned} \tag{1.8}$$

By inspection, neutrino oscillations can occur, $P(\alpha \to \beta) > 0$, if at least two neutrino mass states have different masses, and there are non-zero off diagonal elements of U. The dependence of Equation 1.2 on $\frac{L}{E}$ is vital for informing the design of accelerator experiments as both L and E can be chosen to achieve the greatest sensitivity when measuring oscillation parameters. For example, T2K has a baseline of 295 km at a neutrino energy of 600 MeV which maximises the disappearance probability of muon neutrinos, $P(\nu_\mu \to \nu_\mu) \approx 0$.

Should U have a non-zero complex phase, then $P(\nu_\mu \to \nu_e) \neq P(\nu_e \to \nu_\mu)$ and is not invariant under time reversal symmetry, T. By extension, in order to conserve CPT symmetry; $P(\nu_e \to \nu_\mu) = P(\bar{\nu_\mu} \to \bar{\nu_e})$, then $P(\nu_e \to \nu_\mu) \neq P(\bar{\nu_e} \to \bar{\nu_\mu})$ and CP symmetry is violated. CP symmetry maintains that the laws of physics are identical under C and P transforms, the swapping of a particle with its antiparticle, and the inversion of the spatial dimension.

Table 1.1: Current measurements made for each PMNS parameter.

Parameter	Value	Source
$\sin^2(\theta_{12})$	$0.307^{+0.013}_{-0.012}$	[26]
$\sin^2(\theta_{23})$	$0.547^{+0.018}_{-0.024}$ (NO) $0.534^{+0.021}_{-0.024}$ (IO)	[12]
$\sin^2(\theta_{13})$	$(2.20\pm0.07)\times10^{-2}$	[12]
Δm^2_{12}	$(7.53 \pm 0.18) \times 10^{-5}\text{eV}^2$	[27]
Δm^2_{23}	$(2.437\pm0.033)\times10^{-3}\text{eV}^2$ (NO) $(-2.519\pm0.033)\times10^{-3}\text{eV}^2$ (IO)	[12]
δ_{CP}	$(1.23\pm0.21)\pi rad$	[12]

CP violation is one of the requirements, proposed by A. D. Sakharov [23], for the matter/antimatter asymmetry observed in the universe. Given the importance, measuring CP violation measurements in in particle interactions is a primary target for high energy physics experiments.

From Equation 1.2, the neutrino mass eigenstates (ν_1, ν_2, ν_3) are an admixture of flavour eigenstates (ν_e, ν_μ, ν_τ), related by a unitary matrix, U_{ij},called the Pontecorvo–Maki–Nakagawa–Sakata (PMNS) matrix [24, 25];

$$\begin{bmatrix} \nu_e \\ \nu_\mu \\ \nu_\tau \end{bmatrix} = \underbrace{\overbrace{\begin{bmatrix} 1 & 0 & 0 \\ 0 & c_{23} & s_{23} \\ 0 & -s_{23} & c_{23} \end{bmatrix}}^{\text{Atmospheric}} \overbrace{\begin{bmatrix} c_{13} & 0 & s_{13}e^{-i\delta_{CP}} \\ 0 & 1 & 0 \\ -s_{13}e^{i\delta_{CP}} & 0 & c_{13} \end{bmatrix}}^{\text{Accelerator/reactor}} \overbrace{\begin{bmatrix} c_{12} & s_{12} & 0 \\ -s_{12} & c_{12} & 0 \\ 0 & 0 & 1 \end{bmatrix}}^{\text{Solar/reactor}}}_{U_{ij}} \begin{bmatrix} \nu_1 \\ \nu_2 \\ \nu_3 \end{bmatrix}. \tag{1.9}$$

Where $s_{ij} = \sin\theta_{ij}$ and $c_{ij} = \cos\theta_{ij}$ for $i, j = 1, 2, 3$. The matrix is parameterised by three mixing angles, θ_{ij}, and a complex phase to account for possible CP violation, δ_{CP}. Equation 1.9 is a convenient parameterisation that gathers parameters that neutrino sources are sensitive to. Parameters in the PMNS matrix are measured experimentally in different ways due to the dependence of Equation 1.8 on $\frac{L}{E}$ and that $\Delta m^2_{12} << \Delta m^2_{23} \approx \Delta m^2_{31}$. Since Δm^2_{12} has a low value, it requires $\frac{L}{E} \sim 10^{-5}$ from long baseline reactor or solar measurements. Short baseline reactor experiments are sensitive to θ_{13} and θ_{23} with $\frac{L}{E} \sim 10^{-3}$, so different baselines and energies provide measurements of different parameters. Measurements for each parameter are shown in Table 1.1.

T2K produces muon neutrinos and, like other accelerator experiments, has flexibility in the neutrino energy and baseline, allowing some choice in the measurements that can be made when designing the experiment. Equation 1.8 can be expanded using Equation 1.9 using the above assumptions, to give the survival probability, for a full treatment see [28].

$$P(\nu_\mu \to \nu_\mu) \approx 1 - (\cos^4(\theta_{13})\sin^2(2\theta_{23}) + \sin^2(2\theta_{13})\sin^2(\theta_{23}))\sin^2\left(\frac{\Delta m^2_{31} L}{4E}\right). \tag{1.10}$$

$\sin^2(\theta_{13})$ is known accurately from reactor experiments, known as the reactor constraint (RC). Double Chooz in France [29], Daya Bay in China [30], and RENO in South Korea [31] provide leading measurements on $\sin^2(\theta_{13})$. Nuclear reactors provide intense neutrino flux, combined with good energy resolution in the detectors and baselines chosen to maximise $\bar{\nu}_e$ disappearance mean $\sin^2(\theta_{13})$ is known accurately and can be used in other experiments to constrain their oscillation models. The ν_e appearance probability, expanded to second order with matter effects, is given by;

$$\begin{aligned} P(\nu_\mu \to \nu_e) \approx & \sin^2(\theta_{23})\sin^2(2\theta_{13})\sin^2\left(\frac{\Delta m^2_{32} L}{4E}\right)\left(1 + \frac{2a}{\Delta m^2_{31}}(1 - 2\sin^2(\theta_{13})\right) \\ & - \sin(2\theta_{12})\sin(2\theta_{23})\sin(2\theta_{13})\cos(\theta_{13})\sin(\delta_{CP})\sin^2\left(\frac{\Delta m^2_{32} L}{4E}\right)\sin\left(\frac{\Delta m^2_{21} L}{4E}\right). \end{aligned} \tag{1.11}$$

Where the first term includes a correction for matter effects, $a = 2\sqrt{2}G_F N_e E = 7.56\times10^{-5}\text{eV}^2 \frac{\rho}{\text{gcm}^{-3}} \frac{E}{\text{GeV}}$ [32]. The second term is the CP violating term which changes sign under the transform ($\nu \to \bar{\nu}$). Oscillation parameters are calculated from Equations 1.10 and 1.11, known as the disappearance and appearance channels respectively. Measuring the difference between $P(\nu \to \nu)$ and $P(\bar{\nu} \to \bar{\nu})$ indicates the degree of CP violation in the neutrino sector.

Neutrino oscillation experiments have a general format of measuring the neutrino flux with a near detector at the beam source and the same flux after distance L at a far detector. The difference in neutrino flavours detected at the near and far detectors can be used to calculate neutrino oscillation parameters. Multiple experiments and measurements are needed because of the $\frac{L}{E}$ dependence of neutrino oscillations in Equation 1.8.

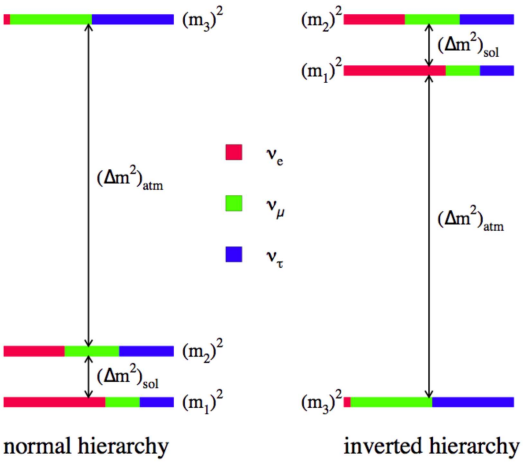


Figure 1.2: Inverted and normal neutrino mass ordering [33].

Neutrino mass

Masses in the standard model are introduced via the Higgs mechanism through spontaneous symmetry breaking [34, 35, 36]. Introducing a coupling between a scalar Higgs field to the $SU(2) \times U(1)$ symmetry produces a mass term proportional to the coupling to the Higgs boson, which was discovered at CERN in 2012 [37, 38]. While this is a monumental success for particle physics, the Higgs mechanism can only provide mass to fermions with left and right-handed fields and so the standard model predicts massless neutrinos.

Currently, it is difficult to provide masses to neutrinos within the standard model and no proven theory for the mechanism which determines neutrino masses. Without an additional mechanism in the standard model to provide masses to neutrinos, sterile right-handed neutrinos are required for a Higgs coupling, though this does not explain the low neutrino mass. Sterile neutrinos do not interact with any SM force and while searches are underway, they have yet to be discovered [39, 40, 41].

Introducing a Majorana mass term [42] where one field describes both neutrinos and antineutrinos provides a promising theoretical framework to describe neutrinos. The introduction of massive right-handed Majorana neutrinos can produce low mass left-handed neutrinos via the see-saw mechanism [43]. A Majorana neutrino allows for neutrino-less double β decay to occur. The simultaneous emission and absorption of a Majorana neutrino during a β decay would allow for no neutrino to be present in the final state [44]. In depth summaries of neutrino mass theories can be found in [12, 45]

The discovery of neutrino oscillations proves that they do have mass, albeit small. Direct mea-

surement of neutrino masses is difficult as they are orders of magnitude smaller than the electron, currently the KATRIN experiment has a leading direct measurement of $\overset{(-)}{\nu}$ mass at < 0.8 eV at 90% confidence [46]. However, studies of the Cosmic Microwave Background (CMB) limits the sum of neutrino masses at $\sum m_\nu < 0.11$eV at 95% confidence [47].

Neutrino masses are given labels ν_1, ν_2 and ν_3, somewhat arbitrarily because the ordering of masses is not known. From solar and reactor neutrino measurements it is possible to measure the mass difference of $\Delta m^2_{12} = (7.53 \pm 0.18) \times 10^{-5}$ eV^2 [27] where $\nu_2 > \nu_1$. The sign of Δm^2_{12} is known thanks to the Mikheyev–Smirnov–Wolfenstein (MSW) effect of neutrinos passing through the varying density of the solar medium [48]. The MSW is a form of matter effect, a full treatment of matter effects on oscillation probabilities can be found in [32].

Electron neutrinos passing through matter experience an effective potential from electrons in matter, leading to effective masses and therefore, different oscillation probabilities which are dependent on Δm^2_{12} [12], this can lead to resonance behaviour and maximal mixing which is the source of the solar neutrino problem from Section 1.1. Currently, long baseline neutrino beam experiments place the tightest measurements on $|\Delta m_{32}|$ [49, 50] but the sign is not known leading to two possible mass orderings; Normal Ordering (NO): $\nu_1 < \nu_2 < \nu_3$ and Inverted Ordering (IO): $\nu_3 < \nu_1 < \nu_2$ as shown in Figure 1.2. Matter effects for long baseline neutrino experiments could be measured given a long enough baseline [21], in addition matter effects affect neutrino and antineutrino oscillation rates differently so must be accounted for when making CP violation measurements [28].

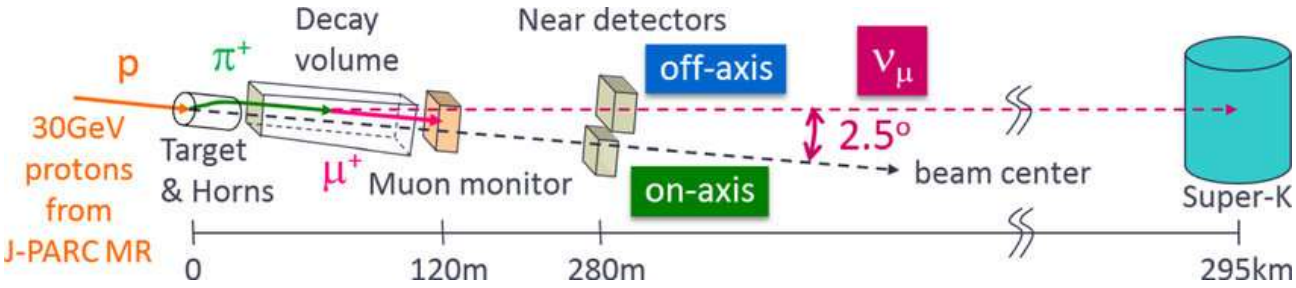


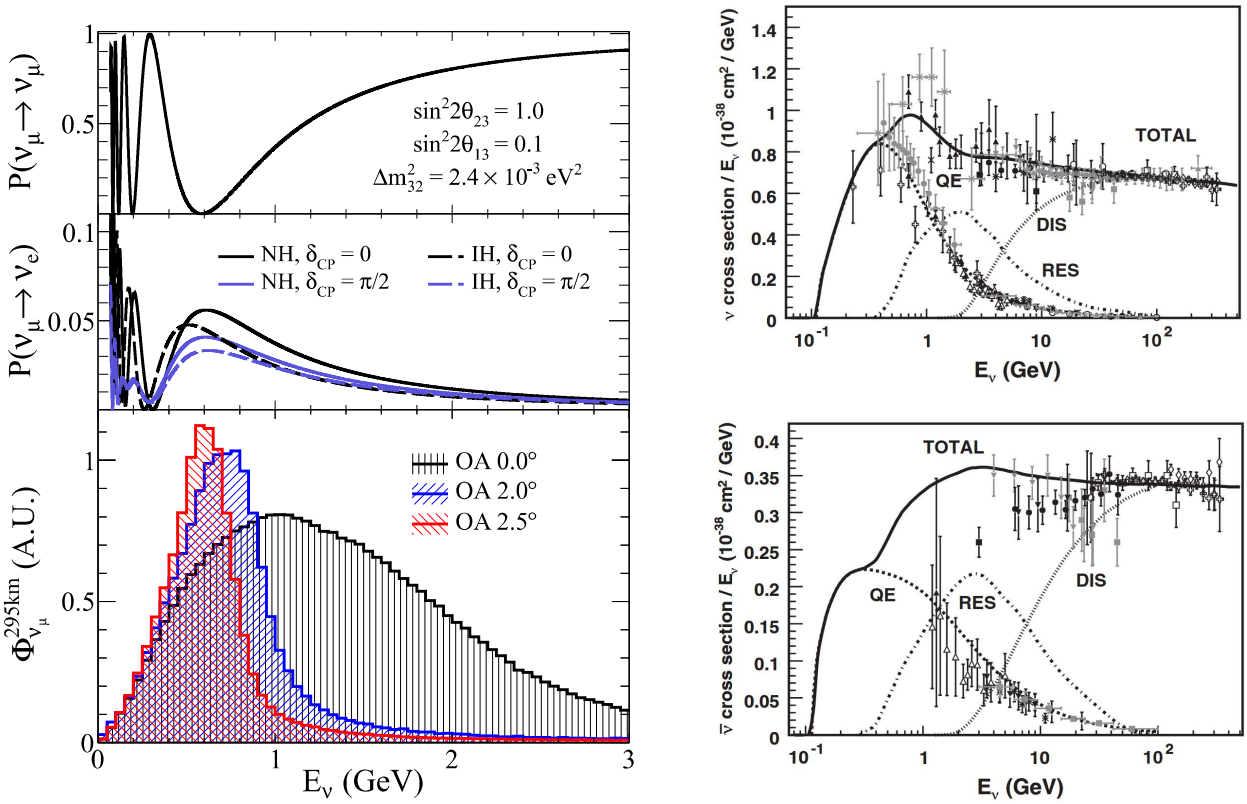
Figure 1.3: T2K experiment using JPARC protons for off-axis long baseline neutrino oscillation measurements. Image from [51]

1.4 The Tokai to Kamioka (T2K) Experiment

T2K [52] is a long baseline neutrino experiment with its source at the Japan Proton Accelerator Research Complex (J-PARC) in Tokai, Japan [53]. The J-PARC accelerator focuses 30 GeV protons onto a graphite target [54] with three magnetic horns, producing kaons and pions which decay and produce neutrinos in a decay volume. Muons and muon neutrinos are produced dominantly via $\pi^{\pm} \rightarrow \mu^{\pm} + \overset{(-)}{\nu}_{\mu}$ and $K^{\pm} \rightarrow \mu^{\pm} + \overset{(-)}{\nu}_{\mu}$ providing a beam of muon neutrinos. The beam is contaminated by ν_e from $\pi^{\pm} \rightarrow e^{\pm} + \overset{(-)}{\nu}_{e}$, $K^{\pm} \rightarrow e^{\pm} + \overset{(-)}{\nu}_{e}$ and $\mu^{\pm} \rightarrow \mu^{\pm} + e^{\mp} + \overset{(-)}{\nu}_{e}$ decays. A decay volume in which muons are stopped before they can decay reduces the ν_e contribution from muon decays.

Magnetic horns are used for beam focusing and their current can be used to select only positive or negative mesons, thereby providing a neutrino beam in Forward Horn Current (FHC) mode or antineutrino beam in Reverse Horn Current (RHC) mode. There are more positive charges created than negative since protons are fired at the target, producing more ν contamination of the beam when in antineutrino mode. The detector setup for T2K is shown in Figure 1.3. INGRID [57] is an on-axis detector used to monitor the neutrino beam profile. Oscillation measurements are made using ND280 [58] as a near detector and Super-K [59] for a far detector that are 2.5° off-axis to the J-PARC beam. Neutrinos are produced with a narrow energy peak around 600 MeV due to the angular dependence of neutrino energies from two body decays [60]. The narrow band beam gives maximal oscillation probability for the baseline in Equation 1.8, as illustrated in Figure 1.4.

T2K measures muon neutrino disappearance and electron neutrino appearance in Super-K and places limits on $|\Delta m_{32}|^2$, $\sin^2(\theta_{23})$, $\sin^2(\theta_{13})$ and δ_{CP} [61, 62].



(a) (b)

Figure 1.4: **(a)**: Top:Survival probability for muon and electron neutrinos at Super-K. $\nu_\mu \rightarrow \nu_e$ oscillation probabilities are given with different values of δ_{CP}. Bottom: Neutrino flux for different off-axis angles. A 2.5° angle gives a narrow peak of neutrino energies at the $\nu_\mu \rightarrow \nu_e$ oscillation maximum. Image from [55].
(b): Neutrino (top) and anti-neutrino (bottom) cross-section predictions for Quasi-Elastic (QE), Resonant (RES), and Deep Inelastic Scattering (DIS) interactions. Predictions are made using the NUANCE generator and data from various neutrino experiments [56].

1.4.1 ND280 and INGRID

ND280 is the off-axis near detector whereas INGRID is on-axis and used primarily for beam monitoring for T2K, shown in Figure 1.5. ND280 is positioned 2.5° off-axis and ≈ 280m away from the beam target. The data collected by ND280 is used in the oscillation analysis to constrain flux and cross-section uncertainties. The measured flux is primarily ν_μ events as the beam is unoscillated close to the target. Cross-section measurements are made on different targets, water measurements are of primary importance given Super-K is a water based detector [63, 64]. ND280 is constructed from several sub-detectors all contained in a 0.2T magnetic field. The P0D is the leading part of ND280 and is used to identify π^0 events and can be operated with or without water in the detector [65]. Two Fine Grain Detectors (FGD1 and FGD2) follow which measure neutrino interactions using plastic

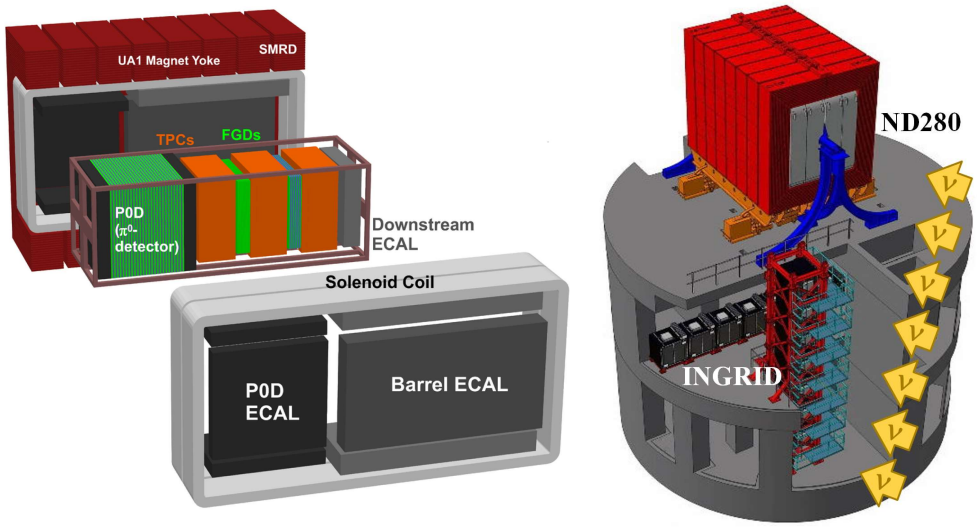


Figure 1.5: Left: ND280 exploded view showing the subdetectors. Right: ND280 and INGRID in the near detector complex, with ND280 positioned 2.5° off-axis.

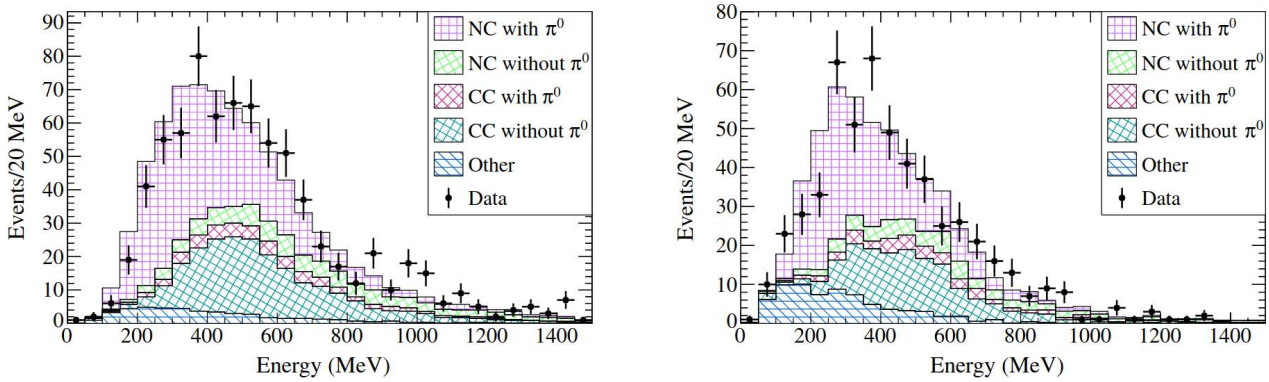


Figure 1.6: NCπ^0 samples from the ND280 P0D detector in water-in (left) and water-out (right) configuration. Expected number of events is normalised to data representing 3.49×10^{20} POT. Figure from [65]

scintillators, FGD2 also has water layers [66]. Time Projection Chambers (TPCs) with an argon gas target provide PID and momentum measurements for particles escaping the FGDs. The FGDs and TPCs are designed to identify Charged Current Quasi-Elastic (CCQE) events which dominate at T2K energies as shown in Figure 1.4.

The P0D can measure the rate of π^0 events on water by measuring the difference in event rates between water-in and water-out operation modes. Samples of events are shown in Figure 1.6 with $106 \pm 41(stat.) \pm 69(syst.)$ NCπ^0 signal events on water [65].

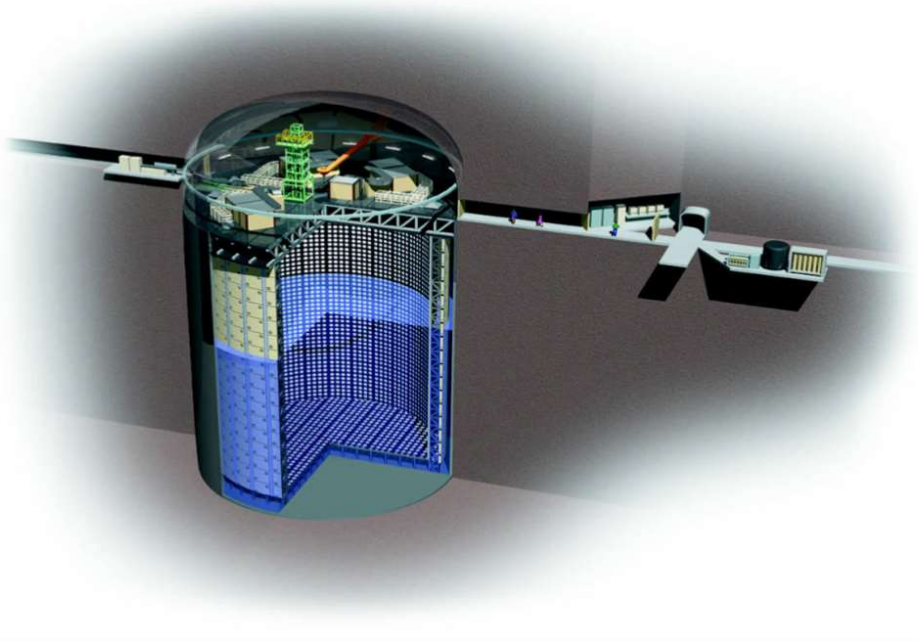
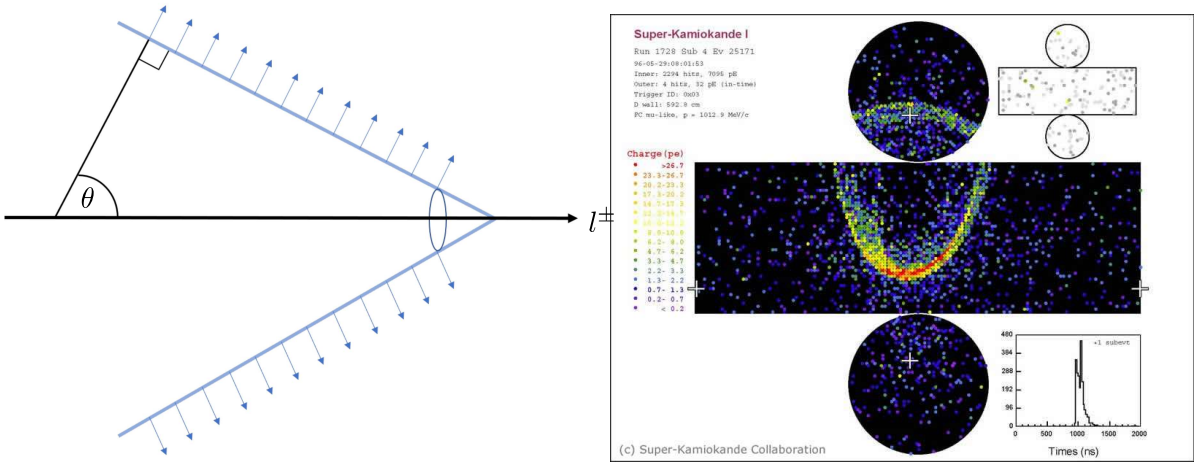


Figure 1.7: The Super-Kamiokande detector beneath Mt. Ikenoyama, Japan. The detector is split into two parts totalling 50kt. The outer detector acts as a veto for particles entering the tank.

1.4.2 The Super Kamiokande (Super-K) Experiment

The Super-K detector [59] is a cylindrical 50 kton ultra-pure water Cherenkov detector in the Kamioka mine, Japan. The mountain above provides the tank with 2805 m water equivalent shielding from cosmic rays. The experiment is separated into an inner and outer detector as shown in Figure 1.7 in order to veto background events. The inner detector is instrumented with 11,000 20 inch Photo-Multiplier Tubes (PMTs) giving 40% coverage of the tank. The PMTs are protected with acrylic shielding after a catastrophic accident caused half of the tank PMTs to implode in a cascade. The exposed tank between PMTs is coated in black sheet to reduce reflections in the tank.

The Super-K Inner Detector (ID) is constructed from columns of steel support structures that hold PMTs in a flat vertical plane in 4×3 blocks called super modules. There are 37 full super module columns and one half super-module 2×3 making up its circumference.



(a) (b)

Figure 1.8: **(a)**: The ring of light produced when a charged particle travels faster than light in a medium, producing a wavefront of photons that can be detected. The Cherenkov angle θ can be measured from the light produced. **(b)**: A muon neutrino event in the Super-K showing the ring of Cherenkov light [67]

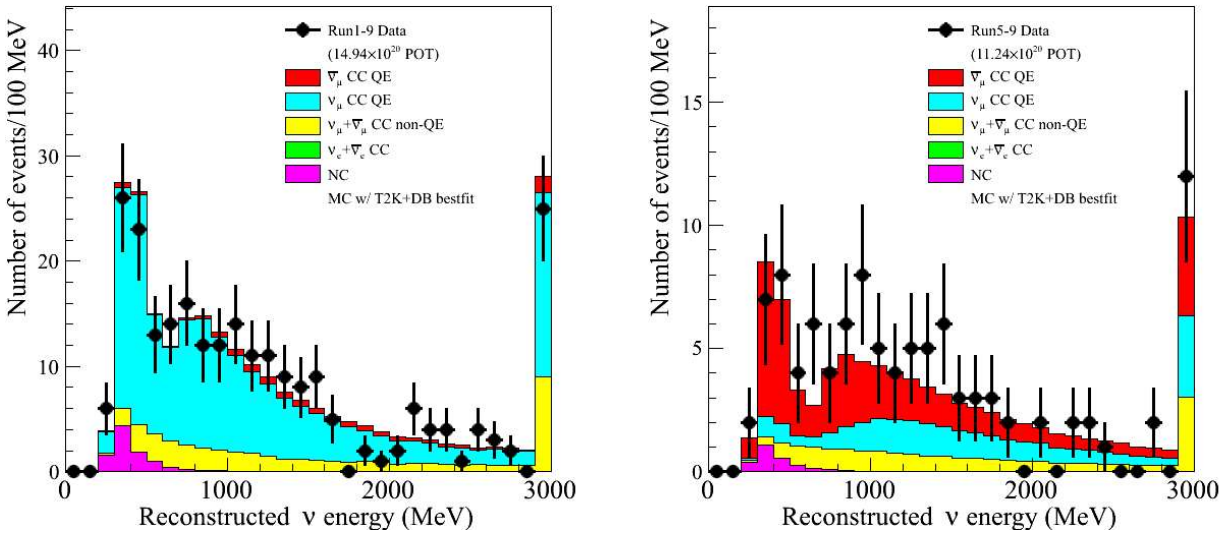
1.5 Neutrino interactions at Super-K

The current official T2K analysis [68] uses charged current (CC) Super-K samples to measure oscillation parameters. The charged current electron-like (e-like) sample is of particular importance for measuring the $\nu_\mu \rightarrow \nu_e$ oscillation probability which from Equation 1.11 allows measurements of δ_{CP}.

Neutrinos can interact with nuclei via a $W^{\pm}$ or a Z boson propagator. Charged current interactions produce charged leptons whose flavour matches the interacting neutrino. Charged particles emit Cherenkov radiation if they travel faster than the local speed of light in a dielectric medium such as water. There is a lower limit of neutrino energies for reconstruction at Super-K as the resultant lepton needs a high enough velocity, v_p, to produce a Cherenkov ring. In the case of water with refractive index n, ;

$$\beta = \frac{v_p}{c} > \frac{1}{n}. \tag{1.12}$$

A lepton with $\beta > \frac{1}{n}$ will produce a ring of light as it loses energy to Cherenkov radiation until $\beta < \frac{1}{n}$ as shown in Figure 1.8. Electrons scatter from other electrons in the water creating photons and electromagnetic showers, producing a fuzzy ring. Muons are much heavier and do not scatter, producing cleaner rings. The difference in rings allows the interacting neutrino flavours to be distinguished from



(a) (b)

Figure 1.9: Neutrino (a) and antineutrino (b) energies at Super-K. The horn current polarity that controls the beam mode produces a purer beam of neutrinos than antineutrinos [69].

each other. Events provide information on the neutrino energy from the amount of light detected. The direction of the incoming neutrino can be measured by reconstructing the neutrino interaction vertex from its ring. Lepton charge information is lost as there is no magnetic field in Super-K, so neutrinos and antineutrinos appear the same. The Super-K events for FHC and RHC beams, selecting neutrinos and antineutrinos respectively, are shown in Figure 1.9.

Recently, the Super-K detector has been doped with Gadolinium in order to capture neutrons from anti-neutrino interactions. SK-Gd [70] will be able to distinguish neutrinos from antineutrinos, the data is not used in the analysis presented in this document because the development is a recent change. Gadolinium neutron capture produces an 8 MeV gamma ray cascade with an average capture time of 30 μs which can be reconstructed in Super-K with an expected efficiency of $(88 \pm 2)\%$ [71].

The charged lepton produced in CC events is detectable if its kinetic energy is above 3.5 MeV [72] in Super-K, the limit to produce Cherenkov ring that can be reconstructed over the PMT dark noise. PMTs have a background of false signals known as dark noise from electrons emitting from the PMT material and is present even when no light is detected. The dark noise is increased when PMTs warm up or are exposed to intense light but reduces down over time, which is important to consider when doing tank open work (TOW) as it can affect the livetime of the detector.

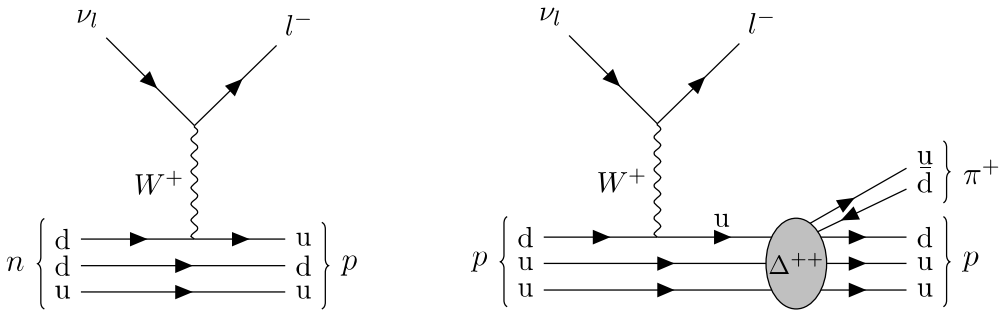


Figure 1.10: Left: CCQE neutrino interaction diagram. Right: CC1π interaction diagram. Dominant CC neutrino interactions in Super-K used for driving event selections for analysis.

The dominant background for the CC e-like samples are NCπ^0 events where the π^0 decays via $\pi^0 \rightarrow \gamma\gamma$. The two photons produce e-like rings in the Super-K ID and can be mis-reconstructed as single ring e-like events when the rings overlap. Chapter 4 discusses NCπ^0 events further.

The neutrino energy peak at Super-K is below 1 GeV, at this energy Quasi Elastic (QE) neutrino interactions dominate as shown in Figure 1.4. CCQE events occur when a neutrino interacts with a bound nucleon through the exchange of a W boson, producing a lepton with flavour matching the incoming neutrino and a proton/neutron. CCQE interactions form the single ring e-like (1Re) and μ-like (1Rμ) samples for oscillation analysis at Super-K which are described further in Chapter 4. CC1π interactions occurs through the intermediate production of an excited Δ^{++} which produces an additional π^+ which are selected as part of the CC1π (1Re1de) Super-K sample. CCQE and CC1π Feynman diagrams are shown in Figure 1.10.

1.5.1 NC1π^0 Events

Previously published T2K oscillation results [49] used 3 Super-K event samples, 1Re, 1Rμ and 1Re1de. The analysis described in this document adds two samples of Neutral Current π^0 (NCπ^0) events in Super-K one where events are reconstructed with one ring and one where events are reconstructed with two rings, these are shown in depth in Chapter 4. Currently, there are no samples of NCπ^0 events in the T2K oscillation analysis. NCπ^0 events can't be used to constrain neutrino oscillation parameters because the interactions are flavour blind. NCπ^0 interactions and how they appear in Super-K are described further in Chapter 4.

1.6 Future experiments and precision measurements

T2K is in the process of upgrades to almost all parts of the experiment seeking to measure δ_{CP} to 3σ [73] as part of the T2K Phase-II plan. The ND280 detector has been upgraded with a new Super Fine Grained Detector (SuperFGD), new TPCs and TOF planes[74]. The purpose of the upgrades is to reach a systematic uncertainty of 4% on flux and cross section measurements. In addition, the Intermediate Water Cherenkov Detector (IWCD) [75, 76] is to be built at a 1 km baseline to further reduce systematic errors. IWCD is an 8 m $\times$ 10 m water Cherenkov detector which is floated in a cylinder of water and can change its off-axis angle. IWCD will be able to probe the effect of changing neutrino energy on water Cherenkov detector response in order to better predict the neutrino flux and event rates at the far detector. A prototype Water Cherenkov Test Experiment (WCTE) is currently being built at CERN [77]. An entire new far detector Hyper-Kamiokande (Hyper-K) [75] is under construction in a mountain 8 km from Super-K with the same baseline and off-axis angle but larger at 258 kton and will have a broad range of neutrino measurement and cosmology applications including resolving the mass ordering problem and measuring δ_{CP} to 5σ. This thesis explores the potential of NCπ^0 event samples at T2K. The new era of precision neutrino oscillation measurements will require accurate knowledge of NCπ^0 backgrounds. NC events are flavour blind, so can potentially provide a strong constraint on far detector neutrino flux estimates.

Chapter 2

Photogrammetry

2.1 Introduction

This chapter investigates possible methods for developing an in-situ 3D digital model of Super-K. The study presented here investigates the application of machine learning for PMT identification and how a subset of Super-K PMTs could be reconstructed. The eventual aim of an in-situ model is to locate the positions, angles of photosensitive areas, and any shifting of PMTs over time.

PMTs could feasible move from their own buoyancy when the detector is filled with water and if the structure of the experiment were to warp over time. The work that follows is a proof of concept that uses machine learning techniques for image reconstruction to initially identify PMTs in images and simplify the image to a list of PMT centres with unique labels. The PMT positions can then be reconstructed using photogrammetry by matching PMTs in many images to triangulate their position in real space and make a 3D model of part of the Super-K tank. A flowchart of the process employed is shown in Figure 2.1.

Photogrammetry is the process of reconstructing 3D models and positions from multiple, overlapping 2D images taken from different camera positions. Features identified in images can then be located relative to each other, and the camera, to locate its real position. In-situ reconstruction would be useful for water Cherenkov experiments where it is difficult to know if PMTs in the detectors shift when filled with water and if there is any effect on event reconstruction uncertainty. Similar techniques have been used in SNO+ using static cameras to locate calibration sources in the detector from

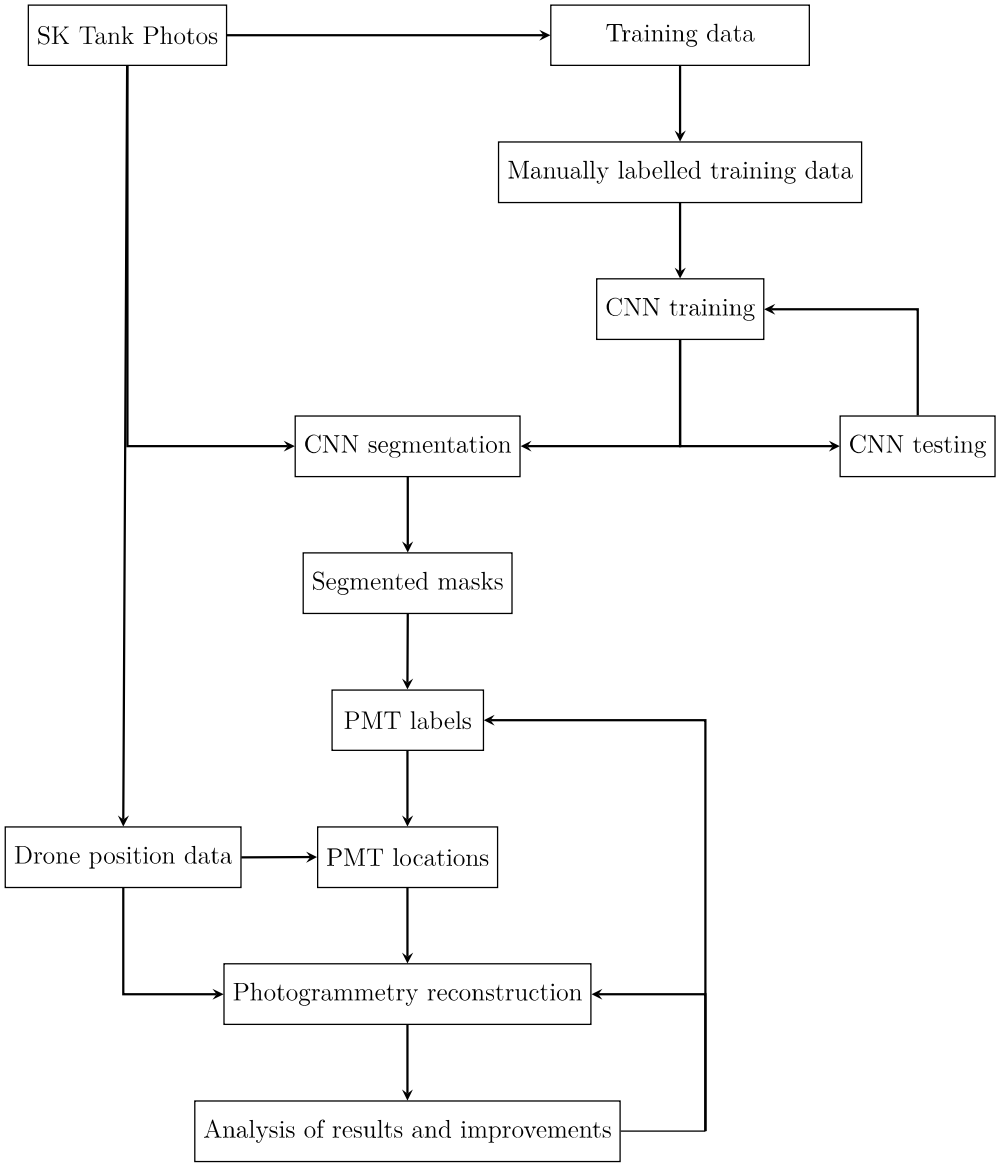


Figure 2.1: The process developed to produce segmented images using machine learningand then reconstruct tank geometry for Super-K using photogrammetry. An iterative process was employed during reconstruction where incorrectly labelled PMTs were identified and manually corrected.

the known PMT positions [78]. An initial survey of the Super-K tank was made using a submersible camera drone with the aim of testing reconstruction methods and PMT identification.

At Super-K, any difference from the design positions introduces systematic errors into event reconstruction that are not measured. Any uncertainty is included in data analysis as part of the discrepancy between data and simulation. T2K analysis uncertainties are statistics dominated, so reducing the error on event reconstruction that may arise from a change in shape of Super-K will likely have minimal effects on results. Future experiments like IWCD and Hyper-K will require precision knowledge of their geometry in order to reduce reconstruction errors on neutrino interaction events

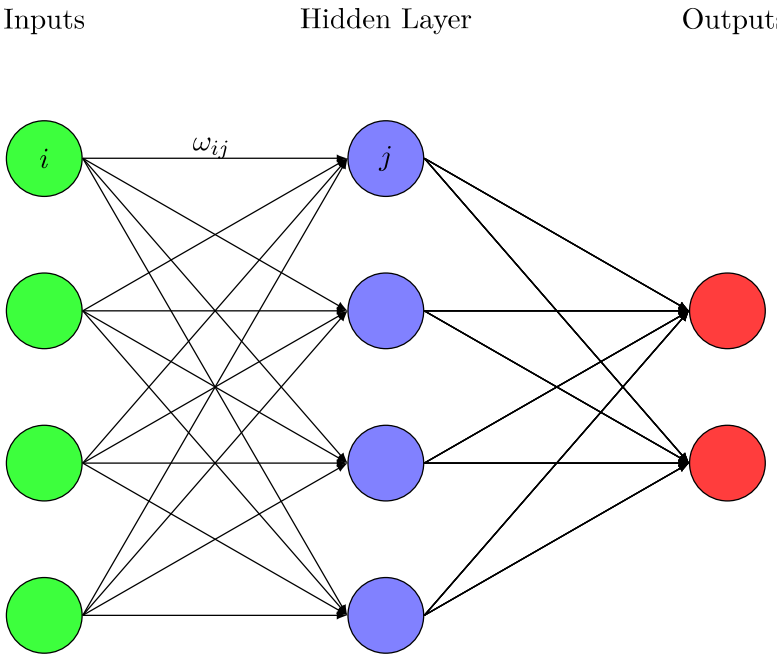


Figure 2.2: A simple neural network with input neurons, one hidden layer of neurons, and outputs. The connectors between neurons carry a weight ω_{ij} which indicates how important that weight is to the neuron.

and make precision measurements.

A 3D reconstruction needs to be accurate enough to evaluate any change in shape of the steel structure of Super-K at the large scale, i.e. squashing or skewing. Eventually it may be possible to evaluate if individual PMTs have shifted. The end goal would be to create a full model of a water Cherenkov detector, with information on the PMT orientation and location, to better understand the angular detection efficiency of each PMT.

This chapter aims to evaluate the possibility of reconstructing a 3D model of Super-K, by applying machine learning to photos of the tank taken by drone. A small subset of images, taken in a known pattern, simplifies the reconstruction for this initial study with the eventual aim of modelling the Super-K ID for changes in the tank geometry.

2.2 Machine Learning

In general, neural networks learn how a set of inputs can be mapped onto a set of given outputs, their performance depends on the quality, diversity and amount of training data. Neural networks are constructed using layers of artificial neurons, which are based on their biological namesake [79], a

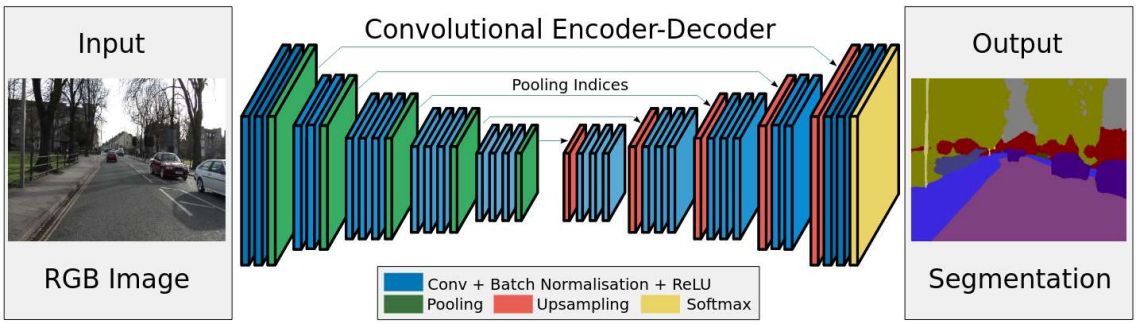


Figure 2.3: An example encoder and decoder structure from SegNet [82]. High resolution images are taken as input and their features learned, reducing the resolution. Spatial information is then added back in, producing high resolution images with feature information.

simple model of a neural network is shown in Figure 2.2. Neurons produce an output based on their weighted inputs, the net weighted input is then fed to an activation function which is a threshold function, outputting ≤ 0 if the threshold is met or >0 if it is. Figure 2.2 shows a feed-forward network where information is propagated from inputs to outputs only.

Convolutional Neural Networks (CNNs) are widely used for image recognition [80] and use supervised learning techniques where a set of training data is accompanied by a truth value. In the context of image processing, the truth level information is a manually labelled image. The training data is passed through the network to produce an output which is compared to the true output. The differences between the output of each neuron and true value is calculated and represents the loss in the network. The network loss is reduced by adjusting the weights of each neuron connection, starting from the outputs, so that the neuron output better represents the true training data. Moving back through the network to reduce loss is called back-propagation [81]. With enough training, the network develops weights that accurately predict the training data.

In order to identify PMTs in images, a technique called semantic segmentation is employed, which segments images into labelled regions. For semantic segmentation; a set of images with the objects present in the image (e.g. car, tree) are labelled pixel by pixel in order to learn which features (e.g. lines, colours, structures) of an image represent a given label. The CNN learns which features are present for each label from a set of images with labelled features. Semantic segmentation is a broad field, a breakdown of the techniques and neural network architectures can be found in [83]

Image segmentation feature learning is performed by passing data through a neural network whose

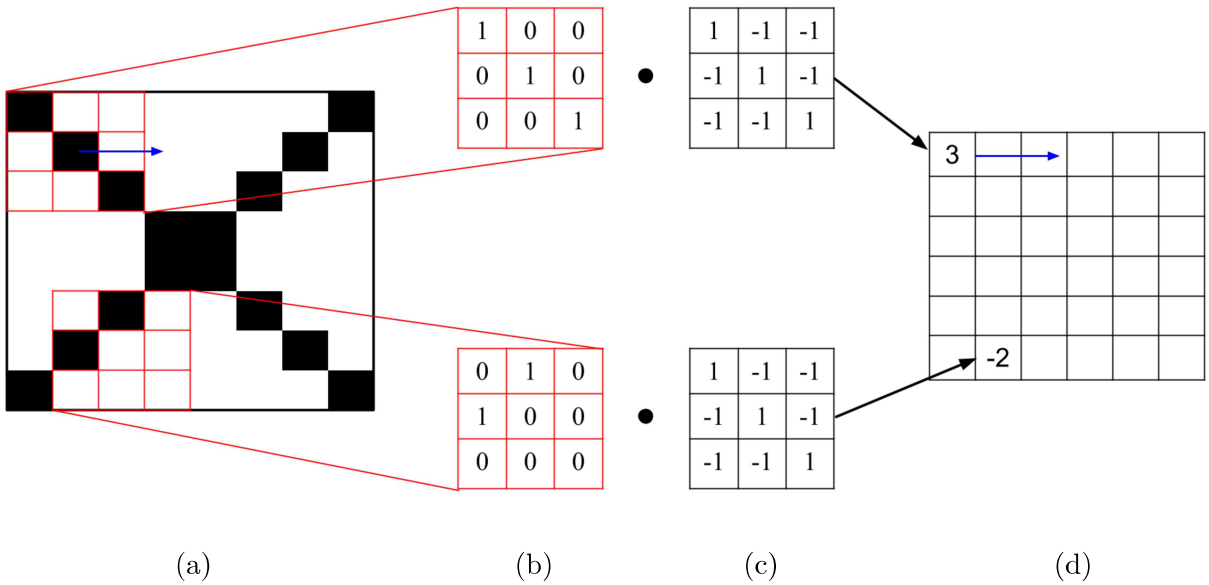


Figure 2.4: **(a)** The image is scanned and the scalar product of the receptive field, **(b)**, and convolution, **(c)**, is calculated for each central pixel. The output takes its place in the feature map, **(d)**, where a high score means the receptive field matched the convolution filter and a low score means it doesn't.

layers identify the contents of the image. The CNN will only learn features that are present in the training data, so a larger, more diverse set of input images shall produce more accurate and flexible results. The end result is an image mask, reducing the pixel information from 255 RGB colour values to just a few labels for further processing. While a large, diverse training data set is important, for the purposes of reconstructing Super-K a smaller dataset can be used than usual because the 11,000 PMTs are identical in structure with a homogeneous background. Difficulty arises because PMTs have internal structure which appears differently in images depending on the angle they are viewed from, so diversity in the training set is required to help learn to account for viewing angle and reflections.

The CNN used for training in this study has an encoder-decoder structure shown in Figure 2.3. The encoder is used to classify feature information at the cost of spatial resolution, while the decoder attempts to put the spatial information back into the feature maps in order to find where in the original image the feature is located. Each general layer of a CNN has three stages, a set of convolutions, a nonlinear activation function and, finally, up (or down) sampling.

Convolutions

CNNs use convolution layers to classify features in images. The convolution itself is a matrix whose

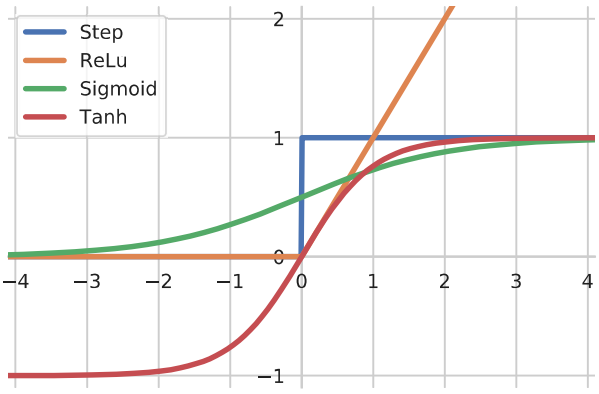


Figure 2.5: Popular activation functions which introduce a nonlinear relationship between input and output.

elements represent a given feature that sweeps across each pixel of an image. The area of the image under the convolution is the receptive field. For each pixel in an image, the convolution is applied to the receptive field using element wise multiplication and summing the results, as demonstrated in Figure 2.4(b). Each element of the feature map is a score of how well that pixel's receptive field represents the convolution filter. Feature maps have a reduction of two in each dimension because the convolution cannot be applied to the corner pixels, padding can be applied to allow this but can introduce learning errors as it requires changing the convolution kernel within a layer.

A convolution layer in a CNN applies a number of convolutions to an image, producing feature maps equal to (number of convolutions) $\times$ (number of image channels). The output is then smaller spatially but with more channels where feature information from the convolutions is encoded in the channels of the convolved images. The output from a convolution layer is passed directly to an activation function.

Activation functions

An activation function takes the linear output of the convolutions and transforms it, introducing nonlinearity to the neural network, in order to learn complex structures. In the context of feature recognition, the activation function will 'activate' if a feature map score is high enough; if the feature in the convolution is present at that part of the image it is kept, otherwise, the pixel is removed.

There are several functions used in machine learning, sigmoid and tanh are popular. However, for

CNNs a rectified linear unit (ReLU) is considered the most appropriate for deep learning and CNN applications [84]. ReLU is a stepwise function which returns 0 if the input is less than 0 and returns the input value otherwise, as shown in Figure 2.5. For neural networks with many layers, sigmoid and tanh functions suffer as their gradients tend to 0 for high activation values, making it difficult to update weights to reduce loss during back propagation.

A ReLU layer is applied after convolutions to remove any elements of the feature map whose value is less than 0. After the activation layer only pixels where the convolution filter is matched in the image and the value where the feature is represented well in the image is increased.

Up/Downsampling

Downsampling is the process of condensing the spatial dimensions of feature maps so that the receptive field of subsequent convolutions effectively covers a larger area of the original image. Larger scale structures can then be 'seen' by the convolution and the neural network is forced to learn the nature of the feature, rather than its location in the image. Upsampling is the reverse process where spatial information is put back into feature maps, in order to estimate where in the image a feature occurs.

Up and downsampling can be achieved using a pooling layer or by using a convolution layer with a stride (the separation between central pixels for convolution operations) of one or more. Max pooling is regularly used in CNNs for object recognition and simply takes the largest activation in the receptive field [85]. The final result of one of these layers is a reduction in the spatial dimensions, in preparation for the next convolution. Upsampling convolutions operate similarly; each pixel is passed through a kernel with learned weights that increases its size, doubling the spatial dimensions and then applying a nonlinear activation function.

The UNet CNN

UNet [86] is a CNN developed for biomedical image segmentation and has become widely used in other fields. UNet requires relatively few training images in order to learn features, making it an attractive option when there are only 11,000 PMTs to label in Super-K. UNet utilises skip connections

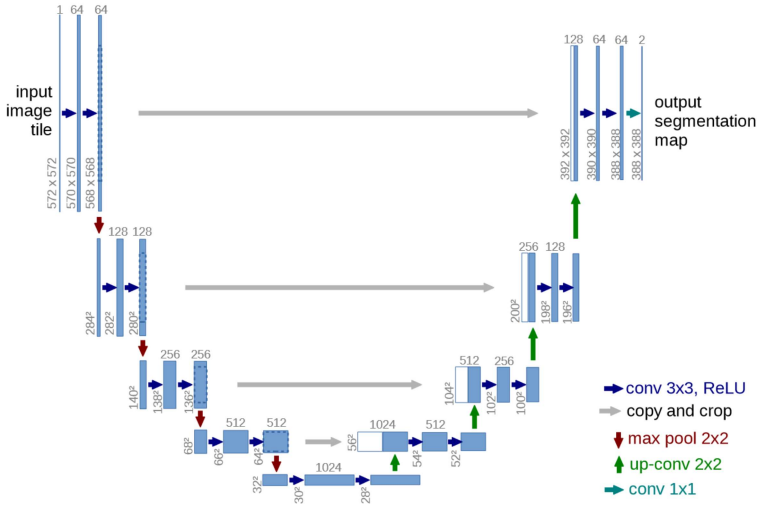


Figure 2.6: UNet with the characteristic 'U' structure. The encoder is on the left and learns feature information at the cost of spatial information, the decoder on the right uses skip connections to try and recover the spatial information.

where, during training, the feature maps from each convolution layer are taken from the encoder and used at each upsampling stage in the decoder, as illustrated in Figure 2.6. The skip connections help each upsampling stage put more spatial feature information, that is lost during encoding, back into the feature maps. Skip connections improve overall feature localisation and segmentation. One of the weaknesses of UNet is the lack of padding in convolution layers. The edges of images never have a convolution centred on them meaning the edges of images are missed in training.

2.3 Drone photos of Super-K

During 2020 Tank Open Work (TOW) at Super-K, a drone was deployed to take photos of the inside of the Super-K ID. Photos had to be taken such that there was overlap between them to allow features (PMTs) to be identified in multiple images and their position located. Sets of photos were taken with similar drone behaviour to aid reconstruction. The entire tank was not imaged during the TOW, instead, a diverse set of surveys was made for testing PMT reconstruction. Surveys of the tank with different scanning patterns; some going top to bottom, some around the ID at constant depth and top/bottom surveys that image the corners and top/bottom PMTs. Images were taken using a few methods. Some photos used long exposure to reduce ISO noise and give clear images. However, this could have exposed the PMTs to too much light and increased their dark rate, the background signal

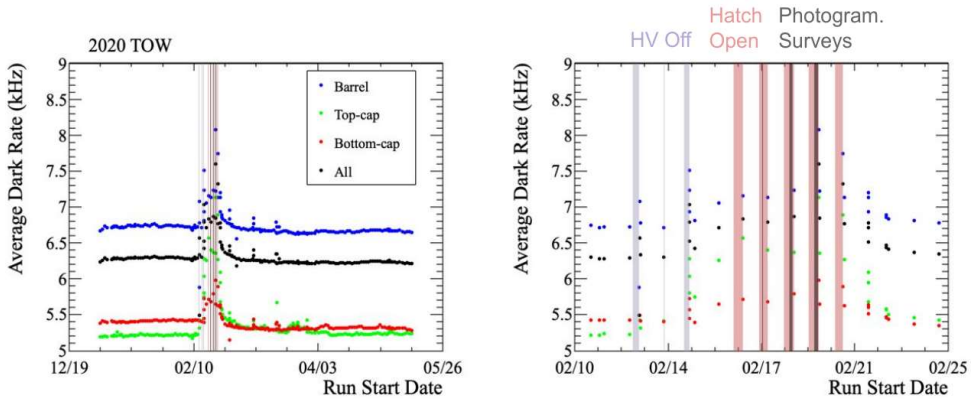


Figure 2.7: Dark noise for the time around the 2020 TOW (left) and during the photogrammetry surveys (right). The dark noise level retured to normal after the TOW.

rate of a PMT when there is no light detected. Most photos are taken in bursts of 10 in quick succession with lower light input into the tank which can then be averaged to reduce ISO noise. For those images taken in bursts, there was additional blurring introduced to the images if the drone moved slightly while taking images. The motion distorts the shape of PMTs in the images and causes unreliable reconstruction. Additionally, test images taken with a yellow filter to try and reduce light input into the tank. The drone was remotely controlled and recorded its depth, pitch, yaw, and roll to provide some position information for the drone but the absolute position was not recorded. The data set of images provides ample training data for use in testing semantic segmentation and reconstruction. Initially the clear, long exposure images are used for training before expanding the training set to include images taken in a burst.

TOW generally lets light into the Super-K tank, which was added to by the drone camera, increasing the dark noise of PMTs. There is a possibility that the additional light can excite the photocathodes of PMTs and increase the dark rate drastically, beyond the end of the TOW, as has been seen during previous maintenance work. However, the dark noise rate was found to decrease back to pre-TOW levels, as shown in Figure 2.7.

2.4 Constraints from Super-K construction

The construction of the Super-K inner detector [87] is used to provide each PMT with a unique label. The Super-K inner detector is constructed of modules of 2×3 PMTs and two together make 4×3 PMT

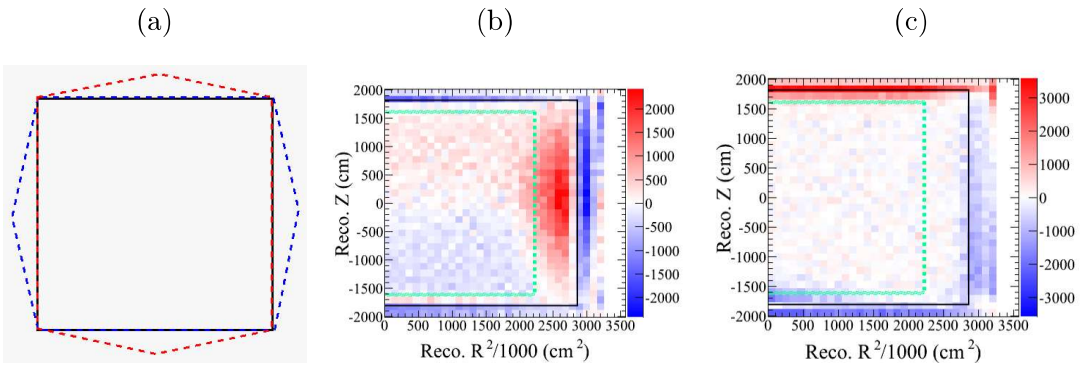


Figure 2.8: The effect on MC event reconstruction when tank geometry is altered: **(a)** (——):Unwarped SK tank, (- - - -): Hexagonal shift of tank barrel outwards by 100 cm max. (- - - -): Outward shift of tank top and bottom by 50 cm max. **(b)** Effect of the hexagonal warp on down-going neutrino events, expected fiducial volume and ID boundary are marked in green and black respectively. The z axis shows the difference in the number of reconstructed events from the nominal tank geometry. **(c)** Effect of Vertical warp on reconstructed events. Both showing a shift toward the detector wall. Plots by R. Akutsu.

super modules. The design is such that the gaps between PMTs are larger between different super-modules than between PMTs within a super-module. Images are split up according to their super modules and tracked between images. This is easier than identifying individual PMTs in separate images because their appearance changes drastically depending on the angle they are viewed at. Geometrical features such as the grid of PMTs and super modules stand a better chance of tracking between images.

There are 37.5 super-modules arranged in a circle for each layer of the inner detector. The half module is a unique feature for each ring of images with a known location in the tank along with calibration tools and hatches. Unique or easily located features are vital as they cross the divide between an arbitrary reconstruction of PMTs to a labelled reconstruction relating to real PMT arrangement. A single unique feature can be used as a seed to label all PMTs with their ID numbers and compared with other features to validate the reconstruction. Super-K PMTs are 20 inches in diameter with a transparent plastic cover to protect them from the pressure of water in the tank. This cover is bolted to the structure of the tank through the black sheet so in images the bolts show up as bright, reflective points.

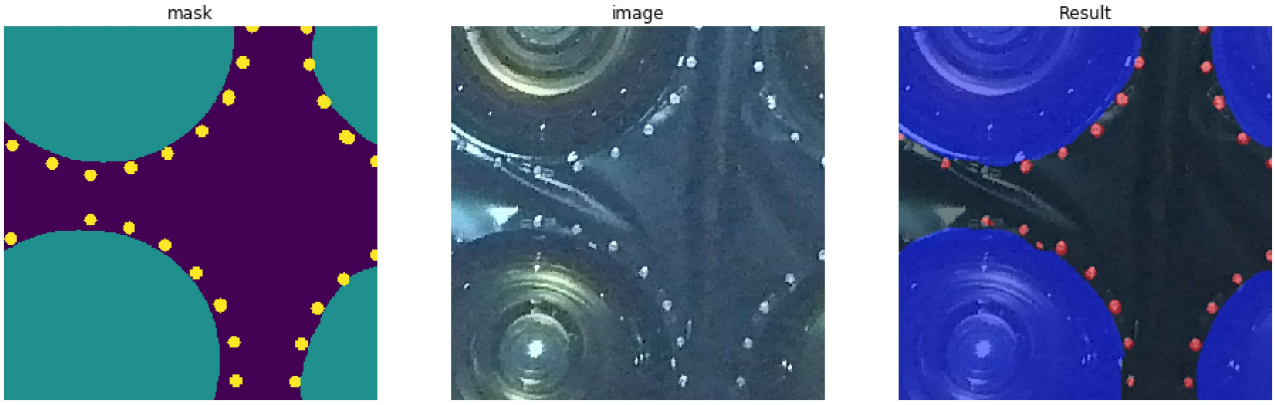


Figure 2.9: Three classes (bolt, PMT and background) output for a central PMT. The accuracy between manual segmentation labelling (left) and that of the neural network (right).

2.5 Tank Geometry

The Super-K tank is 41.4 m high and 39.3 m in diameter with a stainless steel structure to support the PMTs. PMTs are attached to the tank in modules of 6 (3×2) in the same plane, normal to the wall of the tank. Accurate knowledge of PMT positions is required for both calibration and event analysis. The location of 14 PMTs were measured and checked against schematic designs [87] and were in tolerance to the order of centimetres. PMTs could shift position due to distortions in the tank from the buoyancy of PMTs, construction errors, or from warping over time. Such shifts will affect the time of flight of photons; the recorded time will be longer/shorter than in reality and is used to locate the vertex. Studies on the effect of vertex reconstruction from PMT shifts are underway. Figure 2.8 shows studies by R. Akutsu on the difference in position of reconstructed events with unaccounted changes in tank geometry. The two regimes of tank warping show that the reconstructed positions of neutrino events change if the geometry is wrong, which is as yet unaccounted for in Super-K analysis.

2.6 Feature detection in drone images

The data set for training is made by labelling a set of photos of the Super-K ID as PMTs, bolts, and background, giving 3 classes as shown in Figure 2.9. The purpose of training here is to segment an image with high accuracy and coverage of the image. While there is little difference between the PMTs themselves, their appearance in images varies both within the image and between different images.

(a) (b)

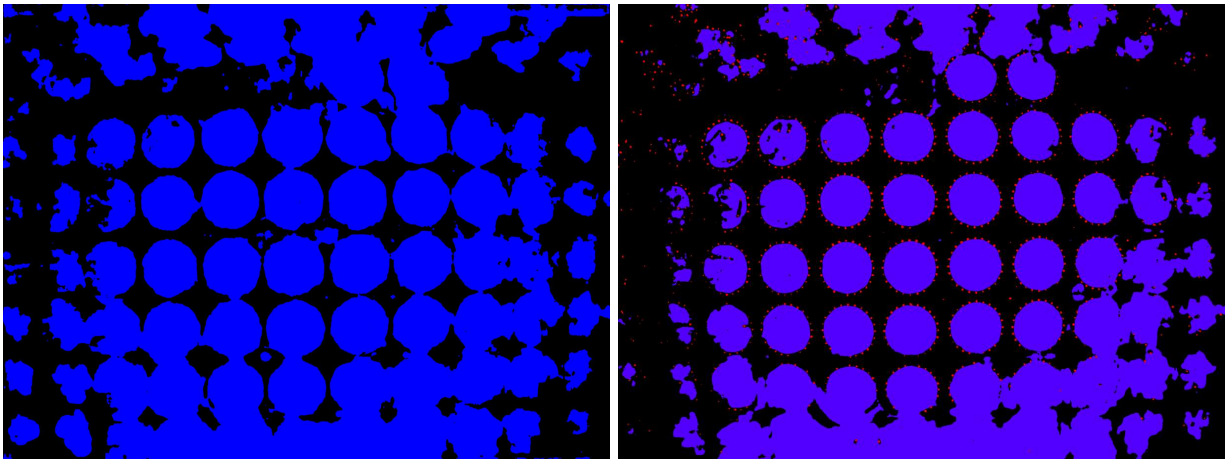


Figure 2.10: **(a)** Two class training (Blue: PMT, black: background) leads to misidentification of background as PMT. The edges of the PMTs are not well confined. **(b)** Three classes (Red:bolt, blue:PMT, black:background) improves the confinement of PMTs with better definition of their edges.

Manually labelling PMT images is a long process, however the identical nature of PMTs means a smaller training data set can be used. More training data may be necessary for reconstructing the entire tank to train for PMTs at more extreme perspectives. For example, most PMTs are pointed in the general direction of the drone in this data set, meaning in the corners of the tanks where PMTs are perpendicular to each other, the segmentation will fail.

The aim of reconstructing a ring of Super-K reduces the complexity of training required for accurate reconstruction in this area while allowing for testing of images from other parts of the tank.

2.6.1 Training and augmentation

The training process uses three sets of 416×416 px images which were randomly cut from larger, 4000×4000 px images that were labelled manually. Random cropping eliminates any bias that could be introduced by having a feature consistently in the centre of training images, ensuring the training encourages the location of features with respect to each other instead of their position in an image. In addition, cropping ensures no features are missed by being in the edges of images. A training set of ∼300 images were used to teach the neural net. An evaluation set of ∼100 images was used for the CNN to compare itself to and evaluate how well the training is progressing. A test data set of ∼20 images was used to test the final neural net on, one example is shown in Figure 2.9.

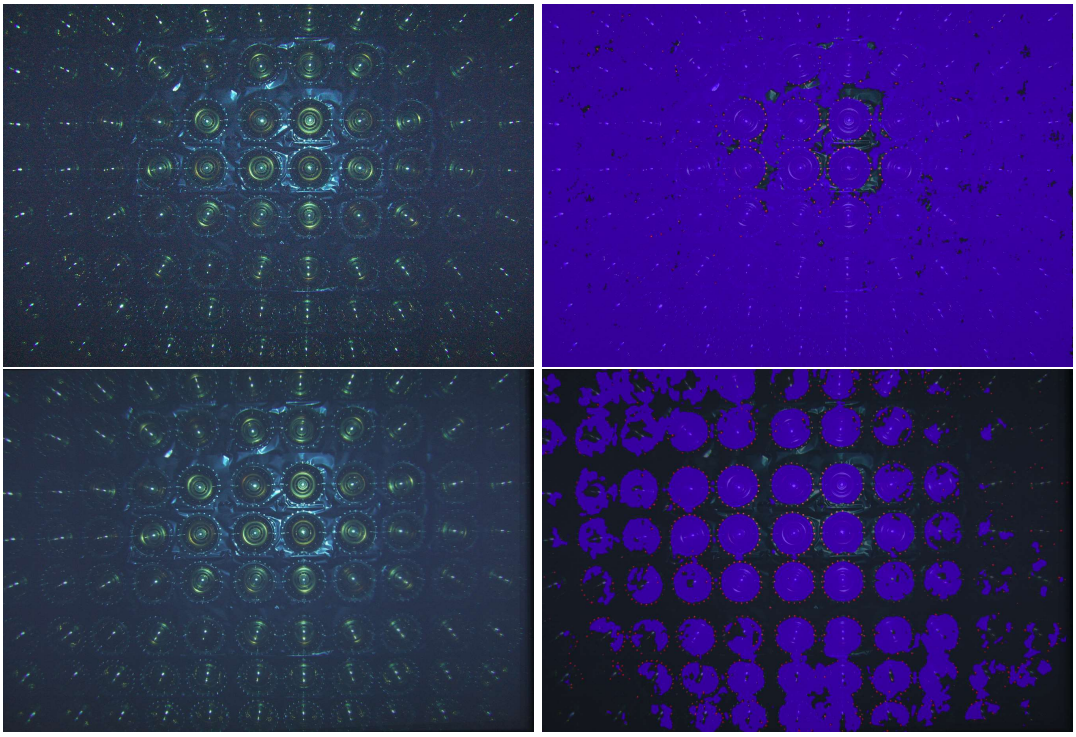


Figure 2.11: Top: A single image has ISO noise that drastically affects the performance of the CNN. Bottom: 10 images averaged with improved performance by reducing ISO noise. The ISO noise is trained on by stacking random numbers of images and adding them to the training and validation image sets.

Different methods of labelling were tested by labelling just the PMT and the PMTs and bolts. The CNN performed far better with the bolts and main body of the PMT as two separate classes, as shown in Figure 2.10. Segmentation around the edge of the PMTs is improved throughout the images even if some bolts are missed, mis-identification of background is reduced, and PMTs further from the centre are resolved.

Data augmentations is the process by which the training data is altered to train a specific behaviour and make the training more versatile and robust, while not adding any more data. Training data is augmented to help account for ISO noise in stacked images.

Where images are composed of an average of 10 photos, subdivisions of the stack of images were added to the training data. For example, some images were added as a stack of 5 images instead of 10. The segmentation of stacked images with high ISO noise is improved, as shown in Figure 2.11. For some images, where the drone moves during a burst, blurry photos are removed to better resolve PMT features at the cost of increased ISO noise.

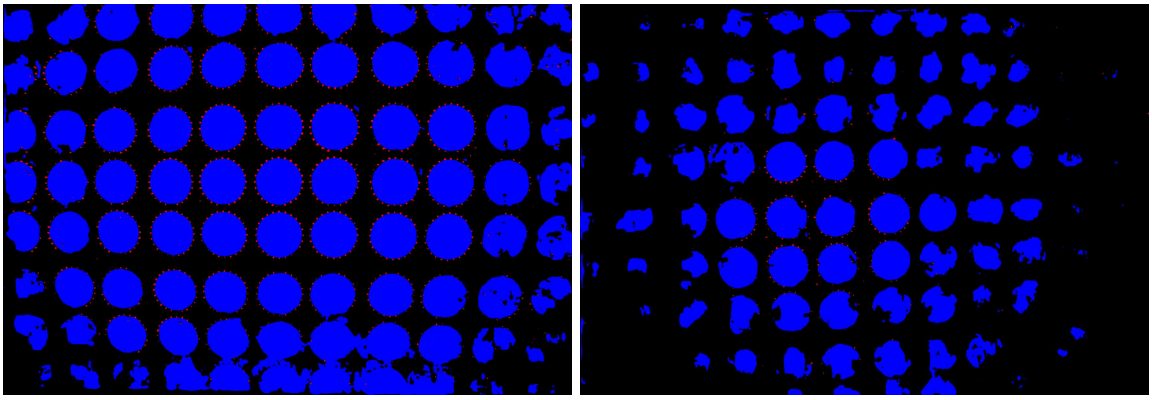


Figure 2.12: Image 755 (left) and 798 (right) segmentation masks. These images demonstrate good and bad examples of segmentation for the analysed ring of images.

2.6.2 CNN performance evaluation

The segmentation of Super-K images to locate PMTs in images is an achievable goal. Visual inspection of the PMT masks, generated from one survey of the 2020 TOW images, shows good separation of PMTs and background of images, with better performance in the centre. Examples of good and bad segmentation in the subset of images is shown in Figure 2.12.

It should be noted that while it is preferable to have images that are completely well segmented out to their edges, it is not a requirement for the end goal of reconstructing the ID PMT structure. Photogrammetry requires matching the same point between multiple images to triangulate the position of a feature, so in the case of poor segmentation at the edges of images, more images can be taken to ensure all PMTs are correctly reconstructed in multiple images.

The success of the CNN for PMT feature identification can be evaluated by counting the number of bolts and the diistance measured between opposite bolts for each PMT. The number of bolts is known to be 24 and the PMTs are circular, comparing the image reconstruction to the known geometry provides a powerful metric for evaluating the CNN. The two classes, bolts and PMTs, can be split up and analysed separately. PMT centres are found after applying a Canny edge detection algorithm to highlight the edges of the PMT class followed by a circular Hough transform [88] to find possible PMTs in the image. Bolts are located with a blob search with a lower limit of 10 px to ensure real bolts are located.

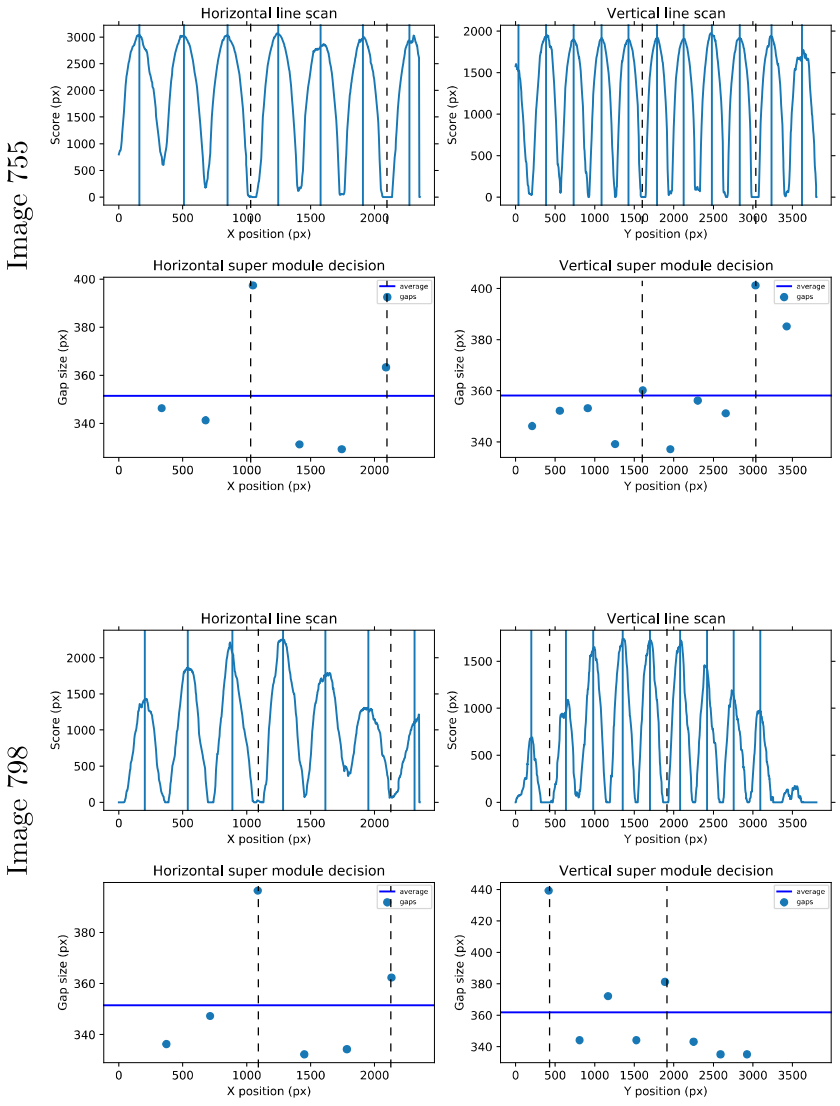


Figure 2.13: Pixel scores (top) and distance between peaks (bottom) for image 775 and 798. Score (px) is the number of pixels of the PMT mask in each row or column of the image, the peaks are approximately the centres of PMTs. The gap size is measured as the pixel distance between the PMT centres. It is expected that the super module gaps will be much larger than average. However, poor segmentation or images taken at an angle can smear the peaks out such that no super module boundary is obvious in the peak spacing. True super module boundaries (- - - -) and the average gap size for each image (——) are added to evaluate the performance of boundary location.

2.7 Analysis of segmented images

The rest of this chapter focuses on using a subset of the TOW images making up a full ring around the barrel of Super-K and distilling the information to a set of uniquely labelled PMT centres in images. The set of images were taken when the drone moved around the Super-K ID at constant depth. The final result is the imaging of the complete circumference of the Super-K ID and serves as a useful test for reconstruction. Many of the images appear identical with few unique features, meaning one of the major challenges of reconstructing Super-K is identifying which PMT is which in every image. Labelling PMTs relies heavily on drone movement assumptions. Once unique labels are applied to PMTs in images, a list of PMT positions in images and their labels can be used to create a 3D model.

2.7.1 Coarse PMT location

In order to locate super module boundaries, the PMT mask for an image is scanned horizontally and vertically by a single line of pixels. The number of pixels that overlap the PMTs gives a score for that line. Figure 2.13 shows peaks in pixel score for each axis in the image, giving an approximate grid on which the PMTs lie. The aim at this stage is to provide a quick approximate location of PMTs and to measure the gaps between them for locating super module boundaries. A blob search can then find segmented PMTs near the points on the grid, and a second search can locate the bolts. The resulting data can be used as an early test of the segmentation of images by counting the number of PMTs per image and number of bolts per PMT, shown in Figure 2.14

2.7.2 Super module boundary location

The known super module pattern is exploited to help label PMTs with their unique IDs and track them between images. The distance between peaks in Figure 2.13 can be used to locate the Super module boundaries, as shown in Figure 2.15. The larger gaps are more likely to be the super module boundaries. However, in the case where the image is not well segmented, the pattern of larger gaps becomes confused and additional information on the super module location is taken by reprojecting the boundaries found in the previous image in the ring onto the new one, as demonstrated in Figure

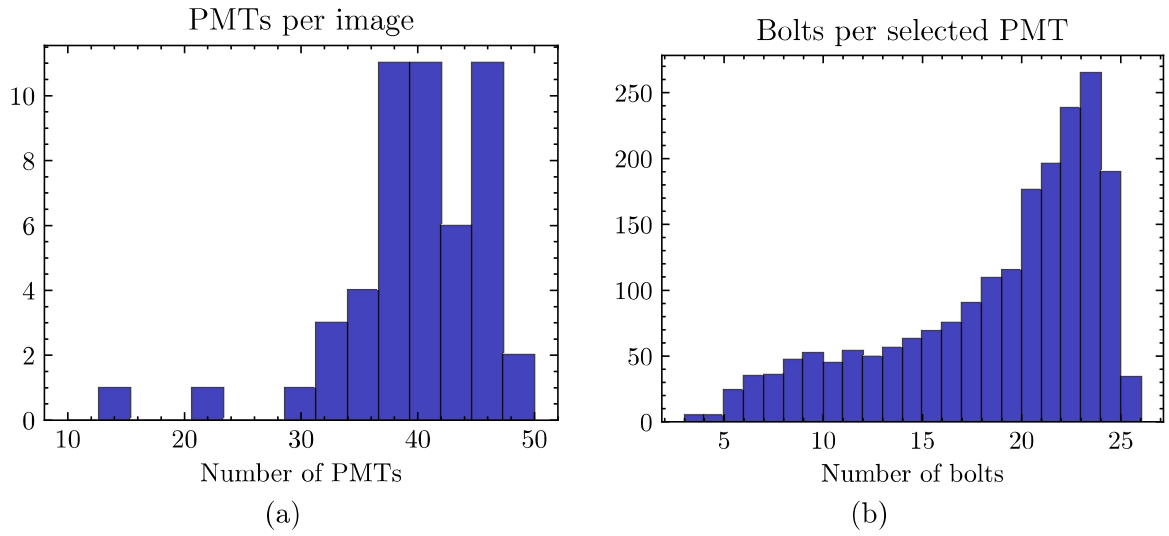


Figure 2.14: **(a)** Initial number of PMTs reconstructed per image and fitted. **(b)** Number of bolts per PMT with a maximum of 24.

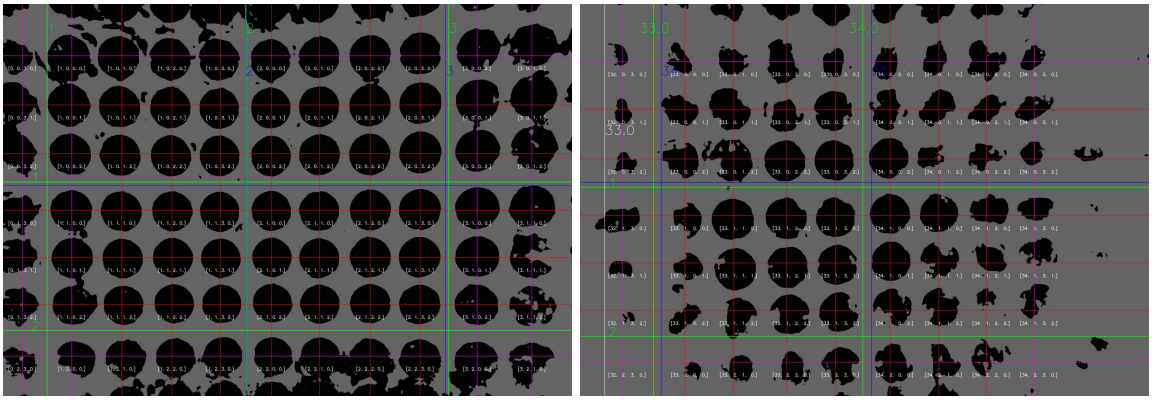


Figure 2.15: PMT masks for image 755 (left) and 798 (right) with the super module boundaries (green) and approximate PMT lines (red) automatically located from the plots in Figure 2.13. PMT labels in these images relate to internal counting of super modules from the start of the images going around the tank.

2.16. The constraints on locating super modules use the following assumptions:

- Gaps between super modules are larger than others in the image.
- Super module boundaries encompass 4 PMTs in the horizontal direction and 3 PMTs in the vertical direction.
- The super module gap in the horizontal direction is likely to be near the predicted position from the previous image using the drone movement.

This last point employs a simple projection from the previous image which is used to also label PMTs; super module location is then not independent for each image and so errors can propagate through

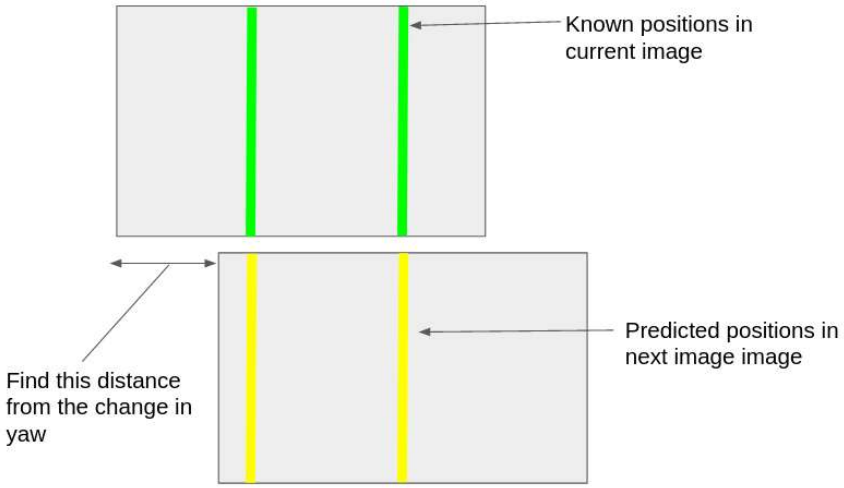


Figure 2.16: Apparent movement of super module boundaries between two images. Tracking this movement is important in order to provide accurate labels in the second image. Using one direction of movement (yaw) proves to be inaccurate.

the ring.

2.7.3 PMT labelling

Super module boundaries are used to define a grid around the ring of images used in reconstruction. Each super module is approximately reprojected from one image to another, and allows PMTs to be labelled with reference to the boundaries and have persistent, unique labels between images. The content of these labels is arbitrary and encodes only its position in the ring of images, not the whole of the ID. The drone is assumed to be at constant depth and the movement around the tank can be characterised using its yaw value.

Predicting where super module boundaries will fall in the next image requires the drone movement to be consistent between images. The first of these assumptions is safe to make, as the depth is easy to keep constant. However, the latter introduces errors into the labelling procedure because the drone has freedom of movement so its yaw, pitch, and roll are difficult to align so that the drone is perpendicular to the wall. The freedom in pitch, roll, and position allows for the drone to be pointed at an unexpected region of the tank given its yaw value, which results in incorrect labelling.

PMTs can be labelled with their unique identification numbers using any known location in the ID. A single correctly identified PMT in the whole image set, with its correct unique number, can

be used to provide all PMTs with their unique numbers. However, any errors from the super module defined labels remain. The PMT points found in images at this stage are not accurate enough for reconstruction. The photogrammetry software constrains each real space PMT position with every available location provided in the images. If the locations of PMTs in the images are inaccurate, the software tries to transform the lattice of PMT points to minimise reprojection error, giving inaccurate results. To improve the issue, a more accurate fit to the PMT position is made by finding the geometric centre of the bolt ring.

2.7.4 Ellipse fit to bolts

The bolts around each PMT are a separate segmentation class from the PMTs themselves. Bolts are generally better segmented and are located in the same plane as the super modules, therefore they provide a more accurate measure of the Super-K ID structure for use in photogrammetry. Alternatively, the centroid of the PMT blob can be used. However, the segmentation of PMTs could be less reliable, as they are transparent and can have badly defined boundaries in images, as shown in Figure 2.12. A Hough transform [88] is used to perform the fit, where an ellipse is drawn over the bolt mask, and the number of pixels that the drawn ellipse overlaps with the mask gives a score for the fit. The highest score for a bolt ring, after a grid search of fit parameters, is taken to be the best fit. This makes the fit for a single image take a long time, however it reliably fits to bolt rings and allows for measurements of 'good' PMTs based on the fit parameters and their expected ranges.

2.7.5 Pruning bad PMTs

Following the ellipse fit, it is necessary to remove PMTs that have not been fit properly, only keeping those that are well resolved and accurately located for use in photogrammetry reconstruction. PMTs will negatively affect the photogrammetry fit if the centre of the PMT is measured to be too far from its real position. The fit will reconstruct the drone to be in a different position than it really is and the PMT location in real space will be reconstructed incorrectly. PMTs are selected using the following parameters, which measure the quality of reconstruction:

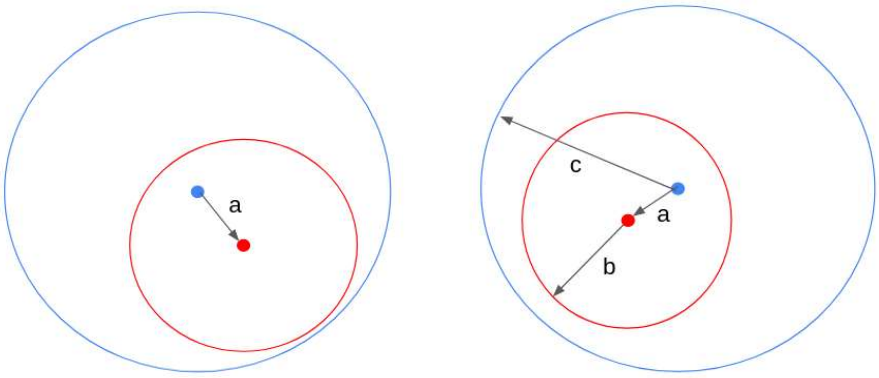


Figure 2.17: The expected location and size (blue) compared to an example fit to a bolt ring (red). (a): Distance between centres, (b) Major radius of fitted ellipse, (c): Radius of expected PMT. It is expected that the fitted ellipse will be approximately circular, close to the centre, and lie inside of the approximated PMT circle. PMTs are rejected if a is large or if $a + b > c$, in which cases either the ellipse fit or the approximate location of the PMT is incorrect.

- Ellipse score (px) - How many pixels of the bolt mask are covered by the fitted ellipse.
- Difference between the expected and fit centres (px) - Figure 2.17.
- Eccentricity of the ellipse - Expect circular PMTs.
- Proximity of the edge of the fit ellipse with the expected PMT (px) - Figure 2.17.

Selection metrics of PMTs were tuned by inspecting the distribution of each of the parameters as a function of distance from the centre of the image as shown in Figure 2.18. PMTs appearing closer to the centre have better localisation with clearer segmentation, as demonstrated in Figure 2.12. The sample of PMTs with centres between 400-800 px of the image center was chosen as the 'good' set of PMTs on which the cuts were tuned, the sample has good reconstruction and contained more PMTs than the $<$ 400 px sample. After pruning, there was a loss of some PMTs in the final sample, however, the remaining PMT fits were of higher quality. For this selection, 451 PMTs remained of the initial 668 PMTs without pruning and the <400 px sample contained 217 PMTs, insufficient for a complete reconstruction of the images.

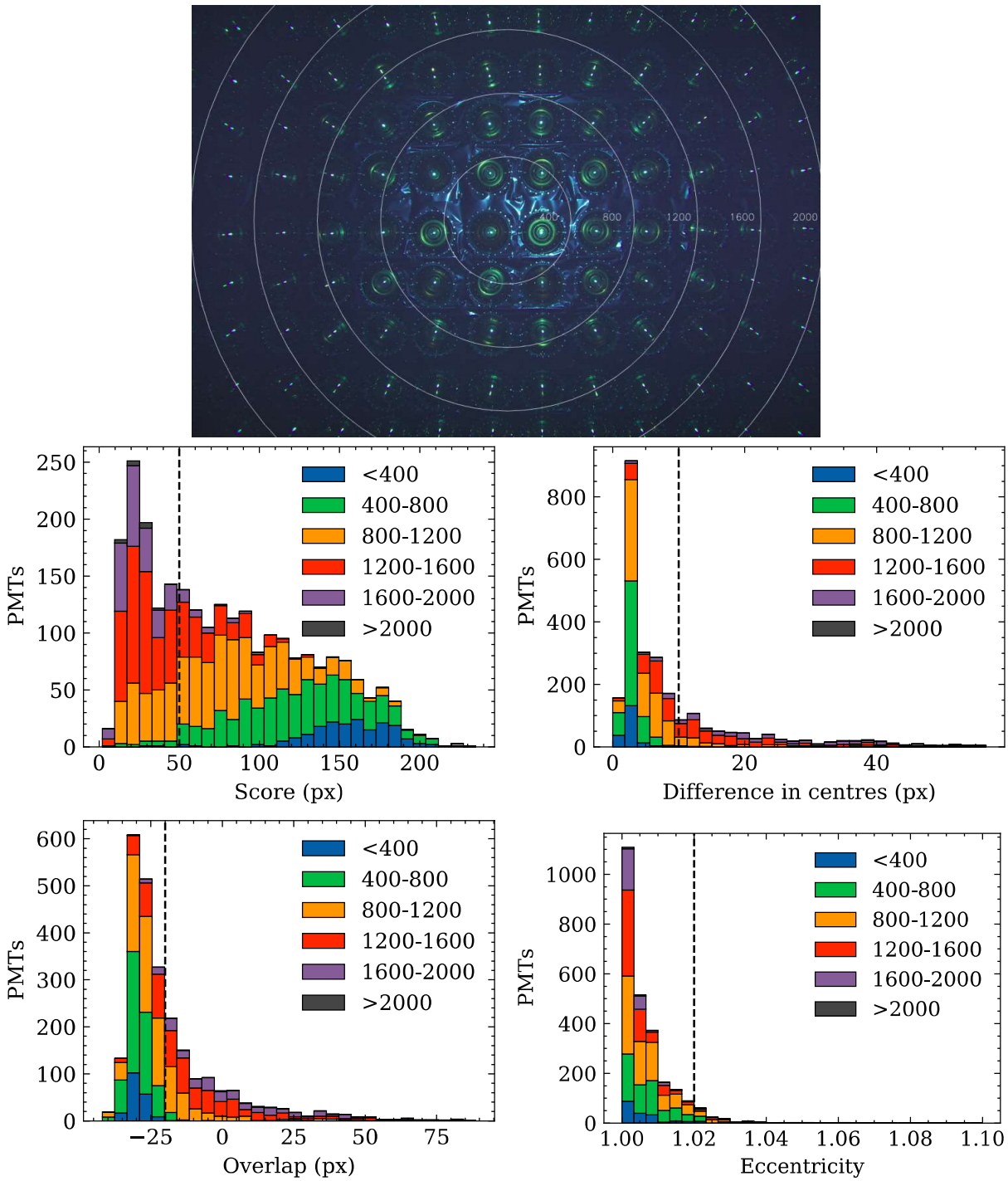


Figure 2.18: Top: Regions of images that select PMTs for analysis of their parameters to select an appropriate set for the photogrammetry software.
Bottom: Distributions of PMT pruning metrics. The score distribution has the greatest difference between the <400px and 400px - 800px regions. The cut is placed to keep and PMTs with score more than 50px, favouring the 400-800px sample.

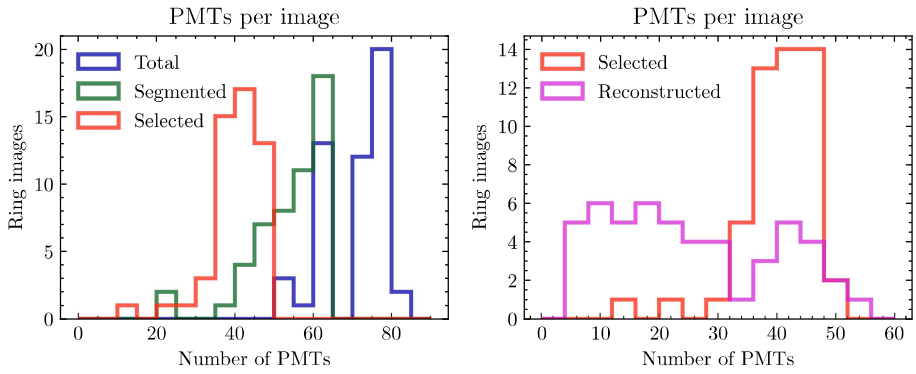


Figure 2.19: Evolution of number of reconstructed PMTs through image processing. Left: Selections of total number of PMTs predicted per image, then are segmented and assigned a PMT blob, before final selection. Right: selected PMTs and the PMTs per image that appear more than twice in multiple images.

2.7.6 Final sample of PMTs

The final sample of PMTs comes from a set of selections on segmented images, where only the best reconstructed PMTs are kept. The selection efficiency at each stage is described in Table 2.1 with results summarised in Figure 2.19. The efficiency is calculated relative to the theoretical maximum number of PMTs imaged for all PMTs in all images and unique PMTs. A unique PMT carries a label that is tracked between images using the reprojection technique described in Figure 2.16. PMT position can then be triangulated when reconstructing the Super-K tank. The blob cut is a simple blob search in the region around line intersections described in Section 2.7.1. It shows 76% efficiency for assigning a blob to a PMT location, in the PMT segmentation. The following cuts are based on a fit to the reconstructed bolt ring and are described in Section 2.7.5. The initial score cut removes all PMTs without a bolt ring and has an efficiency of 60% since the bolt segmentation is worse than that for the PMTs and more localised to the centre of images. Further cuts remove no PMTs, showing the score metric is sufficient to select good PMTs. There are 1420 (40%) reconstructed and labelled PMTs of which 723 are unique. There is a further constraint requiring a PMT to appear at least two times in the images so that their relative 3D positions can be reconstructed. There are 451 unique PMTs appearing more than once to be used in photogrammetry.

Table 2.1: Cut by cut PMTs and efficiencies for analysis of segmented images. Each cut is applied sequentially, though the final pruning cuts have little effect on the sample of PMTs. The constraint of each unique PMT appearing more than once is applied so that 1174 points are passed to the photogrammetry software to be reconstructed into 477 PMTs.
[1]-The number of PMTs in 8 rings with 150 PMTs each, the maximum number of PMTs that could be reconstructed with this image set.

	Total	Efficiency	From Last	Unique	Efficiency	From Last
Imaged	3570	-	-	1200[1]	-	-
Blob Cut	2718	0.76	0.76	965	0.80	0.81
Score Cut	1643	0.46	0.60	780	0.65	0.93
Centre Cut	1424	0.40	0.87	723	0.60	1.0
Overlap cut	1420	0.40	0.997	723	0.60	1.0
Eccentricity cut	1420	0.40	1.0	723	0.60	1.0
Imaged> 1 time	**1174**	**0.33**	**0.83**	**451**	**0.38**	**0.62**

2.8 Photogrammetry reconstruction

The PMT points for each image, along with their labels, are used to reconstruct the in-situ Super-K geometry. Each image has a set of points, calculated from the centre of the bolt rings, with a unique label defined by a UK light injector fitting. Neighbouring images include the same points which the photogrammetry algorithm can align to stitch the points of each image together. The photogrammetry software used was developed by Nick Prouse for Super-K and Hyper-K analyses. The fit minimises the reprojection error of the points in an image which is calculated by reconstructing a point and reprojecting it as the camera would see it. The difference between the reprojected point and true position in the image being the error as shown in Figure 2.20. The photogrammetry software performs bundle adjustment to minimise the reprojection error [89]. While not a measure of the Super-K geometry, the reprojection error gives an indication of how well the photogrammetry software has performed with the supplied features and should be less than 1 px for a good reconstruction.

The reprojection error, as shown in Figure 2.21, is affected by each PMT and the errors introduced from the super module locator and ellipse fitter described previously. Mislabelling of PMTs and errors in locating PMT centres will lead to the higher reprojection error seen in Figure 2.21. An iterative process was used where points were supplied to the photogrammetry software and then manually adjusted if the labels were wrong because it is very difficult to tell from the images themselves.

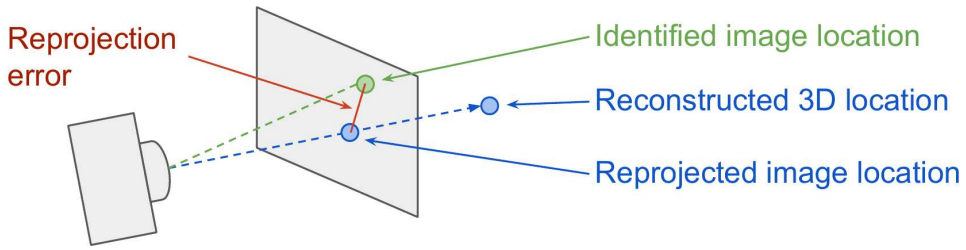
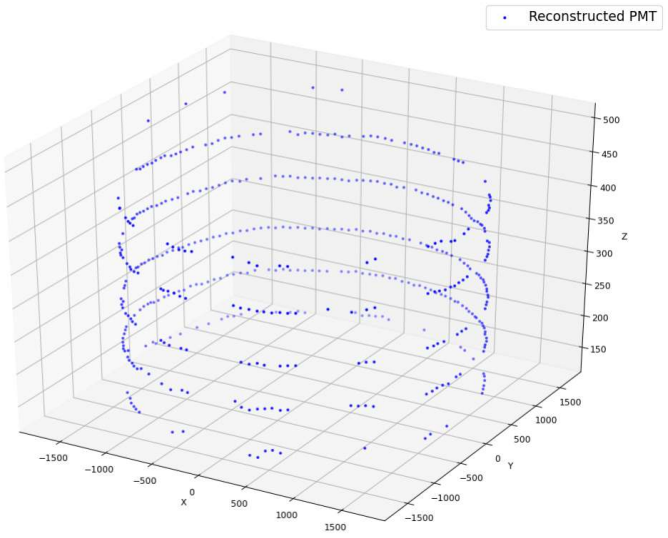


Figure 2.20: The reprojection error for a feature in an image used for photogrammetry is defined as the difference between the point in an image to the projected reconstructed point from the cameras point of view. The error is used to judge how well the photogrammetry software is reconstructing features, and is affected by the labelling of features in images.

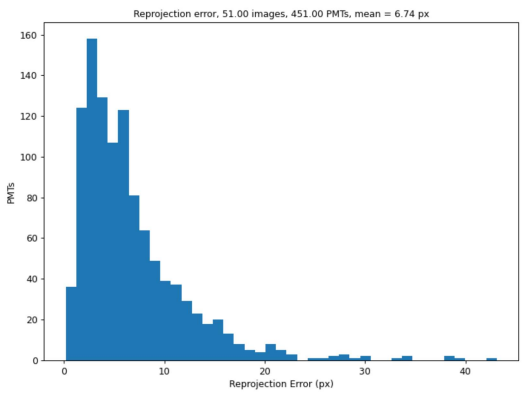
2.8.1 Feature analysis of reconstructed Super-K geometry

Once the photogrammetry software has produced a model of Super-K, it is possible to compare large scale features to known design variables. For example, the tank diameter and eccentricity. By design, the Super-K inner detector is circular with a diameter of 33 m and can be measured from the photogrammetry fit.

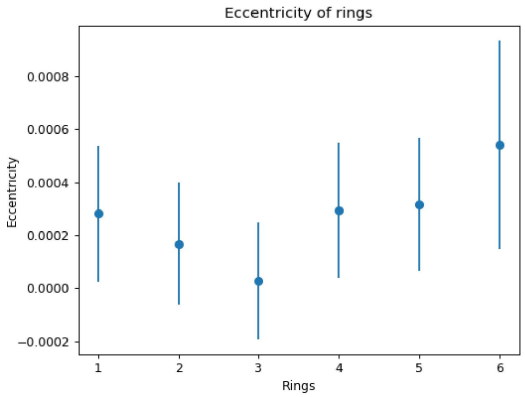
Uncertainties in the PMT positions are introduced from the photogrammetry software and there is slight correlation between points from the fit of the order of 10^{-3} so points are independent of one another. The dominant error is in the radial direction due to the errors introduced in drone positioning. The eccentricity of each ring is shown in Figure 2.21(c) and is a good measure of the performance of the photogrammetry fit, which cannot measure absolute scale. The eccentricity is slightly above 0 at 0.2%; the magnitude of eccentricity is small and no deviation from the circular hypothesis is observed. Taking the area of an ellipse to be $A = \pi ab$, where $a \approx (1 - e)b$ for small e, gives a total volume change of 0.2%, any effect from the in-situ structure deviating from the circular design has a negligible effect on the fiducial volume. Current fiducial volume uncertainties introduce a 2.5 cm error on reconstructed vertex position resulting in a 0.43% uncertainty on event rates [90].



(a)



(b)



(c)

Figure 2.21: **(a)**:The final points from Table 2.1 and **(b)**, their reprojection error, with an average of 6.74. **(c)**:Eccentricity of rings of PMTs in (a). Each ring has eccentricity close to zero and there is minimal deviation from the expected circular barrel shape.

2.9 Conclusions

The methods explored in this study demonstrate the application of machine learning to generate in-situ models of the Super-K geometry. The segmentation required relatively little training data and could be improved further with rigorous augmentation or by training on a broader data set, for which there was not enough time in this study. The weights output from U-Net are specific for Super-K, and it would be unlikely that they could be used in future water Cherenkov detectors for PMT segmentation, especially with the proposed mPMT use in Hyper-K and IWCD whose appearance is much different than the standard 20 inch PMT[75].

The main challenge of analysis is providing unique, accurate labels to each PMT in each image.

Labelling required manual correction to be accurate, better super module position prediction or another label tracking method should be investigated to reduce labour and improve performance. The ultimate aim is to locate the PMT dynode in images with <1 px reprojection error for all PMTs in the Super-K tank, which was not achieved. Currently, the segmentation performance is not good enough for accurate dynode location outside of the central image region. Further developments could be made with additional photos for segmentation training, to increase accuracy of feature detection. Additionally, more photos for in the photogrammetry improves the triangulation power for PMTs.

The biggest flaw for image processing is, in general, labelling PMTs. Errors are introduced from the assumptions made about the movement of the drone and rather than uncertainties on the order of pixels, there are errors on the order of meters if a super module boundary is wrong. These can be corrected manually, however, the process is laborious and would need correcting if scaled up to the entire Super-K ID.

The reconstructed PMTs showed no change in the structure of Super-K. However, the set of images used was limited to a small section of Super-K so the larger scale shifts in Figure 2.8 couldn't be evaluated. Additionally, the segmentation could be developed further to measure individual PMT locations.

This study has served as a proof of concept for the use of photogrammetry for measuring changes in the structure of Super-K. The results have helped to inform the design for future water Cherenkov detectors which will include static cameras identifying marks on PMTs to aid in their identification in images. This will solve many of the processing issues faced during reconstruction.

Chapter 3

SK event simulation, reconstruction, and sample selection

Table 3.1: Software versions used in analysis for MC generation and event reconstruction.

Software	Version
SK Library	19b
NEUT	5.4.0
Flux	21bv2
fiTQun	v4r0b

This chapter details the established process for using Super-K MC for analysis as well as the details of event reconstruction with `fiTQun` which is central to the issues surrounding NCπ^0 misreconstruction. The final section documents the existing Super-K sample selections for runs 1-10 and the problems caused by NC1π^0 event backgrounds. Table 3.1 shows the software versions used.

3.1 Simulation

Super-K MC events are generated using libraries that document the status of the Super-K tank and include PMT gain adjustment, dead channels, and water transparency. MC events are generated inside Super-K then weighted according to the T2K experimental setup, closely following the setup for the 2022 oscillation analysis release [68]. The events are normalised to the T2K protons on target (POT); 19.664×10^{20} in FHC and 16.34556×10^{20} in RHC. Events are weighted by the flux prediction at Super-

K which is regularly updated as understanding of the beam deepens [91]. Finally, the cross-section for interaction at Super-K is simulated using the NEUT event generator [92].

3.2 fiTQun reconstruction

Event information in Super-K is extracted using a maximum likelihood algorithm called `fiTQun` [93]. The raw data from Super-K is interpreted by `fiTQun` and event information is reconstructed. For parameters such as lepton flavour (e-like, μ-like), a likelihood is calculated which is interpreted by taking the ratio of likelihood of two hypotheses to decide which best matches the event.

`fiTQun` likelihoods are calculated using the charge and time information for every PMT hit in an event and determines how likely a given particle topology is represented by the distribution of hits. Each event is split into packets of hits in a 10 μs window, each packet is a sub event containing hits from the initial interaction and any subsequent decay processes. Charge deposited in time windows beyond the first hits in the detector count the number of decay electrons. Each sub-event contains hits from particles that deposit charge in the detector; the likelihood for a single particle track is calculated using the following variables:

- Vertex position (x, y, z)
- Vertex production time
- Direction
- Momentum (θ, ϕ)
- Energy lost along particle track

Collectively these parameters are defined as $\boldsymbol{x}$ and the likelihood is constructed based on the charge and time of hits in PMTs:

$$L(\boldsymbol{x}) = \prod_{i=1}^{N_{\text{unhit}}} P_i(\text{unhit}; \boldsymbol{x}) \prod_{j=1}^{N_{\text{hit}}} P_j(\text{hit}; \boldsymbol{x}) f_q(q_j; \boldsymbol{x}) f_t(t_j; \boldsymbol{x}) \tag{3.1}$$

where $P_j(\text{unhit}|x)$ is the probability of PMT j not registering a hit given x. $f_q(q_j;\boldsymbol{x})$ and $f_t(t_j;\boldsymbol{x})$ are charge and time likelihoods respectively. Evaluation of Equation 3.1 requires calculation of the predicted charge and time, a full description is available in [93, 94]. Events are reconstructed in order to extract the event topology; Number of particles and particle identification (PID), as well as the kinematics of the particles based on the topology hypothesis; location, direction, energy, and momentum.

For this analysis, the multi ring fitter in `fiTQun` is important as it is responsible for the misreconstruction of π^0 events as single ring e-like events. A full description is available in [94], the fitter is summarised here.

Initially, `fiTQun` fits a single ring to the event with e and π like hypotheses (π-like events are very similar to μ-like events). The single ring fit is passed to a multiring fitter that adds a ring with each e or π hypothesis and re-fits the event for ee, $e\pi$, πe, and $\pi\pi$ hypotheses. Care is taken here because adding a ring increases the degrees of freedom in the fit and the likelihood will always be greater than or equal to that of the single ring fit. Simply taking the highest likelihood would be incorrect, so the new ring is only accepted if the increase in likelihood is large enough to be a real second ring. This process is repeated until adding a ring does not improve the fit enough, or 6 total rings is reached. There is then an iterative process of removing fake rings by refitting the event by adjusting each ring in turn as well as applying a muon-like hypothesis to the most energetic ring. The final output is a list of tested hypotheses and associated likelihood values, the number of rings for the event is taken to be the number of rings in the most likely hypothesis. When selections are made, the ratio of likelihoods is used to determine the flavour composition of events rather than the likelihoods directly, e.g. $\frac{L_e}{L_\mu}$ is the cut variable for the e/μ PID, which come from the `fiTQun` fitters.

3.3 Super-K event selections

This section covers current Super-K event selections, made using parameters calculated by `fiTQun` and developed using MC events. All event selections require high quality events that are Fully Contained within the Fiducial Volume (FCFV) of the detector. The FCFV event selection describes events that

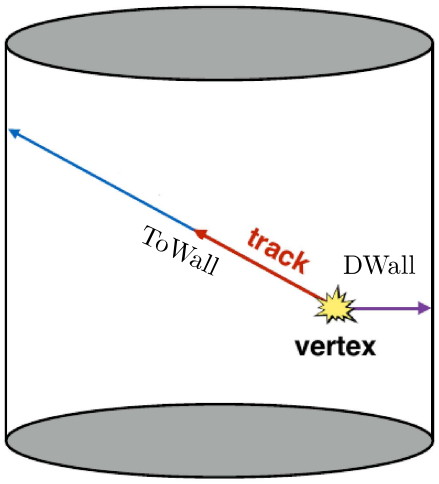


Figure 3.1: Calculation of ToWall and DWall parameters used for fiducial volume cuts. The cut values vary depending on the event type, muons need a greater ToWall and DWall to be reconstructible.

could potentially be reconstructed, it is the baseline for all samples used in Super-K.

From the FCFV selection, samples are defined as μ-like or e-like by their most energetic particle, as well as the presence of decay electrons. Further PID cuts on samples remove background events to improve sample purity. The single ring e-like sample is of particular interest for the inclusion of NCπ^0 samples in an oscillation analysis. Super-K currently has five samples of events, the FHC and RHC single ring e-like (1Re) samples are descried in Section 3.3.2 contain events from $\nu_\mu \rightarrow \nu_e$ oscillations, the appearance channel. The other 3 samples included are single ring μ-like (1Rμ) FHC and RHC and single ring ν_e CC1π^+ (1Re1de) are also covered, more detail can be found in [95].

3.3.1 Events Fully Contained in the Fiducial Volume (FCFV events)

The FCFV requirements are the minimum for an event to be reconstructed. Events must be Fully Contained (FC) meaning none of the light produced by the event is outside of the Super-K tank, otherwise its energy would not be reconstructible. In addition, there must be a minimum light deposited in the inner detector so that there are enough hits to reconstruct a ring. For a ring to be reconstructed it needs to be large enough and cover enough PMTs, this is achieved with fiducial volume cuts given the names ToWall and DWall. ToWall is the distance between the reconstructed event vertex and the nearest wall of the ID in the direction of the particle that produced the ring, ensuring the ring can be

formed and is big enough for particle identification (PID). DWall is the perpendicular distance from the event vertex to the nearest wall, ensuring the event is far enough from the wall that the light from the ring does not miss too many PMTs and light is not lost. The definitions of Dwall and ToWall are shown in Figure 3.1. Fully contained fiducial volume (FCFV) events are selected as:

- Fewer than 16 hits to PMTs in the outer detector.
- More than 30 MeV energy detected by ID PMTs.
- ToWall distance greater than 80/50 cm for e/μ.
- DWall distance greater than 170/250 cm for e/μ.

Plots of FCFV cuts and their effects on the sample are shown in Appendix A.

3.3.2 Single ring e-like selection

The 1Re-like samples selects single ring e-like events which are typical of ν_e interactions where a single electron is produced following a ν_e interaction. 1Re-like events are selected using `fiTQun` cuts in FHC and RHC as:

- FCFV selection detailed in Section 3.3.1, with DWall $>$ 80 cm, ToWall $>$170 cm.
- 1 Reconstructed ring.
- Ring is electron-like rather than muon-like.
- $E_{vis.} > 100$ MeV
- No decay electrons.
- Reconstructed neutrino energy, $E_{\nu}^{rec} < 1250$ MeV.
- Ring is electron-like rather than π^0-like.

The e/μ cut selects fuzzy electron-like rings over sharp muon-like rings, examples in Figure 3.2 and has the form:

$$\frac{L_\mu}{L_e} - 0.2P_{1Re}^{reco} > 0, \tag{3.2}$$

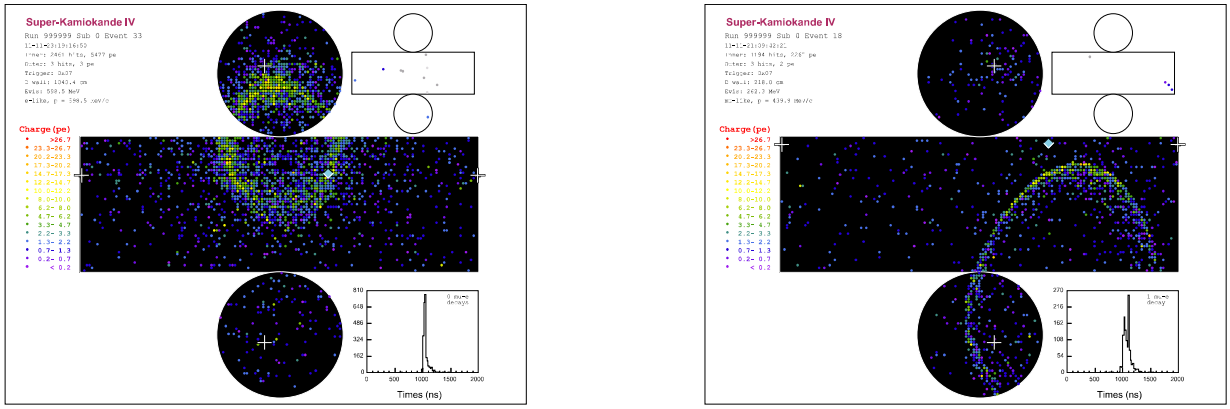


Figure 3.2: Left: e-like event with a fuzzy ring, right: μ-like event with a sharp ring [67].

where L_μ and L_e are the likelihood for single ring muon and electron-like events respectively. P^{reco}_{1Re} is the reconstructed ring momentum assuming a single ring e-like hypothesis. The final π^0 rejection cut is a 2D cut constructed as the likelihood ratio of a single ring e-like hypothesis with an unconstrained π^0 fit, $\frac{L_e}{L_{\pi^0}}$ against the reconstructed π^0 mass for additional separation of the CC and NCπ^0 events:

$$\frac{L_e}{L_{\pi^0}} < 180 - 0.75 M^{reco}_{\pi^0} \tag{3.3}$$

The cut aims to remove NC1π^0 events that are mis-reconstructed as single ring e-like events as they are the dominant background for 1Re-like events. The final samples and the e/π^0 cut are shown in Figure 3.3. The sample is binned in reconstructed neutrino energy which is calculated by assuming the neutrino interacts with a stationary bound nucleon in Oxygen [95]:

$$E^{rec}_\nu = \frac{(M_n - V_{nuc})E_l - \frac{m_l^2}{2} + M_n V_{nuc} - \frac{V_{nuc}^2}{2} + \frac{M_n^2 - M_p^2}{2}}{M_n - V_{nuc} - E_l + P_l \cos(\theta_{beam})}. \tag{3.4}$$

Where M_n, M_p, m_l are the masses of the neutron, proton, and outgoing lepton respectively. V_{nuc} is the binding energy of a nucleon in Oxygen (27 MeV). E_l, P_l, and θ_{beam} are the energy, momentum, and angle relative to the beam of the outgoing lepton. The outgoing lepton is assumed to be an electron for the 1Re sample.

Effect of mis-reconstruction on NCπ^0 events

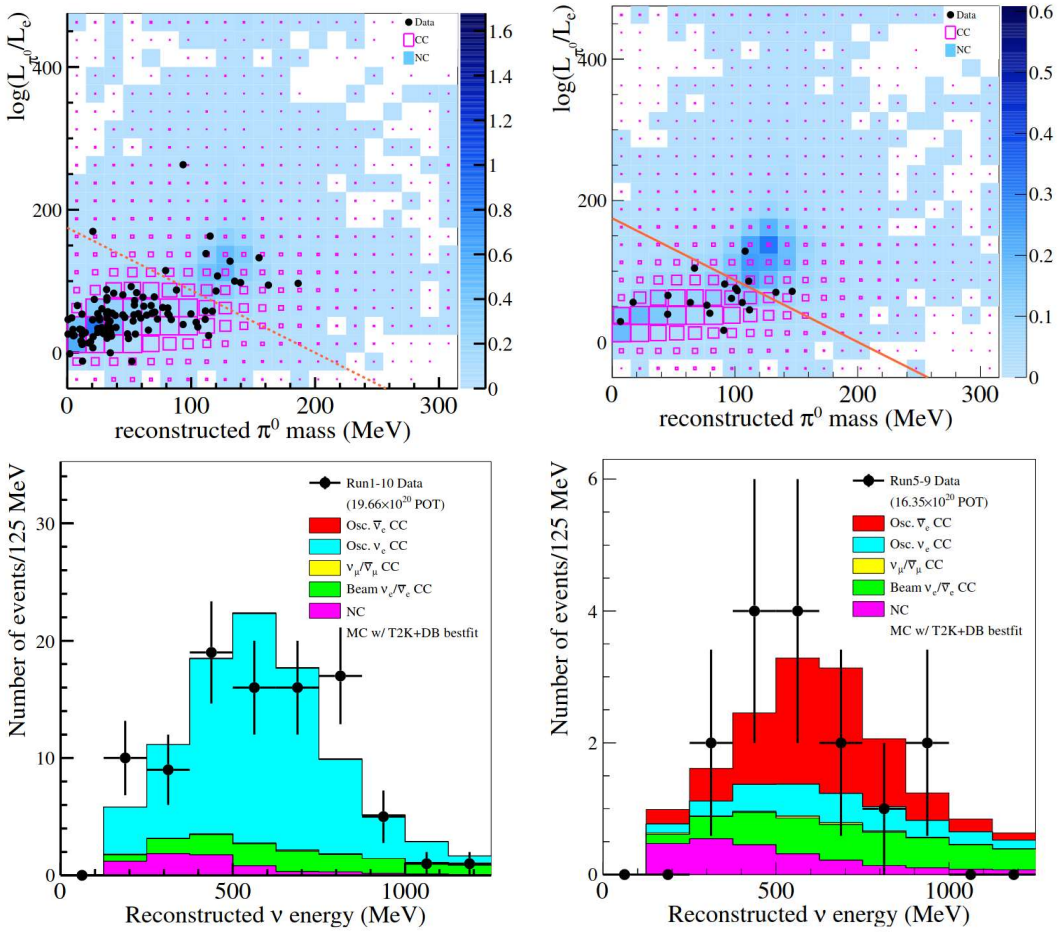


Figure 3.3: Summary plots of the 1Re Super-K samples. Left is FHC, right is RHC. Top: The $e\pi^0$ PID cut showing NC and CC MC predictions and data. Bottom: Total e-like sample after all cuts broken down by interaction mode. Plots from Run 10 data release [95]

NC1π^0 events can be mistaken for e-like events because the two γ rings from the π^0 overlap and can look like a single ring, see Figure 4.1. The `fiTQun` algorithm can classify π^0 events as a single ring e-like event, instead of a π^0, contaminating the 1Re-like sample. The final cut of the e-like selection in Section 3.3.2 helps reduce the NCπ^0 backgound by cutting on the ratio of likelihoods from the single ring e-like fit from the multi ring fitter and an unconstrained π^0 fit, independent of the multi ring fitter. In addition, the cut is a function of reconstructed π^0 mass as the π^0 fit will still accurately reconstruct the π^0 mass from overlapping rings. However, the e-like events will have a different (generally lower) reconstructed π^0 mass as there is no π^0 present.

Applying the e/π^0 cut removes 53% (56%) of the NC background in FHC (RHC) from Table 3.2. The e/π^0 cut also removes 6.077 (1.094) oscillated single ring e-like events in FHC (RHC) for run 1-10 POT. The CCQE events removed appear in a region with high NCπ^0 background and could be

Table 3.2: Top: FHC, bottom: RHC 1Re event rates normalised to 19.664×10^{20} and 16.346×10^{20} POT respectively. Int. $\nu_e + \bar{\nu}_e$ CC are intrinsic ν_e events from the beam.

FHC	Backgrounds				Signal		MC Total
Cut	$\nu_\mu + \bar{\nu}_\mu$ CC	Int. $\nu_e + \bar{\nu}_e$ CC	NC	Total BG	$\nu_\mu \to \nu_e$	$\bar{\nu}_\mu \to \bar{\nu}_e$	
FCFV	886.362	56.685	260.508	1203.555	109.753	0.979	1314.287
Single Ring	397.177	29.511	49.246	475.934	94.001	0.765	570.700
Electron-like PID	11.353	29.491	30.897	71.740	93.885	0.764	166.389
Evis >100 MeV	4.339	29.317	21.197	54.853	92.680	0.760	148.294
One Decay-e	1.196	24.903	18.205	44.304	83.884	0.738	128.927
Erec	0.764	13.129	14.137	28.029	81.240	0.540	109.809
π^0 rejection cut	0.423	11.661	6.607	18.691	76.164	0.461	95.315
RHC							
FCFV	321.130	22.659	89.745	433.534	6.249	9.749	449.532
Single Ring	149.007	11.281	16.923	177.211	4.670	8.516	190.397
Electron-like PID	2.761	11.274	10.605	24.640	4.667	8.512	37.818
Evis >100 MeV	1.533	11.244	7.384	20.161	4.612	8.485	33.258
One Decay-e	0.431	9.930	6.259	16.620	4.051	8.306	28.977
Erec	0.286	4.333	4.699	9.319	3.402	7.825	20.547
π^0 rejection cut	0.142	3.723	2.065	5.929	3.086	7.047	16.062

recovered if the background events were constrained, doing so would increase the oscillation statistics by $\sim 5\%$ in FHC and $\sim 10\%$ in RHC.

3.3.3 Single ring e-like CC1π sample

The ν_e CC1π sample, or 1Re1de, is an appearance Super-K sample that only has a selection in FHC. CC1π events are described in Section 1.5. The sample is similar to the 1Re sample with a single decay electron:

- FCFV selection detailed in Section 3.3.1, with DWall > 50 cm, ToWall >270 cm.
- 1 Reconstructed ring.
- Ring is electron-like rather than muon-like.
- $E_{vis.} > 100$ MeV
- One decay electron.
- Reconstructed neutrino energy, $E^{rec}_{CC\Delta} < 1250$ MeV.
- Ring is electron-like rather than π^0-like.

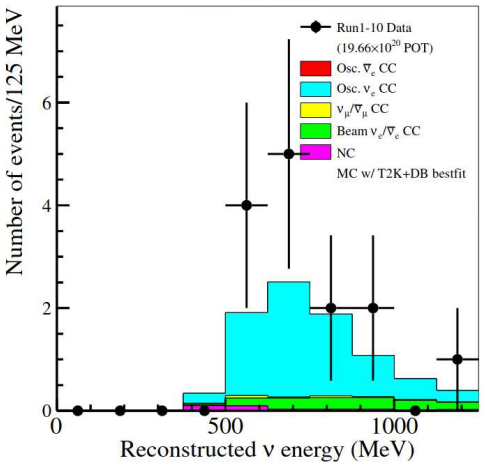


Figure 3.4: 1Re1de sample broken down by interaction mode. Plots from Run 10 data release [95]

CC1π events occur through Δ^{++} resonant production with reconstructed neutrino energy given by:

$$E^{rec}_{CC\Delta} = \frac{2M_n E_e + M^2_{\Delta^{++}} - M^2_n - M^2_e}{M_n - E_e + P_e \cos(\theta_{beam})}. \tag{3.5}$$

where $M_{\Delta^{++}} = 1232.0$ MeVc^{-2} is the Δ^{++} resonance mass. E_e and P_e are the reconstructed neutrino energy and momentum respectively. Figure 3.4 shows the true neutrino energy distribution for the 1Re1de sample.

3.3.4 Single ring μ like sample

The 1Rμ samples are disappearance Super-K samples in FHC and RHC, selecting single ring ν_μ interactions. Events are selected as:

- FCFV selection detailed in Section 3.3.1, with DWall $>$ 50 cm, ToWall $>$250 cm.
- 1 Reconstructed ring.
- Ring is muon-like rather than electron-like.
- Reconstructed muon momentum, $P_\mu > 200$ MeVc^{-1}.
- Fewer than two decay electrons.
- Passes the 2D μ/π^+ likelihood based cut, $\ln\left(\frac{\mathcal{L}_{\pi^+}}{\mathcal{L}_\mu}\right) < 0.15 P_\mu$.

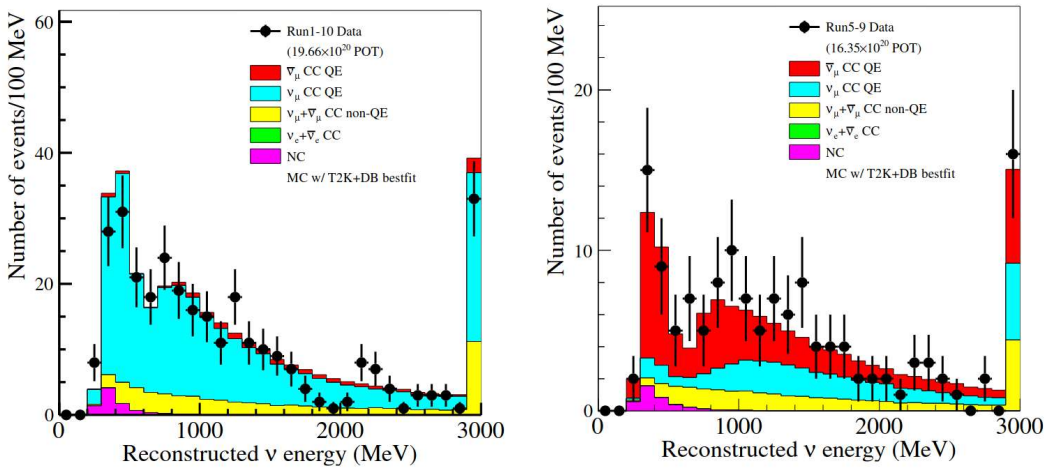


Figure 3.5: Summary plots of the 1Rμ Super-K samples. Left is FHC, right is RHC. Total μ-like sample after all cuts, broken down by interaction mode. Plots from Run 10 data release [95]

The final cut is similar to the π^0 rejection cut in the 1Re samples and rejects π^+ events. The true neutrino energy distribution in FHC and RHC is shown in Figure 3.5. 1Rμ samples are known as disappearance samples and the 1Re and 1Re1de samples are appearance, given that the T2K neutrino beam, is initially made up of muon neutrinos.

3.4 Summary of Super-K Samples

The Super-K samples described in this chapter are the appearance (e-like) and disappearance (μ-like) samples for oscillation measurements. The 1Re sample has a dominant background of NC1π^0 events, CCQE signal events are lost in the removal of the NCπ^0 background. The following chapter describes two samples of NCπ^0 events that could be used to reclaim the removed 1Re events by constraining the NCπ^0 background.

Chapter 4

NCπ^0 Samples

This chapter describes the formation of two samples of NCπ^0 events at Super-K. Section 4.1 describes a sample containing events that are rejected from the 1Re sample in Section 3.3.2by the final e/π^0 cut. The aim of the 1RNCπ^0 sample is to recover the lost 1Re events. Section 4.2 describes a new 2Rπ^0 sample which contains true π^0 events to measure the large NCπ^0 background present in the 1RNCπ^0 sample. Section 4.2 describes the tuning process for the new likelihood cuts in both samples and in Section 4.2.1 the backgrounds present in the 2RNCπ^0 sample are also investigated.

As a dominant background to e-like event reconstruction at Super-K, NCπ^0 events are removed using a cut which also removes some CCQE e-like events in order to increase sensitivity when measuring oscillation parameters. In addition, the flux of NCπ^0 events at ND280 is expected to be the same as at Super-K. NCπ^0 events occur via neutral current weak interactions which are flavour blind and the flux is unaffected by oscillations. A sample of NCπ^0 events at the near and far detector could be used to measure the neutrino flux.

NC1π^0 events are defined as events that produce a single π^0 and are detectable by the π^0 decaying to $\gamma\gamma$ with branching ratio $\frac{\Gamma_{\gamma\gamma}}{\Gamma_{tot}} = (98.823 \pm 0.034)\%$ and a very short lifetime, $(8.43 \pm 0.13) \times 10^{-17}$s [12]. The π^0 mass is reconstructed as:

$$M_{\pi^0} = 2E_{\gamma 1}E_{\gamma 2}(1 - \cos(\theta)). \tag{4.1}$$

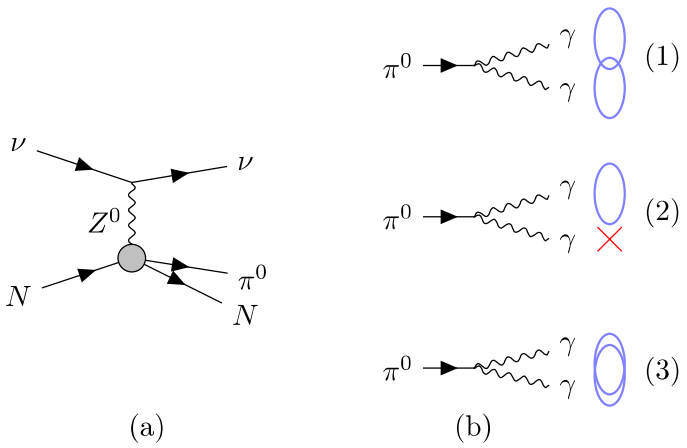


Figure 4.1: (a) A typical NC1π^0 event where a flavour blind neutrino interaction takes place producing a single π^0. In the initial interaction, there are no rings generated. (b) π^0 decay produces two γs that are boosted in the direction of the π^0 each producing a ring but can be reconstructed as a single ring. (b1) Non-overlapping rings are produced if the γs can separate. (b2) A γ can be dim or missed in reconstruction. (b3) Rings can overlap to a large degree and be almost indistinguishable.

Where M_{π^0} is the π^0 mass, E_γ are the photon energies, and $\cos(\theta)$ is the opening angle between photons. NC interactions produce a π^0 either through an excited state nucleon ($\Delta^+ = uud$ or $\Delta^0 = udd$) resonance, or coherently with the entire nucleus [65]. The π^0 decay vertex can be assumed to be the neutrino interaction vertex because of the very short π^0 lifetime. The photons are emitted in opposite directions in the π^0 rest frame but are boosted along the direction of the π^0 and each generate e-like rings in the Super-K ID. With a large enough separation, the rings are identifiable. With a large boost or if one ring is dim, the event is incorrectly reconstructed as a single e-like ring. Figure 4.1(b)(1-3) shows these possible NCπ^0 topologies.

4.1 Single ring π^0 Selection

π^0 events are a major background in the 1Re selection at Super-K, described in Section 3.3.2. The two photons from a π^0 decay can appear in Super-K as a single ring should the two rings overlap or if one ring is missed in reconstruction as shown in Figure 4.1. The single ring π^0 sample contains additional 1Re events that are lost when removing the NCπ^0 background. The purpose of the 1RNCπ^0 sample is to exploit the CC ν_e events it contains by constraining the NCπ^0 background using the 2RNCπ^0 sample.

A sample of 1RNCπ^0 events can be constructed with relative ease by inverting the final cut of the

single ring e-like selection:

- No decay electrons.
- 1 Reconstructed ring.
- Ring is electron-like rather than muon-like.
- Ring is π^0-like rather than electron-like.

The cuts applied are identical to the single ring e-like sample detailed in Section 3.3.2 with the final cut, Equation 3.3, inverted to select π^0-like events. The selection is kept almost identical to the 1Re sample, as the purpose of the 1RNCπ^0 sample is to make use of the signal events removed in the final cut of the 1Re sample. The events selected by this sample are referred to as single ring π^0 events as they are single ring and rejected from the 1Re sample for being too π^0-like in nature, even though the main events of interest in this sample are CCQE e-like events. Plots of the sample selection cut by cut are shown in Figure 4.2 and the final sample in Figure 4.3 with cut by cut event rates in Table 4.1. The reconstructed π^0 mass distribution is used for binning NCπ^0 events in Chapter 7.

The final single ring NCπ^0 samples are split by interaction mode in Table 4.2. The interaction mode is defined by the initial ν interacting in the detector and is truth level information which is only available to the MC generated data. CC events are used in neutrino appearance and disappearance measurements as the flavour information for the interacting neutrino is available. Neutral current (NC) events are flavour blind, so they can't be used in neutrino oscillation measurements directly. NCπ^0 and NCCoh are event types where there is an outgoing π^0 and aim to be constrained. All other NC modes are treated as backgrounds. In comparison to the 1Re sample from Table 3.2, the total number of events 1RNCπ^0 sample correlates to the number of events removed in the final cut of the 1Re-like sample as expected. The NCOther interaction modes are broken down into more specific modes in order to interrogate the backgrounds using the 2RNCπ^0 sample with higher statistics. The dominant background by far is NC1π^0 and NCCo. However, the NCOther interaction mode as a whole contributes ~ 3 (~ 1) events in FHC (RHC) which is not negligible compared to the CCQE events.

Table 4.1: FHC (top) and RHC (bottom) 1R NCπ^0 sample event rates. Each line is a subsequent cut making up the one ring NCπ^0 sample. The second column is the integral of total MC events selected. The third, fourth, and fifth columns are the efficiencies overall, from the FCFV cuts, and from the cut immediately before. The efficiency values are calculated from the total CC mode event rates. Purity is calculated similarly from CC events.

FHC					
Cut	Selected	Efficiency	From FCFV	From last	Purity
FC :	1386.71	0.669	-	-	0.643
+FV:	1257.13	0.617	1	0.922	0.656
+Evis :	1130.17	0.597	0.962	0.961	0.683
+0dcye:	429.36	0.121	0.200	0.204	0.380
+1ring:	169.35	0.044	0.072	0.365	0.647
+elike1:	102.27	0.021	0.03	0.480	0.524
+pi0 :	20.73	0.003	0.004	0.124	0.169
RHC					
Cut	Selected	Efficiency	From FCFV	From last	Purity
FC :	358.33	0.64	-	-	0.57
+FV:	324.47	0.60	1	0.93	0.58
+Evis :	303.41	0.58	0.98	0.98	0.62
+0dcye:	121.43	0.13	0.21	0.21	0.33
+1ring:	41.45	0.045	0.075	0.36	0.57
+elike1:	25.54	0.022	0.037	0.50	0.46
+pi0 :	8.36	0.006	0.010	0.265	0.25

Table 4.2: The 1RNCπ^0 samples broken down by interaction modes, which distinguish events by the initial neutrino interaction and are used during analysis. Each mode is shown in plots of samples and is made up of one or more NEUT mode. *- These modes are grouped into the NCOther mode during the oscillation analysis, they are split up for clarity of NC backgrounds.

Mode	Neut	FHC		RHC	
		Events	Fraction	Events	Fraction
CCQE	1	5.54	0.27	2.52	0.30
CC1π	11, 12, 13	1.41	0.068	0.87	0.10
CCCoh	16	0.033	0.0016	0.036	0.0043
CCmultiπ	21	0.18	0.0087	0.10	0.012
CCDIS	26	0.21	0.010	0.057	0.0068
NC1π^0	31, 32	7.31	0.35	2.37	0.28
NC1$\pi^\pm$	33, 34	0.49	0.024	0.19	0.023
NCCoh	36	1.27	0.062	0.73	0.087
NCOther	35, 44, 45	0.018	0.00088	0.0037	0.00045
CC2p2h	2	0.73	0.035	0.39	0.047
NC1γ	38, 39	0.040	0.0019	0.015	0.0018
CCmisc	15	4.2×10^{-5}	2.0×10^{-6}	0	0
NCmπ*	41	1.10	0.053	0.38	0.045
NCEta*	42, 43	0.0831451	0.0040	0.031	0.0037
NCDIS*	46	2.16	0.10	0.623	0.075
NCElastic*	51, 52	0.13	0.0064	0.049	0.0059

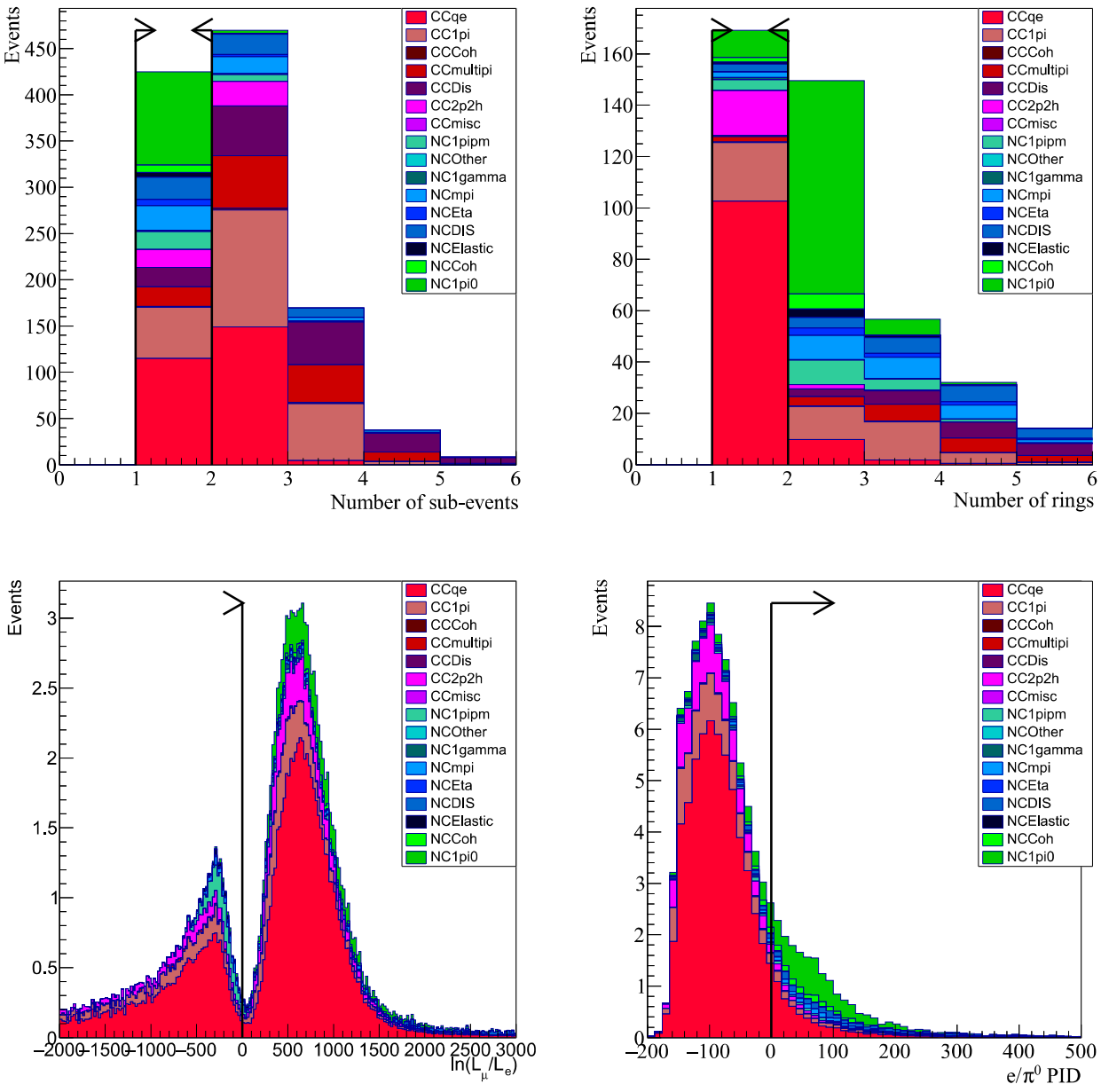


Figure 4.2: Cuts after FCFV selection for FHC events. The likelihood cuts are projected into 1D histograms for clarity of the backgrounds. The eπ^0 cut demonstrates the official 1Re sample being separated from the new 1RNCπ^0 sample with a dominant NCπ^0 event contribution.

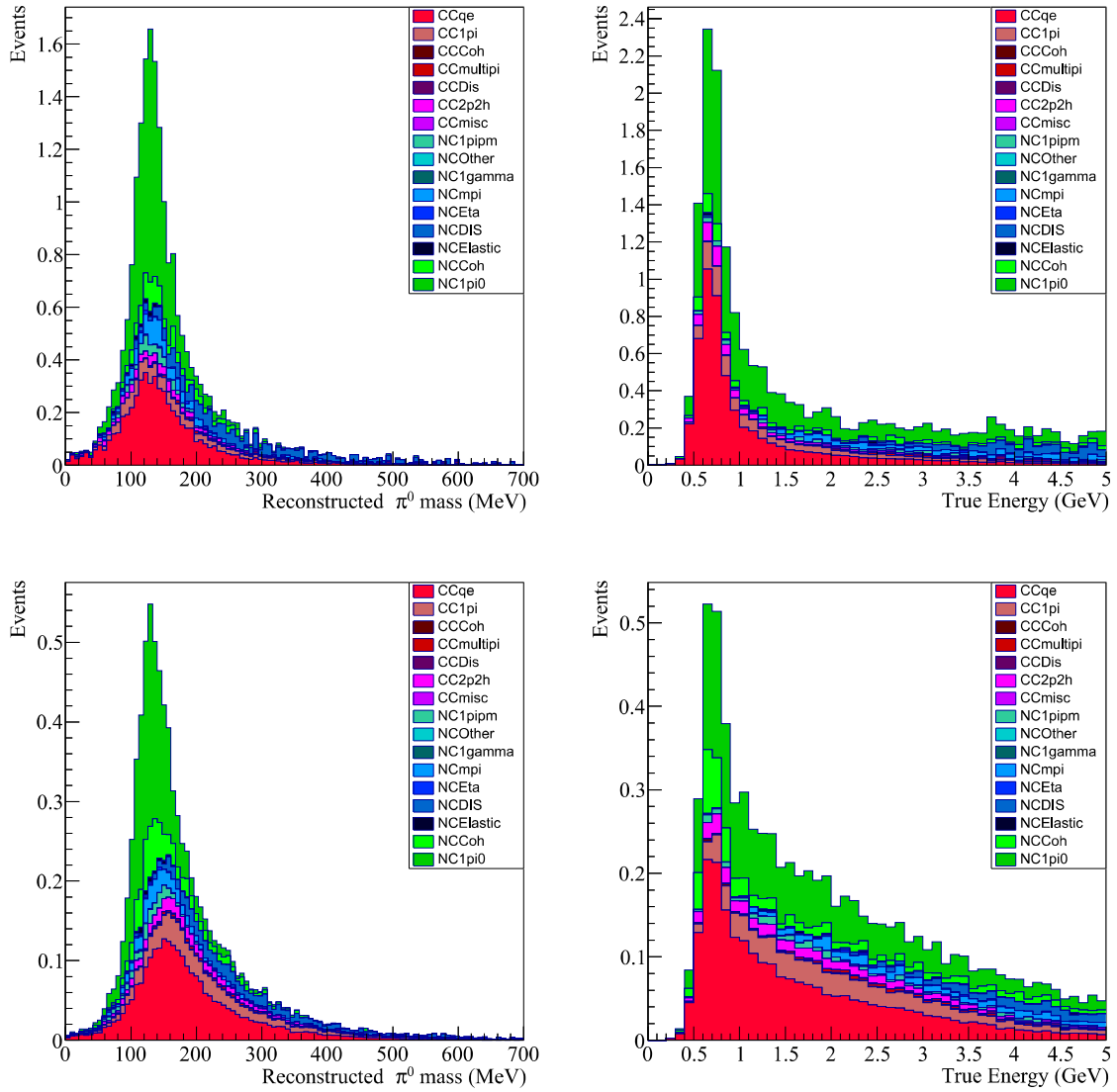


Figure 4.3: Final sample plots for; top: FHC and bottom: RHC 1RNCπ^0 samples. Left: Reconstructed π^0 mass. The CCQE evens appear in a similar region to the NCπ^0 events at the π^0 mass peak.

4.2 Two Ring NCπ^0 Events

For π^0 events, the electron-like hypothesis is used when calculating ToWall and Dwall. The vertex is reconstructed using the brightest ring of the π^0 to ensure both rings have enough distance to develop. Further cuts are applied to select NC1π^0 events based on the visible topology of a π^0 decaying via $\pi^0 \rightarrow \gamma\gamma$ using the criteria:

- No decay electrons
- 2 reconstructed rings
- Both rings identified as electrons
- π^0 hypothesis fit preferred over 1 ring e-like hypothesis

All cuts are made using `fiTQun v4r0b`. The multi-ring fitter is used in the third cut to identify each ring as electron-like. Te ratio of likelihoods is taken for an ee hypothesis to all other multi ring fits individually. After tuning the resultant parameter, see Section 4.2, the cut is optimised to:

$$\frac{L_{ee}}{L_{2ROther}} > 100, \tag{4.2}$$

where L_{ee} is the likelihood for an ee event, and $L_{2ROther}$ is the likelihood value of the best two ring fit for particles other than ee. Likelihoods are extracted from the multi-ring fitter described in Section 3.2. The final cut takes the form of the single ring π^0 rejection cut used in the single ring e-like sample, but is inverted to select π^0-like events. This cut is used to reject single ring e-like events that are mis-reconstructed as π^0 events and is identical to Equation 3.3 with an opposite inequality: The π^0 rejection cut is a 2D cut constructed as the likelihood ratio of a single ring e like fit with an unconstrained π^0 fit, $\frac{L_e}{L_{\pi^0}}$ against the reconstructed π^0 mass:

$$\frac{L_e}{L_{\pi^0}} > 180 - 0.75 m_{\pi^0} \tag{4.3}$$

Equation 3.3 was optimised for highest e-like selection efficiency for the 1Re sample, however, when

FHC						
Cut	Selected	Efficiency	From FCFV	From last	Purity	In peak
FC :	1386.71	0.623	-	-	0.135	0.235
+FV:	1257.13	0.541	1	0.868	0.130	0.232
+Evis :	1130.17	0.512	0.948	0.948	0.133	0.255
+0dcye:	429.363	0.496	0.918	0.968	0.351	0.516
+2ring:	149.974	0.405	0.750	0.817	0.636	0.732
+*ee*-like:	118.34	0.398	0.737	0.984	0.763	0.800
$+\pi^0$:	115.154	0.397	0.733	0.995	0.769	0.807
RHC						
cut	Selected	Efficiency	From FCFV	From last	Purity	In peak
FC :	358.33	0.632	-	-	0.160	0.272
+FV:	324.46	0.547	1	0.865	0.15	0.269
+Evis :	303.41	0.520	0.950	0.950	0.157	0.292
+0dcye:	121.43	0.504	0.921	0.970	0.377	0.540
+2ring:	47.42	0.405	0.741	0.804	0.64	0.733
+*ee*-like:	38.16	0.397	0.727	0.980	0.754	0.796
$+\pi^0$:	37.42	0.395	0.722	0.994	0.760	0.802

Table 4.3: Each line is a subsequent cut making up the two ring NCπ^0 sample. The second column is the integral of total MC events selected. The third, fourth, and fifth columns are the efficiencies overall, from the FCFV cuts, and from the cut immediately before. The efficiency values are calculated from the total NCpi0 and NCCoh interaction modes. The final two columns are the total and peak purity, where the peak is defined by the reconstructed π^0 mass: 0 MeV $< m_{\pi^0} <$ 300 MeV

Equation 4.3 is re-optimised to maximize π^0 selection efficiency, there is negligible change from the current cut as described further in Section 4.2.

Figure 4.4 shows the development of the sample as each cut is applied, after the FCFV selection in Section 3.3.1. The FHC efficiency and purity at each stage is described in Table 4.3. Efficiencies and purities are calculated with NCπ^0 and NCCoh interaction modes as signal events. The peak of non-NCπ^0 events in the π^0 mass distribution in Figure 4.5 is noteworthy because it is near the π^0 mass. This would indicate an event containing a π^0 or $\pi^\pm$, which has similar mass at (139.57039±0.00018) MeV [12]. These events are explored further in Section 4.2.1. The true neutrino energy distribution peak is slightly higher than the 600 MeV beam energy due to higher cross-section for neutrino interactions at higher energy.

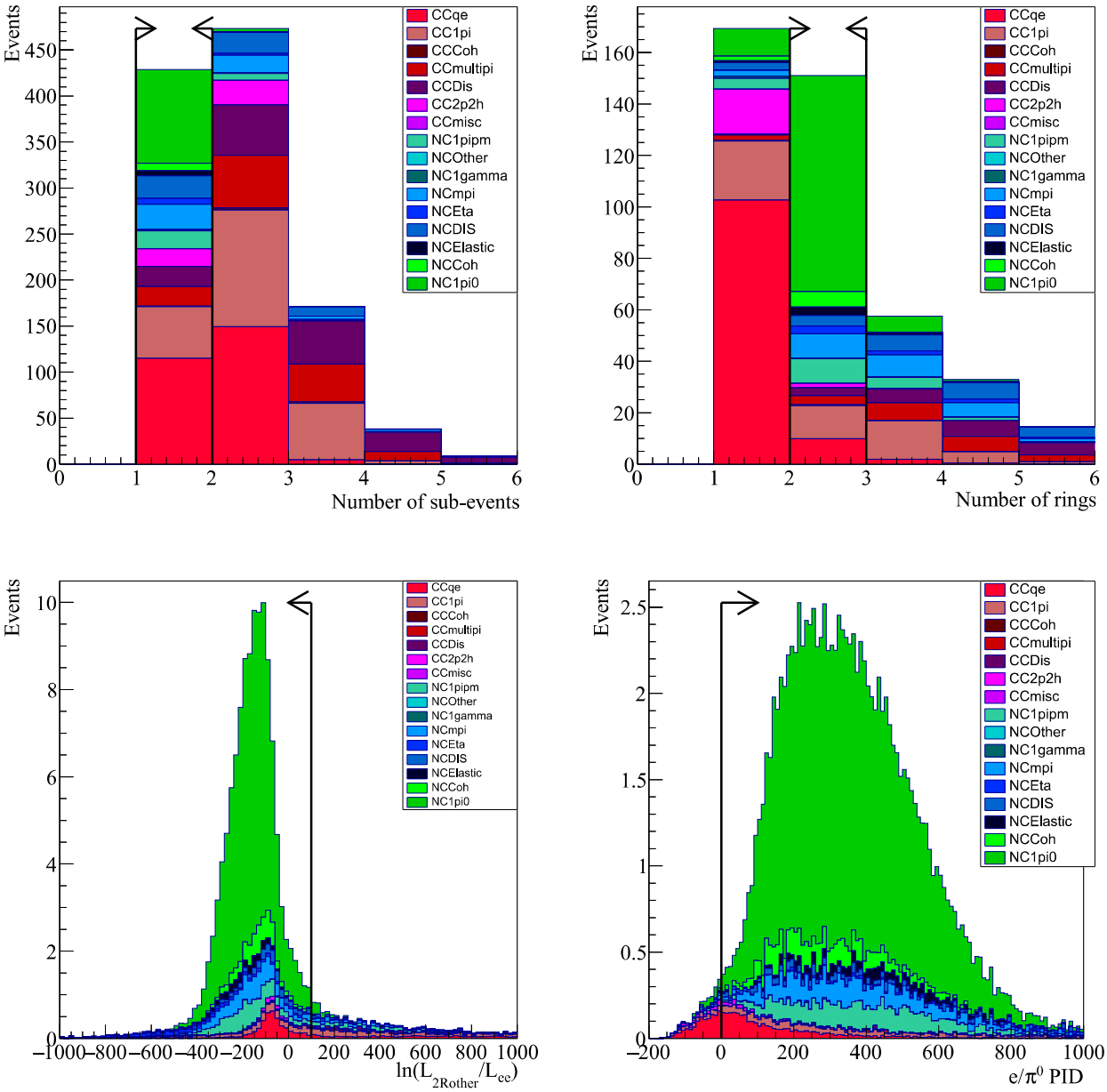


Figure 4.4: Cuts after FCFV selection for FHC events, similar RHC plots are available in Appendix A.

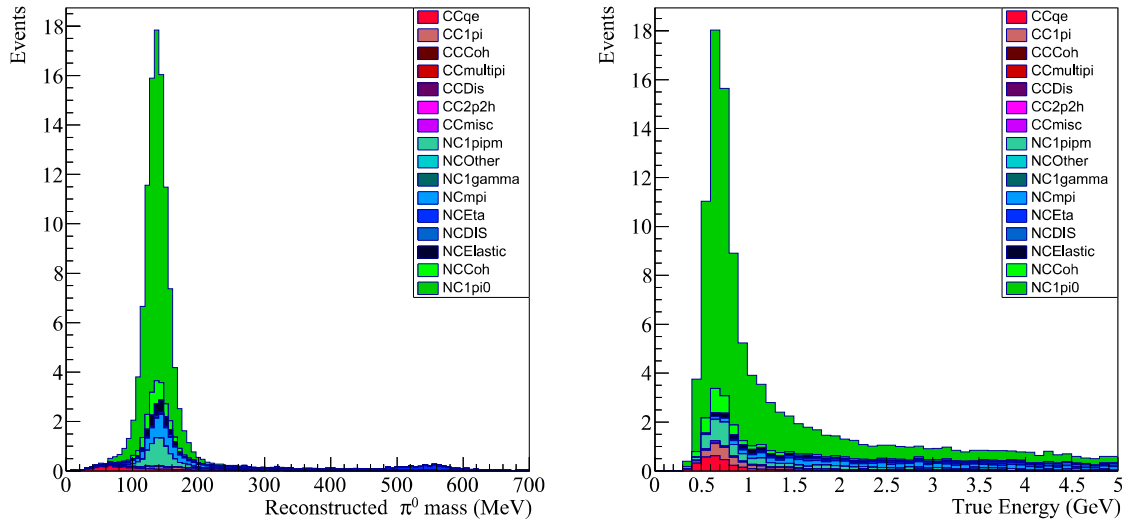


Figure 4.5: Final 2RNCπ^0 sample plots for FHC events. Left: Reconstructed π^0 mass distribution, the NCπ^0 mode dominate, however there are additional NC modes peaking at the NCπ^0 mass peak. Right: True neutrino energy distribution. The sample in predominantly NC interactions, with some CC events in the low π^0 mas region. RHC plots are similar and displayed in Appendix A

Table 4.4: The 2RNCπ^0 samples broken down by interaction modes which distinguish events by the initial neutrino interaction and are used during analysis. Each mode is shown in plots of samples and is made up of one or more NEUT modes. *- These modes are grouped into the NCOther mode during the oscillation analysis, they are split up for clarity of NC backgrounds.

Mode	Neut	FHC		RHC	
		Events	Fraction	Events	Fraction
CCQE	1	2.97	0.026	0.75	0.020
CC1π	11, 12, 13	3.1	0.027	1.01	0.027
CCCoh	16	0.044	0.00039	0.046	0.0012
CCmultiπ	21	0.51	0.0045	0.26	0.0063
CCDIS	26	0.46	0.0041	0.13	0.0035
NC1π^0	31, 32	82.3	0.72	24.8	0.67
NC1$\pi^{\pm}$	33, 34	7.48	0.066	2.38	0.064
NCCoh	36	5.64	0.050	3.56	0.096
NCOther	35, 44, 45	0.063	0.0006	0.025	0.0007
CC2p2h	2	0.43	0.0038	0.1	0.003
NC1γ	38, 39	0.06	0.0005	0.01	0.0004
CCmisc	15	7.9e-05	6.9e-07	6.9e-05	1.9e-06
NCmultiπ*	41	7.94	0.070	2.93	0.079
NCEta*	42, 43	2.77	0.024	1.15	0.031
NCDIS*	46	2.85	0.025	0.87	0.024
NCElastic*	51, 52	3.12	0.027	1.05	0.028

Tuning

The final two cuts of the two ring NCπ^0 selection are likelihood based and tuned to best separate signal from background using a figure of merit (FOM):

$$\text{FOM} = \frac{S}{\sqrt{S+B}}. \tag{4.4}$$

Where S is the signal selected by a cut and B is the background selected by the same cut, defined as all other events. Various forms of these cuts were tested for their effectiveness, either as 1D cuts on the log-likelihood ratio or as a 2D cut against reconstructed kinematic parameters, to best separate signal and background. Figure 4.6 demonstrates the tuning procedure for PID parameters used in the two ring NCπ^0 sample where one or two dimensional cuts are adjusted. The $\frac{L_e}{L_{\pi^0}} > 180 - 0.75 m_{\pi^0}$ cut was previously optimised to select single ring e-like events, for the NCπ^0 samples it is re-tuned to select NCπ^0 events. The existing $\frac{L_e}{L_{\pi^0}} > 180 - 0.75 m_{\pi^0}$ was tested in Figure 4.6(a) and (b); there is $< 1\%$ difference in FOM between a newly optimised cut and the 1R e-like sample cut, so no change is made. In addition, using a different e/π^0 cut in the single ring e-like and π^0 samples would complicate the systematic error evaluation as there would be regions of the single ring e-like and single ring π^0 like sample that overlapped and the samples would not be independent. For the new $\frac{L_{ee}}{L_{2ROther}}$ parameter, a flat cut at $\frac{L_{ee}}{L_{2ROther}} = 100$ is used based on Figure 4.6(c). Minimal signal/background separation can be gained from introducing a second variable, as in Figure 4.6(d).

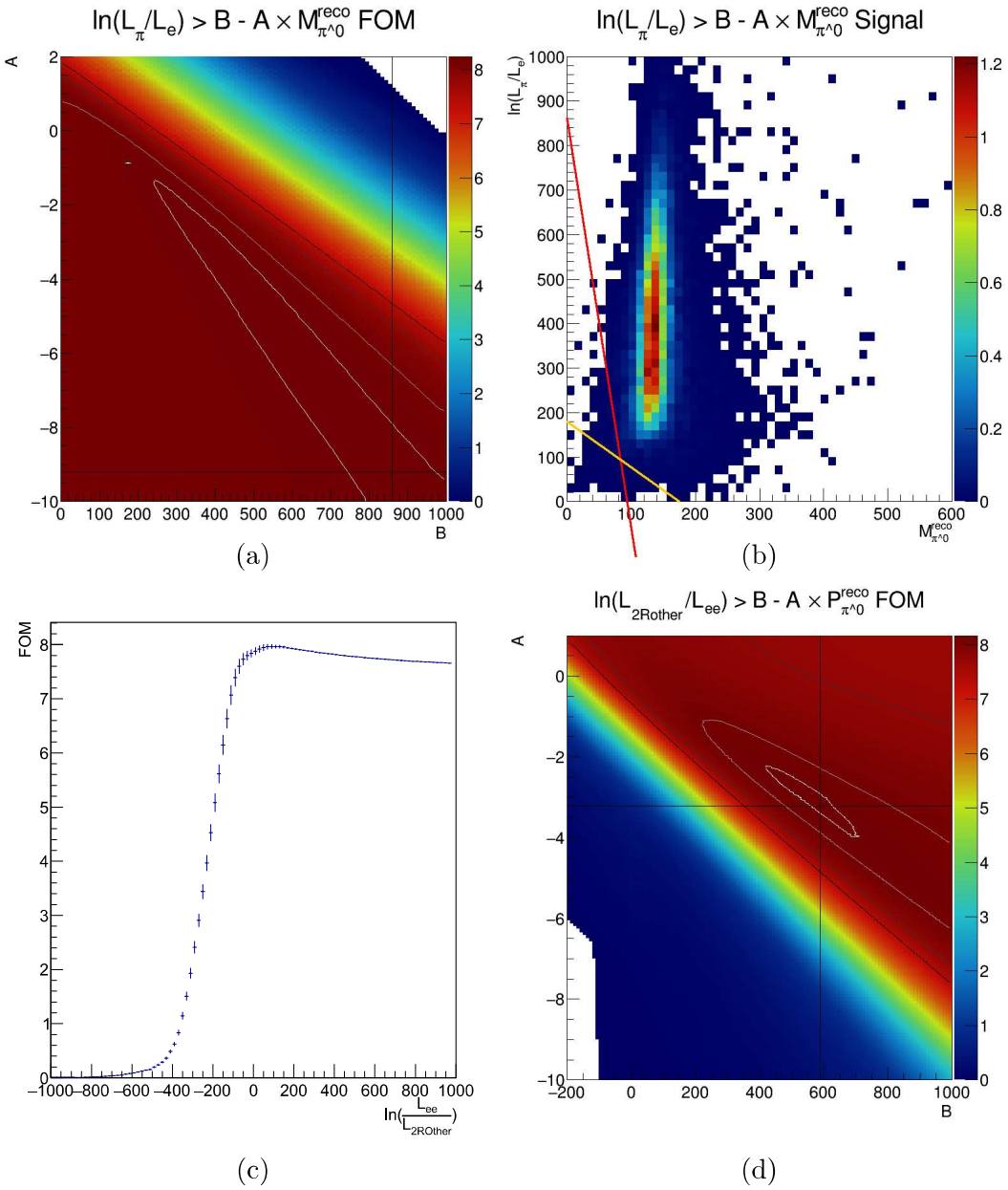


Figure 4.6: **(a)**: FOM values for a straight line PID cut as a function of $\ln(\frac{L_{\pi 0}}{L_e})$ and m_{π^0}. The contours represent the top 99.9% 99% 95% and 90% of the maximum FOM point indicated by the black crosshairs and a white dot represents the current cut. The highest FOM cut is shown by the red line in **(b)** and the current cut by the yellow line. **(c)** is a 1D FOM scan for the $\frac{L_{ee}}{L_{2ROther}}$ cut with a maximum at $\frac{L_{ee}}{L_{2ROther}} > 100$. When trying to optimise the cut further by cutting as a function of π^0 momentum in **(d)** there is <5% difference in FOM between the highest FOM and 1D cut point.

Table 4.5: The final states shown in MC selection plots. The final states are not the same as those used in the analysis and are more specific to the NCπ^0 samples to help investigate the backgrounds.The topologies consider secondary particles that are above their Cherenkov threshold with the aim of representing the ring generating particles for events that get selected. The first 6 entries are standard topologies used in T2K analyses, the rest are specific to investigating the neutral current backgrounds of NCπ^0 events. 2γOther estimates the false tagging of 2γ as a π^0. 1π^0 ChEx estimates the rate of production of π^0 events through charge exchange. The rest estimate the number of π^0 events that are categorised as not π^0 events as they have other ring generating particles present.

Topology	Description
1e	One electron only
1μ	One muon only
1eOther	One electron and one other only
1muOther μ	One muon and one other only
1$\pi^{\pm}$	One $\pi^{\pm}$ only
1π^0	Single π^0 that decays via $\pi^0 \rightarrow \gamma\gamma$
1π^0 ChEx	Single π^0 produced through charge exchange
2γ Other	Two γ s not from a π^0 decay
1π^0 Not2γ	Single π^0 that does not decay via $\pi^0 \rightarrow \gamma\gamma$
1π^0 N$\pi^{\pm}$	One π^0 with one $\pi^{\pm}$*only*
1π^0 1P	One π^0 with one proton
1π^0 Other	One π^0 and one other particle above Cherenkov
Other	Any other final state

4.2.1 Backgrounds

The purpose of splitting the NC backgrounds into events containing a π^0 with other particles in Table 4.5 is to understand the peaking background of Figure 4.5.The peak appears within the π^0 mass peak but is not classified as a single π^0 interaction mode, indicating a more complex interaction is either being mis-reconstructed or inadvertently selected.

The dominant background in the π^0 mass peak region, 0 MeVc^{-2} $< m_{\pi^0} <$ 300 MeVc^{-2}, is NC1$\pi^{\pm}$ events at 7%(6%). However, there is also a peak of NCmpi NCDIS and NCElastic events which, from Table 4.4, make up 17 (6) events in FHC (RHC) or 15%(16%) of the total sample. The final state topology of events is investigated, instead of the interaction mode, to understand the particles being reconstructed as two ring *e*-like events. Event topologies are defined by counting the particles that are above Cherenkov threshold and could potentially be reconstructed. A π^0 is given a Cherenkov threshold of 0 given the photons would be visible in the detector from the decay of a π^0 at rest.

Figure 4.7 shows the FHC two ring sample and NC backgrounds by final state mode; most of the peaking background appears to contain a π^0. Table 4.6 shows the event rates for each topology. Note

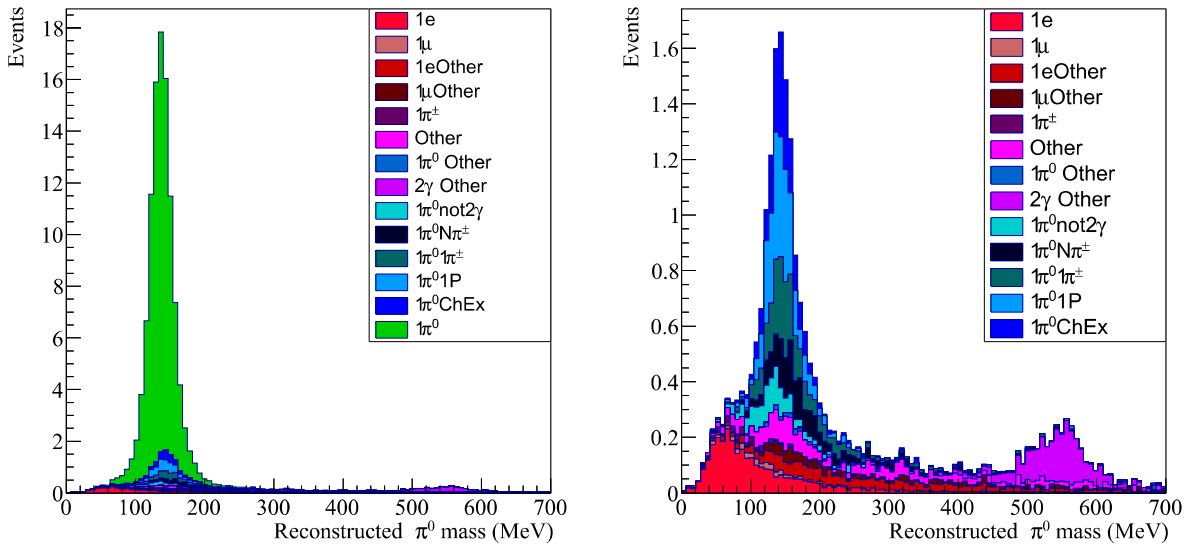


Figure 4.7: **(a)**: FHC two ring NCπ^0 sample by final state topology. **(b)**: FHC NC backgrounds only from **(a)**.The toplogy labels are the number of each particle in the final state, the same as in Table 4.6.

that the NCπ^0 and NCCoh interaction modes are 72.5% of the FHC 2RNCπ^0 sample in Table 4.4, but the final state 1π^0 topology is higher at 78% in Table 4.6. The increase in 1π^0 event topologies indicates some mis-classification of events that cannot be accounted for because the interaction modes produce single π^0 events in the Super-K ID.

It could be argued that the 1$\pi^0$1P topology in reality is a single π^0 being reconstructed, as protons have a low tagging efficiency in Super-K. Due to their high mass they quickly drop below their Cherenkov threshold producing sharp thin rings that are difficult to reconstruct. When accompanied by a π^0, an elastic scatter could put the proton just above its Cherenkov threshold and the event could be classified as an NCπ^0. The remaining topologies, where other particles are present, have a number of $\pi^\pm$ present. These are likely misreconstructed in a similar way as $\pi^\pm$ rings are generally sharper and more μ-like in appearance.

The ChEx topology denotes an event whose final state particles were generated via a charge exchange interaction where a charged pion can interact with a nucleon, resulting in a π^0:

$$\pi^- + p \rightarrow \pi^0 + n \tag{4.5}$$

$$\pi^+ + n \rightarrow \pi^0 + p \tag{4.6}$$

Table 4.6: FHC final state breakdown for the two ring and single ring NCπ^0 samples. The final state topology definitions are listed in Table 4.5.The breakdown of topologies is to identify events that contain a real π^0.

Mode	Two ring sample				One Ring sample			
	FHC		RHC		FHC		RHC	
	Events	Fraction	Events	Fraction	Events	Fraction	Events	Fraction
1e	3.05	0.0255	0.824	0.0211	6.49	0.313	3.24	0.387
1μ	0.345	0.00288	0.0746	0.00191	0.2	0.00964	0.0521	0.00623
1eOther	2.43	0.0203	0.988	0.0253	0.978	0.0472	0.575	0.0687
1muOther μ	1.45	0.0121	0.361	0.00923	0.374	0.018	0.0981	0.0117
1π^0	93.9	0.783	30.4	0.776	8.58	0.414	3.06	0.366
1$\pi^\pm$	0.265	0.00221	0.103	0.00264	0.0727	0.00351	0.0315	0.00377
Other	3.49	0.0291	1.12	0.0287	2.12	0.102	0.659	0.0788
1π^0 Other	0.282	0.00236	0.111	0.00283	0.00801	0.000386	0.0106	0.00127
2γOther	2.8	0.0234	1.07	0.0274	0.0452	0.00218	0.0136	0.00163
1π^0 Not2γ	1.39	0.0116	0.44	0.0113	0.251	0.0121	0.098	0.0117
1π^0 N$\pi^\pm$	2.82	0.0235	1.03	0.0262	0.584	0.0282	0.183	0.0218
1π^0 1P	3.14	0.0262	1.16	0.0296	0.42	0.0202	0.151	0.018
1π^0 N$\pi^\pm$ NP	2.2	0.0184	0.763	0.0195	0.505	0.0244	0.157	0.0188
1π^0 ChEx	2.28	0.019	0.705	0.018	0.101	0.00485	0.0336	0.00402

A charge exchange interaction produces a π^0 from a $\pi^\pm$ and would appear as a π^0 in the detector. This is not an issue as these are still NC interactions, but are classed as NC$\pi^\pm$ in Table 4.4.

There is 2% contribution to the two ring π^0 sample with 2γOther events, where the two photons that are reconstructed are not from a π^0, which increases the number of predicted NCπ^0 interactions and has a negligible contribution to the single ring sample. The 2γOther topology accounts for misreconstruction of gammas and is irreducible, however, it has low event rates and minimal effect. The Other category in Table 4.6 counts events that do not contain a π^0 and has a low event rate distributed across the π^0 mass region of Figure 4.7(b) indicating the majority of π^0 events are accounted for in different topologies. All NC background events are reconstructed as 2R e-like events despite having extra ring-generating particles and more complicated topologies, indicating there are missed rings or the rings are too dim to reconstruct.

The NC backgrounds are present in the 1RNCπ^0 sample at the ~15% level in Table 4.2 and are primarily due to mis-reconstruction. The effect of the NCOther and NC$\pi^\pm$ backgrounds can be accounted for when calculating detector systematics in Chapter 6, by treating them separately from NCπ^0 events. Including extra systematics for NCOther and NC$\pi^\pm$ events means the events will have their own error assigned and wont bias the constraint of the NCπ^0 events on the 1RNCπ^0 samples.

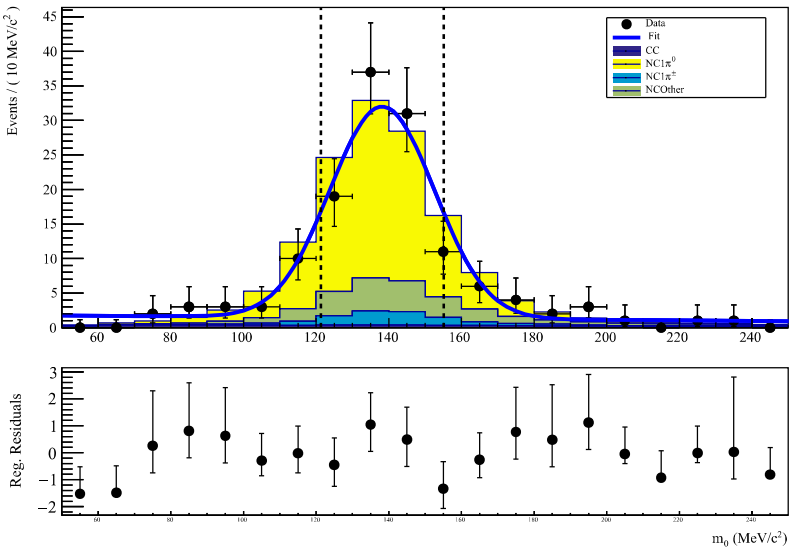


Figure 4.8: Combined FHC and RHC NCπ^0 sample mass distribution. Data is from T2K runs 1-10 where the errors are statistics only. SK nominal MC is normalised to the same POT for reference. The fit model is a linear background and a Gaussian signal centred at the π^0 mass with mean $\mu = (138.2 \pm 1.6)\text{MeVc}^{-2}$, standard deviation, $(\sigma = 14.4 \pm 1.5)$ MeVc^{-2} and $\chi^2 = 13.36$. Dashed lines mark the full width half maximum at (34 ± 1.5) MeV.

4.2.2 NCπ^0 sample mass peak fit

The 2R NCπ^0 sample is a high purity sample of π^0 events which are of interest independently of the single ring sample. Other experiments have made π^0 sample measurements [96, 97, 98] including at the ND280 P0D in Figure 1.6 with a width of $\sim$ 120 MeV. The π^0 mass distribution width is dependent on detector resolution and reconstruction as there is a single dominant decay mode, $\pi^0 \rightarrow \gamma\gamma$.

The 2RNCπ^0 samples are combined giving 145 total events Figure 4.8 shows the mass distribution of the 2R FHC and RHC NCπ^0 samples for T2K runs 1-10 at SK. The peak is fitted with a Gaussian signal model and a linear background model motivated by the MC distribution in Figure 4.5. The mean π^0 mass is extracted as $\mu = (138.202 \pm 1.57737)\text{MeVc}^{-2}$, standard deviation, $(\sigma = 14.3681 \pm 1.51399)$ MeVc^{-2} and $\chi^2 = 13.36$. The fit to data is good, with a χ^2 similar to the degrees of freedom and the mean is in agreement with the known π^0 mass. The width is calculated at (34 ± 1.5) MeV and is competitive with other π^0 samples, although the full systematic errors are not treated here. The low width shows Super-K is well suited to π^0 reconstruction with good energy resolution.

Chapter 5

Bayesian statistics and MaCh3

Both the atmospheric fit in Chapter 6 and the Oscillation analysis in Chapter 7 use the Markov Chain for 3 flavour oscillations (MaCh3) framework for Log-likelihood minimisation. MaCh3 uses Markov Chain Monte-Carlo (MCMC) and Bayesian inference to perform oscillation fits and extract oscillation parameters using data from ND280 and Super-K. This chapter will outline Bayesian statistics, MCMC, and how they are used in the operation of MaCh3.

MCMC techniques are vital, given both the atmospheric and oscillation analysis fits are multivariate with up to ~800 parameters. Instead of performing a lengthy analysis of the entire parameter space, MaCh3 is able to vary parameters and find the region of parameter space that best matches collected data to MC data generated based on theoretical models.

MCMC uses a semi random walk to sample the multivariate space; extracting a posterior probability density which describes the observables of the fit. Bayesian inference states that the posterior completely describes the observables and, from this, the best fit and credible intervals of oscillation parameters can be extracted.

The specific execution of the atmospheric and oscillation analysis fit are described in Chapter 6 and Chapter 7 respectively, this chapter serves to lay a foundation that is common to both fits.

5.1 Bayesian statistics

In the Bayesian consideration of statistics, there is no fundamental difference between observables and parameters in models, both are considered random quantities. For a set of observed data, D, and parameters of a model that fully describes the data, θ, the joint probability distribution for all random quantities can be defined as [99]:

$$P(D, \theta) = P(D|\theta)P(\theta). \tag{5.1}$$

$P(D|\theta)$ is the likelihood of measuring D given the parameters θ and is extracted by comparing data simulated at θ to D. $P(\theta)$ is the prior constraint that describes information known about θ. Using Bayes theorem, the posterior distribution can be constructed,

$$P(\theta|D) = \frac{P(D|\theta)P(\theta)}{P(D)} = \frac{P(D|\theta)P(\theta)}{\int P(D|\theta)P(\theta)d\theta}. \tag{5.2}$$

The posterior distribution allows for easy extraction of parameter estimates. The denominator in Equation 5.2 is the integral of the joint probability distribution over all parameters, a normalisation constant that is difficult to evaluate. For MaCh3 analyses, it is sufficient to say $P(\theta|D) \propto P(D|\theta)P(\theta)$.

Marginalisation

The high dimensionality of the MaCh3 analysis makes it difficult to interpret the posterior distributions directly, so the marginalised posterior is constructed. In MaCh3, as well as other T2K analysis groups (P-Theta [100] and VaLOR [101]), the oscillation parameters are of primary interest and other systematic 'nuisance' parameters are integrated over. The marginal posterior condenses the information from the joint posterior into a few parameters of interest. Nuisance parameters alter various factors in the fit that control event rates and uncertainties on the MC events. Marginalisation converts the nuisance parameter distributions into uncertainties on oscillation parameters.

5.2 Markov Chain Monte Carlo (MCMC)

Monte Carlo simulation traditionally uses a random walk to sample high dimensional parameter spaces. MCMC replaces the random walk with a semi-random walk algorithm where steps are proposed and accepted/rejected depending on the change in likelihood. MCMC can efficiently sample a target distribution by proposing parameter values at which to calculate the posterior.

The Markov Chain has to be carefully constructed in order to be able to use the chains for statistical interpretations. The semi-random walk is required to propose steps in the parameter space, X_{n+1}, that are dependent only on the previous step, X_n. Initially the chain must be started with a given set of parameters, usually randomly decided, at X_0. Each step is dependent only on the previous step, so the chain eventually becomes independent of the parameters it started with at X_0, reaching a stationary distribution where X_n does not depend on n. The chain can be constructed so that the stationary distribution is directly proportional to the underlying posterior distribution, allowing the use of Bayesian inference to draw conclusions.

The number of steps required for X_n to be independent of X_0 is called burn in; in this time the chain converges to its stationary state. Reducing burn in time is an important consideration, since computing resources can be limited. MaCh3 uses the Metropolis-Hastings algorithm to perform a semi random walk and converge chains to their stationary distributions quickly.

5.2.1 Metropolis-Hastings

The Metropolis-Hastings algorithm [102] is simple in its execution and steps the Markov Chain as follows:

1. The current step n with parameters X_n
2. X_n is used to propose a new step Y_n using a proposal function $f(Y_n|X_n)$
3. Y_n is evaluated and either; accepted ($X_{n+1} = Y_n$) or rejected ($X_{n+1} = X_n$)
4. Algorithm is repeated with $X_n = X_{n+1}$

To accept or reject a step, the acceptance probability is calculated:

$$\alpha(X_n, Y_n) = min\left(1, \frac{P(Y_n|D)f(X_n|Y_n)}{P(X_n|D)f(Y_n|X_n)}\right) = min\left(1, \frac{P(Y_n|D)}{P(X_n|D)}\right) \tag{5.3}$$

where, in the case for MaCh3, $f(Y_n|X_n) = f(X_n|Y_n)$. A random number, β is chosen, where $0 < \beta < 1$, and the step is accepted if $\alpha < \beta$. From Equation 5.3 this means the step is always accepted if $P(Y_n|D) > P(X_n|D)$, alternatively the step has a probability to be accepted of α. Allowing the chain to burn in quickly to its stationary state and then explore the area of highest posterior probability. The result of using Metropolis-Hastings is that a step is always added to the chain whether Y_n is accepted or not. The density of steps is proportional to the posterior distribution, with more steps in the regions of higher probability.

5.3 MaCh3

The MCMC properties are remarkable where the oscillation parameters credible intervals can be calculated directly from steps taken in a multivariate space. In order to achieve this however, care must be taken when defining parameters and running the chain in MaCh3.

Prior distributions can constrain parameters if it there is information known from outside T2K. For example, neutrino oscillation experiments at nuclear reactors can provide a tight constraint on $\sin^2(\theta_{13})$, which can be applied to fits with a Gaussian prior around the measurement $\sin^2(\theta_{13}) = 0.0220 \pm 0.0007$ [12]. The reactor constraint is a special case where, by virtue of Equation 5.2, the fit can be run without the prior applied and the chain reweighted afterwards. In the case of nuisance parameters, many are not Gaussian and have physical limits. Should a step be proposed outside of any parameter limits, the step is rejected. Non-Gaussian behaviour can appear to bias the resulting marginal posterior as the steps will be more constrained to a specific region. This is to be expected as many nuisance parameters are non-Gaussian, but it is a feature of the marginal posterior and the effect on parameters of interest is real.

The step proposal function used is a Gaussian distribution for each parameter in the fit, whose

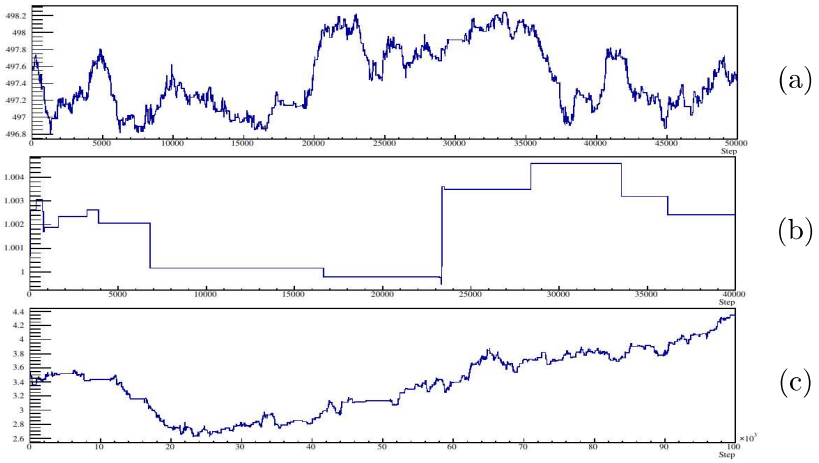


Figure 5.1: Traces of parameter variation in MCMC chains that exhibit different stepping behaviour. **(a)** Appropriate step size, the chain explores a range of parameter values quite quickly. **(b)** Step size is too large, the chain is jumping around the range of acceptable values and not exploring the region. **(c)** Step size is too small, note this parameter is over 100,000 steps, the chain takes many steps to explore a range of values.

width is determined by a step scale that is set for each parameter. Figure 5.1 shows the steps taken for particular parameters as the Markov Chain moves. The step scale determines how well the chain will move around the multivariate space, and setting them correctly has drastic effects on fit convergence and acceptance rates. Step size tuning takes a lot of time but is vital to ensure the chain explores the parameter space properly. If step sizes are too small, the chain will not move far from its initial position, too large and steps will be rejected. In either case, many more steps are required to effectively explore the posterior surface at best. However, a step size that is too small can artificially constrain a parameter to a region of its range e.g. in a local minimum. The resulting step distribution would be constrained and not represent the underlying posterior.

The traces in Figure 5.1 are from fits run in Chapter 6, showing how step sizes affect the exploration of the chain. The accepted principle of step size tuning is to aim for a step acceptance rate of ≈0.23 [103]. However, for the fits in Chapter 6 the acceptance rate is ≈ 0.06 due to a complex likelihood surface and many parameters with priors and boundaries causing steps to get rejected. Figure 5.1(a) shows good mixing for the atmospheric fit, whereas in literature it would likely be categorised as a chain that is not mixing well [103]. In order to ensure the likelihood region is explored properly, more steps are taken.

The proposal of a step is dependent only on the previous step, however, a step can still be correlated

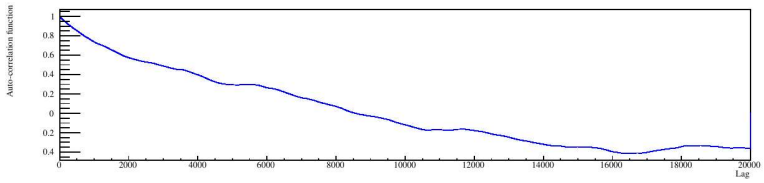


Figure 5.2: Autocorrelation plot of a single parameter.

to one taken many more steps before, especially when many parameters are correlated. To evaluate the independence of steps, the correlation between two steps separated by a number of steps (lag) is calculated, known as the autocorrelation. Figure 5.2 shows an example where the autocorrelation is plotted as a function of lag. Step size tuning aims to have the autocorrelation drop to ~ 0.2 with a lag of 10,000-20,000, which gives good mixing and exploration of parameter space in an acceptable number of steps.

Chapter 6

Super-K Detector Systematics

Systematic errors on for reconstructing Super-K events used in T2K analyses are calculated from a Super-K atmospheric neutrino data fit to MC generated events and is explained in Section 6.1. The fit uses data collected from atmospheric neutrino events, occurring at the same time as T2K is collecting beam data for neutrino oscillation measurements. Detector systematics can change over time e.g. with changing dark noise rates, water quality, and detector configuration. For example, as of run 11, Super-K contains Gadolinium. Should the analysis in Chapter 2 have shown any changing shape of the Super-K ID, it could have been included here.

The aim of the atmospheric fit is to quantify the difference between collected data and MC predictions to understand the errors on reconstructing different events at Super-K. It is assumed that the detector response to atmospheric events is the same as for T2K events. The uncertainties on reconstruction errors are quantified in a covariance matrix for use in oscillation analysis measurements. In order to add the NCπ^0 samples, systematic uncertainties are required on each sample in the oscillation analysis fit. Throws are taken from the atmospheric fit chains to get distributions of event rates in each oscillation sample event type. The systematics are encoded in the Super-K detector covariance matrix, constructed in Section 6.3. The MaCh3 version used was developed for the joint T2K beam and Super-K atmospheric fit [104], only the atmospheric Super-K fit is used for this study.

Table 6.1: Parameters that are shifted and smeared for each event. The ring counting parameter has an corresponding likelihood that is shifted and smeared which is then compared to a table of results to transform it from a continuous likelihood to a discrete number of rings.

Variable	Form	Samples used in
Ring counting parameter	Look-up table	All
e/μ PID	$\ln(\frac{L_{mu}}{L_e})$	1Re 1Rmu 1ReCC1π 1RNCπ^0
e/π^0 PID	$\ln(\frac{L_e}{L_{\pi^0}})$	1Re 2RNCπ^0 1RNCπ^0
μ/π^+ PID	$\ln(\frac{L_{\pi^+}}{L_\mu})$	1Rmu
ee/2ROther PID	$\ln(\frac{L_{ee}}{L_{2ROther}})$	2RNCπ^0

Table 6.2: Visible energy bins used for detector systematic uncertainty evaluation.

Visible energy (MeV)
0 - 300
300 - 700
700 - 1330

6.1 Atmospheric Fit

The atmospheric neutrino data fit uses atmospheric data collected at Super-K during T2K beam runs 1-10 or 3224.4 days of data. The detector systematic uncertainties due to `fiTQun` reconstruction are calculated using atmospheric data because of the higher statistics in a similar energy range. Detector response from atmospheric data is assumed to be identical to that of T2K beam data. The systematic uncertainties are parameterised with shift and smear parameters that act on `fiTQun` reconstructed variables used to construct the Super-K samples described in Chapters 3 and 4.

The samples have five variables, L^i, for which the uncertainty is calculated using the atmospheric fit, shown in Table 6.1. There are three visible energy bins, j, shown in Table 6.2, and seven final state topologies, k, shown in Table 6.3. The visible energy bins and topologies are chosen to be specific to the Sub-GeV samples, where a different detector response is expected at different visible energies and topologies. There are a total of 210 detector systematic parameters when each have an associated α and β which adjust the `fiTQun` parameters as follows:

$$L^i_j k \rightarrow \alpha^i_{jk} L^i_{jk} + \beta^i_{jk}. \tag{6.1}$$

The shift and smears are calculated by fitting generated MC to collected data, where the MC is reweighted at each step of the chain with the parameters at that step, exploring which parameter

Table 6.3: Final state topologies considered when calculating detector systematics. The topologies are decided based on truth information from simulation.

Name	Final state topology
$1e$	Only 1 electron above Cherenkov threshold
1μ	Only 1 muon above Cherenkov threshold
$1e$+Other	One electron and one or more charged particles above Cherenkov threshold
1μ+Other	One muon and one or more charged particles above Cherenkov threshold
$1\pi^0$	Only one π^0
$1\pi^\pm$ or $1p$	Only one charged hadron above Cherenkov threshold
Other	Any other final state

values are preferred. The Markov chain will explore the maximum posterior region and the shift and smear parameters are free to move in the fit so that sampling the posterior provides variations of α and β that can be used to estimate the uncertainty on `fiTQun` reconstruction.

A likelihood function can be constructed to compare atmospheric MC to data [104]:

$$\mathcal{L}(\boldsymbol{a}, \boldsymbol{x}, \boldsymbol{o}, \boldsymbol{skc}, \boldsymbol{skd}|D) = P(D|\boldsymbol{a}, \boldsymbol{x}, \boldsymbol{o}, \boldsymbol{skc}, \boldsymbol{skd}) \times \pi(\boldsymbol{a}) \times \pi(\boldsymbol{x}) \times \pi(\boldsymbol{o}) \times \pi(\boldsymbol{skc}) \times \pi(\boldsymbol{skd}), \quad (6.2)$$

where D is the atmospheric data, $\boldsymbol{a}$ are atmospheric neutrino flux parameters, $\boldsymbol{x}$ are cross-section parameters, $\boldsymbol{o}$ are oscillation parameters, $\boldsymbol{skc}$ are Super-K calibration parameters, $\boldsymbol{skd}$ are Super-K detector systematic parameters, and π is any prior information.

The atmospheric data collected by Super-K is separated into 18 samples based on the visible energy ($E_{vis.}$) and final state topology. Broadly, there are Sub-GeV ($E_{vis.}$ <1.33 GeV), Multi-GeV ($E_{vis.}$ >1.33 GeV) and multi-ring samples. Only the Sub-GeV samples are used for calculating shift and smear parameters for the detector covariance matrix, as these samples have energy similar to the T2K beam at Super-K. The multi-ring and Multi-GeV samples are used for independent systematic error evaluation on the atmospheric neutrino flux and other external parameters [105, 106].

Figure 6.1 shows the $P_{lep}/\cos(\theta_z)$ nominal MC distributions used in the atmospheric fit. These are fitted to data with the same binning and are weighted to 3224.4 days of livetime. Data and pre-fit data-MC ratio plots are available in Appendix A

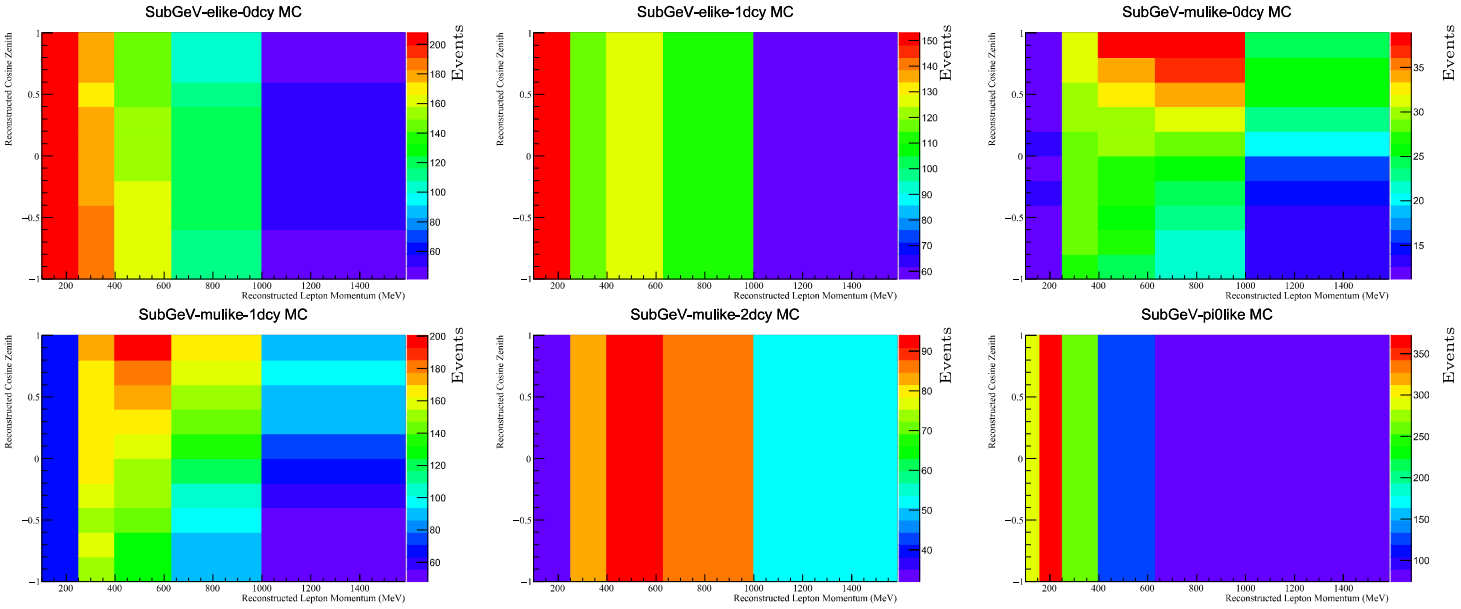


Figure 6.1: Nominal MC Sub-GeV samples used in the atmospheric fit. Samples are binned in reconstructed lepton momentum and $\cos(\theta_Z)$. The event rates correspond to Super-K nominal event weights before fitting to data.

6.1.1 Hybrid π^0 sample

An important prior constraint for the $1\pi^0$ atmospheric fit topology comes from a set of hybrid-π^0 events. The prior is used on each `fiTQun` parameter and is implemented with separately generated χ^2 maps. The hybrid-π^0 data sets are not re-made for this analysis and use the 14c Super-K library.

The hybrid-π^0 samples are used to estimate the π^0 tagging efficiency of π^0 events and extract a systematic uncertainty. since a π^0 decay is expected to have two rings, there are two hybrid-π^0 samples created in order to estimate the uncertainty on reconstructing the higher energy ring (primary sample) and lower energy ring (secondary sample). For each sample there is a data and MC set of events and the comparison gives the systematic error on π^0 reconstruction.

A π^0 event (data or MC) is turned into a hybrid-π^0 event by swapping one of the rings (higher energy for primary, lower for secondary) for a data or MC electron event. The other ring is regenerated with parameters extracted from the original ring, the resulting hits make up the hybrid event of one original ring and one new MC ring.

There are four samples in the end; data-MC and MC-MC events for primary and secondary rings. Full details on the construction and analysis are available in [107]. The systematic error is calculated

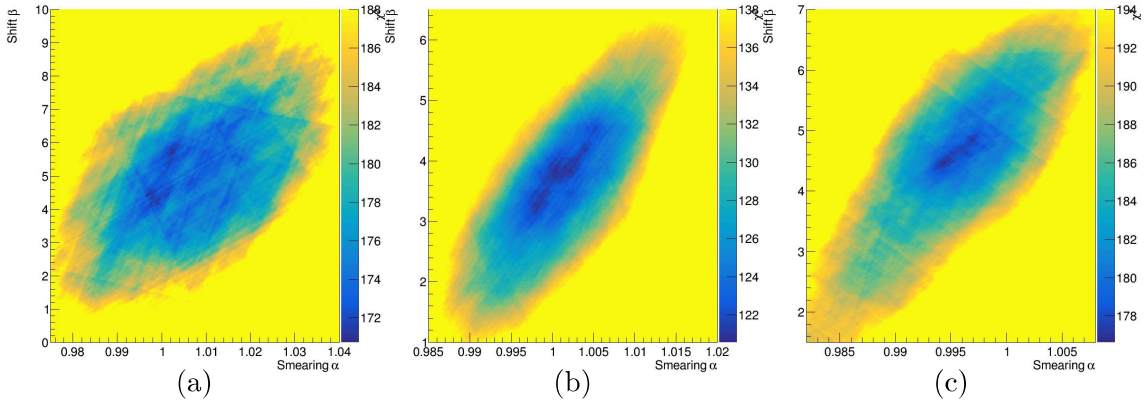


Figure 6.2: hybrid-π^0 sample likelihood scan for $\frac{L_{ee}}{L_{2ROther}}$ in E_{vis} bins; **(a)**:0 $< E_{vis} <$ 300 MeV, **(b)**:300 MeV$< E_{vis} <$ 700 MeV, and **(c)**:700 MeV $< E_{vis} <$ 1330 MeV. Each plot is for each E_{vis} bin. The Z-axis is limited to $(\chi^2_{min} + 16)$ in order to highlight the area that the Markov chain will spend the majority of its steps exploring. Lower statistics in E_{vis} bins gives more stripes of χ^2 due to the nature of shift and smear parameters.

using the difference between data-MC and MC-MC samples as a χ^2 penalty [108];

$$\chi^2 = \sum_{L^i bins} \frac{(N_{data} - N_{MC})^2}{\sigma^2_{data} + \sigma^2_{MC}}. \tag{6.3}$$

Where $\sigma = \sqrt{N}$, L^i are the `fiTQun` parameters in Table 6.1. The χ^2 is calculated as a function of α and β for each L^i and E_{vis} bin.

The result is a χ^2 map binned in α and β for each visible energy bin. The maps are added to the atmospheric fit and take the χ^2 value from the corresponding bin for a given α, β in the π^0 topology as a penalty term to the likelihood when the Markov chain is exploring the posterior distribution. New χ^2 maps made for the $\frac{L_{ee}}{L_{2ROther}}$ variable for the two ring NCπ^0 sample are shown in Figure 6.2. The minima contain discontinuities due to the nature of the variables plotted. The shift and smears move events into and out of samples, altering the χ^2. For events close to the $\frac{L_{ee}}{L_{2ROther}}$ boundary a smear can move an event in and a shift can move it back out of L^i bins, changing the χ^2, giving rise to diagonal lines which are especially stark in low statistics bins.

The χ^2 maps in Figure 6.2 are those added to the atmospheric fit and physically limit the ranges of α and β. The ranges are chosen to restrict α and β to the minimum, $(\chi^2_{min} + 16)$ which is where the Markov chain will spend most of its time exploring anyway as the penalty to step further away reduced the chance of the step being accepted.

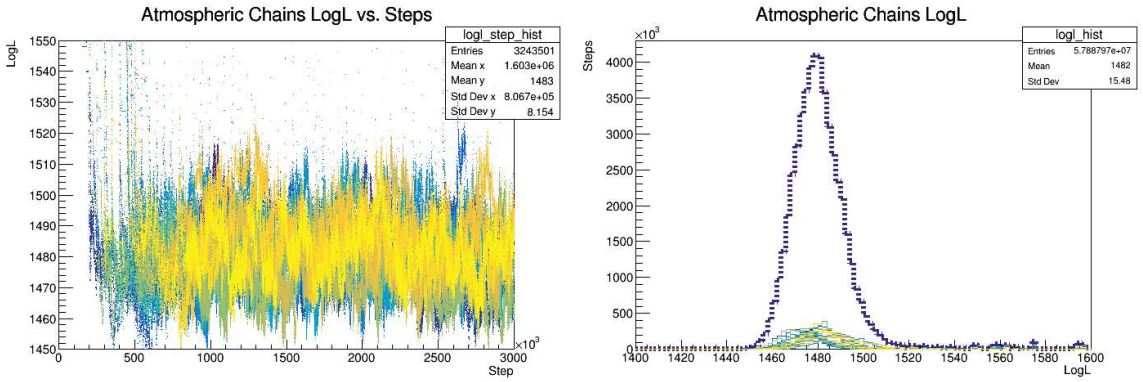


Figure 6.3: **(a)**$\ln(\mathcal{L})$ for 20 chains as a function of step, at 750,000 steps the step sizes decreases to better explore the minimum. **(b)** $\ln(\mathcal{L})$ distribution for step>750,000.

6.2 Atmospheric fit results

The aim of the Super-K atmospheric fit is to identify values of shift and smear parameters that are viable when applied to MC events such that data and MC are still in agreement. The MCMC steps encode the ranges of values of α and β that give good agreement of data and MC when moving events into and out of samples. The atmospheric fit MCMC chains are used to estimate sample uncertainties from event mis-reconstruction in Section 6.3, for use in the oscillation analysis in Chapter 7.

The number of parameters in the fit produces a complicated likelihood surface, with many local minima, so it is difficult for chains to step around the parameter space, leading to chains not exploring at all. A two stage burn in process was used, with large step sizes to allow the chain to navigate close to the minimum point, and smaller step sizes thereafter to explore the minima. The latter steps were then sampled for shift and smear parameters when constructing the detector covariance matrix. The log-likelihood distribution in Figure 6.3 is well localised and the chains mix well overall and explore similar $\ln(\mathcal{L})$ values, which would indicate they are all in the same minimum.

Examples of step distributions of fit parameters are shown in Figure 6.4. Some parameters are poorly constrained, and the chains are dispersed in the parameter space instead of mixing together. The resulting distribution has isolated peaks where chains could be stuck in local $\ln(\mathcal{L})$ minima, broadening the overall distribution. While the chains are certainly not exploring the space, the overall likelihood value for the chains are similar in Figure 6.3 so it is not possible to choose to remove chains that could be stuck, because they have the same posterior probability of being in the correct region.

All chains are used in the calculation of the detector systematics. Super-K detector systematic errors are based on the distribution of throws from the parameter steps, a broader distribution increases the resulting error of that bin. In bins with isolated peaks larger errors will be calculated, which is correct because the likelihood in those peaks is similar across chains so the preference of that parameter values is the same for each peak and cannot be discounted.

Extensive step size tuning was performed for almost all parameters in the fit, namely cross-section and the shift and smears, so that the fit would converge to a stable minimum for sampling. Autocorrelations are shown for all parameters in Figure 6.5 with all parameters reaching an autocorrelation of 0.2 at 20,000 lag indicating the chains are exploring well. The colour coding of Figure 6.5 allows the worst performing parameters to be picked out. Comparing Figure 6.5 to Figure 5.1 shows the step size is likely too small in this case, but it is not severe and should still explore the posterior. Figure 6.6 shows MC with parameters reweighted by throws taken from the atmospheric fit chains. The distribution of MC throws in $p_{lep}/\cos(\theta_z)$ are well localised for each bin and good agreement is seen with data. The MC over-predicts the number of Sub-GeV π^0-like events compared to data, this could be due to π^0 mis-modelling or the hybrid-π^0 χ^2 maps may be over constraining the shift and smears leading to a narrower distribution of throws.

Further developments to the atmospheric fit as a whole are underway in order to improve the acceptance rate. In addition, the introduction of adaptive step size tuning will assist chains in exploring the parameter space, unfortunately these developments were not ready at the time of this analysis.

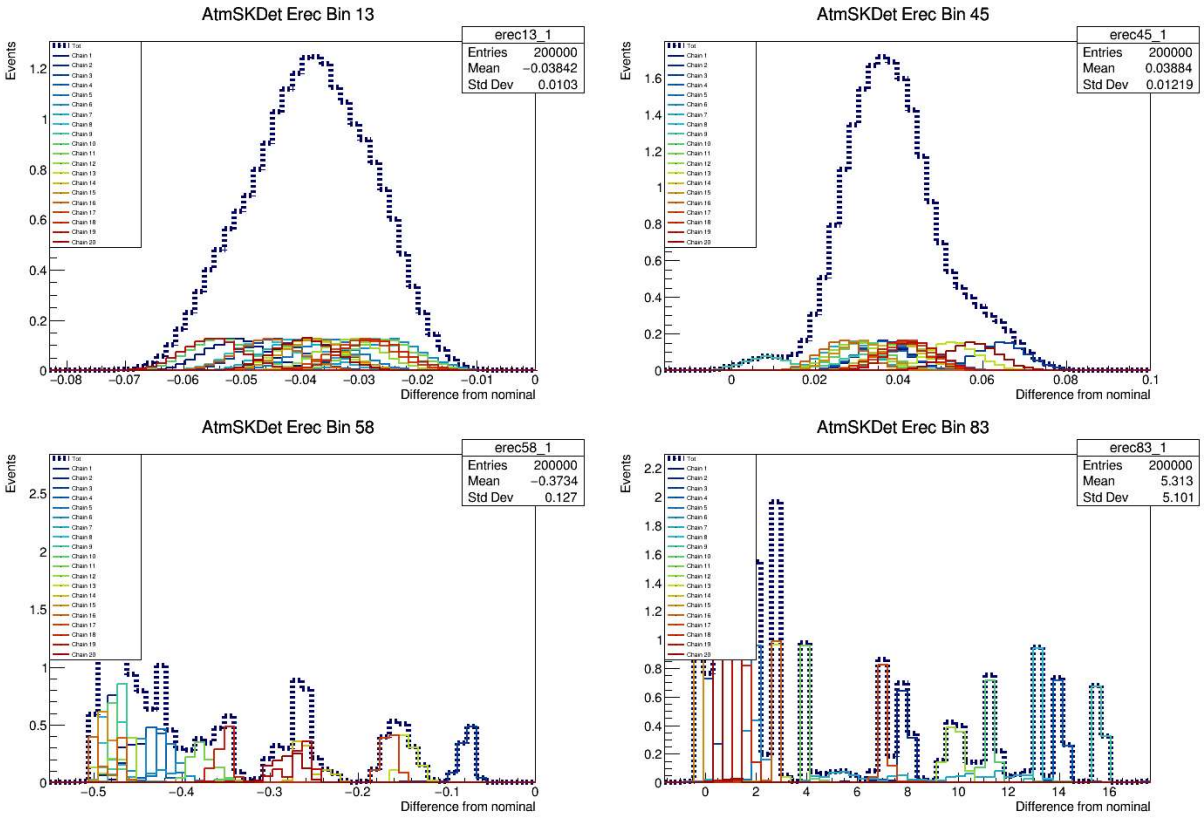


Figure 6.4: Examples of fractional difference of throws from nominal in the detector covariance matrix after the tmospheric data fit. Top: Well behaved bins have a Gaussian-like shape and the chains mix in a similar region. Bottom: Bins with seperate peaks where there is little constraint from the atmospheric fit have poor mixing of chains and larger distribution width of throws, resulting in higher errors.

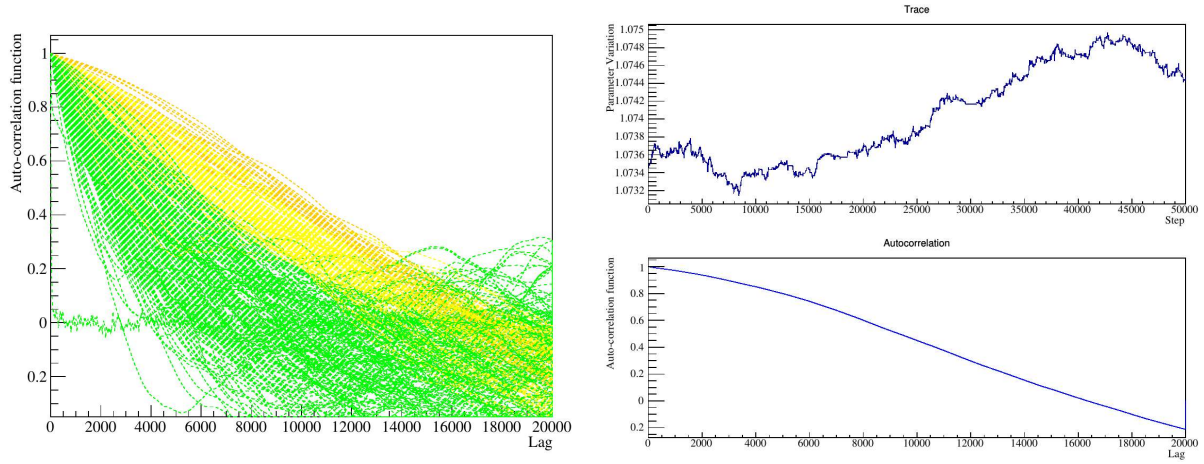


Figure 6.5: Left: Autocorrelations for all parameters in the fit. Line colour is determined by the autocorrelation value at 10,000 lag orange if > 0.4, yellow if > 0.2, green if < 0.2. Right: one of the worst parameters and the trace of its value.

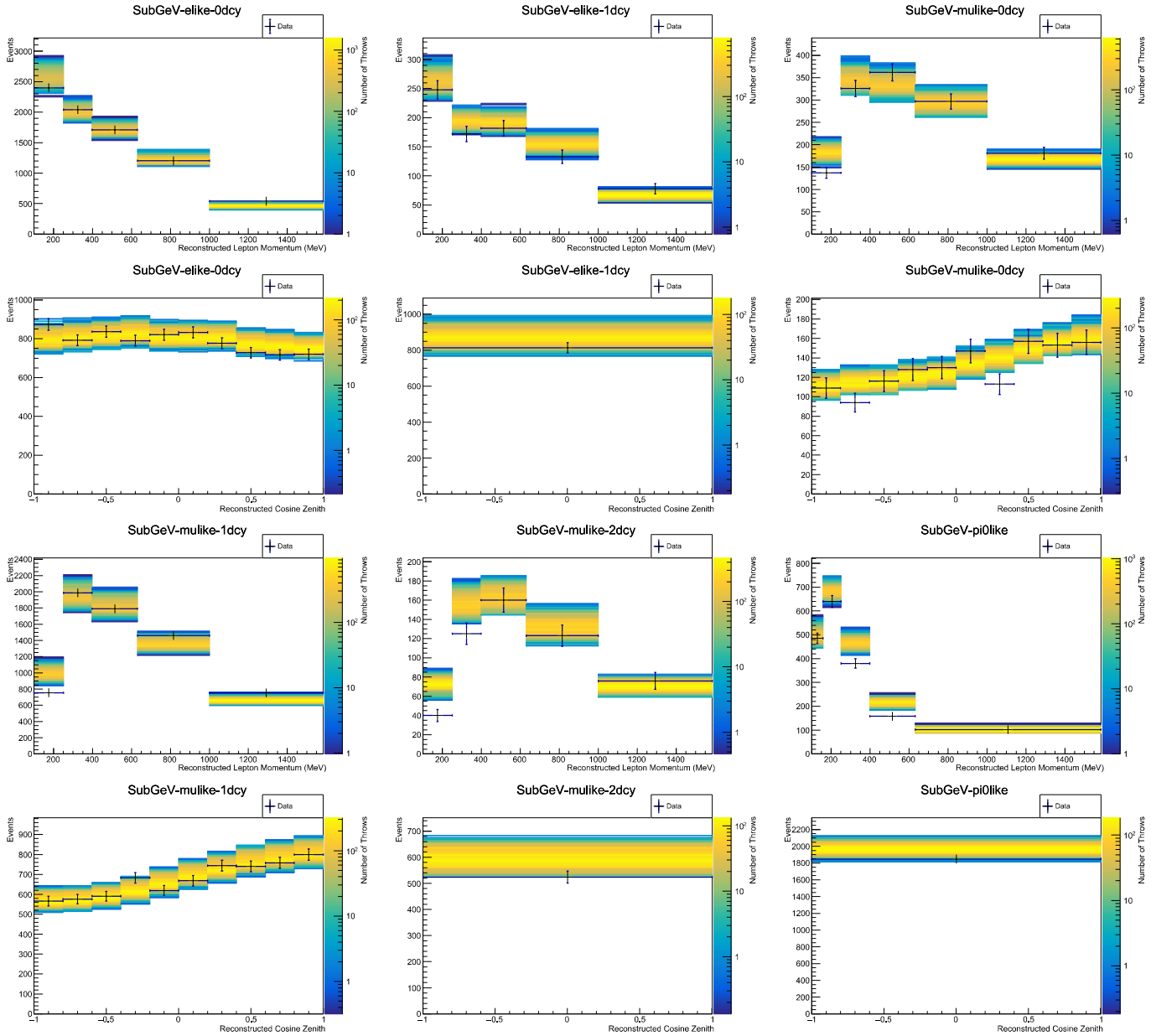


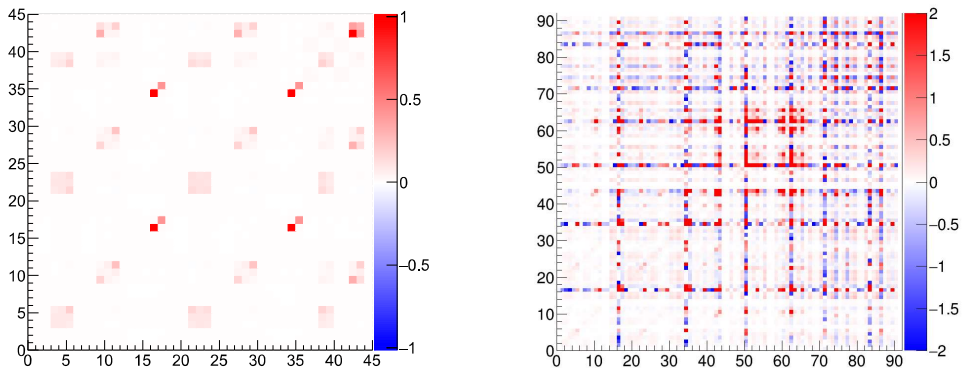
Figure 6.6: Projections of the 2D $P_{lep}/\cos(\theta_z)$ atmospheric fit sample histograms. MC is reweighted with parameters randomly thrown from the Markov chains 3000 times. Good agreement is seen with the data projections, however, here is an excess of MC events in the π^0-like sample.

Sample	Topology	π^0 mass range	FHC Bin	Nominal	RHC Bin	Nominal
1Re	-	-	0-11		18-28	
1Rmu	-	-	12-17		30-35	
1Re1de	-	-	36-43		-	
2R NCπ^0	NCπ^0	0-100	44	1.84	56	0.605
		100-220	45	64.7	57	20.7
		220-5000	46	0.592	58	0.249
	CC	0-100	47	1.79	59	0.313
		100-220	48	2.69	60	0.719
		220-5000	49	5.06	61	2.05
	NC$\pi^{\pm}$	0-100	50	0.161	62	0.072
		100-220	51	3.79	63	1.18
		220-5000	52	0.185	64	0.063
	Other	0-100	53	0.483	65	0.165
		100-220	54	10.1	66	3.76
		220-5000	55	5.57	67	2.05
1RNCπ^0	NCπ^0	0-100	68	0.679	80	0.240
		100-220	69	5.66	81	2.02
		220-5000	70	0.377	82	0.189
	CC	0-100	71	1.97	83	0.393
		100-220	72	8.77	84	3.31
		220-5000	73	4.76	85	2.37
	NC$\pi^{\pm}$	0-100	74	0.0294	86	0.0222
		100-220	75	0.250	87	0.0938
		220-5000	76	0.0125	88	0.0035
	Other	0-100	77	0.225	89	0.0715
		100-220	78	1.80	90	0.58
		220-5000	79	1.42	91	0.480

Table 6.4: Binning of the π^0 samples is by reconstructed π^0 mass and true interaction mode. The π^0 mass ranges are chosen to reflect the peak and two tails of the π^0 mass distribution. The interaction modes are chosen to represent modes of interest in both samples. Standard SK samples are included for reference, their full binning is shown in Appendix A.

6.3 Detector Covariance Matrix

The detector covariance matrix is constructed by altering the 1Re, 1Rμ, 1Re1de, and NCπ^0 samples with the shift and smear variation of PID parameters randomly thrown from the atmospheric fit chains. The shifting and smearing of events according to the Markov chain migrates events in and out of samples with each throw, changing the event rates in the resulting T2K samples. After many throws, the uncertainty on each sample can be calculated. The detector covariance matrix is binned in reconstructed neutrino energy (E_ν^{rec}) for each sample, the same as for the oscillation analysis in Chapter 7, and their final state topologies appearing in the sample. However, E_ν^{rec} cannot be calculated for NC



(a) (b)

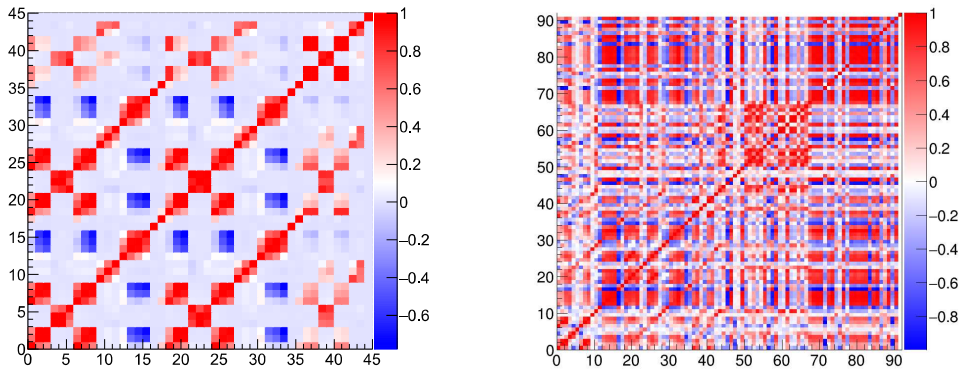
Figure 6.7: **(a)**: Official Covariance matrix for previous T2K analysis. **(b)**: New covariance matrix including NCπ^0 samples, limited to ± 2 for clarity.

events, so the NCπ^0 samples are binned in reconstructed π^0 mass and split into true interaction modes, detailed in Table 6.4. The binning for the 1Re 1Rμ and 1Re1de samples is in Table A.1 in Appendix A. The NCπ^0 binning is chosen such that the π^0 mass range covers the lower edge ($0 < m^0_\pi <= 100$) MeVc^{-2}, the peak ($100 < m^0_\pi <= 220$) MeVc^{-2}, and the tail ($220 < m^0_\pi <= 5000$) MeVc^{-2} from Figure 4.5. Each m^0_π bin covers the NCπ^0, CC topologies, and dominant NC background, NC$\pi^\pm$, motivated by the studies in Section 4.2.1. All other topologies are grouped into the Other group. There are an additional 48 bins in the detector covariance matrix for both NCπ^0 samples in FHC and RHC. The general form of a covariance matrix of size i can be written as:

$$C_{ij} = \begin{pmatrix} \sigma_0^2 & \dots & \sigma(0, x_j) \\ \dots & \sigma_1^2 & \dots \\ \sigma(x_i, 0) & \dots & \sigma_i^2 \end{pmatrix} \tag{6.4}$$

where the elements in the atmospheric fit are calculated as:

$$\sigma(x_i, x_j) = \frac{1}{n-1} \sum_{i,j=0}^{n} \left(\frac{x_i - \bar{x}_i}{\bar{x}_i}\right)\left(\frac{x_j - \bar{x}_j}{\bar{x}_j}\right). \tag{6.5}$$



(a) (b)

Figure 6.8: Correlation matrix for the detector covariance matrix in Figure 6.7. **(a)**: Original T2K matrix, **(b)**: Updated, including NCπ^0 samples.

The diagonal elements represent the variance of sample x:

$$\sigma_i^2 = \frac{1}{n-1}\sum_{i=0}^{n}(\frac{x_i - \bar{x}_i}{\bar{x}_i})^2. \tag{6.6}$$

For the atmospheric detector covariance matrix, x is the event rates in each sample bin (from Table 6.4) thrown from the Markov chain, $\bar{x}$ is the nominal event rate for that bin, and n is the number of throws. The covariance matrix is calculated using the difference of the throws from the nominal values, and is shown in Figure 6.7(b).

A correlation matrix can be calculated from the covariance matrix:

$$\rho(x_i, x_j) = \frac{\sigma(x_i, x_j)}{\sigma_i \sigma_j}. \tag{6.7}$$

The corresponding correlation matrix is shown in Figure 6.8. There are high correlations between samples throughout the matrix. The blocks of high correlation, seen from bin 65 onwards, are of interest. Close to the diagonals indicates high correlations within the 1RNCπ^0 sample, however, there are also highly correlated blocks between the FHC 1Rμ sample and RHC samples. This indicates the e/μ cut used in these samples is having a large effect. Considering the 1Rπ^0 sample is identical to the 1Re sample, except for the final inverted e/π^0 cut, the lack of correlation indicates there are few event migrations around the final cut.

The errors on each bin (σ_x) are plotted in Figure 6.9. The diagonal errors are generally larger than the official SK detector matrix, with the largest error difference in 1Rμ bins. Notably, the oscillated ν_e 1Re bins have a much larger errors than the original T2K matrix. Increasing the uncertainties in these bins will provide a weaker constraint on ν_e events in the oscillation fit which constrain δ_{CP} and $\sin^2(\theta_{13})$.

There are large spikes in bins containing few nominal events of Figure 6.9 which will be poorly constrained by the Super-K detector systematics. Bins with lower event rates have lower impact on the oscillation analysis, so the large errors are less of a concern. The large spikes also indicate that the binning for NCπ^0 samples in Table 6.4 could be made more coarse in future analyses. The binning is left as is in order to not over constrain events that are not well understood in the detector systematics.

In each NCπ^0 sample, the NC$\pi^{\pm}$ 0-100 MeVc^{-2} bin has a large error, as well as the CC 0-100 MeVc^{-2} bins in the 1RNCπ^0 sample, events in these bins will be poorly constrained. The NCπ^0 low mass bins have a lower error, indicating NCπ^0 events are more constrained in the lower π^0 mass region. This will help constrain NCπ^0 event rates in the 1Re samples during the oscillation analysis.

The covariance matrix produced in this chapter encodes the systematic uncertainties for the new NCπ^0 samples which are not present in the old detector covariance matrix. The additional systematic ensure the uncertainties of misreconstructing NCπ^0 events are incorporated correctly, which is vital when adding the new NCπ^0 samples whose purpose is to help constrain the NCπ^0 background for recovering 1Re events.

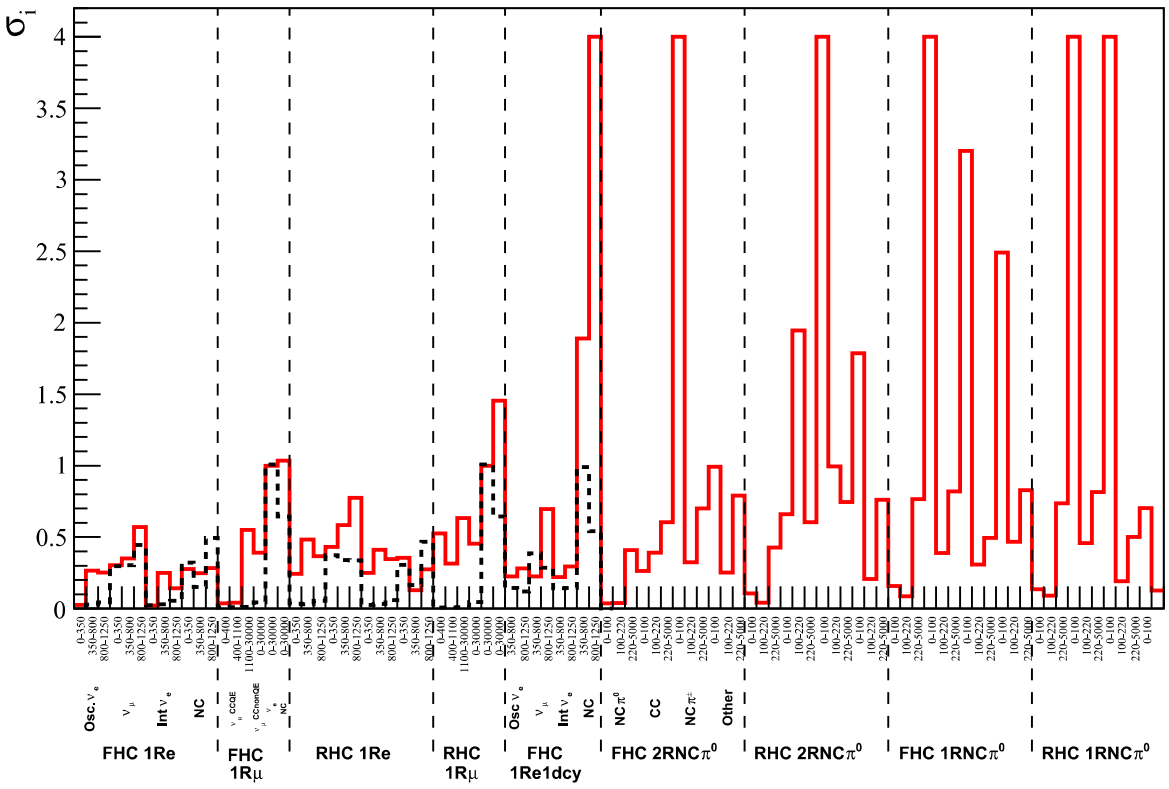


Figure 6.9: SK detector covariance matrix errors from atmospheric fit (red) compared to the official 2020 SK detector covariance matrix (black). Bins with large errors are capped at 400% for clarity. The official MaCh3 samples (1Re, 1Rμ and 1Re1de) are binned in reconstructed neutrino energy. The 1R and 2R NCπ^0 samples are binned in reconstructed π^0 mass.

Chapter 7

Oscillation analysis

This chapter presents the results of the MaCh3 oscillation analysis with the addition of the new 1R and 2R NCπ^0 samples from Chapter 4 and systematics from Chapter 6. Section 7.1 details the operation of the oscillation fit, and its inputs. The NCπ^0 samples are added incrementally using Asimov fits in Sections 7.2 and 7.3 to understand the effect of changes made on the MaCh3 fitter before the final data fit. Section 7.4 details fit to T2K data using the new systematics and NCπ^0 samples.

7.1 The MaCh3 oscillation fit

The likelihood for the oscillation analysis is constructed by comparing data and MC generated events with additional contributions from systematic parameters. The flux, cross section (xsec), ND280, and Super-K detector systematics are nuisance parameters that are marginalised over in order to extract the oscillation parameters. In order to marginalise over nuisance parameters, each parameter is given a prior, depending on any known constraints. The posterior, $P(D|\theta)$, required for Bayesian inference is given by the likelihood, [68]

$$
\begin{aligned}
-\ln(\mathcal{L}) = & \sum_{i}^{ND280bins} N_i^{ND,p}(\overrightarrow{b},\overrightarrow{x},\overrightarrow{d}) - N_i^{ND,d} + N_i^{ND,d}\ln\left(\frac{N_i^{ND,d}}{N_i^{ND,p}(\overrightarrow{b},\overrightarrow{x},\overrightarrow{d})}\right) + \frac{(\beta_i-1)^2}{2\sigma_{\beta_i}}{}^2 \\
& + \sum_{i}^{SKbins} N_i^{SK,p}(\overrightarrow{b},\overrightarrow{x},\overrightarrow{skd},\overrightarrow{o}) - N_i^{SK,d} + N_i^{SK,d}\ln\left(\frac{N_i^{SK,d}}{N_i^{SK,p}(\overrightarrow{b},\overrightarrow{x},\overrightarrow{skd},\overrightarrow{o})}\right) \\
& + \frac{1}{2}\sum_{i}^{osc}\sum_{j}^{osc}\Delta o_i (V_o^{-1})_{i,j}\Delta o_j \\
& + \frac{1}{2}\sum_{i}^{flux}\sum_{j}^{flux}\Delta b_i (V_b^{-1})_{i,j}\Delta b_j \\
& + \frac{1}{2}\sum_{i}^{xsec}\sum_{j}^{xsec}\Delta x_i (V_x^{-1})_{i,j}\Delta x_j \\
& + \frac{1}{2}\sum_{i}^{NDdet}\sum_{j}^{NDdet}\Delta d_i (V_d^{-1})_{i,j}\Delta d_j \\
& + \frac{1}{2}\sum_{i}^{SKdet}\sum_{j}^{SKdet}\Delta skd_i (V_{skd}^{-1})_{i,j}\Delta skd_j
\end{aligned}
\tag{7.1}
$$

.

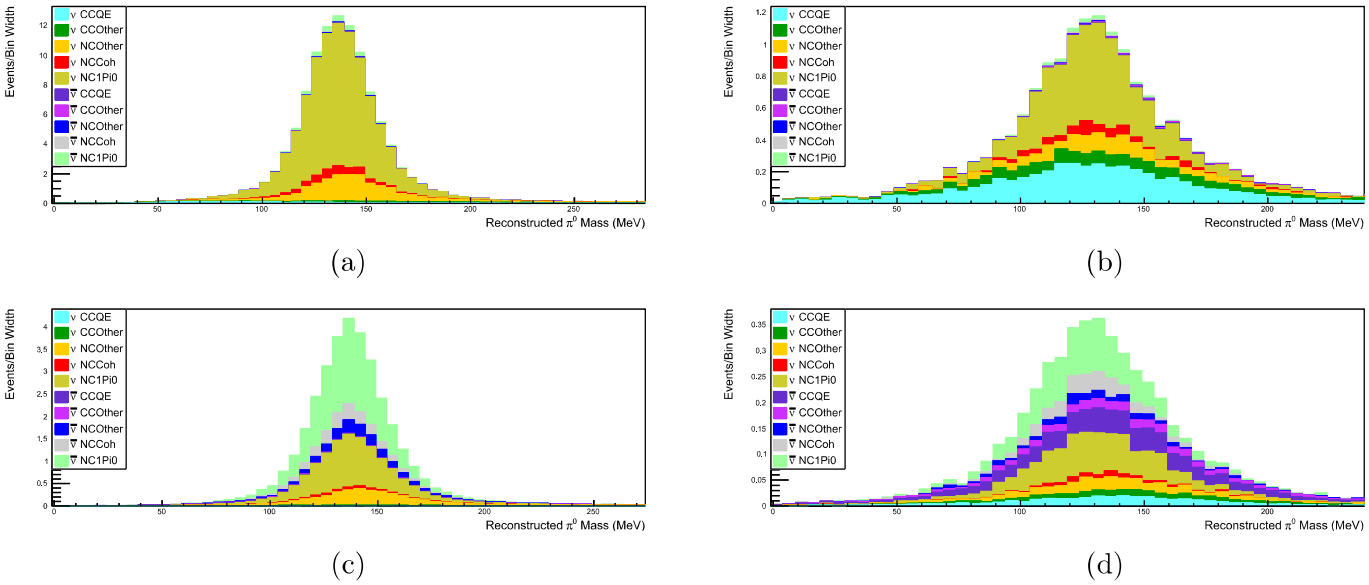
The likelihood is used to determine if a step is accepted or rejected, $-\ln(\mathcal{L})$ is calculated and minimised through the MCMC operation, effectively maximising the posterior probability.

MaCh3 does not provide a 'best fit' value, given the Bayesian nature of MCMC. However, for comparison purposes, the highest posterior probability bin is taken as the most probable value of fit parameters. The purpose of the fit is to measure the credible intervals for oscillation parameters. Credible intervals are calculated using contours constructed by filling a histogram with steps from the Markov chain. The contour is drawn such that the 1σ contour contains the highest 68% of steps and 2σ contains the highest 95% of steps by posterior probability. The resultant steps are not required to be in contiguous bins, for example Δm^2_{23} has Normal and Inverted Ordering (NO and IO) steps with a disfavoured region around $\Delta m^2_{23} \approx 0$ resulting in two separate credible regions. 2D contours are made to reduce marginalisation effects that are more apparent in 1D contours. The parameters plotted are δ_{CP} vs. $\sin^2(\theta_{13})$ and $\sin^2(\theta_{23})$ vs. Δm^2_{23}.

Asimov fits use MC generated data, reweighted with a known set of parameters. This allows for comparisons between fits when adding features or updating inputs, without fitting to real data. For

Table 7.1: Oscillation parameters used in Asimov fits and their priors. After fitting, the chain can be reweighted to impose a Reactor Constraint (RC) on $\sin^2(\theta_{13})$.

Parameter	Asimov value	Prior
$\sin^2(\theta_{12})$	0.307	Gaussian (0.307 ± 0.013)
$\sin^2(\theta_{13})$ woRC	0.022	Flat
$\sin^2(\theta_{13})$ wRC	0.022	Gaussian (0.0220 ± 0.0007)
$\sin^2(\theta_{23})$	0.561	Flat
Δm^2_{12}	7.53×10^{-5}	Gaussian $(7.53 \pm 0.18) \times 10^{-5} eV^2$
Δm^2_{23}	2.494×10^{-3}	Flat
δ_{CP}	-1.601	Flat



(a) (b)

(c) (d)

Figure 7.1: Nominal distributions of MC events for each NCπ^0 samples used for fits, broken down by interaction mode and oscillation channel. (**a**): FHC 2RNCπ^0, (**b**): FHC 1RNCπ^0, (**c**): RHC 2RNCπ^0, (**d**): RHC 1RNCπ^0. The 1Re, 1Rμ, and 1RCC1π sample distributions are shown in Appendix B.1

this analysis the Asimov point used is the T2K best fit shown in Table 7.1. When fitting, the oscillation parameters are varied according to their priors, a flat prior indicates the parameter has freedom to move around in the fit. A Gaussian prior incurs a penalty when the parameter value moves away from the mean value. T2K is not sensitive to $\sin^2(\theta_{12})$ or Δm^2_{12} so they are given a Gaussian prior from the PDG 2021 values [109].

Figure Figure 7.1 shows the pre-fit distributions using the Asimov point in Table 7.1, 19.664×10^{20} POT in FHC and 16.346×10^{20} POT in RHC.

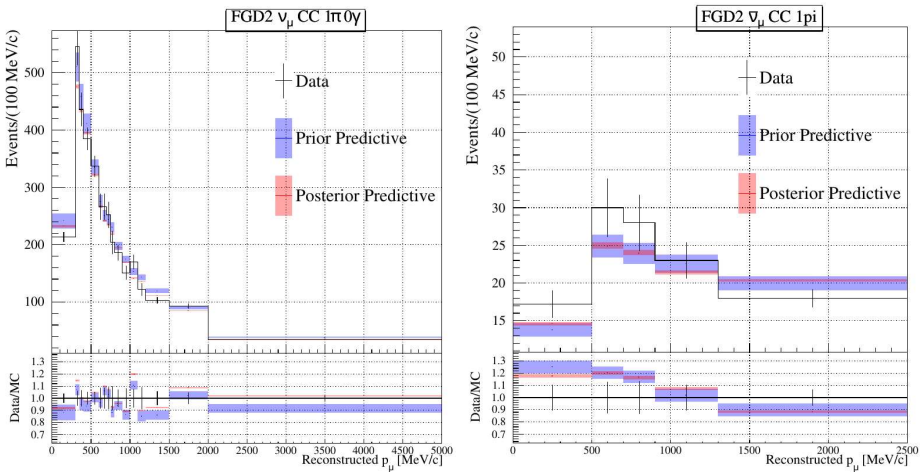


Figure 7.2: Left: FHC CC1π sample, right: RHC CC1π sample made from tagging a single μ and $\pi^{\pm}$ in events. ND280 fit distributions which provide constraints to flux and cross section parameters. CC1π samples affect the NCπ^0 event rate at Super-K. Plots from [110].

7.1.1 ND280 Samples

Samples at ND280 contain CC μ-like events (decided by a PID cut) that originate in one of the FGDs and pass through the next TPC. μ-like events are then split into samples by topology; number of pions, protons, and photons identified. In FHC; CC0π-0p-0γ, CC0π-Np-0γ, CC1π-0γ, CCOther-0γ and CCPhoton. In RHC; CC0π, CC1π, and CCOther .

There are a total of 22 samples, 6 in FHC, 5 in RHC, for events in FGD1 and FGD2, binned in outgoing muon momentum, p_μ, and angle $\cos(\theta_\mu)$. The analysis presented here uses ND280 data from runs 2-9, samples are shown in Appendix B.1.

Flux and cross section models are fitted to ND280 data to provide constraints to flux and cross section parameters, the ND280 fit is described in [110]. Pre and post-fit CC1π samples are shown in Figure 7.2, the CC1π samples constrain NCπ^0 production at Super-K. The prediction of CC1π is low compared to data in RHC.

7.1.2 Systematic parameters

There are four sets of systematics in Equation 7.1 that affect event rates other than neutrino oscillations. The systematics have to be carefully accounted for in order for the MCMC chain to accurately explore a posterior representing the uncertainties and constraints in the fits. Neutrino flux, cross sec-

tion for neutrino interactions, and detector efficiencies directly affect the number of events detected;

$$N_{ND280} = \phi_{ND280} \times \sigma_{ND280} \times \epsilon_{ND280}$$
$$N_{SK} = \phi_{SK} \times \sigma_{SK} \times \epsilon_{SK} P(\nu_\mu \rightarrow \nu_e). \tag{7.2}$$

Where ϕ is the neutrino flux, σ is the cross section for interaction, and ϵ is the detection efficiency. Systematic parameters are used to accommodate additional information available when fitting near and far detector events which are all marginalised over when extracting oscillation parameters.

Each parameter has a prior distribution, commonly Gaussian, that gives the fit a penalty if the parameter is altered away from its initial value. Some parameters, for example δ_{CP}, are given a flat prior such that there is no constraint on its value. Systematic parameters sometimes have flat priors when there is limited knowledge of their true values. Parameters have correlations within groups e.g. flux parameters can correlate with each other, however, different systematic groups are independent. There are 100 flux parameters, 73 cross-section parameters, 552 ND280 detector systematic parameters, and 92 Super-K detector systematic parameters. Super-K has an energy scale error of 2.1% [90] which the reconstructed π^0 mass is sensitive to, the inclusion of the 2RNCπ^0 samples in the fit can aid in constraining the energy scale as they add large number of events at a known energy.

Flux

The flux model constrains the neutrino flux expected at ND280 and Super-K by simulating the interaction of 30 GeV protons with a graphite target and the subsequent decay of hadrons to neutrinos at J-PARC [111]. The hadron production is tuned using data from the NA61/SHINE experiment at CERN [112]. One of the primary reasons for constructing NA61/SHINE was to help constrain hadron production models, the dominant error in neutrino flux predictions at long baseline neutrino experiments. The flux prediction uncertainty is $\sim 5\%$ at 600 MeV neutrino energy, the T2K peak [91]. The neutrino flux is calculated at ND280 and Super-K and is binned in true neutrino energy in FHC and RHC. The flux model acts as an additional aid in predicting event rates that is independent of the detectors and cross-section. Detector samples measure the rate in Equation 7.2, which correlates the

flux and cross-section, additionally, ND280 has mostly plastic scintillator target whereas Super-K is water, so any flux constraint from detector data is correlated to the detectors themselves.

Cross-section

The cross-section parameters control the interactions of neutrinos on various nuclei that are present in ND280 and Super-K. The NEUT framework is used for event generation for MC in ND280 and Super-K, the models it uses determine the cross section parameters that can go into the fit, for a full breakdown see [113]. NEUT uses a relativistic Fermi gas model along with the Benhar spectral function [114] for CCQE interactions. The spectral function is tuned for ^{12}C, ^{16}O, and ^{56}Fe interactions, any other target nuclei only implement the relativistic Fermi gas model. Single pion production uses the Rein-Sehgal model [115]. The two major parameters that control single pion production are C_5^A and M_{Res}^A, from form factors derived from $\Delta(1232)$ resonances which dominate CC and NC pion production in T2K [116]. There is an additional parameter $I_{1/2}$ for non-resonant pion production and NC_{coh} for coherent production where the neutrino interacts with the nucleus as a whole. CCQE interactions are modelled with the axial mass parameter, M_A^{QE}, from the axial form factor for neutrino-nucleon interactions [117]. Though Super-K cannot reconstruct outgoing protons ejected during neutrino interactions, known as 2p2h they take away energy from an interaction and then bias the reconstructed neutrino energy calculation and parameters are added to the fit to account for the uncertainty. At higher neutrino energies, deep inelastic scattering of neutrinos which produces multiple outgoing particles in the detector can occur.

C_5^A and M_{Res}^A are important for modelling NCπ^0 events so the additional 2R samples which contain many more NC events than the other Super-K samples could have an affect. The 2RNCπ^0 also add various other NC events e.g. NC1γ and NCCoh which could affect the cross section parameters governing their rates. The CCQE interaction cross-section parameters will affect the CC events in the 1RNCπ^0 samples which are largely CCQE.

Parameters from the NEUT models are varied in the MaCh3 fit as part of the cross-section systematics. Unlike the flux model, where the parameter in the fit is the binned flux, the cross-section

parameters control the model as they are varied. At Super-K in order to calculate the cross-section response to changing parameters, events are binned in true neutrino energy, the cross-section parameters are then adjusted and the response for each bin can be seen. The response is then interpolated between each bin using polynomial splines, which give a response function for each bin and parameter that the fitter uses. ND280 uses event-by-event weights where each event has cross-section response splines.

ND280 detector systematics

The ND280 detector systematics aim to evaluate event reconstruction errors in ND280, the errors stem from uncertainties in TPC and FGD reconstruction, PID, and detection efficiency as well as background events from outside the detector [118]. Detector systematics are calculated from control samples for each ND280 analysis sample. Systematic parameters are varied 2000 times which moves events into and out of samples and bins and the variation in event rate for each bin represents the systematic error. Consecutive bins with similar systematic values are merged and reduces the number of systematic parameters in the oscillation fit [119]. The ND280 detector systematic uncertainties are included in the oscillation fit as a covariance matrix which encodes the correlations between FGD1 and FGD2 in the ND280 samples.

Oscillation parameters

Oscillation parameters that T2K is sensitive to are given a flat prior so their values are free in the fit. $\sin^2(\theta_{12})$ and Δm^2_{12} have Gaussian priors of ; $\sin^2(\theta_{12}) = (0.307 \pm 0.013)$ and $\Delta m^2_{12} = (7.53 \pm 0.18) \times 10^{-5} eV^2$ [12]. The mass ordering for neutrinos is unknown. As explained in Section 1.3, there is a normal and inverted ordering of masses. The choice affects the MC predictions for oscillation parameters and, therefore, the likelihood surface that the chain steps around. In order to accommodate this variation in the fit, there is a 50% chance at each step that the ordering will flip for the likelihood calculation. In this way, the chain samples both orderings which can be investigated separately or together from the resulting steps.

Fit Name	Description
T2K Asimov	Asimov fit with configuration the same as the 2022 T2K oscillation analysis
T2K Data	Data fit with configuration the same as the 2022 T2K oscillation analysis
New SKDetSyst Asimov	Asimov fit with the new Super-K detector systematics from Chapter 6
Asimov NCπ^0	Asimov fit with the new Super-K detector systematics and the NCπ^0 samples
Data NCπ^0	Data fit with new Super-K detector systematics and NCπ^0 samples

Table 7.2: Oscillation fits performed and names used to identify them in figure legends. 2022 T2K Oscillation Analysis from [68]

7.1.3 Fits performed

The fits performed in order are shown in Table 7.2. Asimov fits of ∼25 million steps are performed to evaluate the fitter. The covariance matrix from Chapter 6 is added without the NCπ^0 samples and compared to the T2K results using the same configuration as for the 2022 analysis without any additions [68]. Then the NCπ^0 samples are added with the same binning as for the Super-K detector systematics in Table 6.4. A final data fit is performed, of ∼ 75 million steps to evaluate the 3σ contours, with all samples and the new SK covariance matrix. The fits are run without the reactor constraint (woRC), and after steps have been accumulated it is possibly to reweight the chain and impose the external reactor constraint on $\sin^2(\theta_{13})$ in Table 7.1 without re-running the analysis (wRC).

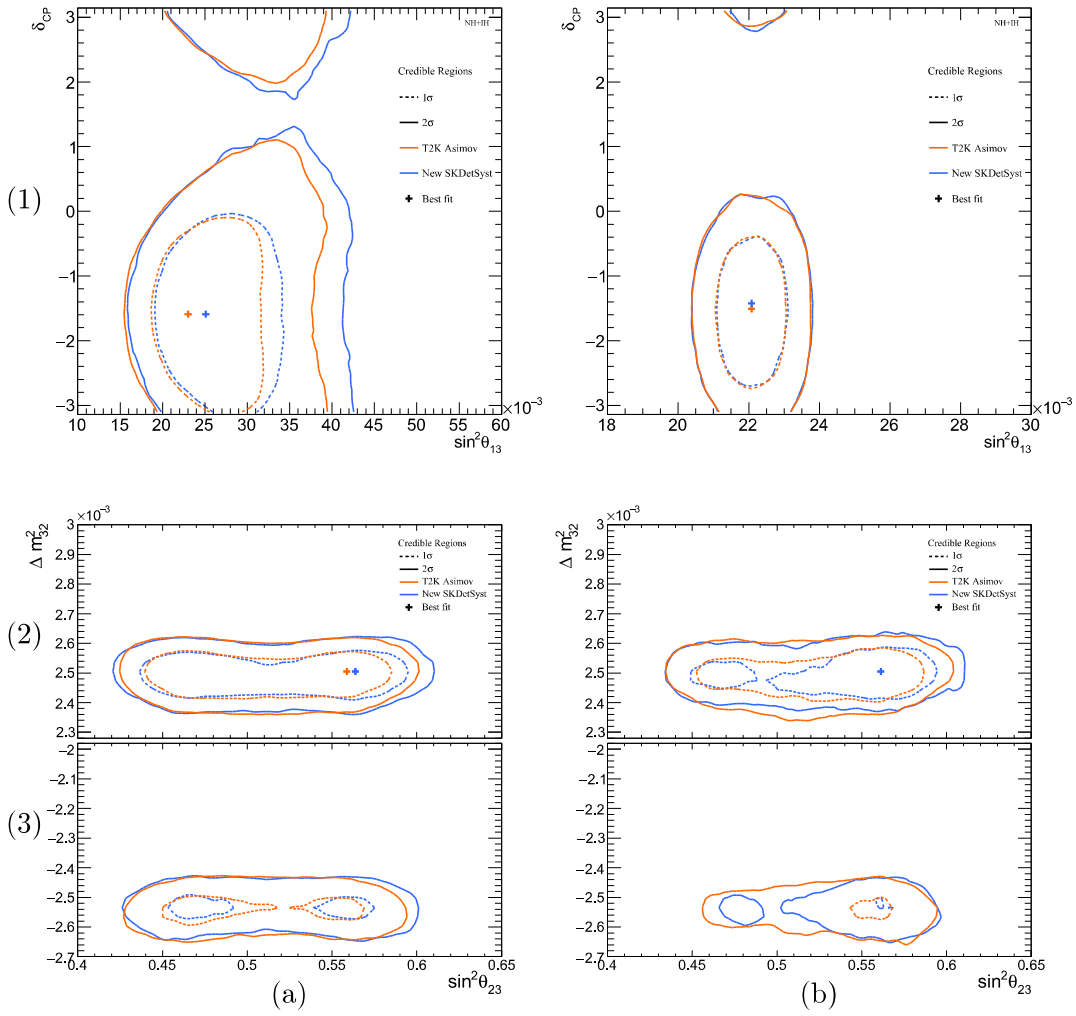


Figure 7.3: **(a)**: without reactor constraint (woRC), **(b)**: with reactor constraint (wRC). **(1)**: $\sin^2(\theta_{13})$ vs. δ_{CP}, **(2)**: $\sin^2(\theta_{23})$ vs. Δm^2_{23} normal ordering, **(3)**: $\sin^2(\theta_{23})$ vs. Δm^2_{23} inverted ordering. The addition of the new Super-K detector covariance matrix broadens the contours in the woRC fits. The changes in contours are due to the new, larger, Super-K detector systematic errors on the 1Re, 1Rμ, and 1Re1de samples.

7.2 Asimov fit with new Super-K detector matrix

The covariance matrix in Figure 6.9 has much larger errors for the 1Re, 1Rμ, and 1Re1de samples compared to the T2K Asimov fit. The covariance matrix is used without adding NCπ^0 samples such that the only difference between the contours in Figure 7.3 are the errors introduced from the Super-K detector covariance matrix. The purpose of this fit is to observe the effect of the increased errors independent of the NCπ^0 samples.

Figure 7.3(a) has a widening of contours without the reactor constraint applied, meaning the oscillation parameters are less constrained by the fit. The broadening of the contours is expected

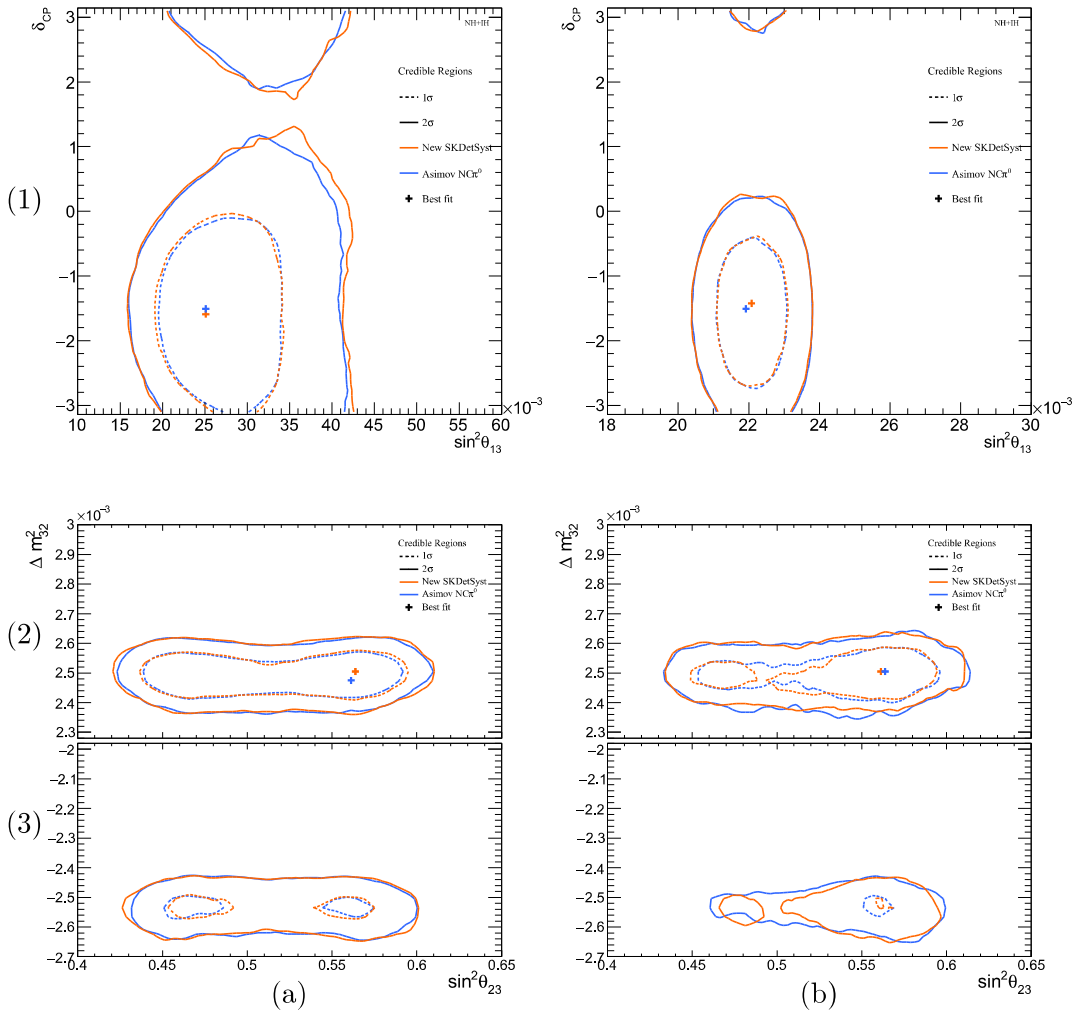


Figure 7.4: **(a)**: woRC, **(b)**: wRC. **(1)**: $\sin^2(\theta_{13})$ vs. δ_{CP}, **(2)**:$\sin^2(\theta_{23})$ vs. Δm^2_{23} normal ordering, **(3)**:$\sin^2(\theta_{23})$ vs. Δm^2_{23} inverted ordering. Addition of NCpi0 samples to the Asimov fit. Contours are mostly unchanged with the addition of NCπ^0 samples.

given the larger errors, however with the application of the reactor constraint, the contours line up for δ_{CP} vs. $\sin^2(\theta_{13})$. The plots in Figure 7.3 set the baseline for inclusion of the NCπ^0 samples for comparison in the following fit. $\sin^2(\theta_{13})$ is likely affected by the large oscillated ν_e errors in Figure 6.9. The disappearance parameter contours in Figure 7.3(c) and (d) are less affected because the errors in FHC ν_μ CCQE are in more agreement with the previous Super-K detector systematic matrix, though larger errors are seen in CCnon-QE bins. There does appear to be some narrowing of the contours in $\sin^2(\theta_{23})$ with the new detector matrix, which is unexpected given the increase in errors, this effect should be investigated further but is beyond the scope of this analysis.

7.3 Asimov fit with additional NCπ^0 samples

Another Asimov fit was performed with the additional NCπ^0 samples added in order to verify that the fitter is performing correctly. Several inputs besides the covariance matrix had to be regenerated, such as splines which predict the response for changing cross-section parameters in the fit and are produced beforehand. In addition, modifications were made to MaCh3 itself in order to accommodate four new samples. Figure 7.4 shows the contours with and without the NCπ^0 samples added. The contours are largely unchanged and no significant change in the width of the contours or their position is apparent.

1D δ_{CP} contours for both Asimov fits are shown in Figure 7.5, there is a slight tightening of the contours after adding the NCπ^0 samples indicating a small increase in sensitivity to δ_{CP} in the reduction of the 90% contours by 3.5%. The 1RNCπ^0 samples could only potentially add $\sim$ 5% to the total CCQE ν_e appearance data, and combined with the increase in Super-K detector systematics any affect is encouraging.

The mass ordering and $\sin^2(\theta_{23})$ octant preference can be summarised by counting the number of steps in each ordering/octant quadrant, as shown in Figure 7.6. The four plots show that there is a preference for normal mass ordering and upper octant $\sin^2(\theta_{23})$, which is stronger when the reactor constraint is applied. Adding the NCπ^0 samples gives a slight increase in sensitivity to the octant and ordering because there is an increase in posterior percentage in the upper octant and normal ordering which is where the Asimov point is set in Table 7.1.

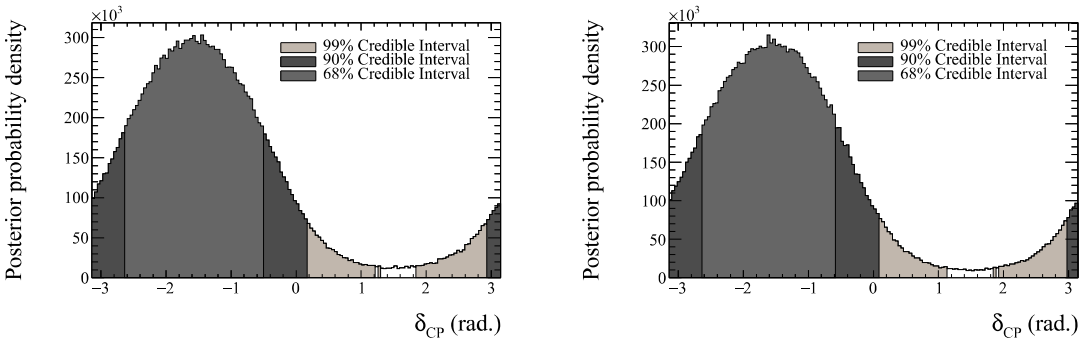


Figure 7.5: 1D Asimov δ_{CP} contours wRC. Left: New Super-K detector systematics only with 90% credible limit:[-π-0.167] [2.932-π]. Right: NCπ^0 samples and Super-K detector systematics with 90% credible limit: [-π-0.083] [2.974-π] . There is a very slight tightening of the contours by 3.5%.

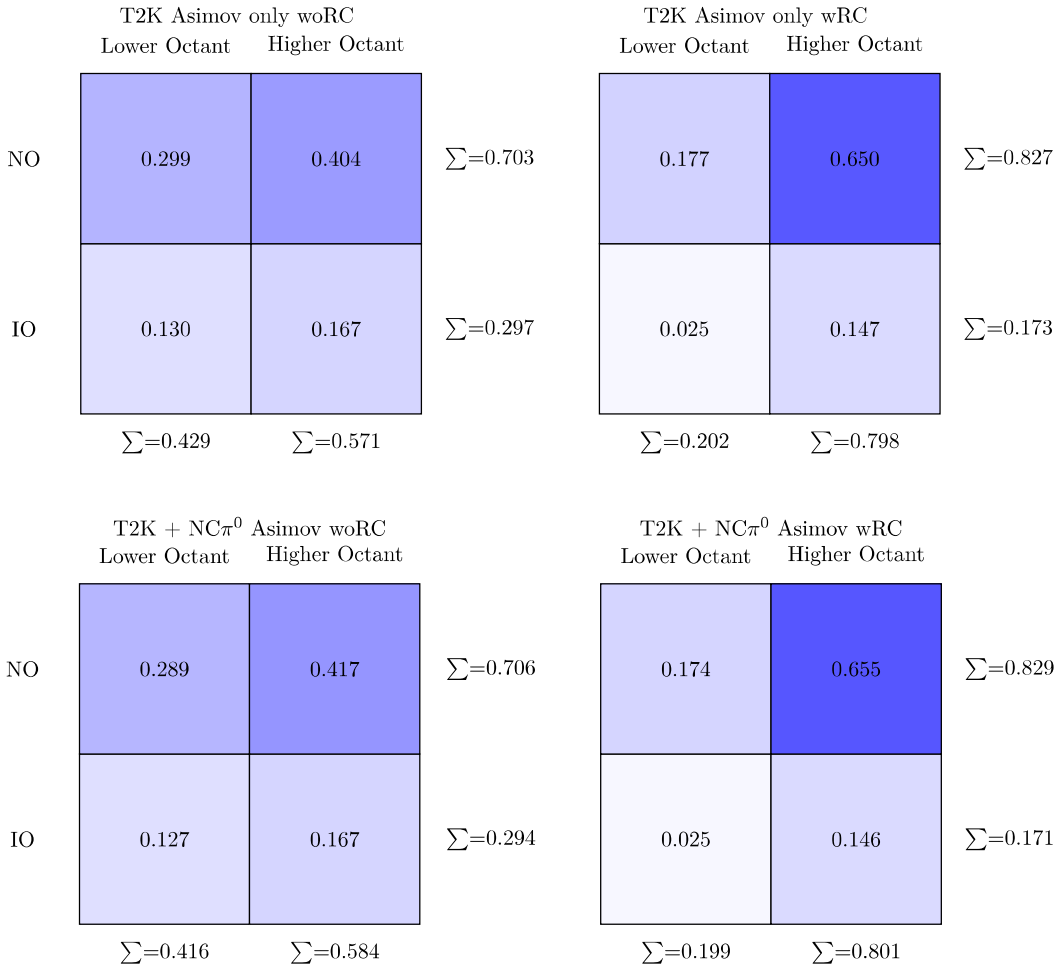


Figure 7.6: Posterior percentages for Δm^2_{23} mass ordering and $\sin^2(\theta_{23})$ octants extracted from the number of steps in each bin in the T2K only and NCπ^0 Asimov fits. There is an increase in sensitivity to the mass ordering and $\sin^2(\theta_{23})$ octant with the NCπ^0 samples added.

Sample	Events	MC
FHC 1Rμ	321	330.65
RHC 1Rμ	137	137.81
FHC 1Re	94	83.51
RHC 1Re	16	15.80
RHC 1Re+1dcye	14	10.36

Sample	Events	MC
FHC 2RNCπ^0	104	114.20
RHC 2RNCπ^0	41	36.78
FHC 1RNCπ^0	14	16.47
RHC 1RNCπ^0	4	5.10

Table 7.3: Total data and MC event rates for T2K and NCπ^0 samples. MC event rates use Asimov parameters in Table 7.1.

7.4 Data fit with the additional samples and covariance matrix

The final NCπ^0 data fit uses run 1-10 Super-K data with event rates shown in Table 7.3, corresponding to 19.664×10^{20} POT in FHC and 16.346×10^{20} in RHC. Before the oscillation parameter results, goodness of fit tests and posterior predictions are made to show the MC compares to data.

7.4.1 Posterior predictions

Figure 7.7 shows mostly good agreement between prediction and data, with the exception of the second bin of the RHC 2RNCπ^0 sample which under-predicts the number of data events. The discrepancy is similar to the RHC CC1π sample at ND280 in Figure 7.2 which could be pulling the NCπ^0 event rates down at Super-K. Spectra for the original T2K samples are shown in Appendix B.2. There is a slight deficit of data events in the second bin of the 1RNCπ^0 samples which could be an indication of NCπ^0 mis-modelling. The RHC MC in Figure Figure 7.2 and the 2RNCπ^0 sample is lower than data which is not seen in the RHC 1RNCπ^0 sample. The predictions still agree with data overall, given the low statistics.

Mis-moddeling of NCπ^0 events in the 1RNCπ^0 samples is important to consider. The 1Re and 1RNCπ^0 samples are separated only by the e/π^0 PID cut shown in Figure 3.3, and there are data events close to that cut which are close to being part of the 1Re samples. A deficit of events in the 1RNCπ^0 samples could produce an excess of 1Re events if the deficit is caused by PID errors. This is contrary to the correlation matrix in Figure 6.8, which shows little correlation between the 1Re and 1RNCπ^0 samples. However, the errors on π^0-like events in the SK detector systematics could be over constrained as seen in the data-MC discrepancy in Figure 6.6. Low event rates in these samples means the tensions are not conclusive, however, it is something that will be investigated further at T2K.

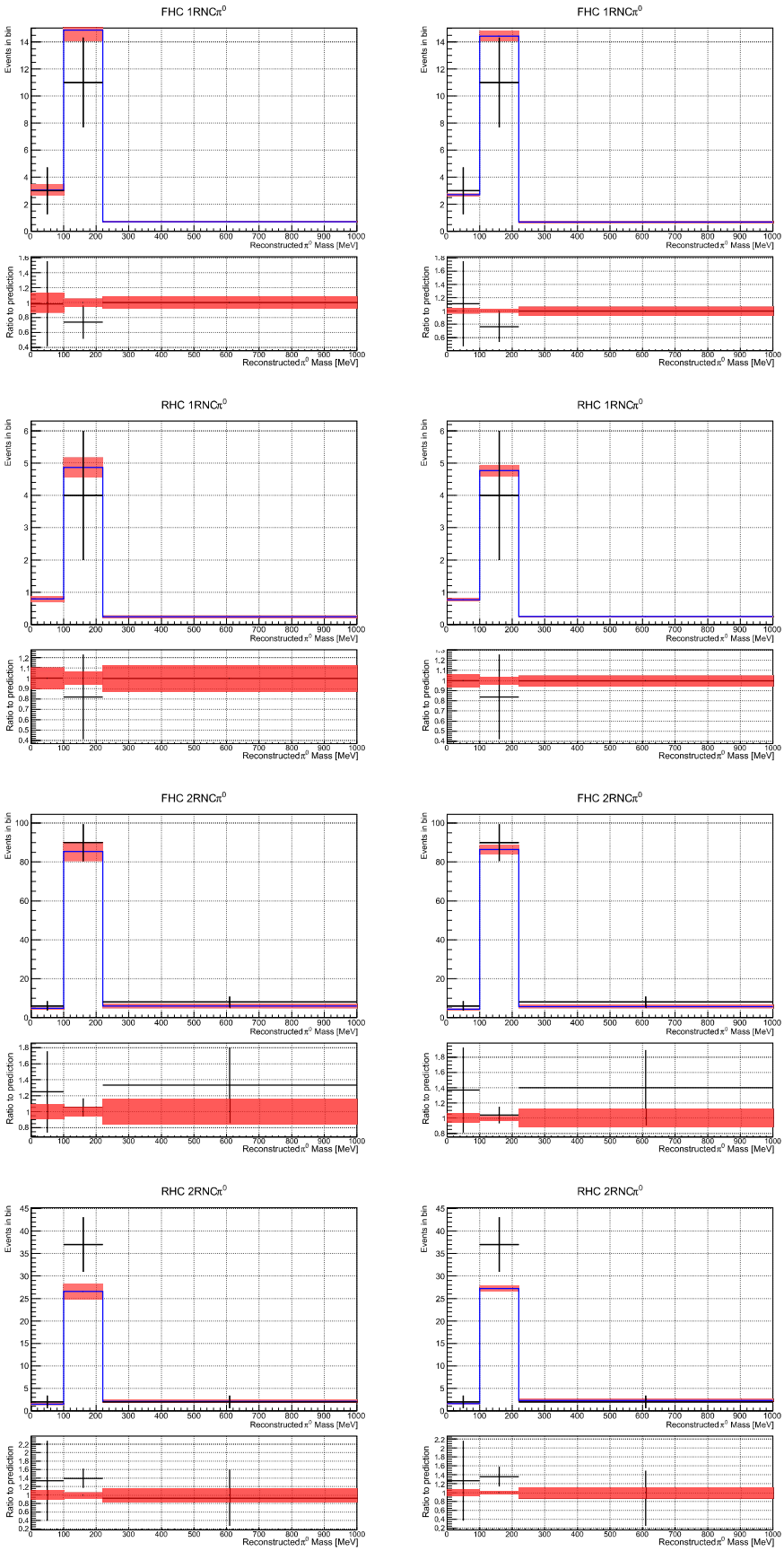
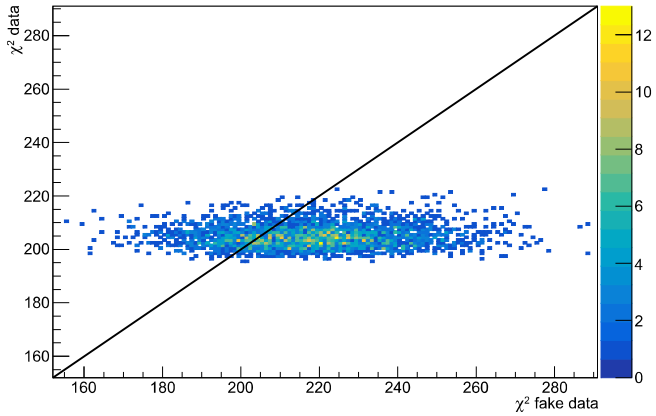


Figure 7.7: Post-fit posterior predictive plots with (left) and without (right) reactor constraint for NCπ^0 samples.



Sample	Rate	Rate+Shape
FHC 1Re	0.50	0.13
RHC 1Re	0.53	0.64
FHC 1Rmu	0.20	0.48
RHC 1Rmu	0.52	0.82
FHC 1Re1de	0.44	0.90
FHC 2RNCpi0	0.53	0.78
RHC 2RNCpi0	0.09	0.35
FHC 1RNCpi0	0.27	0.52
RHC 1RNCpi0	0.38	0.57
Total	**0.28**	**0.73**

Figure 7.8: Left: χ^2_{data} is calculated by comparing the MC to data and $\chi^2_{fakedata}$ is calculated by comparing MC to a randomly thrown value from the posterior of the data fit. The p-value is calculated as the percentage of points where $\chi^2_{fakedata} < \chi^2_{data}$, the marked diagonal line. Right: Posterior p-values calculated from overall rate and bin by bin χ^2 values for each sample.

7.4.2 P-values

The agreement between data and MC can be quantified by calculating the posterior p-value. Using the total number of events in data and MC gives a rate only p-value of 28%, whereas using the bin by bin differences, the shape of the distribution can be accounted for giving shape plus rate p-value of 73% shown in Figure 7.8. The p-value can be individually calculated for each sample, as shown in Table 7.8. The p-values show no evidence for disagreement between data and MC [68]. The RHC 2RNCπ^0 sample has the lowest p-value in the rate only calculation due to the excess of 5 data events in the second bin of Figure 7.7 which is the largest discrepancy but not enough to cause concern.

7.4.3 Post-fit Parameters

Figure 7.9 shows post-fit parameters and how their values are pulled from their prior values. The NCπ^0 samples add a lot of NC events to the fit so it is important to make sure those events are not pulling any fit parameters around too much. C_5^A and M_{Res}^A control pion production and are pulled from their prior prediction. However, they agree with the post-fit values when no NCπ^0 samples are added, indicating NCπ^0 event rate predictions are constrained by the ND280 samples more than the new NCπ^0 Super-K samples. This is further reinforced by the data/MC differences in the RHC 2RNCπ^0 in Figure 7.7 which could indicate some mis-modelling of NC antineutrino events.

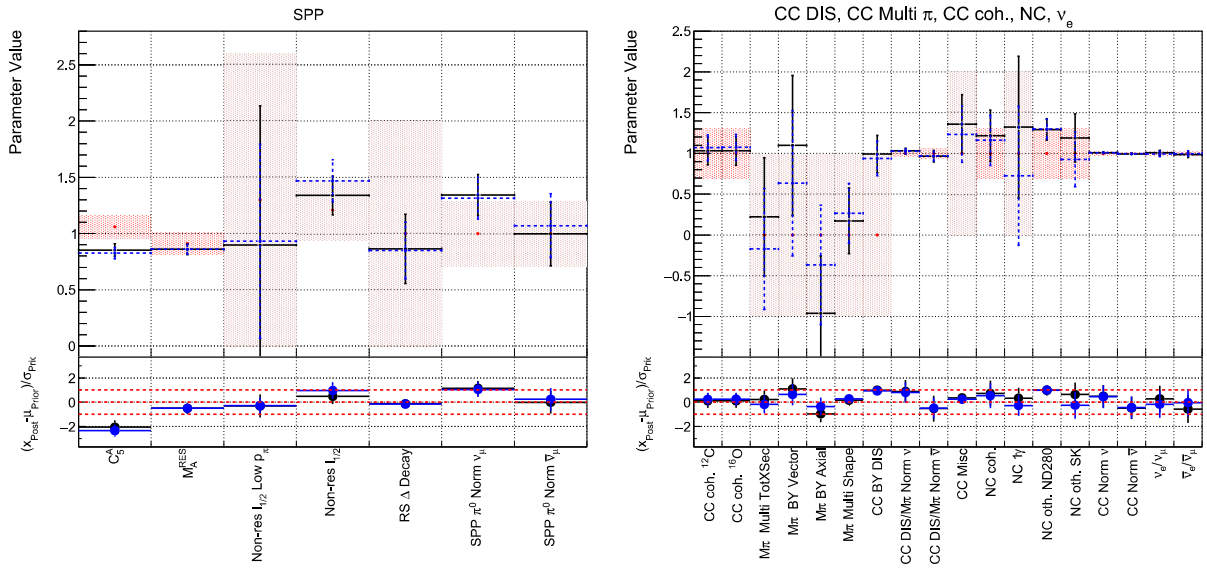


Figure 7.9: Some of the cross-section parameter post-fit values relevant to NCπ^0 events. (▨): prior value and error, (- - - -): Initial T2K data post-fit, (——): T2K and NCπ^0 samples post-fit. Other plots are shown in Appendix B.2

.

The 2RNCπ^0 samples may provide additional constraint to flux predictions because they are unoscillated events. Figure 7.10 shows no significant differences in flux parameter in ND280 or Super-K samples, see Appendix B.2. However, the addition of the NCπ^0 samples does have an effect, even though the event rate in Super-K samples are far lower than ND280 samples which drive the flux predictions.

7.4.4 Oscillation parameter contours and credible intervals

Figure 7.11 shows 2D data fit contours with steps from both mass orderings with and without reactor constraint, and the credible intervals are presented in Table 7.4 which are extracted from the 1D contours in Figure 7.12. The contours are compared to the T2K release data in Figure 7.14. The NCπ^0 fit has a much wider $\sin^2(\theta_{13})$ contour compared to the T2K data fit, but is comparable to the Asimov fits in Figures 7.3(1) and 7.4(1).

The oscillation parameter contours are pulled in when the reactor constraint is applied to almost completely match the T2K data fit, in a similar manner to the Asimov fits. There is a slight shift in the best fit point of δ_{CP} in the positive direction and a slightly tighter constraint on δ_{CP}. Figure 7.14(2,3) shows the Δm^2_{23} vs. $\sin^2(\theta_{23})$ 2σ contours are slightly narrower in Δm^2_{23} with a more pronounced

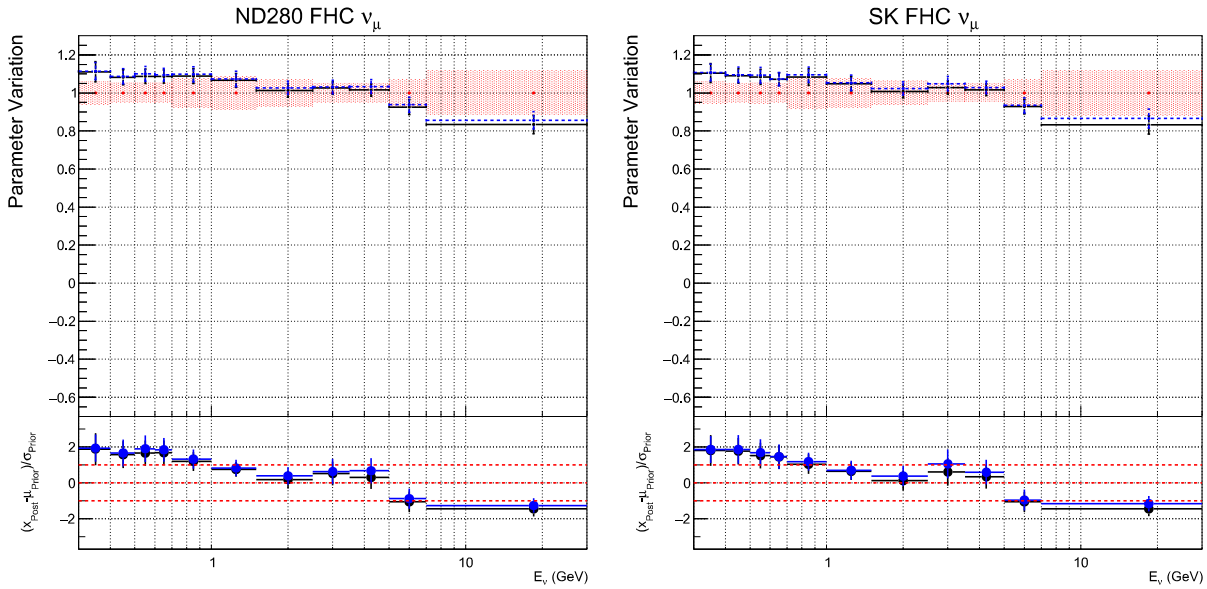


Figure 7.10: Pulls on flux parameters show the addition of the NCπ^0 affect the neutrino flux. (▨): prior value and error, (- - - -): Initial T2K data post-fit, (——): T2K and NCπ^0 samples post-fit. Other plots are shown in Appendix B.2

.

preference for normal ordering of masses.

From the Asimov fits in Figures 7.3 and 7.4, the 1σ contours do move around with each stage of the analysis. The Super-K detector systematics added generally increase the original T2K errors so would not at first guess produce tighter contours. The Super-K detector systematics do have relatively low errors on NCπ^0 events which in combination with the large number of NCπ^0 events added could be providing constraints to the flux, as seen in Figure 7.10, or through a better constraint on Super-K energy scale from the large number of NCπ^0 events with well known reconstructed energy.

Figure 7.13 shows there is a preference for normal ordering and the upper octant of $\sin^2(\theta_{23})$, which is also seen without NCπ^0 samples. In comparison to the initial T2K analysis, the octant/ordering preference is more pronounced in both wRC and woRC fits which can also be seen in the 2D Δm^2_{23} vs.$\sin^2(\theta_{23})$ contours in Figure 7.11.

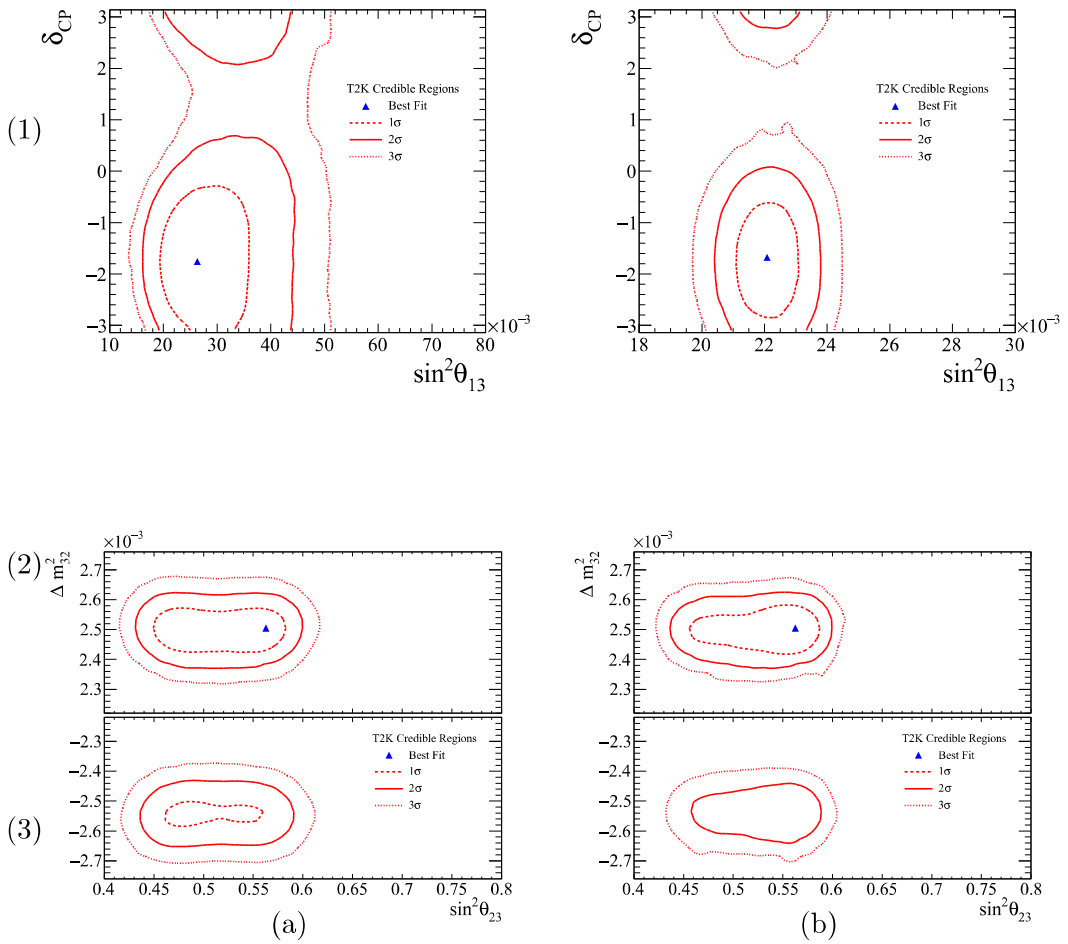


Figure 7.11: **(a)**: woRC, **(b)**: wRC. **(1)**: $\sin^2(\theta_{13})$ vs. δ_{CP}, **(2)**:$\sin^2(\theta_{23})$ vs. Δm^2_{23} normal ordering, **(3)**:$\sin^2(\theta_{23})$ vs. Δm^2_{23} inverted ordering. Data fit contours with steps for both mass orderings. Additional plots with separate orderings are available in Appendix B.3. Contours are plotted up to 3σ, δ_{CP} =0 is not excluded with or without reactor constraint.

Parameter	Best fit	2σ CI woRC	2σ CI wRC	T2K results (NO, wRC)
$\sin^2(\theta_{13})$	0.0258	[0.0185, 0.0417]	[0.0207, 0.0235]	-
$\sin^2(\theta_{23})$	$0.56^{+0.03}_{-0.05}$	[0.44, 0.58]	[0.45, 0.58]	$0.561^{+0.021}_{-0.032}$
Δm^2_{23} ($\times 10^{-3}$eV^2) NO	$(2.49^{+0.05}_{-0.05})\times 10^{-3}$	[2.4, 2.6]	[2.4, 2.6]	$(2.494^{+0.041}_{-0.058})\times 10^{-3}$
Δm^2_{23} ($\times 10^{-3}$eV^2) IO	$(2.49^{+0.05}_{-0.05})\times 10^{-3}$	[-2.6, -2.4]	[-2.6, -2.5]	-
δ_{CP}	$-1.84^{+0.84}_{-0.72}$	[$-\pi$, -0.251] [2.555, π]	[$-\pi$, -0.209]	$-1.97^{+0.97}_{-0.70}$

Table 7.4: Highest posterior probability point extracted from data fit and 1D credible intervals. Best fit points are extracted from 2D plots of $\sin^2(\theta_{23})$ vs. Δm^2_{23} and δ_{CP} vs. $\sin^2(\theta_{13})$ in Figure 7.11. 1σ uncertainties are added to the best fit values for comparison to published T2K results from [120].

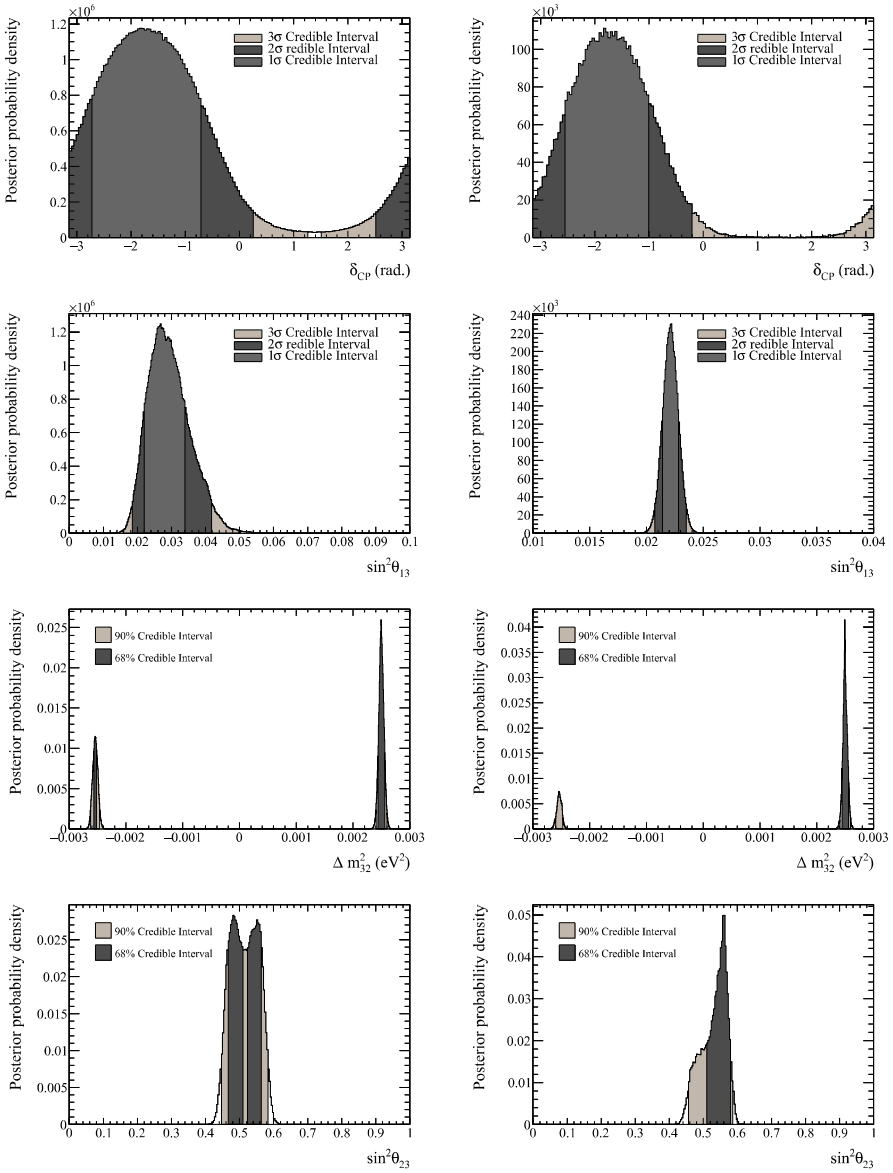


Figure 7.12: Left: woRC, right: wRC, 1D oscillation parameter contours. Credible intervals are extracted from the contours. Inverted ordering is excluded to 1σ level when the reactor constraint is applied.

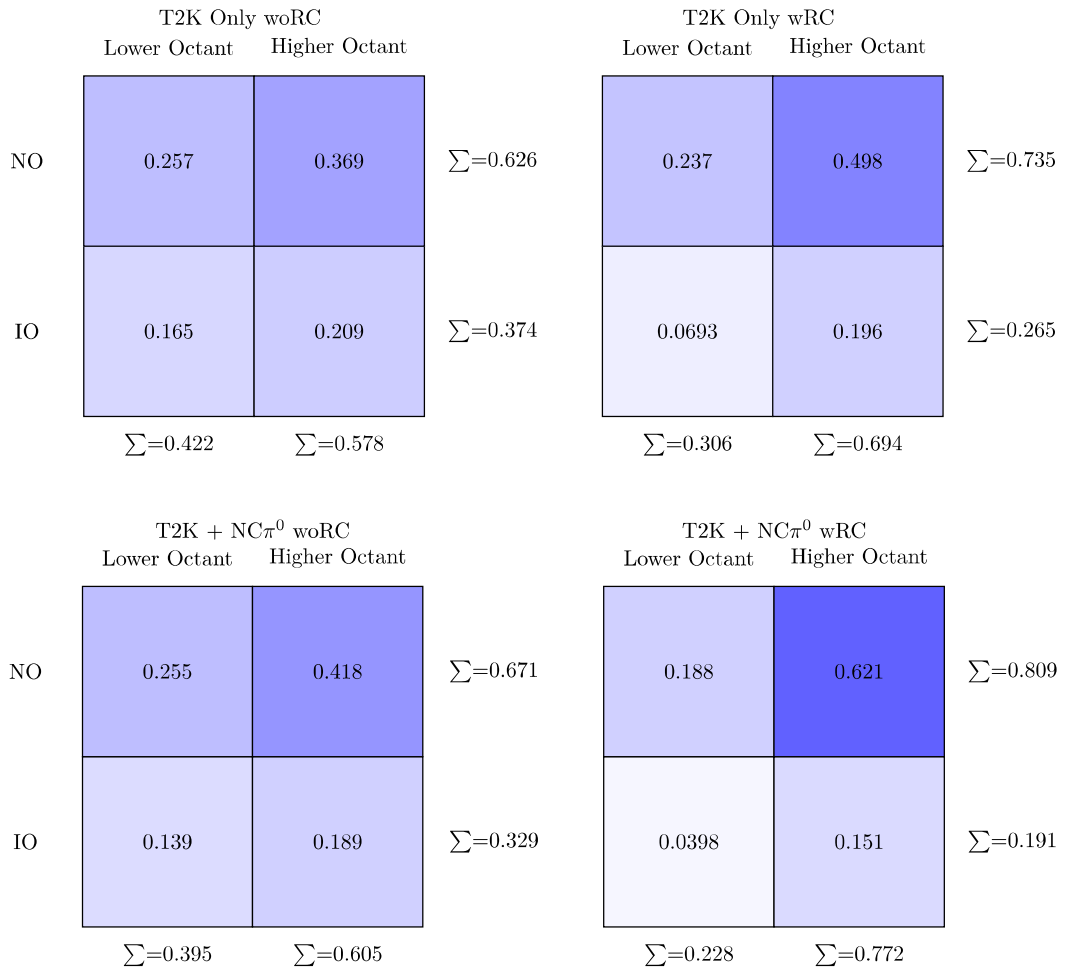


Figure 7.13: Posterior percentages for Δm^2_{23} mass ordering and $\sin^2(\theta_{23})$ octants extracted from the number of steps from data fits for each bin. There is a clear preference for higher octant. Normal ordering values in both the T2K and NCπ^0 fits. The preference is more pronounced in NCπ^0 fits.

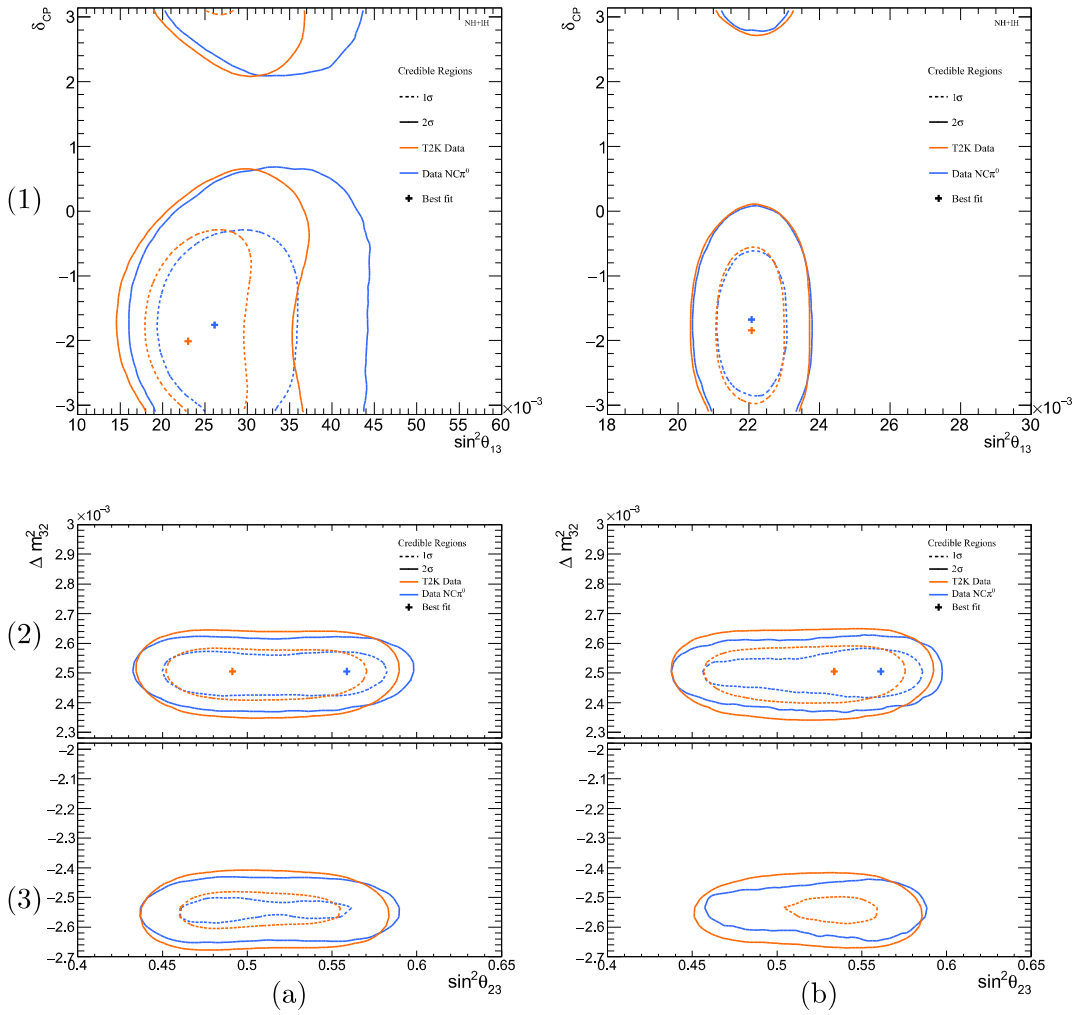


Figure 7.14: **(a)**: woRC, **(b)**: wRC. **(1)**: $\sin^2(\theta_{13})$ vs. δ_{CP}, **(2)**: $\sin^2(\theta_{23})$ vs. Δm^2_{23} normal ordering, **(3)**: $\sin^2(\theta_{23})$ vs. Δm^2_{23} inverted ordering. Contours for oscillation data fit with NCπ^0 samples and updated Super-K detector systematics compared to T2K data fit.

7.5 Result summary

Incrementally adding the new Super-K detector covariance matrix and NCπ^0 samples shows good internal agreement for the fits. Adding the new Super-K detector systematics in Figure 7.2 shows a considerable increase in $\sin^2(\theta_{13})$ woRC contour size compared to the T2K Asimov fit, size which is present for the rest of the fits. This is likely due to the increase in 1Re errors in the Super-K detector systematics. The wRC $\sin^2(\theta_{13})$ contours have better agreement with the T2K Asimov fit. Adding the NCπ^0 samples to Asimov fits in Section 7.3 gives a slight increase in sensitivity to δ_{CP} of 3.5% on the 90% credible interval.

Adding the NCπ^0 samples to the data fit has a small effect on the contours and credible intervals which is encouraging given the larger errors in the Super-K covariance matrix. There is a shift in the best fit point from the T2K data fit, as seen in Figure 7.14 and the lower region of δ_{CP} contour is pulled in slightly. A stronger preference for normal mass ordering and upper octant $\sin^2(\theta_{23})$ values is seen in Figure 7.13. The best fit value for $\delta_{CP} = -1.84^{+0.84}_{-0.72}$ with 1σ errors is in agreement with published T2K results and slightly tighter at the lower bound of δ_{CP}.

The posterior predictions show that the MC and Data match well and p-values for the NCπ^0 samples are all acceptable so the samples are not impeding the fits ability to constrain the oscillation parameters. There is some tension between data and MC and a lower p-value for the RHC 2RNCπ^0 sample which could be an indication of NCπ^0 mismoddeling. The 1RNCπ^0 samples add some additional CCQE events to the ν_e appearance channel MC as seen in Figure 7.1, and from Asimov fits are shown to increase the sensitivity to δ_{CP}. The increase in sensitivity is small, reducing the 90% contours by 3.5% compared to the same Asimov fit without 1RNCπ^0 samples.

Chapter 8

Conclusions

Chapter 2 explored the possibility of reconstructing the Super-K in-situ PMT positions with promising results, producing a 3D model of a ring of PMT positions. The process highlighted the difficulties in labelling the PMTs and matching them between images, requiring manual correction. The project helped inform the design of future Cherenkov water detectors which are likely to use static cameras instead of drones, and identifying marks on PMTs for labelling. The photogrammetry reconstruction performed well with $\sim 6px$ average reprojection error. The most difficult part of the process was applying accurate labels to PMTs. The process involved assumptions based on the yaw value of the drone which was inaccurate in some cases, requiring manual alteration of PMT labels. The Super-K ID eccentricity was measured at 0.2% using the reconstructed PMT locations and in agreement with the circular design of Super-K.

Chapter 4 outlined the production of two NCπ^0 Super-K event samples in FHC and RHC, demonstrating a high purity 2RNCπ^0 sample could be made, with the aim of recovering CCQE e-like events in the 1RNCπ^0 sample by constraining the NCπ^0 backgrounds. In addition, the 2RNCπ^0 sample π^0 mass peak was fitted to data and gives a competitive width measurement compared to other detectors at 35 MeV. The 2RNCπ^0 samples could be used as additional energy scale constraint due to the narrow peak observed at a known value.

The high statistics and purity of the 2RNCπ^0 samples means they could be used in the future for a powerful neutrino flux constraint not dependent on simulations because they measure the unoscillated

T2K neutrino flux. The potential flux constraint is further motivated by some additional pulls seen in flux parameters for the MaCh3 fit in Figure 7.10.

Two single ring π^0 samples were created based on the existing Super-K 1Re samples. The aim of the 1Rπ^0 samples was to recover CCQE events removed from the 1Re samples due to NCπ^0 backgrounds. The 2R and 1R NCπ^0 samples were added to the MaCh3 oscillation analysis to constrain the NCπ^0 backgrounds enough that additional sensitivity to oscillation parameters could be gained from the CC events in the 1RNCπ^0 samples.

Chapter 6 performs an atmospheric neutrino fit at Super-K to calculate systematic errors on reconstructing the NCπ^0 sample events. The fit used MCMC methods to explore a multi-variate parameter space and calculated shift and smear values for `fiTQun` reconstruction parameters. The fit used 20 separate MCMC chains to explore the posterior distribution, some fit parameters would get stuck in local minima and not explore the space appropriately despite extensive step size tuning. The chains all explored similar posterior values, there was no reason to choose a selection of chains over others as they were all valid. Using all available steps, instead of a subset of chains, increased the errors on most bins in the Super-K detector covariance matrix when compared to the published T2K results. The Super-K detector systematics overestimate the uncertainties on bins, however, the steps used in the systematics legitimately plot out the posterior of the atmospheric fit, so the behaviour should be investigated further at T2K but is beyond the scope of this thesis.

The systematic error analysis of the NCπ^0 samples produced large errors in the Super-K detector systematics, which impacted the oscillation analysis sensitivities. There were no additional constraints observed on oscillation parameters compared to published T2K results when performing a data fit. There is a stronger preference for normal mass ordering upper octant $\sin^2(\theta_{23})$ values compared to the T2K data fit with a 62.1% posterior probability in Figure 7.13. Additionally, there is some increased sensitivity to δ_{CP} when adding the NCπ^0 samples in Asimov fits in Figure 7.5. The data fit in Figure 7.11 show larger credible intervals on $\sin^2(\theta_{13})$ are seen without the reactor constraint applied due to the increase in systematic errors, however, the T2K fit 1σ and 2σ contours are matched with the additional $\sin^2(\theta_{13})$ reactor constraint.

There is a tightening of Δm^2_{23} 2σ contours compared to the original T2K data fit, the reason could be from the new Super-K systematics which, from Asimov fits, show some affect on 1σ contours, or from the NCπ^0 samples providing additional constraints. Further investigation of the Super-K detector systematic effects on the oscillation analysis is recommended. The larger errors and correlations shift the $\sin^2(\theta_{13})$ contours quite dramatically which is understandable given the increase in 1Re and 1Rμ sample uncertainties. However, the contours for other oscillation parameters are largely unaltered in Asimov fits, especially with the reactor constraint applied.

Posterior predictive plots of the NCπ^0 samples in Figure 7.10 show some slight discrepancy in data and MC with a deficit of 1RNCπ^0 data events and an excess of RHC 2RNCπ^0 data events at the π^0 mass peak, highlighted by the low p-value of the 1RNCπ^0 sample. The discrepancies could be due to mis-modelling or PID issues and warrant further investigation, however, given the low statistics, the tensions are not conclusive.

The studies in this thesis lay the groundwork for further development of NCπ^0 samples at Super-K. The samples have potential to provide additional constraints to δ_{CP}, NCπ^0 production, flux constraints, and energy scale at Super-K for oscillation analyses. As T2K moves to the next generation of precision neutrino oscillation measurements with ND280 upgrades, IWCD, and Hyper-K, NCπ^0 events could play an important role with additional constraints and CC event recovery.

Bibliography

[1] Laurie M Brown. "The idea of the neutrino". *Physics Today* 31.9 (1978), pp. 23–28. DOI: 10.1063/1.2995181. URL: https://doi.org/10.1063/1.2995181.

[2] Fred L Wilson. "Fermi's Theory of Beta Decay". *American Journal of Physics* 36.12 (1968), pp. 1150–1160. DOI: 10.1119/1.1974382. URL: https://doi.org/10.1119/1.1974382.

[3] C. L. Cowan, F. Reines, F. B. Harrison, H. W. Kruse, and A. D. McGuire. "Detection of the free neutrino: A confirmation". *Science* 124.3212 (1956), pp. 103–104. DOI: 10.1126/science.124.3212.103.

[4] G. Danby et al. "Observation of high-energy neutrino reactions and the existence of two kinds of neutrinos". *Physical Review Letters* 9.1 (July 1962), pp. 36–44. DOI: 10.1103/PhysRevLett.9.36.

[5] DONUT Collaboration. "Observation of Tau Neutrino Interactions". *Physics Letters, Section B: Nuclear, Elementary Particle and High-Energy Physics* 504.3 (Dec. 2000), pp. 218–224. DOI: 10.1016/S0370-2693(01)00307-0. URL: http://arxiv.org/abs/hep-ex/0012035%20http://dx.doi.org/10.1016/S0370-2693(01)00307-0.

[6] B. Pontecorvo. "Mesonium and anti-mesonium". *Sov. Phys. JETP* 6 (1957), p. 429.

[7] Ziro Maki, Masami Nakagawa, and Shoichi Sakata. "Remarks on the Unified Model of Elementary Particles". *Progress of Theoretical Physics* 28.5 (Nov. 1962), pp. 870–880. DOI: 10.1143/PTP.28.870. URL: https://doi.org/10.1143/PTP.28.870.

[8] Raymond Davis, Don S. Harmer, and Kenneth C. Hoffman. "Search for Neutrinos from the Sun". *Phys. Rev. Lett.* 20 (21 1968), pp. 1205–1209. DOI: 10.1103/PhysRevLett.20.1205. URL: https://link.aps.org/doi/10.1103/PhysRevLett.20.1205.

[9] S Turck-Chièze. "The Standard Solar Model and beyond". *Journal of Physics: Conference Series* 665.1 (Jan. 2016), p. 012078. DOI: 10.1088/1742-6596/665/1/012078. URL: https://dx.doi.org/10.1088/1742-6596/665/1/012078.

[10] Q. R. Ahmad et al. "Measurement of the Rate of $\nu_e + d \rightarrow p + p + e^-$ Interactions Produced by ^8B Solar Neutrinos at the Sudbury Neutrino Observatory". *Phys. Rev. Lett.* 87 (7 July 2001), p. 071301. DOI: 10.1103/PhysRevLett.87.071301. URL: https://link.aps.org/doi/10.1103/PhysRevLett.87.071301.

[11] Y. Fukuda et al. "Evidence for Oscillation of Atmospheric Neutrinos". *Phys. Rev. Lett.* 81 (8 1998), pp. 1562–1567. DOI: 10.1103/PhysRevLett.81.1562. URL: https://link.aps.org/doi/10.1103/PhysRevLett.81.1562.

[12] R. L. Workman et al. "Review of Particle Physics". *PTEP* 2022 (2022), p. 083C01. DOI: 10.1093/ptep/ptac097.

[13] L.J. Wen, J. Cao, and Y.F. Wang. "Reactor Neutrino Experiments: Present and Future". *Annual Review of Nuclear and Particle Science* 67.1 (2017), pp. 183–211. DOI: 10.1146/annurev-nucl-101916-123318. URL: https://doi.org/10.1146/annurev-nucl-101916-123318.

[14] Wikimedia Commons. *Standard Model of Elementary Particles*. 2019. URL: https://en.wikipedia.org/wiki/File:Standard_Model_of_Elementary_Particles.svg.

[15] Gerard 't Hooft. "The making of the standard model". *Nature* 448.7151 (July 2007), pp. 271–273. DOI: 10.1038/nature06074. URL: https://www.nature.com/articles/nature06074.

[16] Steven Weinberg. "A Model of Leptons". *Phys. Rev. Lett.* 19 (21 1967), pp. 1264–1266. DOI: 10.1103/PhysRevLett.19.1264. URL: https://link.aps.org/doi/10.1103/PhysRevLett.19.1264.

[17] G. Arnison et al. "Experimental observation of isolated large transverse energy electrons with associated missing energy at s=540GeV". *Physics Letters B* 122 (1 Feb. 1983), pp. 103–116. DOI: 10.1016/0370-2693(83)91177-2.

[18] M. Banner et al. "Observation of single isolated electrons of high transverse momentum in events with missing transverse energy at the CERN p collider". *Physics Letters B* 122 (5-6 Mar. 1983), pp. 476–485. DOI: 10.1016/0370-2693(83)91605-2.

[19] C. S. Wu, E. Ambler, R. W. Hayward, D. D. Hoppes, and R. P. Hudson. "Experimental Test of Parity Conservation in Beta Decay". *Phys. Rev.* 105 (4 1957), pp. 1413–1415. DOI: 10.1103/PhysRev.105.1413. URL: https://link.aps.org/doi/10.1103/PhysRev.105.1413.

[20] Patrick Janot and Stanisław Jadach. "Improved Bhabha cross section at LEP and the number of light neutrino species". *Phys. Lett. B* 803 (2020), p. 135319. DOI: 10.1016/j.physletb.2020.135319.

[21] Vernon Barger, Danny Marfatia, and Kerry Whisnant. *The Physics of Neutrinos*. Princeton: Princeton University Press, 2013. DOI: doi:10.1515/9781400845590. URL: https://doi.org/10.1515/9781400845590.

[22] Evgeny Akhmedov. *Quantum mechanics aspects and subtleties of neutrino oscillations*. 2019.

[23] Andrei D Sakharov. "Violation of CP invariance, C asymmetry, and baryon asymmetry of the universe". *Soviet Physics Uspekhi* 34.5 (May 1991), p. 392. DOI: 10.1070/PU1991v034n05ABEH002497. URL: https://dx.doi.org/10.1070/PU1991v034n05ABEH002497.

[24] M. et al. Tanabashi. "Review of Particle Physics". *Phys. Rev. D* 98 (3 2018), p. 030001. DOI: 10.1103/PhysRevD.98.030001. URL: https://link.aps.org/doi/10.1103/PhysRevD.98.030001.

[25] Claudio Giganti, Stéphane Lavignac, and Marco Zito. "Neutrino oscillations: the rise of the PMNS paradigm". *Prog. Part. Nucl. Phys.* 98 (2018), pp. 1–54. DOI: 10.1016/j.ppnp.2017.10.001.

[26] K. Abe et al. "Solar Neutrino Measurements in Super-Kamiokande-IV". *Phys. Rev. D* 94.5 (2016), p. 052010. DOI: 10.1103/PhysRevD.94.052010.

[27] A. Gando et al. "Reactor On-Off Antineutrino Measurement with KamLAND". *Phys. Rev. D* 88.3 (2013), p. 033001. DOI: 10.1103/PhysRevD.88.033001.

[28] Kai Zuber. *Neutrino Physics*. Boca Raton: Taylor & Francis, 2020. DOI: 10.1201/9781315195612.

[29] H. de Kerret et al. "Double Chooz $\theta 13$ measurement via total neutron capture detection". *Nature Physics* 16.5 (May 2020), pp. 558–564. DOI: 10.1038/s41567-020-0831-y. URL: https://www.nature.com/articles/s41567-020-0831-y.

[30] D. Adey et al. "Measurement of the Electron Antineutrino Oscillation with 1958 Days of Operation at Daya Bay". *Phys. Rev. Lett.* 121 (24 Dec. 2018), p. 241805. DOI: 10.1103/PhysRevLett.121.241805. URL: https://link.aps.org/doi/10.1103/PhysRevLett.121.241805.

[31] C. D. Shin et al. "Observation of reactor antineutrino disappearance using delayed neutron capture on hydrogen at RENO". *Journal of High Energy Physics* 2020.4 (Apr. 2020), p. 29. DOI: 10.1007/JHEP04(2020)029. URL: http://link.springer.com/10.1007/JHEP04(2020)029.

[32] S.M. Bilenky, C. Giunti, and W. Grimus. "Phenomenology of neutrino oscillations". *Progress in Particle and Nuclear Physics* 43 (Jan. 1999), pp. 1–86. DOI: 10.1016/s0146-6410(99)00092-7. URL: http://dx.doi.org/10.1016/S0146-6410(99)00092-7.

[33] Wikimedia Commons. *Neutrino Mass Heirachy*. 2020. URL: https://en.wikipedia.org/wiki/File:Hierfig.pdf.

[34] F. Englert and R. Brout. "Broken Symmetry and the Mass of Gauge Vector Mesons". *Phys. Rev. Lett.* 13 (9 Aug. 1964), pp. 321–323. DOI: 10.1103/PhysRevLett.13.321. URL: https://link.aps.org/doi/10.1103/PhysRevLett.13.321.

[35] P. W. Anderson. "Plasmons, Gauge Invariance, and Mass". *Phys. Rev.* 130 (1 1963), pp. 439–442. DOI: 10.1103/PhysRev.130.439. URL: https://link.aps.org/doi/10.1103/PhysRev.130.439.

[36] Peter W. Higgs. "Broken Symmetries and the Masses of Gauge Bosons". *Phys. Rev. Lett.* 13 (16 1964), pp. 508–509. DOI: 10.1103/PhysRevLett.13.508. URL: https://link.aps.org/doi/10.1103/PhysRevLett.13.508.

[37] G. Aad et al. "Observation of a new particle in the search for the Standard Model Higgs boson with the ATLAS detector at the LHC". *Physics Letters B* 716.1 (2012), pp. 1–29. DOI: https://doi.org/10.1016/j.physletb.2012.08.020. URL: https://www.sciencedirect.com/science/article/pii/S037026931200857X.

[38] S. Chatrchyan et al. "Observation of a new boson at a mass of 125 GeV with the CMS experiment at the LHC". *Physics Letters B* 716.1 (2012), pp. 30–61. DOI: https://doi.org/10.1016/j.physletb.2012.08.021. URL: https://www.sciencedirect.com/science/article/pii/S0370269312008581.

[39] Carlos Blanco, Dan Hooper, and Pedro Machado. "Constraining sterile neutrino interpretations of the LSND and MiniBooNE anomalies with coherent neutrino scattering experiments". *Phys. Rev. D* 101 (7 Apr. 2020), p. 075051. DOI: 10.1103/PhysRevD.101.075051. URL: https://link.aps.org/doi/10.1103/PhysRevD.101.075051.

[40] R. Abbasi et al. "Search for Unstable Sterile Neutrinos with the IceCube Neutrino Observatory". *Phys. Rev. Lett.* 129 (15 Oct. 2022), p. 151801. DOI: 10.1103/PhysRevLett.129.151801. URL: https://link.aps.org/doi/10.1103/PhysRevLett.129.151801.

[41] P. Adamson et al. "Search for Sterile Neutrinos in MINOS and MINOS+ Using a Two-Detector Fit". *Phys. Rev. Lett.* 122 (9 2019), p. 091803. DOI: 10.1103/PhysRevLett.122.091803. URL: https://link.aps.org/doi/10.1103/PhysRevLett.122.091803.

[42] Ettore Majorana. *Scientific Papers of Ettore Majorana*. Ed. by Luisa Cifarelli. Springer International Publishing, 2020. DOI: 10.1007/978-3-030-23509-3.

[43] Tsutomu Yanagida. "Horizontal Symmetry and Masses of Neutrinos". *Progress of Theoretical Physics* 64.3 (Sept. 1980), pp. 1103–1105. DOI: 10.1143/PTP.64.1103. URL: https://doi.org/10.1143/PTP.64.1103.

[44] Samoil M. Bilenky, Samoil M. Bilenky, and Carlo Giunti. "Neutrinoless Double-Beta Decay: a Probe of Physics Beyond the Standard Model". *arXiv: High Energy Physics - Phenomenology* (2014). URL: https://api.semanticscholar.org/CorpusID:53459820.

[45] Alessandro Strumia and Francesco Vissani. *Neutrino masses and mixings and...* 2010.

[46] M. Aker et al. "Direct neutrino-mass measurement with sub-electronvolt sensitivity". *Nature Phys.* 18.2 (2022), pp. 160–166. DOI: 10.1038/s41567-021-01463-1.

[47] Nathalie Palanque-Delabrouille et al. "Hints, neutrino bounds, and WDM constraints from SDSS DR14 Lyman-α and Planck full-survey data". *Journal of Cosmology and Astroparticle Physics* 2020.04 (Apr. 2020), p. 038. DOI: 10.1088/1475-7516/2020/04/038. URL: https://dx.doi.org/10.1088/1475-7516/2020/04/038.

[48] S. P. Mikheyev and A. Yu. Smirnov. "Resonance enhancement of oscillations in matter and solar neutrino spectroscopy". *Yadernaya Fizika* 42 (Jan. 1985), pp. 1441–1448.

[49] K. Abe et al. "Constraint on the matter/antimatter symmetry-violating phase in neutrino oscillations". *Nature* 580.7803 (2020). [Erratum: Nature 583, E16 (2020)], pp. 339–344. DOI: 10.1038/s41586-020-2177-0.

[50] M. A. Acero et al. "Improved measurement of neutrino oscillation parameters by the NOvA experiment". *Phys. Rev. D* 106.3 (2022), p. 032004. DOI: 10.1103/PhysRevD.106.032004.

[51] Luis Alvarez-Ruso, Y Hayato, and Joel Nieves. "Progress and open questions in the physics of neutrino cross sections". *New Journal of Physics* 16 (July 2014). DOI: 10.1088/1367-2630/16/7/075015.

[52] K. Abe et al. "The T2K experiment". *Nuclear Instruments and Methods in Physics Research Section A: Accelerators, Spectrometers, Detectors and Associated Equipment* 659.1 (2011), pp. 106–135. DOI: https://doi.org/10.1016/j.nima.2011.06.067.

[53] M. Friend. "J-PARC accelerator and neutrino beamline upgrade programme". 888 (2017), p. 012042. DOI: 10.1088/1742-6596/888/1/012042. URL: https://doi.org/10.1088%2F1742-6596%2F888%2F1%2F012042.

[54] T. Nakadaira et al. "T2K target". *AIP Conference Proceedings* 981 (Feb. 2008). DOI: 10.1063/1.2898964.

[55] K. Abe et al. "T2K neutrino flux prediction". *Phys. Rev. D* 87.1 (2013). [Addendum: Phys.Rev.D 87, 019902 (2013)], p. 012001. DOI: 10.1103/PhysRevD.87.012001.

[56] J. A. Formaggio and G. P. Zeller. "From eV to EeV: Neutrino cross sections across energy scales". *Rev. Mod. Phys.* 84 (3 Sept. 2012), pp. 1307–1341. DOI: 10.1103/RevModPhys.84.1307. URL: https://link.aps.org/doi/10.1103/RevModPhys.84.1307.

[57] K. Abe et al. "Measurements of the T2K neutrino beam properties using the INGRID on-axis near detector". *Nuclear Instruments and Methods in Physics Research A* 694 (2012), pp. 211–223. DOI: 10.1016/j.nima.2012.03.023.

[58] S. Assylbekov et al. "The T2K ND280 Off-Axis Pi-Zero Detector". *Nucl. Instrum. Meth.* A686 (2012), pp. 48–63. DOI: 10.1016/j.nima.2012.05.028.

[59] S. Fukuda et al. "The Super-Kamiokande detector". *Nuclear Instruments and Methods in Physics Research Section A: Accelerators, Spectrometers, Detectors and Associated Equipment* 501.2 (2003), pp. 418–462. DOI: https://doi.org/10.1016/S0168-9002(03)00425-X.

[60] Sacha E Kopp. "Accelerator neutrino beams". 439.3 (2007), pp. 40–42. DOI: 10.1016/j.physrep.2006.11.004.

[61] K. Abe et al. "Measurement of neutrino and antineutrino oscillations by the T2K experiment including a new additional sample of ν_e interactions at the far detector". *Phys. Rev. D* 96.9 (2017). [Erratum: Phys.Rev.D 98, 019902 (2018)], p. 092006. DOI: 10.1103/PhysRevD.96.092006.

[62] K. Abe et al. "Constraint on the matter–antimatter symmetry-violating phase in neutrino oscillations". *Nature* 580.7803 (2020), pp. 339–344. DOI: 10.1038/s41586-020-2177-0.

[63] K. Abe et al. "First measurement of the muon neutrino charged current single pion production cross section on water with the T2K near detector". *Physical Review D* 95.1 (Jan. 2017). DOI: 10.1103/physrevd.95.012010. URL: http://dx.doi.org/10.1103/PhysRevD.95.012010.

[64] K. Abe et al. "Measurement of the Inclusive Electron Neutrino Charged Current Cross Section on Carbon with the T2K Near Detector". *Phys. Rev. Lett.* 113 (24 Dec. 2014), p. 241803. DOI: 10.1103/PhysRevLett.113.241803. URL: https://link.aps.org/doi/10.1103/PhysRevLett.113.241803.

[65] K. Abe et al. "Measurement of the single π^0 production rate in neutral current neutrino interactions on water". *Phys. Rev. D* 97 (3 Feb. 2018), p. 032002. DOI: 10.1103/PhysRevD.97.032002. URL: https://link.aps.org/doi/10.1103/PhysRevD.97.032002.

[66] P.-A. Amaudruz et al. "The T2K fine-grained detectors". *Nuclear Instruments and Methods in Physics Research Section A: Accelerators, Spectrometers, Detectors and Associated Equipment* 696 (2012), pp. 1–31. DOI: https://doi.org/10.1016/j.nima.2012.08.020. URL: https://www.sciencedirect.com/science/article/pii/S0168900212008789.

[67] The University of Tokyo. Kamioka Observatory ICRR (Institute for Cosmic Ray Research). *Super-K Neutrino Event Display*. URL: https://t2k-experiment.org/photo/super-kamiokande/.

[68] E. Atkin et al. "MaCh3 Run 1-10 Analysis". *T2K Technical Note* 393 (2023). URL: https://t2k.org/docs/technotes/393.

[69] T2K Collaboration. *fiTQun Samples*. URL: https://t2k.org/docs/plots/055/t2k-sk-plots/tn355/sec4plots/images.

[70] Chenyuan Xu and. "Current status of SK-Gd project and EGADS". *Journal of Physics: Conference Series* 718 (2016), p. 062070. DOI: 10.1088/1742-6596/718/6/062070.

[71] Takaaki Mori. "Development of a gadolinium-doped water cherenkov detector for the observation of supernova relic neutrinos" (2015).

[72] Hiroyuki Sekiya. "Low energy neutrinos in Super-Kamiokande". *Journal of Physics: Conference Series* 718 (2016), p. 062052. DOI: 10.1088/1742-6596/718/6/062052.

[73] K. Abe et al. *Proposal for an Extended Run of T2K to* 20×10^{21} *POT*. 2016.

[74] K. Abe et al. *T2K ND280 Upgrade – Technical Design Report*. 2020.

[75] Hyper-Kamiokande Proto-Collaboration et al. *Hyper-Kamiokande Design Report*. 2018.

[76] Mark Scott. "An Intermediate Water Cherenkov Detector at J-PARC". *JPS Conf. Proc.* 12 (2016), p. 010039. DOI: 10.7566/JPSCP.12.010039.

[77] WCTE Collaboration. *Water Cherenkov Test Experiment Status Report (2022)*. Tech. rep. Geneva: CERN, 2022. URL: https://cds.cern.ch/record/2810964.

[78] Kalpana Singh, Pierre Gorel, Aksel Hallin, Carsten Krauss, and Zachary Petriw. "Underwater Photometry System of the SNO+ Experiment". *Journal of Physics: Conference Series* 1342 (2020), p. 12130. DOI: 10.1088/1742-6596/1342/1/012130. URL: https://doi.org/10.1088%7B%5C%%7D2F1742-6596%7B%5C%%7D2F1342%7B%5C%%7D2F1%7B%5C%%7D2F012130.

[79] Simon Haykin. *Neural Networks: A Comprehensive Foundation*. 1st. USA: Prentice Hall PTR, 1994.

[80] Jonathan Long, Evan Shelhamer, and Trevor Darrell. *Fully Convolutional Networks for Semantic Segmentation*. 2015.

[81] David E. Rumelhart, Geoffrey E. Hinton, and Ronald J. Williams. "Learning representations by back-propagating errors". *Nature* 323.6088 (Oct. 1986), pp. 533–536. DOI: 10.1038/323533a0. URL: https://www.nature.com/articles/323533a0.

[82] Vijay Badrinarayanan, Alex Kendall, and Roberto Cipolla. *SegNet: A Deep Convolutional Encoder-Decoder Architecture for Image Segmentation*. 2016.

[83] Irem Ulku and Erdem Akagündüz. "A Survey on Deep Learning-based Architectures for Semantic Segmentation on 2D Images". *Applied Artificial Intelligence* 36.1 (Feb. 2022). DOI: 10.1080/08839514.2022.2032924. URL: http://dx.doi.org/10.1080/08839514.2022.2032924.

[84] Tomasz Szandała. "Review and Comparison of Commonly Used Activation Functions for Deep Neural Networks". *Bio-inspired Neurocomputing*. Ed. by Akash Kumar Bhoi, Pradeep Kumar Mallick, Chuan-Ming Liu, and Valentina E. Balas. Singapore: Springer Singapore, 2021, pp. 203–224. DOI: 10.1007/978-981-15-5495-7_11. URL: https://doi.org/10.1007/978-981-15-5495-7_11.

[85] Ian Goodfellow, Yoshua Bengio, and Aaron Courville. *Deep Learning*. http://www.deeplearningbook.org. MIT Press, 2016.

[86] Olaf Ronneberger, Philipp Fischer, and Thomas Brox. "U-Net: Convolutional Networks for Biomedical Image Segmentation". *arXiv e-prints*, arXiv:1505.04597 (2015), arXiv:1505.04597.

[87] K. Abe et al. "Calibration of the Super-Kamiokande Detector". *Nucl. Instrum. Meth.* A737 (2014), pp. 253–272. DOI: 10.1016/j.nima.2013.11.081.

[88] Richard O. Duda and Peter E. Hart. "Use of the Hough Transformation to Detect Lines and Curves in Pictures". *Commun. ACM* 15.1 (Jan. 1972), pp. 11–15. DOI: 10.1145/361237.361242. URL: https://doi.org/10.1145/361237.361242.

[89] Richard Hartley and Andrew Zisserman. "Multiple View Geometry in Computer Vision". 2nd ed. Cambridge University Press, 2004. Chap. 18.1.

[90] J. Imber et al. "T2K-SK Systematic Error Summary for the 2017 Oscillation Analysis". *T2K Technical Note* 326 (2017). URL: https://t2k.org/docs/technotes/326.

[91] Lukas Berns et al. "Flux Prediction and Uncertainty with NA61/SHINE 2010 Replica Target Measurements". *T2K Technical Note* 401 (2022). URL: https://t2k.org/docs/technotes/401.

[92] Y. Hayato, S. Cao, and V. Nguyen. "The NEUT Neutrino Monte Carlo Generator: Physics and User Manual". *T2K Technical Note* 351 (2018). URL: https://t2k.org/docs/technotes/351.

[93] S. Berkman et al. "fiTQun: A New Reconstruction Algorithm for Super-K". *T2K Technical Note* 146 (2013). URL: https://t2k.org/docs/technotes/146.

[94] S. Berkman. "ν_μ CC1π^+ Events Produced in the T2K Beam at Super-Kamiokande". *Thesis* (2018). URL: https://t2k.org/docs/thesis/092.

[95] D. Barrow L. Mohan Y. Nakajima M. Reh C. Vilela J. Xia R. Wendell. "Super-Kamiokande Data Quality, MC, and Systematics in Run 10". *T2K Technical Note* 399 (2020). URL: https://t2k.org/docs/technotes/399.

[96] A. A. Aguilar-Arevalo et al. "Measurement of ν_μ and $\overline{\nu}_\mu$ induced neutral current single π^0 production cross sections on mineral oil at $E_\nu \sim \mathcal{O}$ (1 GeV)". *Phys. Rev. D* 81 (1 Jan. 2010), p. 013005. DOI: 10.1103/PhysRevD.81.013005. URL: https://link.aps.org/doi/10.1103/PhysRevD.81.013005.

[97] S. Nakayama et al. "Measurement of single π^0 production in neutral current neutrino interactions with water by a 1.3 GeV wide band muon neutrino beam". *Physics Letters B* 619.3 (2005), pp. 255–262. DOI: https://doi.org/10.1016/j.physletb.2005.05.044. URL: https://www.sciencedirect.com/science/article/pii/S0370269305007161.

[98] P. Abratenko et al. "Search for an anomalous excess of inclusive charged-current ν_e interactions in the MicroBooNE experiment using Wire-Cell reconstruction". *Phys. Rev. D* 105 (11 June 2022), p. 112005. DOI: 10.1103/PhysRevD.105.112005. URL: https://link.aps.org/doi/10.1103/PhysRevD.105.112005.

[99] Galin Jones and Qian Qin. "Markov Chain Monte Carlo in Practice". *Annual Review of Statistics and Its Application* 9 (Mar. 2022). DOI: 10.1146/annurev-statistics-040220-090158.

[100] Berns L. Bronner C. Guigue M. Kasetti S. Quilain B. "Five Sample Joint Oscillation Analysis with T2K Run1–10 Data". *T2K Technical Note* 397 (2021). URL: https://t2k.org/docs/technotes/399.

[101] C. Andreopoulosa et al. "T2K Neutrino and Anti-Neutrino 3-Flavour Joint Analysis of Run 1-10 data sets". *T2K Technical Note* 394 (2021). URL: https://t2k.org/docs/technotes/394.

[102] Nicholas Metropolis, Arianna W. Rosenbluth, Marshall N. Rosenbluth, Augusta H. Teller, and Edward Teller. "Equation of State Calculations by Fast Computing Machines". *The Journal of Chemical Physics* 21.6 (Dec. 2004), pp. 1087–1092. DOI: 10.1063/1.1699114. URL: https://doi.org/10.1063/1.1699114.

[103] Steve Brooks, Andrew Gelman, Galin Jones, and Xiao-Li Meng, eds. *Handbook of Markov Chain Monte Carlo*. Chapman and Hall/CRC, May 2011. DOI: 10.1201/b10905. URL: https://www.taylorfrancis.com/books/9781420079425.

[104] D. Barrow et al. "SK atmospheric T2K beam joint fit technical note, MaCh3 details". *T2K Technical Note* 426 (2022). URL: https://t2k.org/docs/technotes/426.

[105] E. Richard et al. "Measurements of the atmospheric neutrino flux by Super-Kamiokande: Energy spectra, geomagnetic effects, and solar modulation". *Phys. Rev. D* 94 (5 Sept. 2016), p. 052001. DOI: 10.1103/PhysRevD.94.052001. URL: https://link.aps.org/doi/10.1103/PhysRevD.94.052001.

[106] K. Abe et al. "Atmospheric neutrino oscillation analysis with external constraints in Super-Kamiokande I-IV". *Phys. Rev. D* 97 (7 Apr. 2018), p. 072001. DOI: 10.1103/PhysRevD.97.072001. URL: https://link.aps.org/doi/10.1103/PhysRevD.97.072001.

[107] K. Okumura. "π^0 background study using hybrid π^0 sample at Super-K". *T2K Technical Note* 29 (2011). URL: https://t2k.org/docs/technotes/029.

[108] S.M. Lakshmi, Y. Nakajima, M. Reh, C. Vilela1, and R. Wendell. "Super-Kamiokande detector systematic uncertainty including the multi-ring $1\mu1\pi^+$ sample". *T2K Technical Note* 448 (2022). URL: https://t2k.org/docs/technotes/448.

[109] P.A. Zyla et al. "Review of Particle Physics". *PTEP* 2020.8 (2020). and 2021 update, p. 083C01. DOI: 10.1093/ptep/ptaa104.

[110] T. Doyle et al. "Constraining the flux and cross section models for the 2021 oscillation analysis using ND280 data". *T2K Technical Note* 423 (2023). URL: https://t2k.org/docs/technotes/423.

[111] K. Abe et al. "T2K neutrino flux prediction". *Phys. Rev. D* 87 (1 Jan. 2013), p. 012001. DOI: 10.1103/PhysRevD.87.012001. URL: https://link.aps.org/doi/10.1103/PhysRevD.87.012001.

[112] N Abgrall et al. "NA61/SHINE facility at the CERN SPS: beams and detector system". *Journal of Instrumentation* 9.06 (June 2014), P06005. DOI: 10.1088/1748-0221/9/06/P06005. URL: https://dx.doi.org/10.1088/1748-0221/9/06/P06005.

[113] Yoshinari Hayato and Luke Pickering. "The NEUT neutrino interaction simulation program library". *The European Physical Journal Special Topics* 230 (2021), pp. 4469–4481. URL: https://doi.org/10.1140/epjs/s11734-021-00287-7.

[114] O. Benhar, A. Fabrocini, S. Fantoni, and I. Sick. "Spectral function of finite nuclei and scattering of GeV electrons". *Nuclear Physics A* 579.3 (1994), pp. 493–517. DOI: https://doi.org/10.1016/0375-9474(94)90920-2. URL: https://www.sciencedirect.com/science/article/pii/0375947494909202.

[115] Dieter Rein and Lalit M Sehgal. "Neutrino-excitation of baryon resonances and single pion production". *Annals of Physics* 133.1 (1981), pp. 79–153. DOI: https://doi.org/10.1016/0003-4916(81)90242-6. URL: https://www.sciencedirect.com/science/article/pii/0003491681902426.

[116] Krzysztof M. Graczyk and Jan T. Sobczyk. "Form factors in the quark resonance model". *Phys. Rev. D* 77 (5 Mar. 2008), p. 053001. DOI: 10.1103/PhysRevD.77.053001. URL: https://link.aps.org/doi/10.1103/PhysRevD.77.053001.

[117] S. Bolognesi et al. "NIWG model and uncertainties for 2017 oscillation analysis". *T2K Technical Note* 315 (2017). URL: https://t2k.org/docs/technotes/315.

[118] L. Munteanu et al. "Constraining the Flux and Cross Section Models with Data from ND280 using FGD1 and FGD2 for the 2020 Oscillation Analysis". *T2K Technical Note* 395 (2023). URL: https://t2k.org/docs/technotes/395.

[119] S. Bienstock, A. Kaboth, M. Scott, and Clarence Wret. "Constraining the Flux and Cross Section Models with Data from the ND280 Detector using FGD1 and FGD2 for the 2017 Joint Oscillation Analysis". *T2K Technical Note* 324 (2017). URL: https://t2k.org/docs/technotes/324.

[120] K. Abe et al. "Measurements of neutrino oscillation parameters from the T2K experiment using 3.6×10^{21} protons on target". *The European Physical Journal C* 83.9 (2023). DOI: 10.1140/epjc/s10052-023-11819-x. URL: http://dx.doi.org/10.1140/epjc/s10052-023-11819-x.

Appendix A

Appendix 1

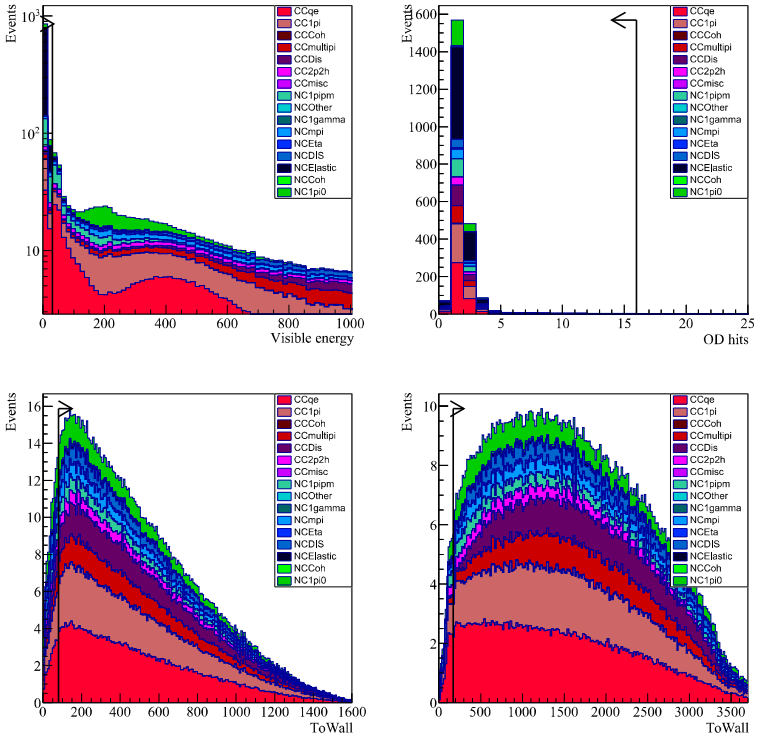


Figure A.1: Plots of FCFV cuts for FHC events in runs 1-10.

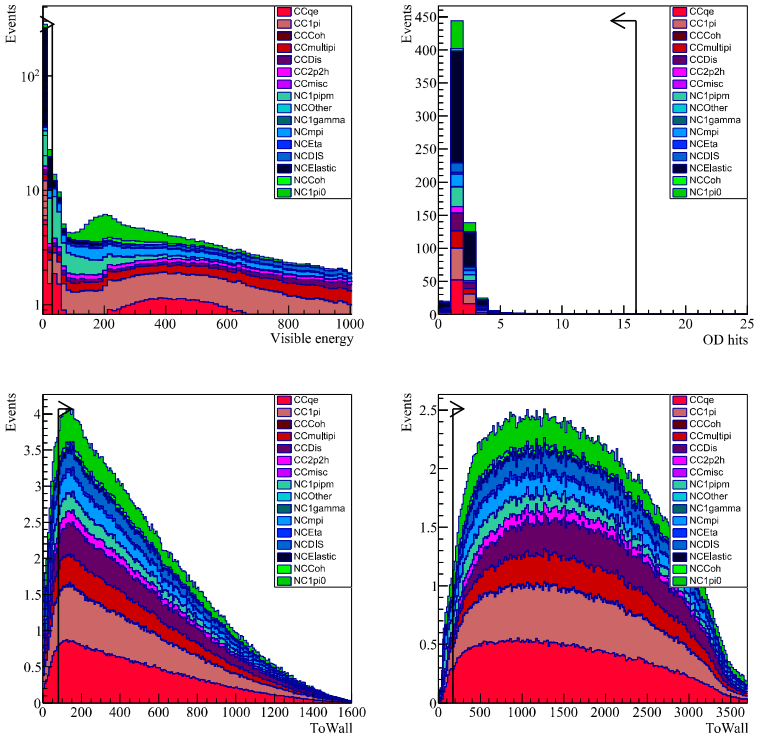


Figure A.2: Plots of FCFV cuts for RHC events in runs 5-9.

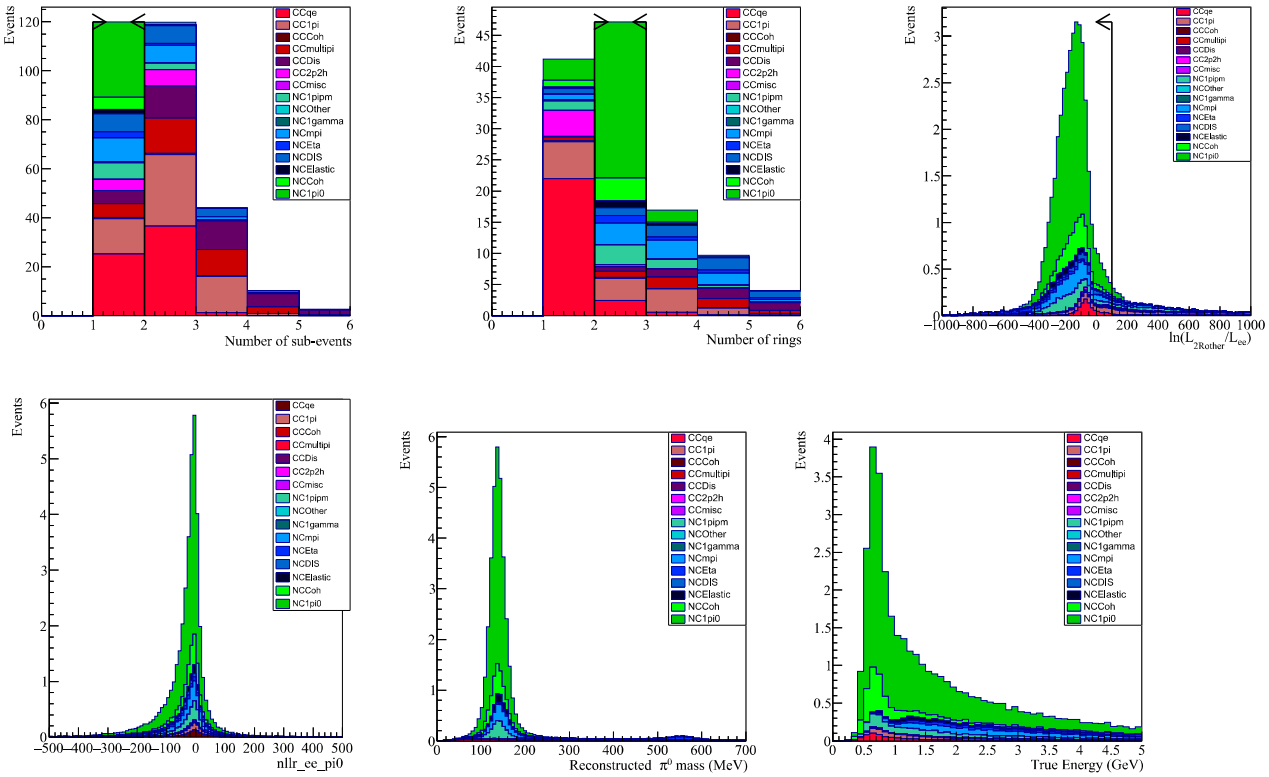


Figure A.3: RHC 2RNCπ^0 cut by cut and summary plots.

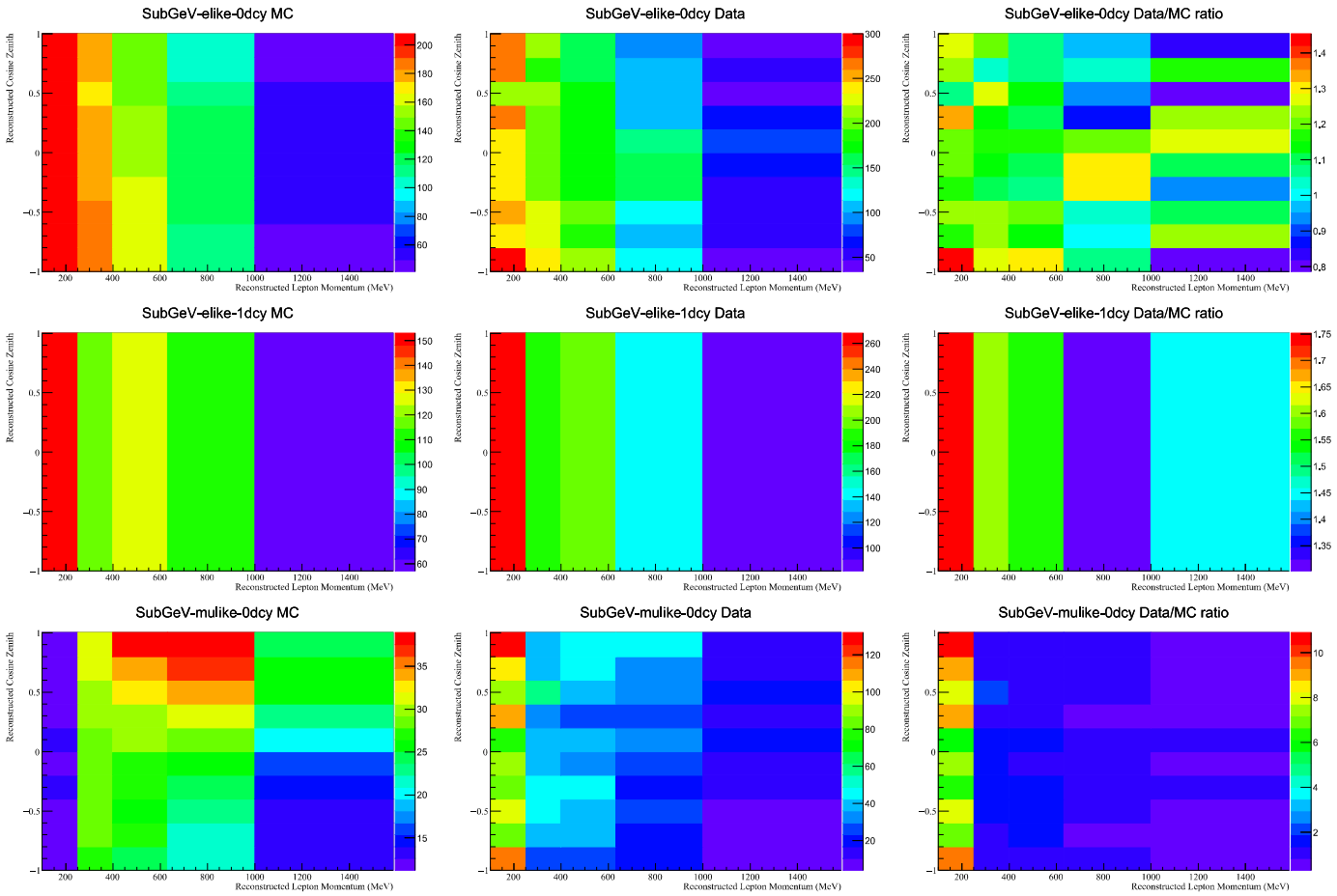


Figure A.4: SubGeV sample nominal MC, data, and data/MC ratio used for atmospheric neutrino data fit.

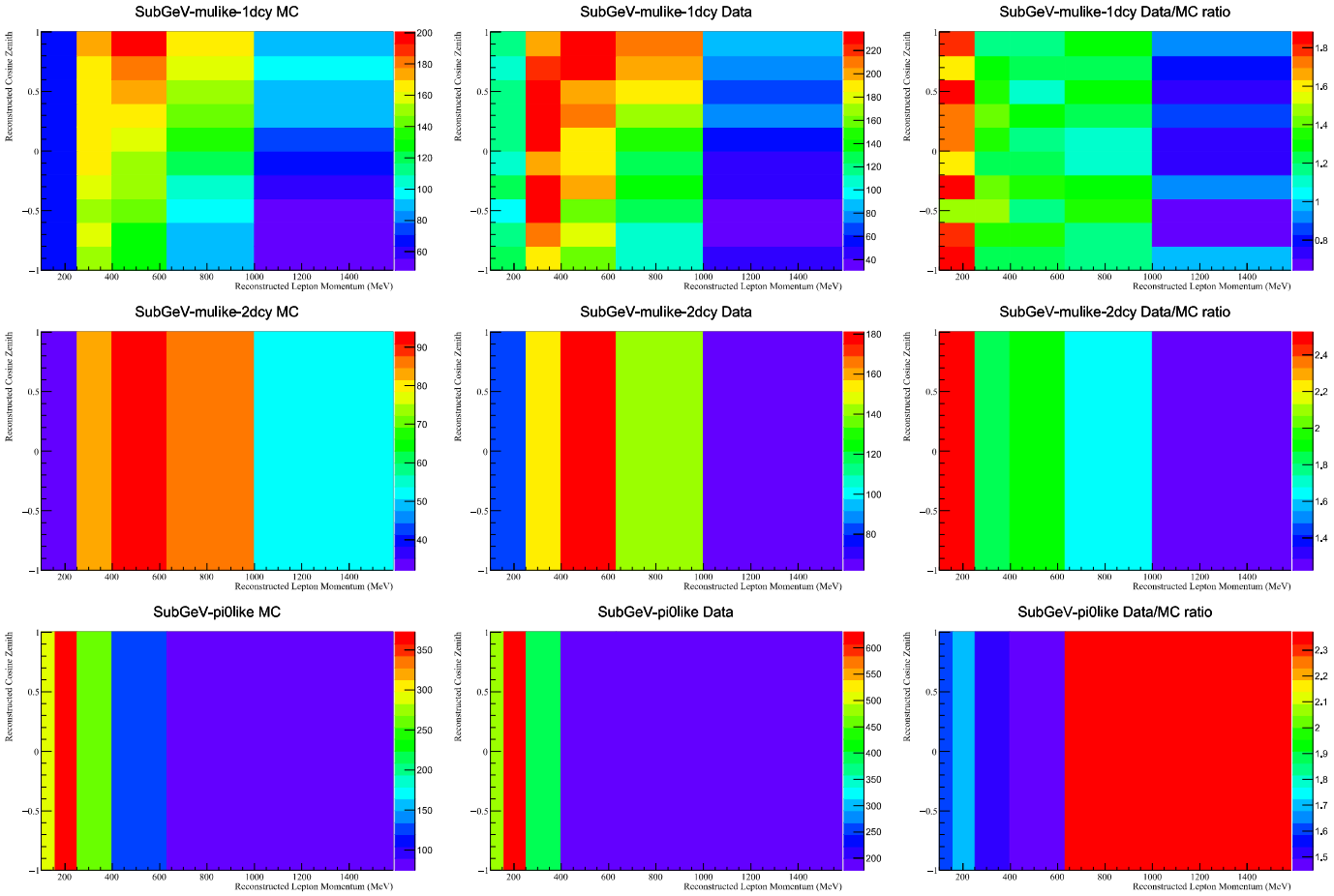


Figure A.5: SubGeV sample nominal MC, data, and data/MC ratio used for atmospheric neutrino data fit.

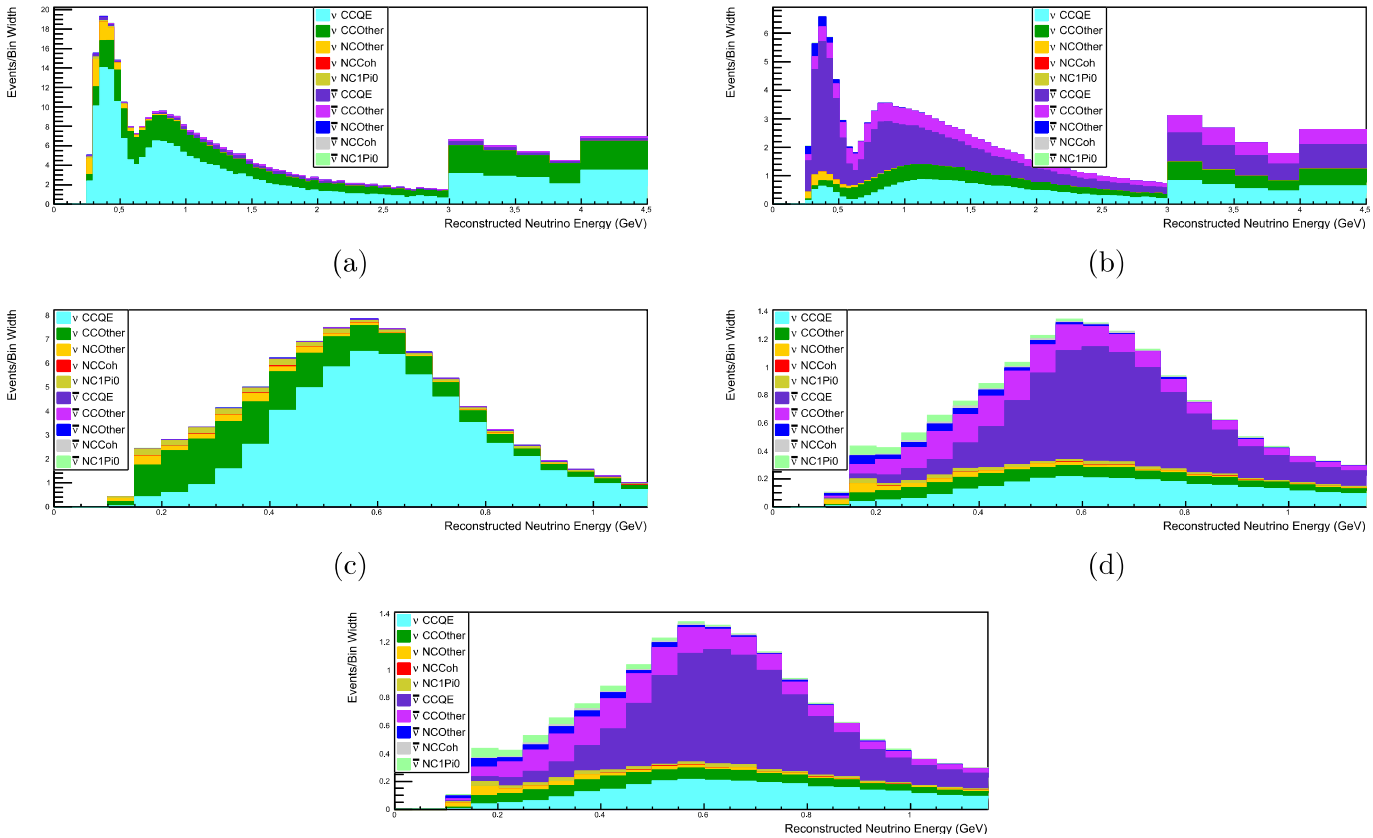
Table A.1: Binning by reconstructed neutrino energy and true interaction mode. Osc. is for oscillated ν_e events, Int. is intrinsic ν_e events.

Sample	Topology	Erec mass range	FHC Bin	Nominal	RHC Bin	Nominal
1Re	Osc. ν_e	0-350	0	9.36	18	0.885
		350-800	1	55.49	19	7.30
		800-1250	2	11.38	20	2.23
	ν_μ	0-350	3	0.076	21	0.021
		350-800	4	0.288	22	0.099
		800-1250	5	0.058	23	0.023
	Int. ν_e	0-350	6	1.41	24	0.396
		350-800	7	6.25	25	1.92
		800-1250	8	4.03	26	1.51
	NC	0-300	9	2.04	27	0.648
		300-800	10	2.46	28	0.741
		800-1250	11	0.500	29	0.201
1Rμ	ν_μ CCQE	0-400	12	30.1	30	10.8
		400-1100	13	125.7	31	36.8
		>1100	14	123.6	32	61.2
	ν_μ CC non-QE	-	15	56.9	33	24.2
	ν_e	-	16	0.122	34	0.012
	NC	-	17	8.88	35	2.85
1Re1dcye	Osc. ν_e	350-800	36	4.78	-	-
		800-1250	37	2.35	-	-
	ν_μ	350-800	38	0.107	-	-
		800-1250	39	0.072	-	-
	Int. ν_e	350-800	40	0.465	-	-
		800-1250	41	0.698	-	-
	NC	350-800	42	0.236	-	-
		800-1250	43	0.100	-	-

Appendix B

Appendix 2 - Additional OA fit plots

B.1 Super-K and ND280 samples

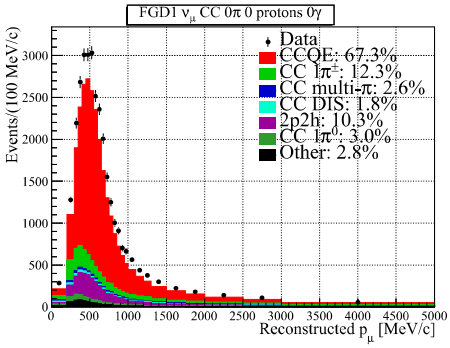


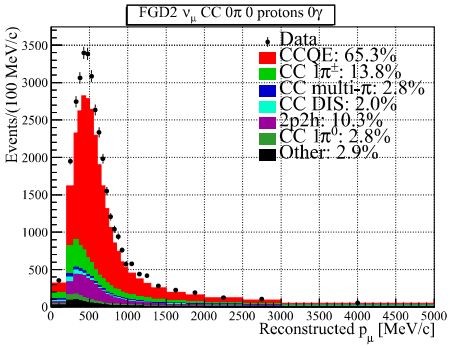
(a) (b)

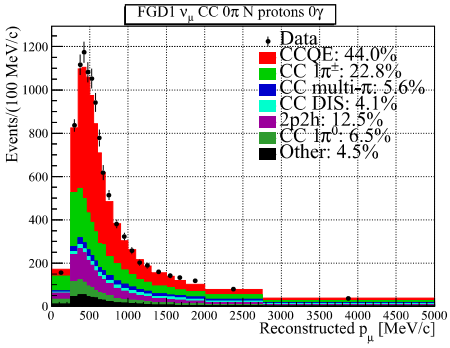
(c) (d)

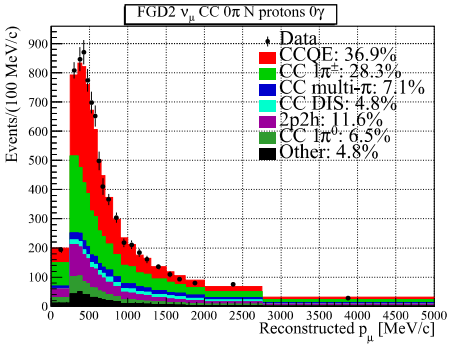
(e)

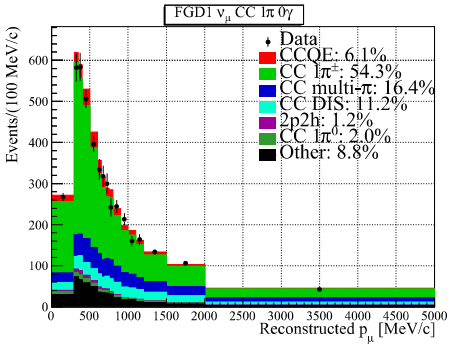
Figure B.1: Nominal **(a)**: FHC 1Rμ, **(b)**: RHC 1Rμ **(c)**: FHC 1Re, , **(d)**: RHC 1Re, and **(e)**:1RCC1π sample MC distributions used in fits.

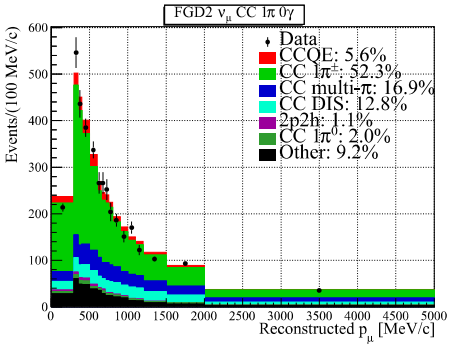


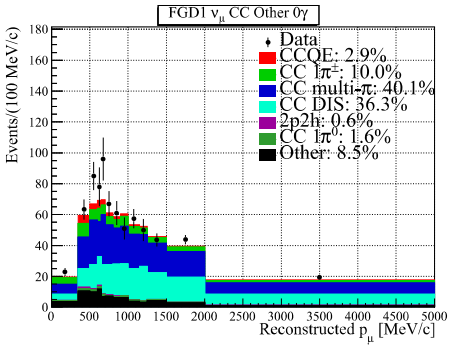


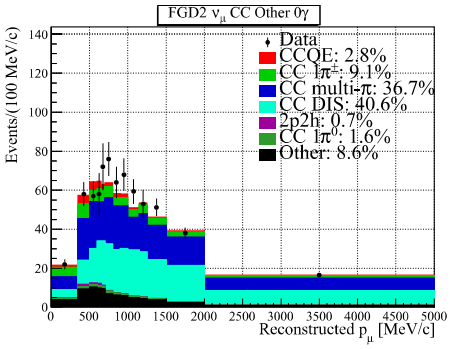


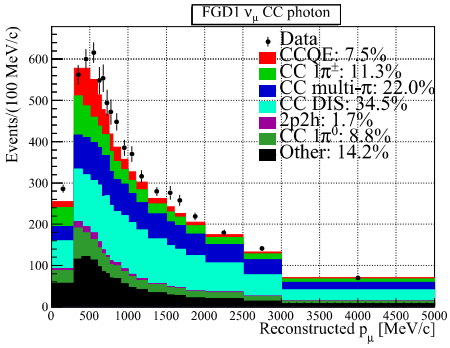


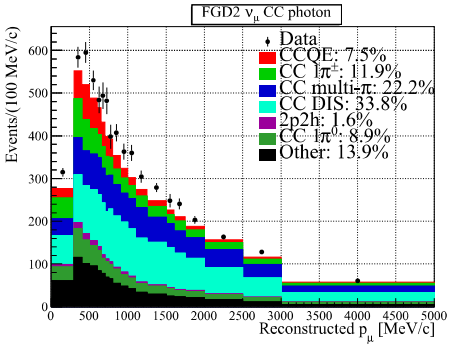




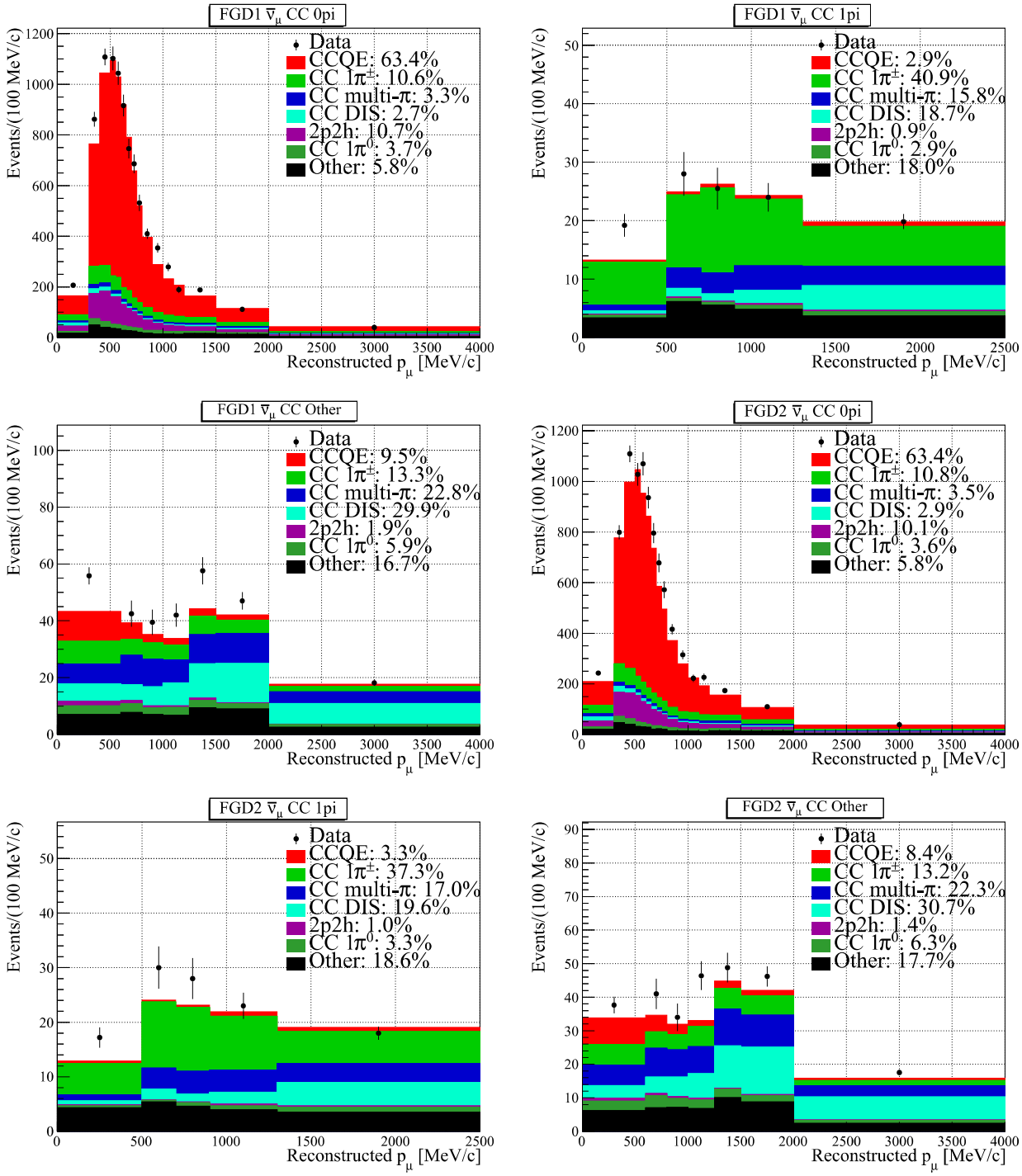




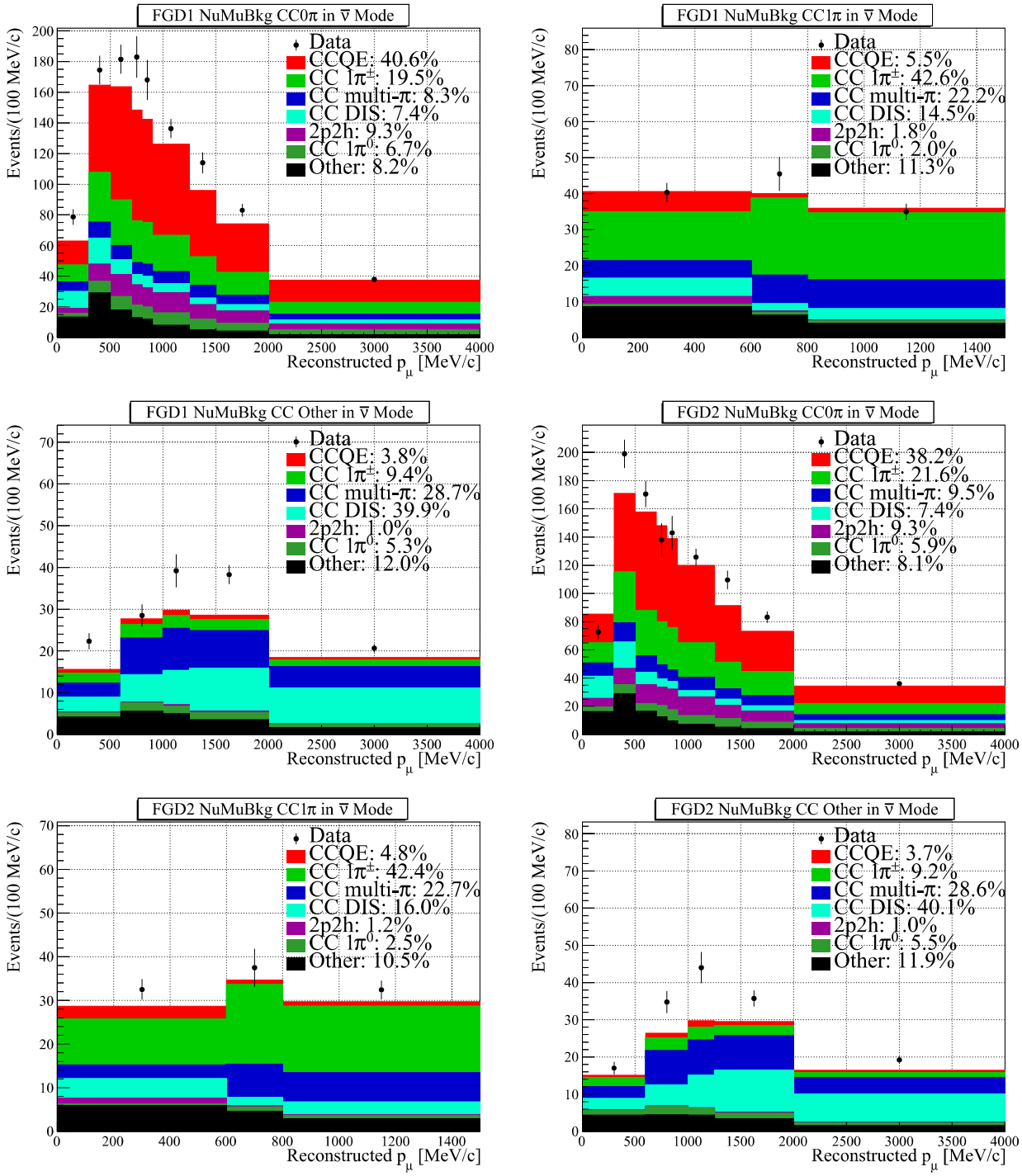




ND280 FHC samples for FGD1 and FGD2.

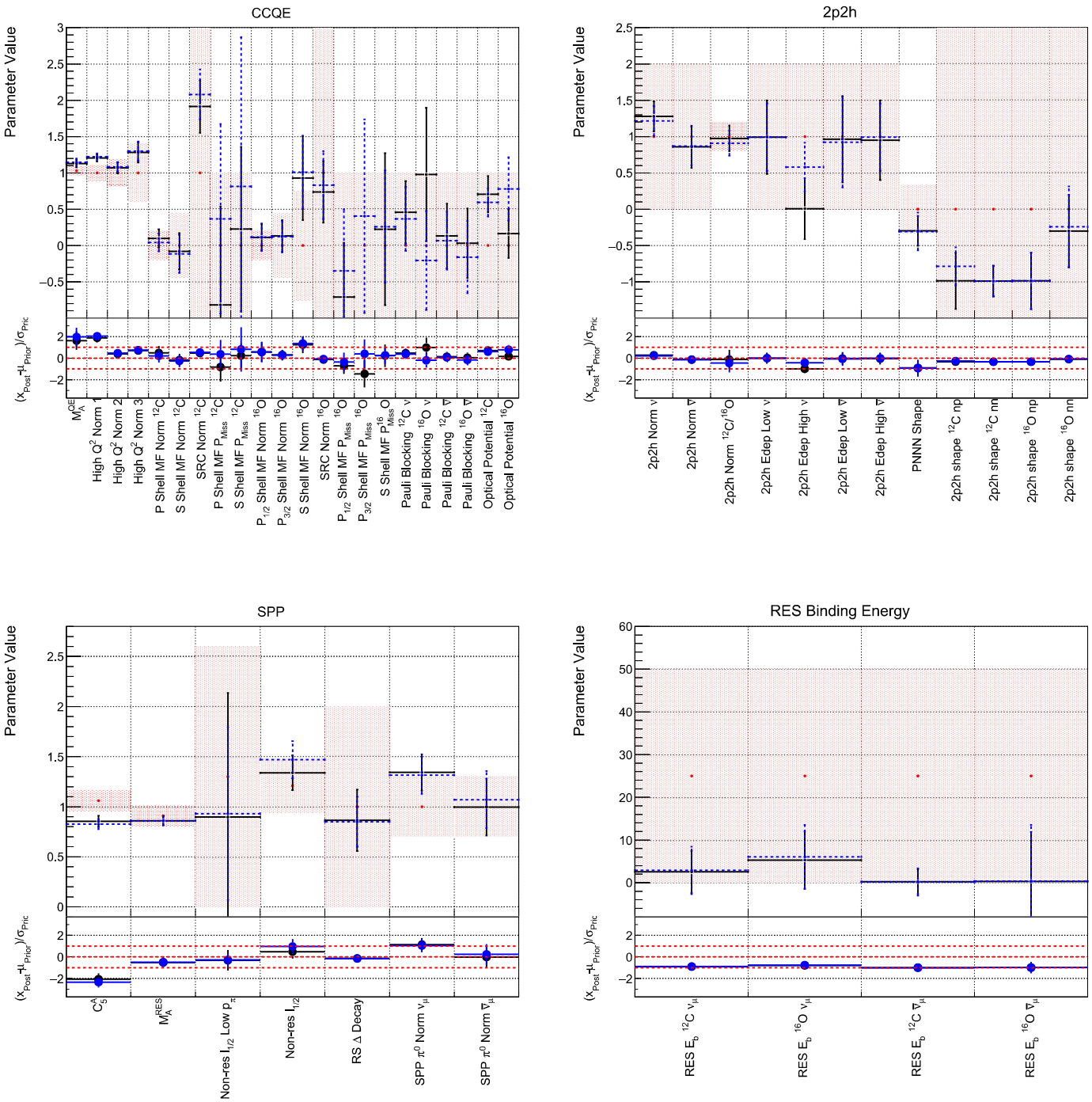


ND280 RHC ν samples for FGD1 and FGD2.

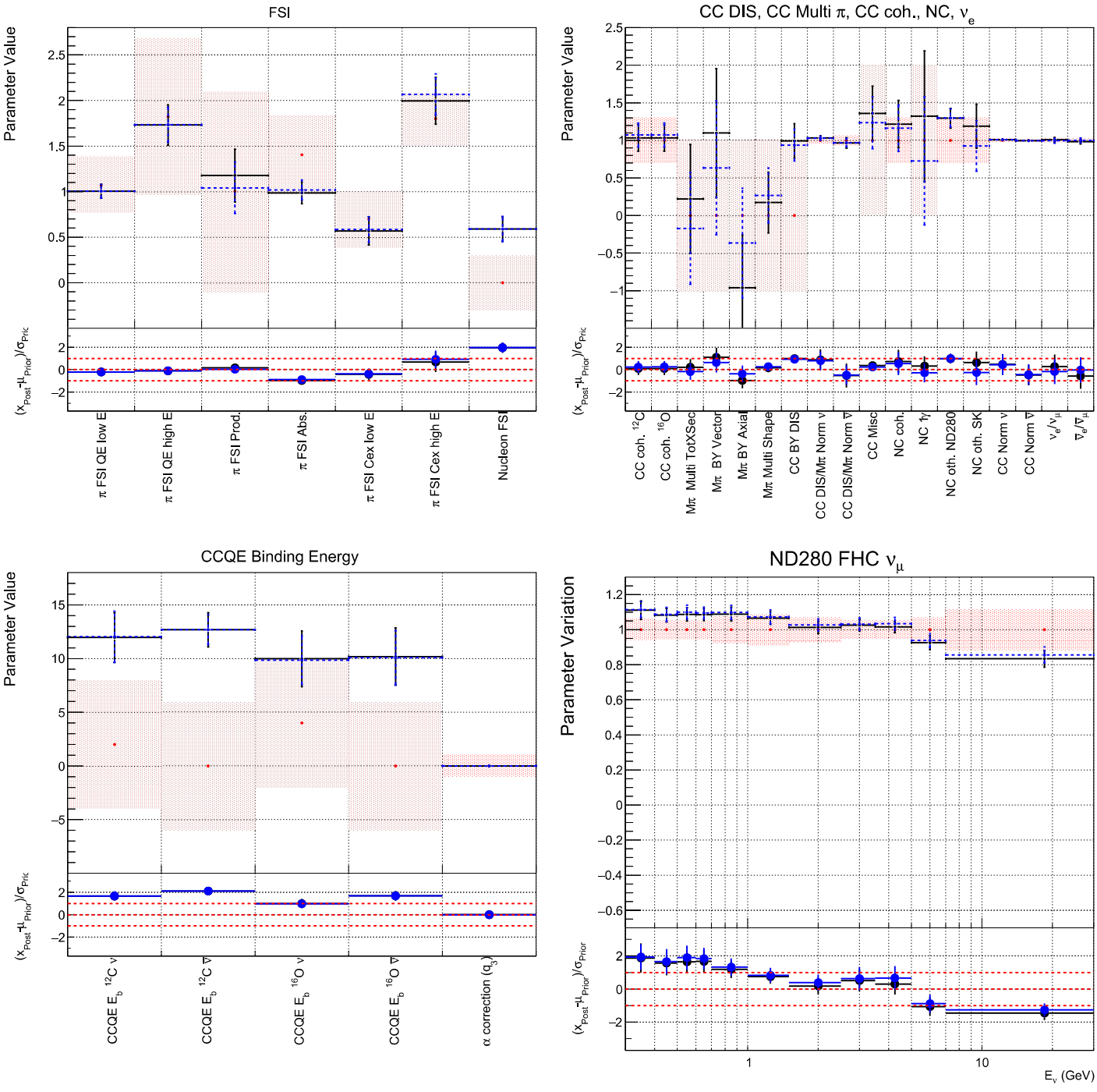


ND280 RHC $\bar{\nu}$ samples for FGD1 and FGD2.

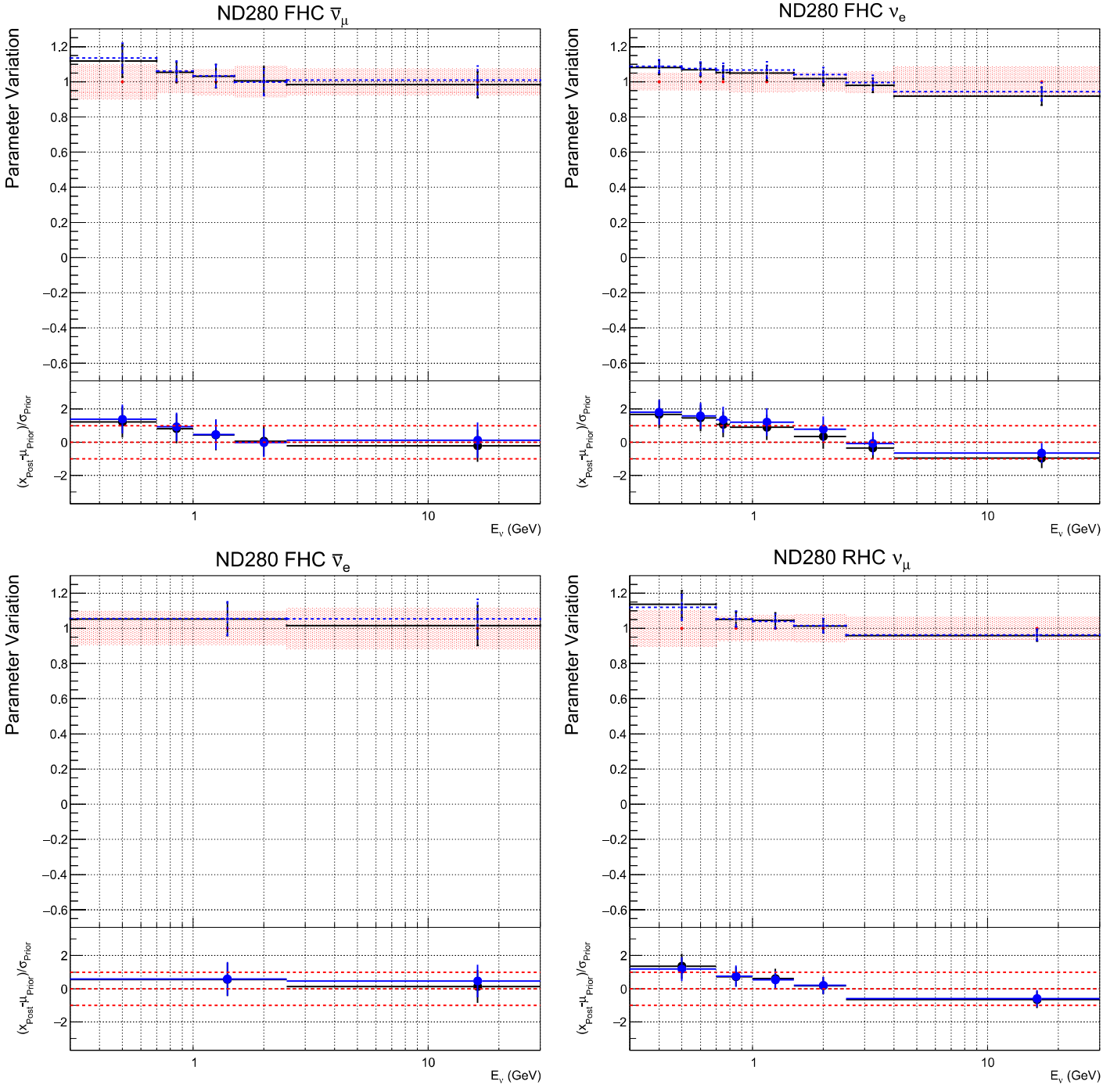
B.2 Additional Posterior Predictions



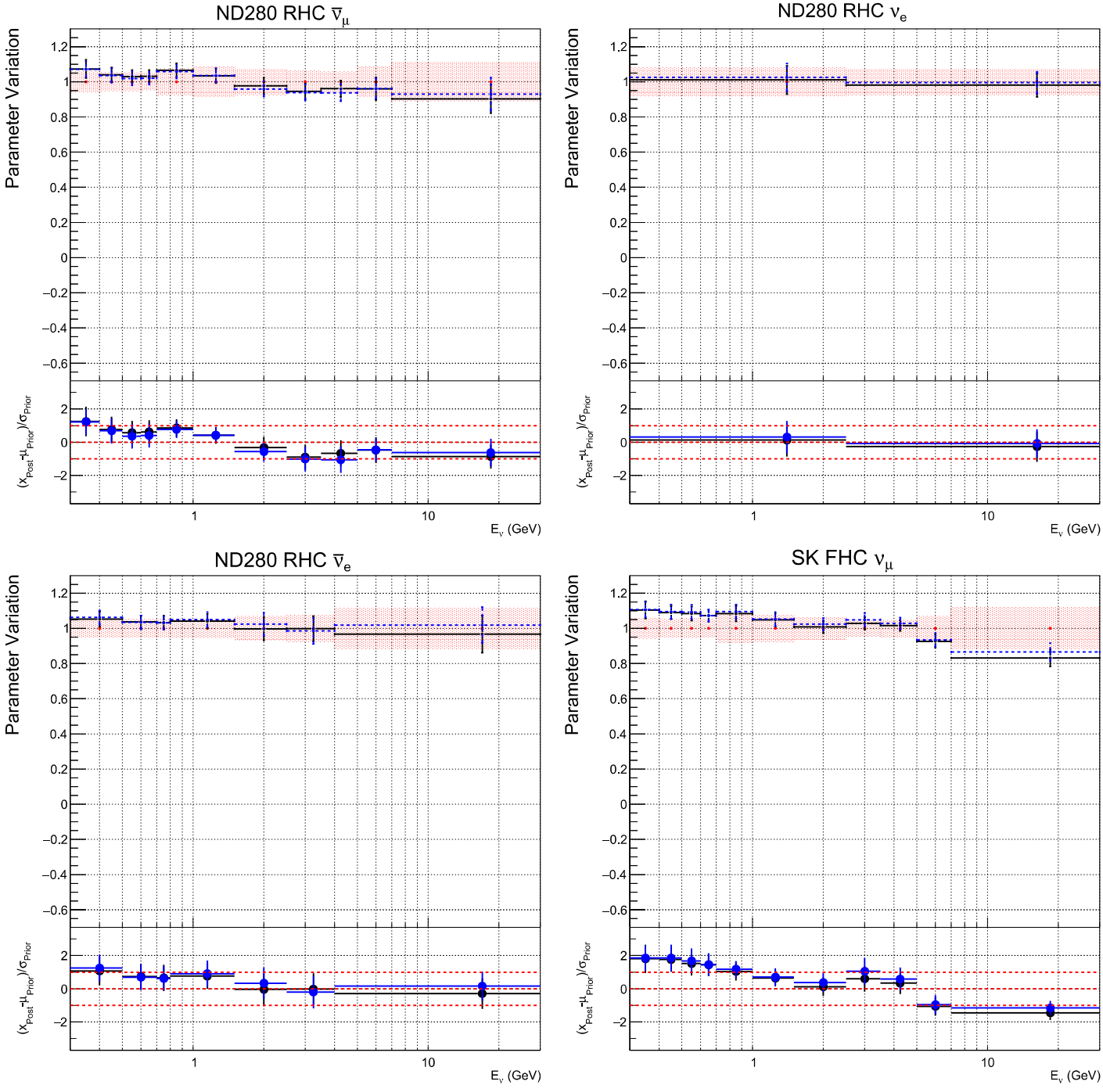
Cross section and flux parameters. (▨): prior value and error, (- - - -): OA21 official samples post-fit, (——): OA21 with NCπ^0 samples.



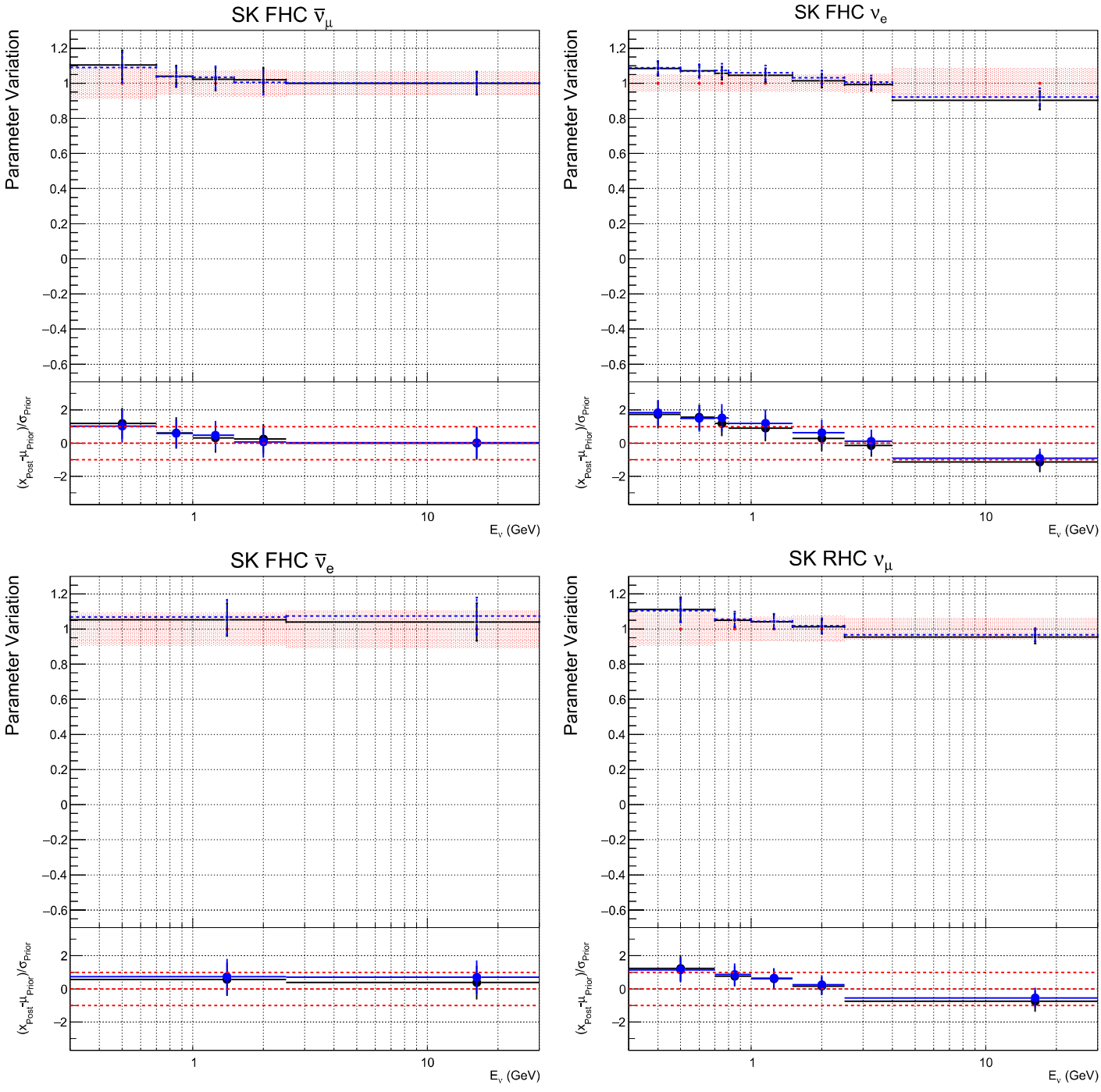
Cross section and flux parameters. (▨): prior value and error, (- - - -): OA21 official samples post-fit, (——): OA21 with NCπ^0 samples.



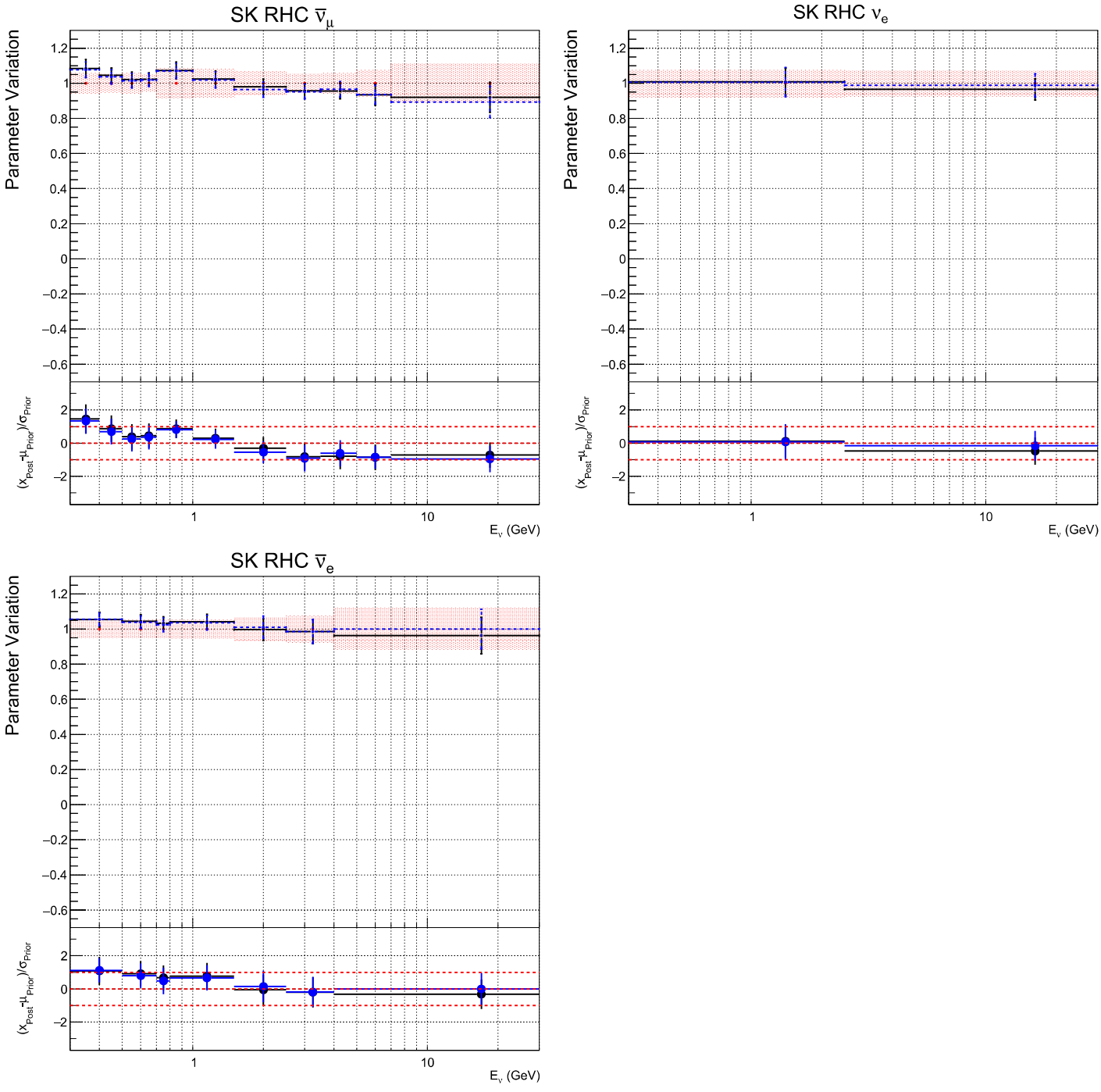
Cross section and flux parameters. (▨): prior value and error, (- - - -): OA21 official samples post-fit, (——): OA21 with NCπ^0 samples.



Cross section and flux parameters. (▨): prior value and error, (- - - -): OA21 official samples post-fit, (——): OA21 with NCπ^0 samples.



Cross section and flux parameters. (▨): prior value and error, (- - - -): OA21 official samples post-fit, (——): OA21 with NCπ^0 samples.



Cross section and flux parameters. (▨): prior value and error, (- - - -): OA21 official samples post-fit, (——): OA21 with NCπ^0 samples.

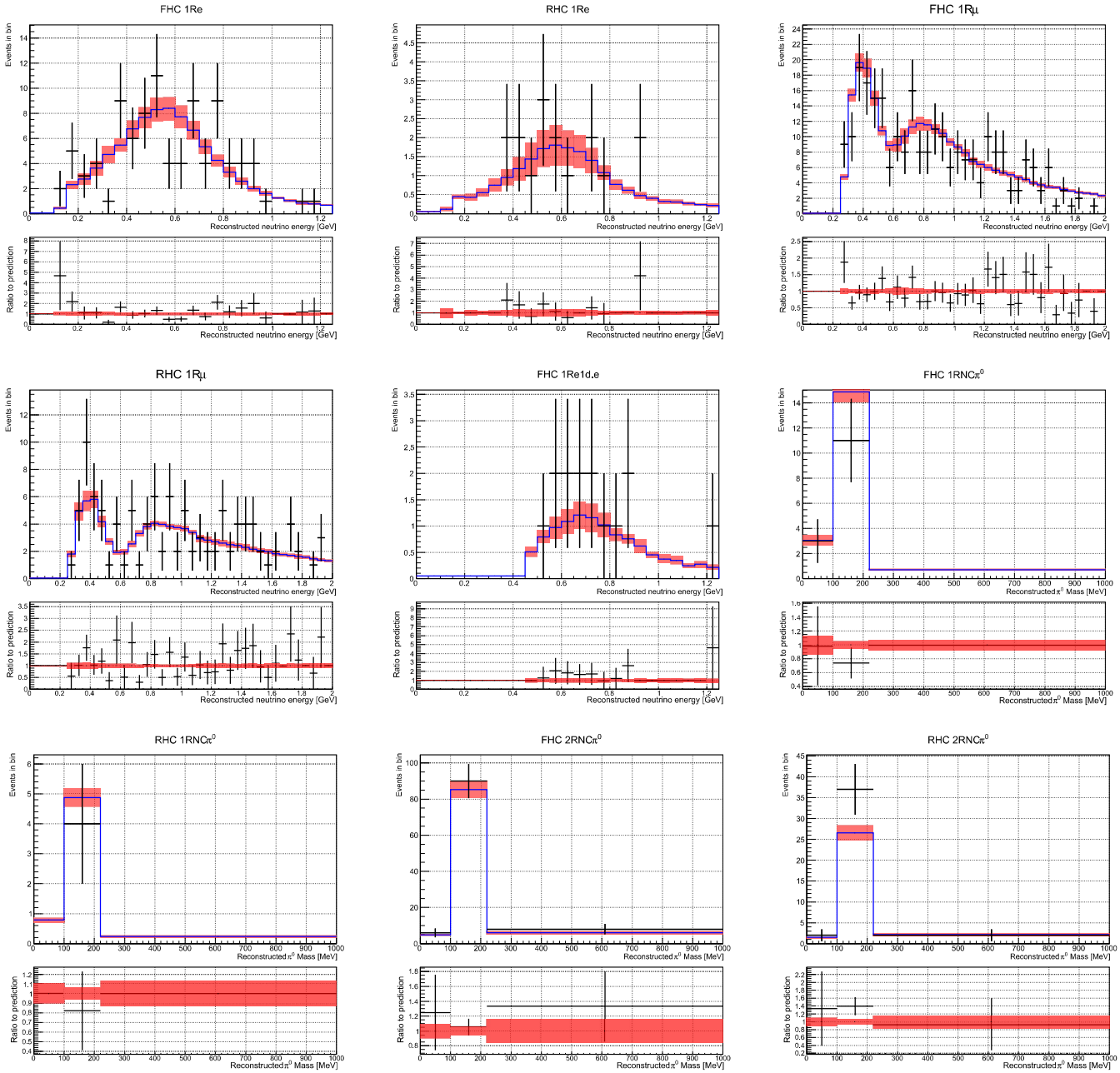


Figure B.2: Posterior predictions for the official T2K samples from the final data fit with NCπ^0 samples without RC.

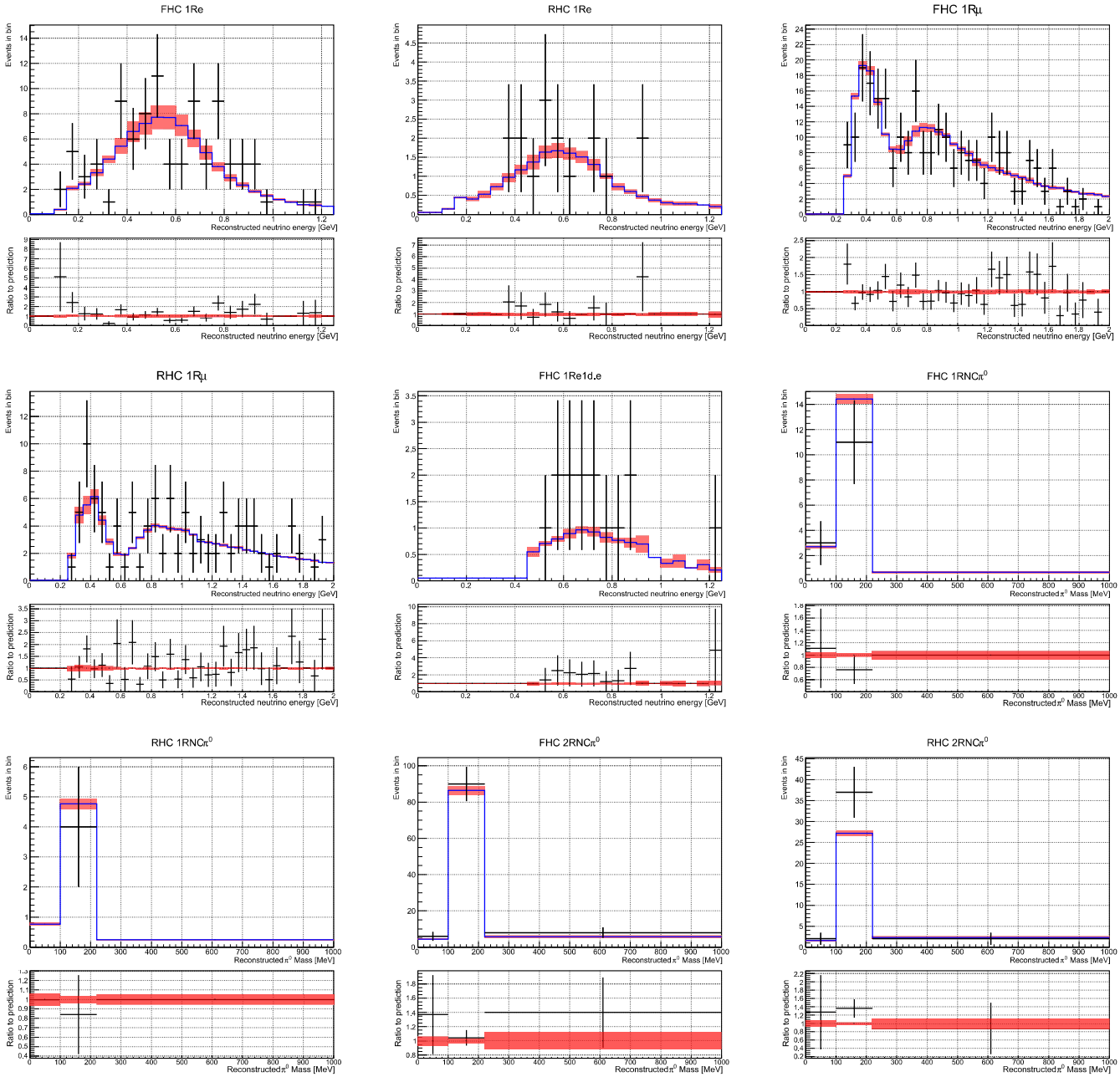


Figure B.3: Posterior predictions for the official T2K samples from the final data fit with NCπ^0 samples with RC.

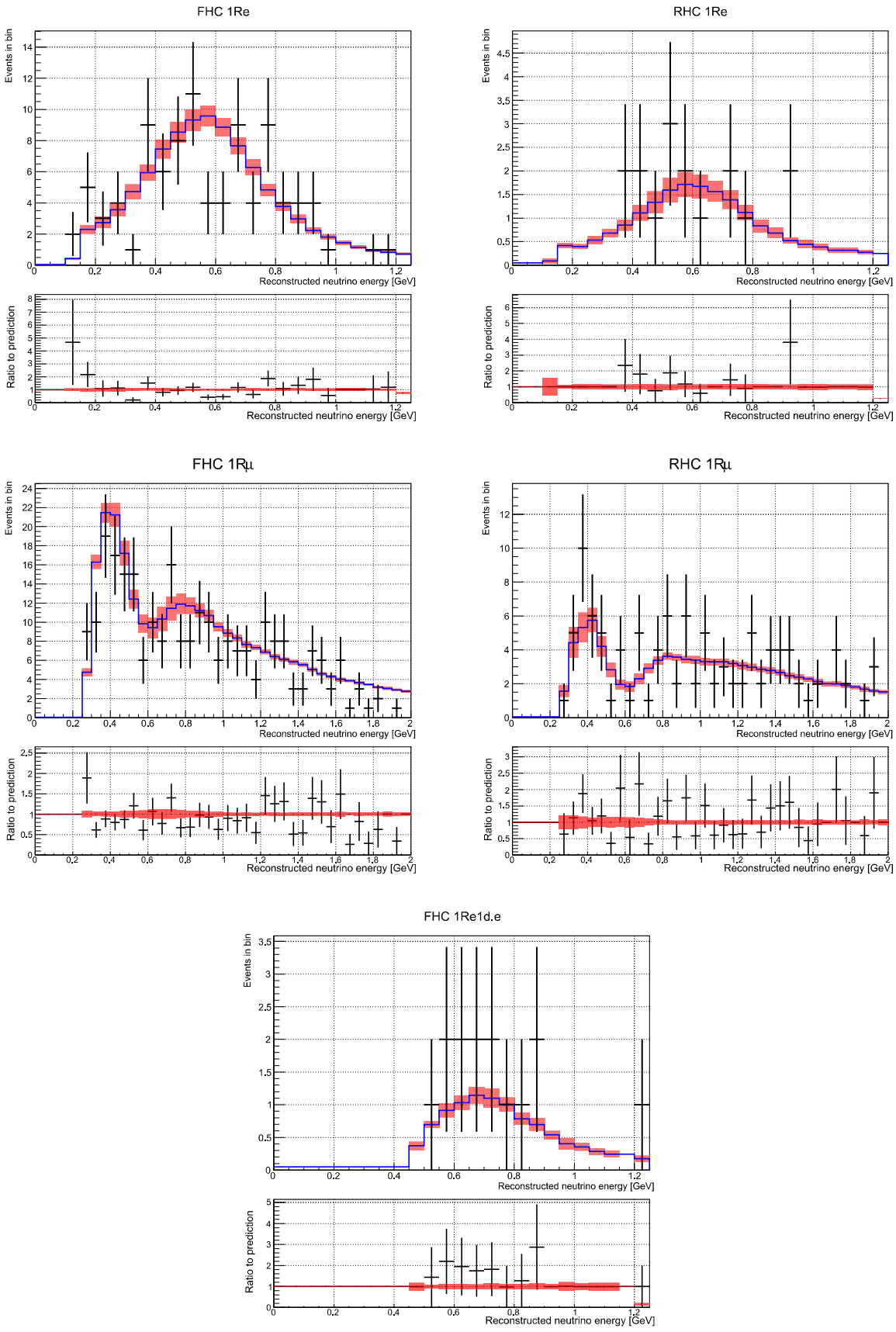


Figure B.4: Posterior predictions for the official T2K samples with updated SK detector systematics and no NCπ^0 samples without RC.

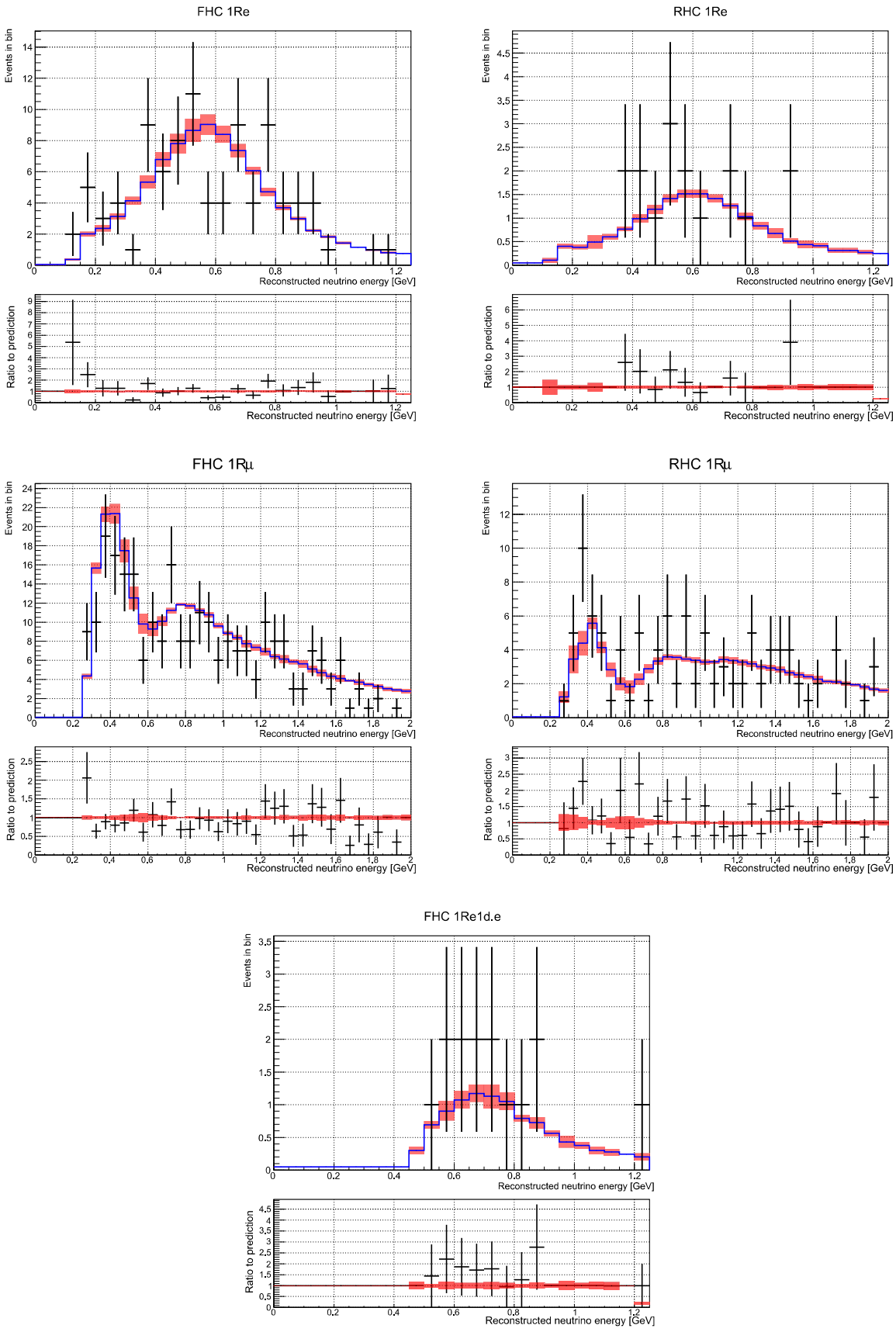


Figure B.5: Posterior predictions for all T2K samples with updated SK detector systematics and no NCπ^0 samples with RC.

B.3 Additional Data Fit Contours

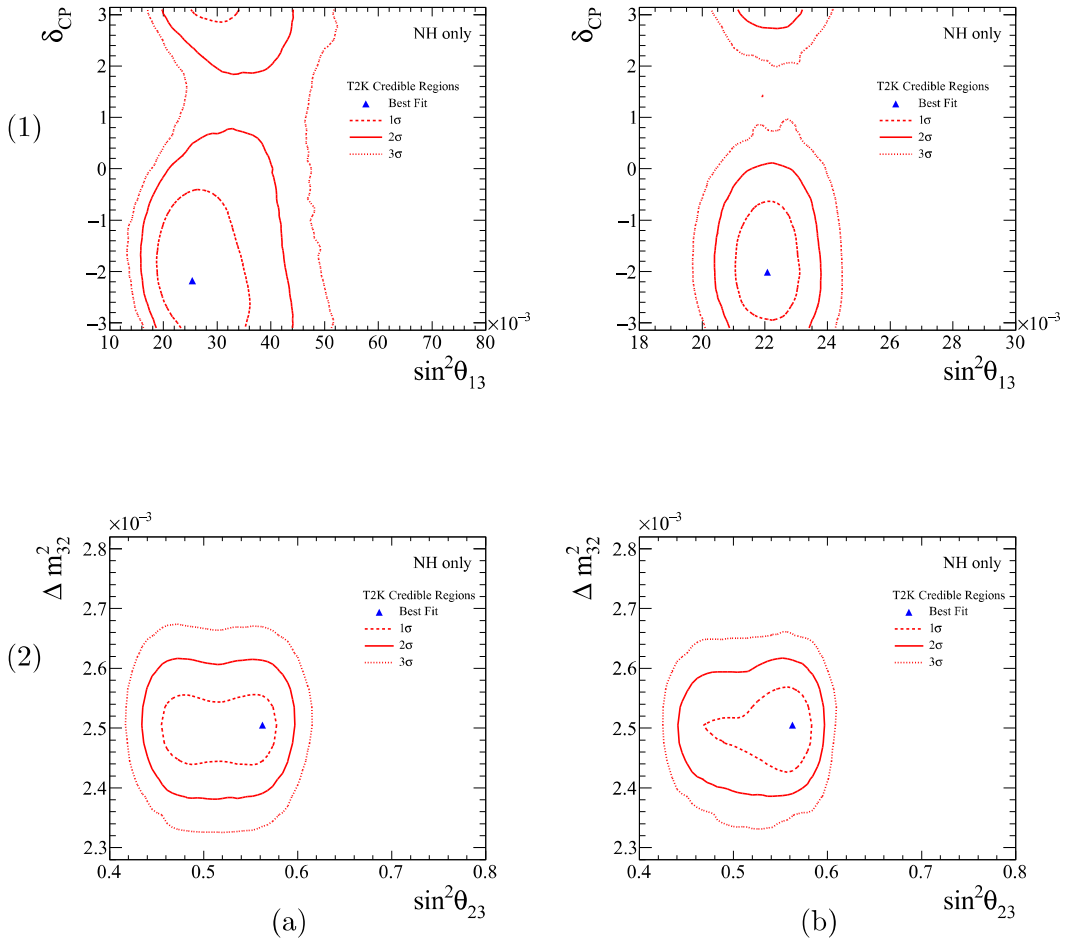


Figure B.6: Data fit contours with normal ordering. Left:woRC, Right: wRC

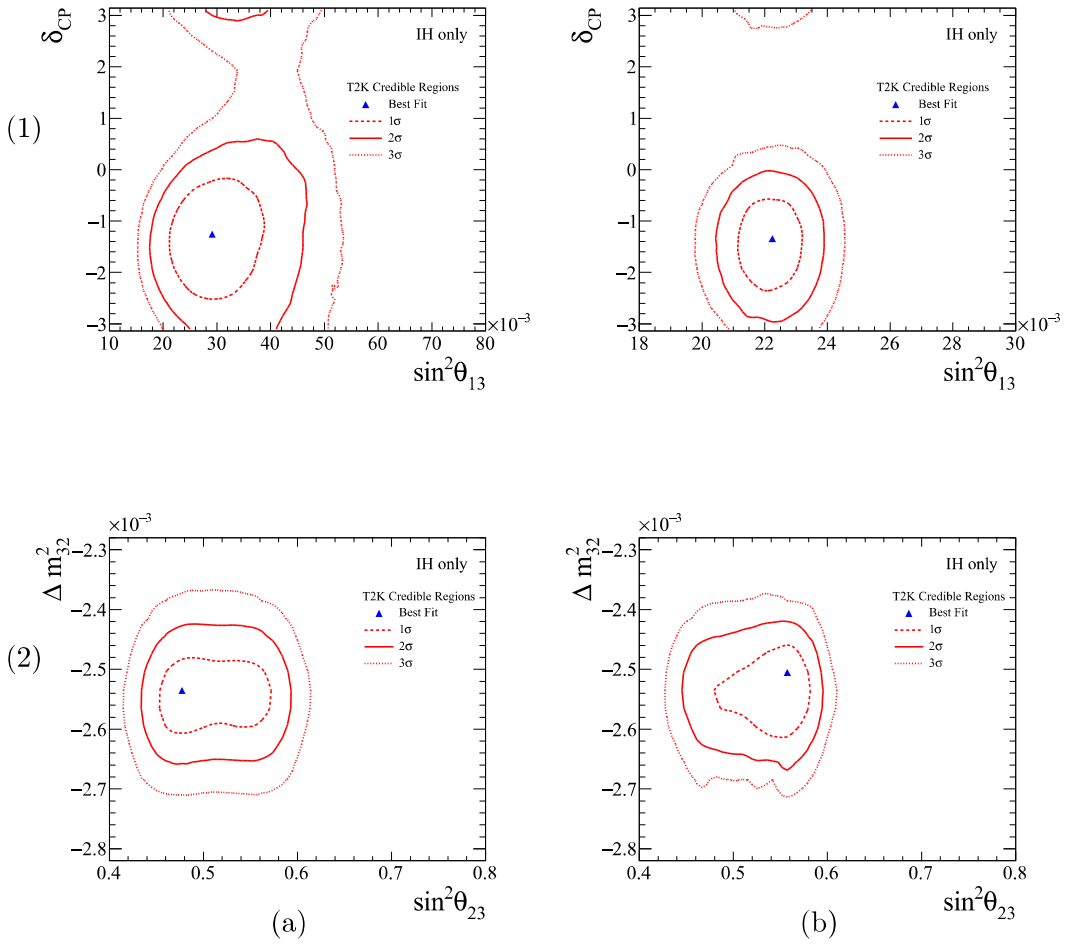


Figure B.7: Data fit contours with inverted ordering. Left:woRC, Right: wRC